GAS PHASE SWITCHING FOR PULSED POWER APPLICATIONS

A Dissertation

by

WILLIAM NICHOLS POLLARD

Submitted to the Office of Graduate and Professional Studies of
Texas A&M University
in partial fulfillment of the requirements for the degree of

DOCTOR OF PHILOSOPHY

Chair of Committee,	David Staack
Committee Members,	Gerald Morrison
	Sy-Bor Wen
	Edward White
Head of Department,	Andreas Polycarpou

May 2016

Major Subject: Mechanical Engineering

ABSTRACT

This dissertation serves to increase the understanding of applied pulsed plasma. Pulsed plasmas are experimentally studied in three contexts 1) fundamentally as switches, 2) applied in a dense plasma focus (DPF), and 3) applied as flow actuators. In these contexts the systems were studied with voltage, repetition frequency, energy, and pulse duration, ranges from 10 – 100 kV, 1 to 20 kHz, 1 mJ to 1 J, and 5 to 100 ns respectively depending on the requirements of ultimate application. These high voltages at high frequency push the current limits of spark switches. Attaining desired conditions required an understanding of the plasma switching characteristics, electrical coupling with the load, and the ultimate application. In the first experimental study plasma pulsing limitation were determined. In these experiments a DC pulsed plasma is pushed to its limits (within constraints) to determine maximum pulsing frequency while maintaining 10 kV available to drive novel applications. In these experiments 137 mJ of energy were pulsed at a frequency of 20 kHz with full-width half-max of 8 ns. Similar pulsing at 42 kHz was observed while maintaining roughly 5 kV. Operating performance was governed by electrode material, discharge gas/flow, chamber pressure, and circuit elements, both intentional and parasitic.

In the second experiment, the dense plasma focus (DPF) compresses stored energy through dynamic plasma processes to initiate fusion reactions. This requires controlled short duration pulsing. The DPF in this work is, at the time of this writing, the smallest of its kind to show evidence of pinching based on ns resolution image analysis.

The reduction in size was made possible by introducing Knudsen scaling to DPF design criteria. The motivation for investigating microscale DPFs is that neutron production efficiency may scale as a^{-3}, where a is the DPF anode radius. Smaller sized systems are also more amenable to portability. Because these devices can fuse, they are capable of generating 15 MeV neutrons and other high energy particles, and they otherwise make for convenient observation of complex plasma dynamics.

The plasma actuator for flow control was used for the delay of separation. Short duration plasma pulses were required to produce high velocity synthetic jets. Geometrically and electrically varied sets of individual actuators were computationally and experimentally investigated, compared and characterized. Also a 93 kV, 700 A peak current, 100 ns pulse duration linear array of 23 pulsed plasma actuators in series was designed and tested on a 58 cm span airfoil at Re = 400,000. At a pulsing frequency of 40 Hz and 11° stall was prevented and a drag reduction of 12% was measured. This study supplements current literature on individual actuators and is unique in reporting on full span actuated airfoils.

All of the aforementioned studies show both the capabilities and limitations of plasma-pulsed pulsed-plasmas. But, also the necessary understanding of coupling between the pulsing mechanism and its applications. A better understanding of breakdown processes, specifically charged particle generation and diffusion, both in the switch and the load will advance capabilities of such pulsed plasma applications.

ACKNOWLEDGEMENTS

I would first like to express my thanks to Prof. David Staack and Dr. Andrew Duggleby. Their insight, guidance and support have been invaluable resources throughout my education. I always enjoyed the occasional close of business "Just one thing before I go…" conversations that developed into 30+ minute technical discussions on all manner of topics. I named such occurrences 'Staack attaacks,' but I can assure you this is a tongue in cheek moniker. These casual chats encouraged critical thinking and were fantastic for improving my engineering intuition. It is satisfying to look back and see how far I have progressed as an engineer/scientist. I am grateful to have been provided such conditions for growth.

I would like to thank Prof. Gerald Morrison, Prof. Sy-bor Wen, and Prof. Ed White for their participation as my committee members. Your comments and cross-field expertise have been helpful in preparing this research.

I would like to thank my fellow PEDL students, both past and present, for their comments and assistance. Discussions with you were always enlightening and often entertaining. Special thanks goes to Nick Gawloski, John LaSalle and Matthew Burnette for their help with experimentation and data analysis on the HV switch project.

Last but certainly not least, I would like to thank both my father and my wife for their support and encouragement. Any future success will have been made possible because of them.

TABLE OF CONTENTS

Page

LIST OF FIGURES

Page

LIST OF TABLES

Page

1. INTRODUCTION

1.1 Background

Controllably switching high voltages at rapid time scales is important for wide variety of applications such as biological treatment [1] [2], reacting systems [3] [4], and materials processing [5] [6]. Current challenges are high voltage, high frequency, device lifetime, controllable energy, and matching these to the application. Presently, much of the high voltage switching is performed using transistors, but prior to the advent of semiconductors, high voltage switching relied on the use of electrical discharges in vacuum tubes. Both of these approaches have limitations and can involve complicated circuit topologies. In this work, high pressure gas phase switches are investigated. Compared to semiconductor switches these are generally higher voltage, and compared to vacuum transistors, plasma switches are more durable and efficient [7]. Plasma switches are robust – they are difficult to permanently damage, can operate in a variety of environments, and their output can be tailored to specific application. This dissertation 1) explores limits of pulsed plasmas with respect to their discharge voltage, pulsing frequency and waveform shape and then discusses two unique pulsed plasma applications: 2) the dense plasma focus (DPF), and 3) actuators for flow control.

The pulsed plasmas in this work rely on gas phase spark discharges and are a subset of transistors/switches. The image in Figure 1 shows a diagram of the basic circuit used in all experiments and pictures of the various experiments have been incorporated to highlight circuit elements where research was focused. The term ‘spark’ is used here to describe electrical discharges in gas medium which are transient in nature. These

sparks may be repetitive, but the repetition frequency is generally low compared to the time scale of the spark discharge. This work shows that repetitive sparking is capable of switching 10's kV within 100 ns or less. The state of the switching medium changes from nearly infinite resistance to a highly conductive medium, where electron number density is on the order of 10^{18} cm^{-3}, rapidly and then recover to near its initial state prior to the next spark. The ability to switch high voltage with a spark plasma at greater pulsing frequencies is limited by transition to a stable glow discharge in which no pulsing occurs. Presented here are how switching in a high pressure environment, minimizing parasitic circuit effects and convection through the spark gap/electrodes will increase conductivity, reduce pulse rise time, shorten the recovery time and delay transition to a stable mode.

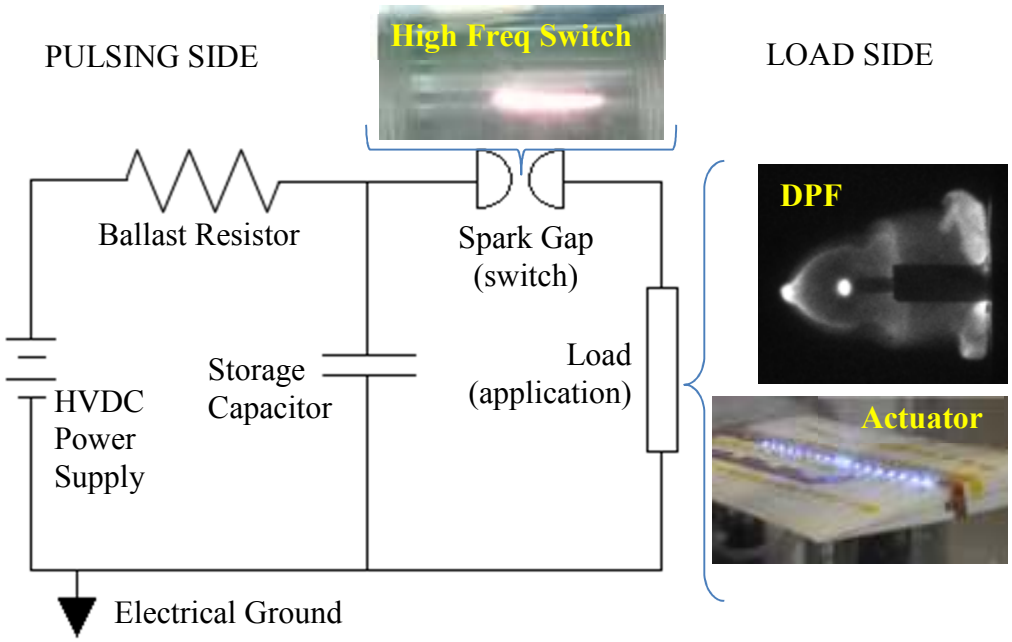

Figure 1. Basic DC pulsed circuit used in dissertation research. Essential circuit elements are labeled and inserted images show where in the circuit research was performed. A high frequency high voltage switch was used to drive DPF and actuator applications.

With regards to the first application of spark switches, the microscale dense plasma focus uses a plasma to switch 5-20 kV at 1 Hz rep rates. The DPF pulses kA on ns time scales, and spark switches are the only ones capable of doing so. The novelty of this device is its small unit size and potential to be arrayed. Currently, it is the smallest DPF studied in the literature. This work introduces Knudsen scaling as a DPF design parameter, and maintaining this scaling can assist in the development of similar devices. One challenge in this application, is to be able to switch this potential on ns timescales to get the necessary plasma condition for fusion. In order to achieve such rapid switching, a

low inductance circuit must be used. Ideally, load side inductance is on the order of nH. Because the inductance is so small, parasitic inductance in the connecting wires becomes significant, and wire length should be minimized. Arrays of such devices and higher rep rates are required for some dense plasma focus applications, such as a neutron source for active interrogation or an activator for a subcritical mass of fissile material.

In the second application, the spark plasma actuators operate in the 10-100 Hz band and switch up to 100 kV with pulse durations of 100 ns. The actuator is essentially a double spark gap circuit where the first (switch) spark gap is used to control the energy of the discharge in the second (actuator). The energy contained in the actuator discharge is used to rapidly heat the gas in the actuator cavity. High velocity jets are produced when discharge in the actuator is such that $\tau_{dis} < \ell/c$, where τ_{dis} is actuator discharge time, ℓ is an actuator characteristic length, and c is local sound speed heating. On these time scales cavity heating is a constant volume process and greater internal pressure is produced. Thermal instability (described in section 2.6) in the spark increases $\frac{dn_e}{dt}$, which allows greater current in the spark channel and consequently greater heating. The generated jet(s) can be directed to modify near surface flows. Successful flow actuation is defined in this work to be reattachment of a separated boundary layer and this requires pulsing frequency on a time scale that is characteristic of a residence time for external flow conditions. Applications in higher speed flows will require increased pulsing frequency.

1.2 Dissertation objective and motivation

The objective of this dissertation is to enable and investigate new technologies which use pulsed plasmas to drive unique applications that require good control over energy delivery. The plasma in the switching technology, the plasma in the applied device, the effects of the plasma, and how these interrelate are investigated. Motivating this work is the fact that the plasma dynamics are governed by the operating conditions and cannot be operated arbitrarily. For example, there exist low pressure applications where rapid high energy input is required and plasma discharges tend to transition to pulseless stable modes. Therefore, a robust switching systems is needed wherein pulse energy and pulsing frequency can be independently controlled for application in low pressure environments. This is made possible by controlling the switching environment and circuit parameters which provide the needed plasma properties and waveform shaping, respectively.

Sparks are good switches for several reasons. Sparks essentially create a conductor out of thin air (and other gases) via ionization processes. Therefore, the gas phase switching medium, even outside of designed operating ranges, is nearly impossible to destroy and can be considered a "self-healing" circuit element. This is in stark contrast to solid state switches that are sensitive to extreme conditions and do not heal. Air is an excellent dielectric and is capable of withstanding 0.4 to 40 kV when pd, where p is gas pressure and d is distance between electrodes, is in the range of 1-1000 torr-cm. Other factors (e.g. gas species, gas pressure, electrode material, temperature, geometry, convection) can also affect breakdown behavior, and some preferred

combination of these factors can be selected as dictated by the application. Both circuit elements and driven loads influence waveform shape (duration and amplitude) and are investigated.

This work will serve to expand the body of knowledge regarding plasma operation at high electron density and low temperature. Upon breakdown, ionization and diffusive processes can result in electron densities on the order of 10^{18} cm^{-3}, transforming the once neutral gas into a highly conductive medium on ns timescales. High pulsed power is possible because of this phenomenon – because the density of charged particles is so high, large currents can be achieved quickly and sparks are capable of transferring a proportionally large amount of power. Without regard to inherent power supply limitations, sparks can carry arbitrarily high currents indefinitely. Also, through rapid recombination, sparks readily and rapidly return to their initial non-conductive initial state. The sparks used in this work have a characteristic temperature of approximately 1 eV. This temperature can be obtained by applying conservation of energy to an atmospheric spark channel. Sparks similar to those used in this research can be created using a 1 nF capacitor charged to 10 kV, and the energy in this discharge would be 50 mJ. If the spark channel is a 5 mm cylinder with 1 mm diameter, the corresponding temperature increase of the gas in the cylinder is ~ 15,000 K (1 eV = 11,600 K) The image in Figure 2 shows regions of various plasma phenomenon as described by characteristic temperature and electron density [8]. This figure shows how expansive the plasma field is and describes where in the plasma domain this research falls by describing it in terms of electron temperature and electron number density. Gray

areas are those under current research, and the purple region indicates the operation of the switching sparks used in this research. This area is an extension of traditional low temperature plasma applications such as plasma enhanced chemical vapor deposition, and fluorescent lighting into high number density regimes.

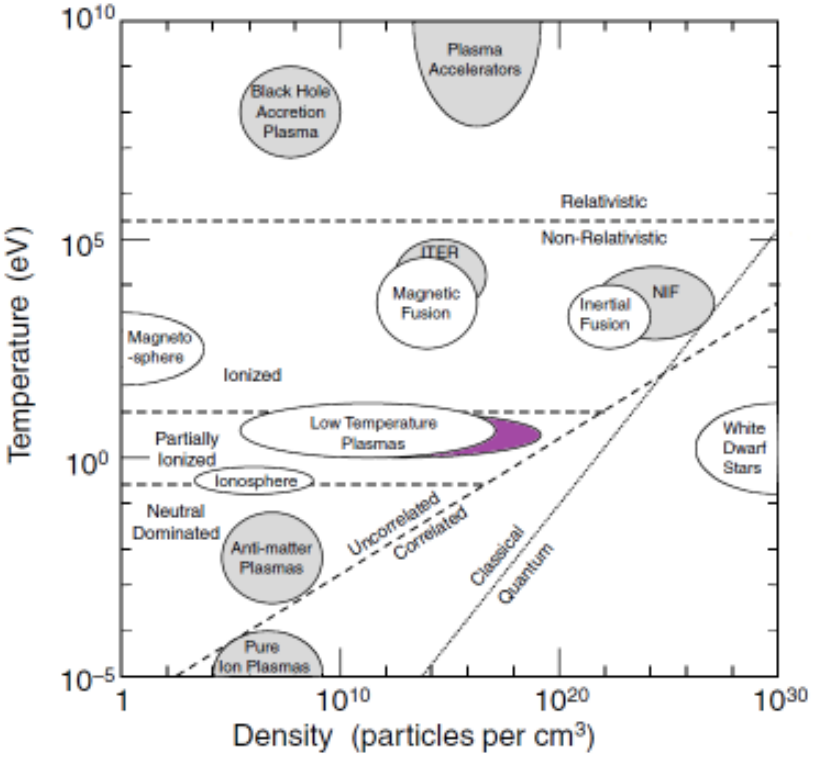

Figure 2. Temperature versus electron density map of plasma phenomenon. Regions of current research are shown in grey. The region belonging to the spark plasmas central to this research is shown in purple. Figure reprinted under fair use from **[8]**.

1.3 Dissertation overview

The topics investigated in this dissertation all involve the use of a pulsed DC circuit similar to that shown in Figure 1. Plasma switching and pulsed plasma applications are central themes of this dissertation. As such, Chapter 2 of this dissertation provides a description of plasma behavior. Mechanisms of plasma generation are introduced, and special attention is given to breakdown processes involving the use of externally applied DC electric fields. Distinctions are made between continuous and pulsed operation and how driving circuits can control this behavior. Because breakdown processes are important to plasma initiation, the Townsend avalanche and streamer/leader formation breakdown processes are explained. Background information on other relevant topics are subsections in other chapters.

In Chapter 3 the operating space of a DC pulsed plasma switch capable of delivering 10 kV at 20 kHz operation is examined (operating spaces includes power supply, geometry, gas species, gas pressure, material selection, and load characteristics). Various configurations of complex loads were tested to investigate their respective effects on pulse shaping. Such a pulsed plasma system would be capable of pulsing energy into a load which might typically not pulse. This work uses the DC pulsed plasma to drive a unipolar dielectric barrier discharge (DBD) which is characterized by Lissajous analysis. The electromagnetic interference (EMI) generated from such switching is quantized, and then EMI levels are compared to those measured when shielding is incorporated into the switch design. Similar pulsed plasmas are used to drive two unique applications and their details are described in subsequent chapters.

Chapter 4 investigates the DPF as a pulsed plasma application. A spark gap controls energy input to a low duty cycle inertial/magnetic compression discharge that is capable of creating fusion reactions. The load in this application is a single specialized geometry spark gap in 50-200 torr helium environment. Pulsed energies are in the 1-10 mJ range at frequencies below 1 Hz where currents on the order of kA have pulse widths of 100s of nanoseconds. In this application, the load is not so sensitive to energy input and pulsing frequency as it is to the speed and timing at which the energy is delivered. This limitation is mainly imposed by inductance in the external load circuit. One of the DPFs in this study has anode radius, a, of 100 μm and is the smallest reported on to date. Going to small size is motivated by the fact that neutron production efficiency may scale as a^{-3} and that smaller size is more amenable to portability. Under various pressures and pulsed energies microscale DPF pinching behavior was assessed using ns time resolved image analysis and peak current timing.

Chapter 5 studies the use of pulsed jets issuing from a pulsed plasma spark actuator to delay boundary layer separation over a stalling airfoil. In this application 100s of mJ are pulsed at frequencies in the 10-100 Hz range. The design of unique slotted plasma actuators is assisted by CFD studies and subsequent generations of actuators are characterized with high speed schlieren video, infrared temperature measurement, and impulse bit generation. Jets of air issue from slotted cavities due to the thermal expansion of air caused by rapid energy input from a spark discharge. Moreover, an array of these actuators is powered through a single spark gap discharge in air at near ambient conditions and tested on a stalled airfoil in a wind tunnel at Re =

400,000. Drag measurement and flow visualization was used to describe full span actuator performance.

Chapter 6 concludes the dissertation by summarizing the performed work within the context of dissertation objectives. First, the dissertation objectives are reintroduced and then a brief discussion follows on how those objectives were met. Then, significant experimental tasks are identified and presented in a Gantt chart that shows a timeline of the performed work. Relevant results of these experimental tasks are highlighted and reviewed. Concluding remarks about the various technologies are made and their real world application is discussed. The chapter finishes with lists of recommended future experiments that would be helpful to improve understanding of the applications and to bring them closer to real-world use.

2. REQUISITE PLASMA KNOWLEDGE

2.1 Description of plasmas

Plasma is a partially or fully ionized quasineutral gas comprised of neutral species, ions and free electrons that exhibits collective behavior. The plasma is quasineutral because the numbers of ions and electrons in the bulk plasma are approximately equal, and they exhibit collective behavior in that charged particles in the plasma respond to external electric and magnetic fields as well as internal fields that may arise from space charge distributions and local current paths. Examples of naturally occurring plasmas include the sun, lightning and polar auroras, and examples of man-made plasmas include neon lights, plasma display panels, and welding arcs.

A significant amount of energy must be absorbed by a gas for it to ionize and begin to show plasma behavior. Ionization relies on collisions between particles where the energy transferred between the two is sufficient to eject an electron from one. This is a gas species dependent threshold process requiring ~10 eV. Ionizing collisions can be induced via heat input, known as thermal ionization, or external electric fields, known as electron impact ionization, and these two methods are explained in Figure 3 and Figure 4, respectively.

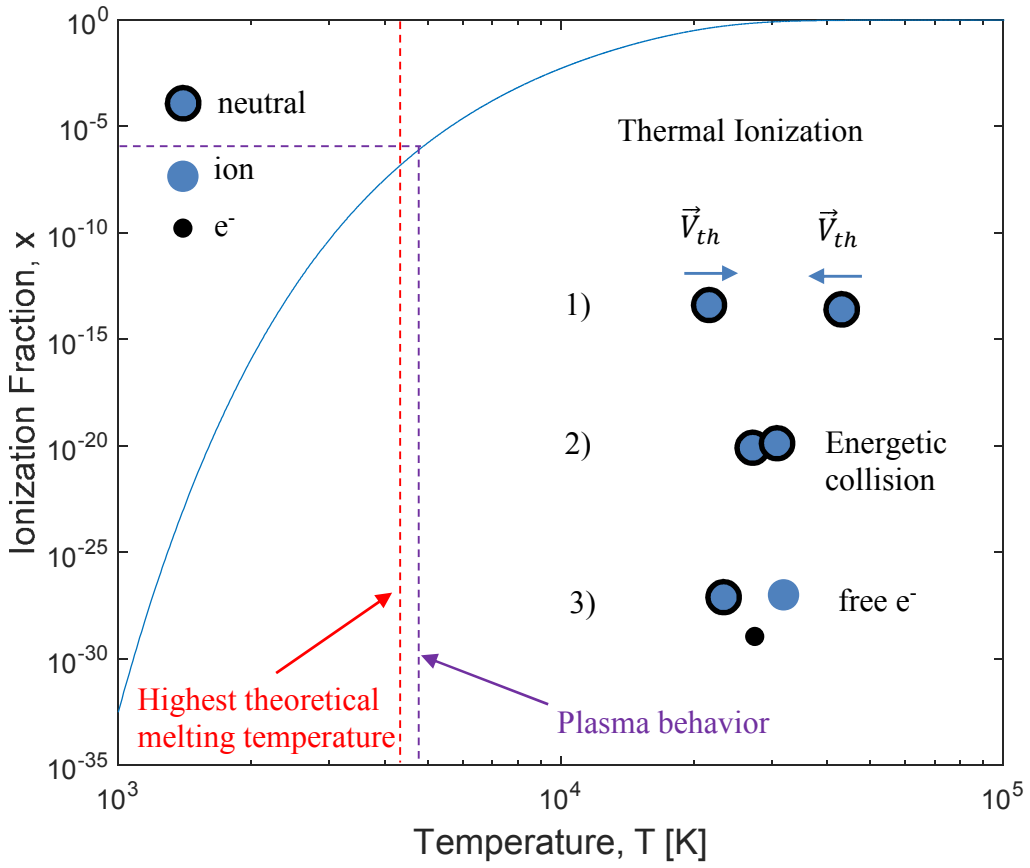

Figure 3. Ionization fraction of atomic hydrogen at atmospheric pressure as function of neutral gas temperature predicted by Saha's Equation. Highest theoretical melting temperature **[9]**.

Thermal ionization occurs when gas species have a thermal velocity great enough to ionize another neutral during a collision, and this process is shown pictorially in Figure 3. The plot in Figure 3 shows the ionization fraction of atomic hydrogen at atmospheric pressure as a function of the neutral gas temperature as predicted by Saha's Equation which assumes equilibrium conditions. Saha's Equation is given in Equation 1 below

$$\frac{x^2}{1-x} = \frac{1}{n}\left(\frac{2\pi m_e k_B T}{h^2}\right)^{1.5} \exp\left[\frac{-\varepsilon}{k_B T}\right] \quad (1)$$

where, x is the ionization fraction, n is the species number density, m_e is the electron mass, h is Planck's constant, k_B is Boltzmann's constant and ε is ionization energy (~13 eV). The ionization fraction is defined as the number of ions relative to the number of all heavy particles (neutrals and ions). Gases begin to exhibit plasma behavior at an ionization fraction of around 1 ppm. This is when electrostatic collisions begin to dominate over ordinary particle-particle interactions. To obtain plasma behavior thermally requires temperatures around 5000 K as shown in Figure 3. Not only is this a prohibitive temperature to maintain, but there are no known materials that can withstand this harsh of an environment. Thus, if plasmas are to be made thermally some method of confinement must be used to keep the plasma from contacting its surroundings. This is one of the main problems with fusion where temperatures are ~10^8 K.

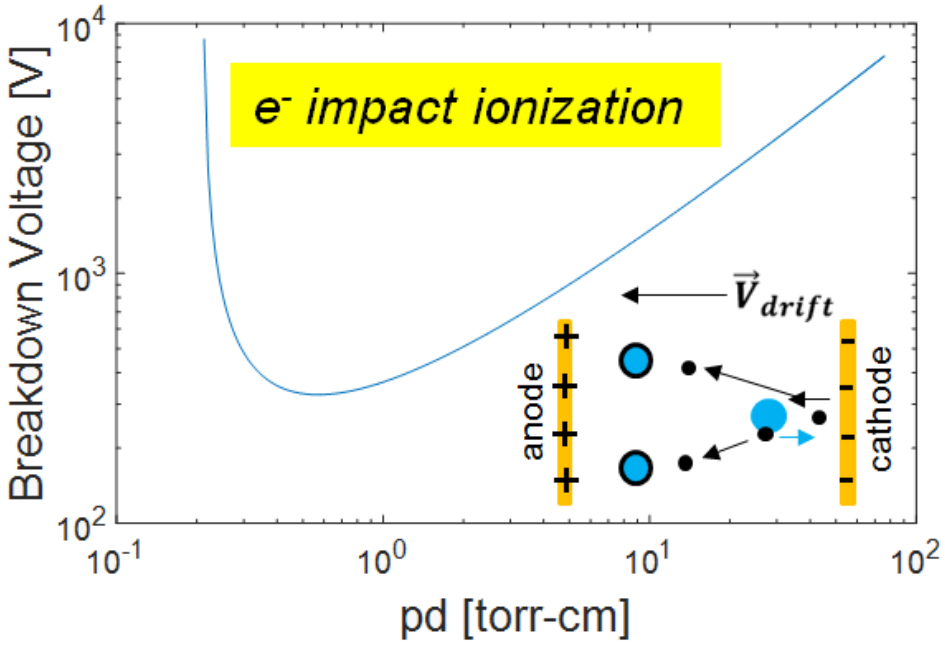

Figure 4. Representative Paschen curve (not for any specific gas) showing breakdown voltage as a function of pd (Knudsen) scaling. Species follow same naming convention as enumerated in Figure 3.

A common method for generating many lab plasmas is electron impact ionization. This method takes advantage of the fact that electrons rapidly respond to external fields, and the fact that there always exist some background seed electrons. The inset of Figure 4 describes the energy transfer of electron impact ionization. Two electrodes, the anode and cathode, are separated by some distance, *d*, and a voltage is applied across the electrodes setting up and electric field that accelerates the seed electrons in the gap towards the anode. If the electron has sufficient time between collisions, the electron's drift velocity can become sufficient to ionize a neutral upon collision. If an ionizing collision occurs, an additional electron is created in the gap and

is available to create future generations. In this way, electron impact ionization increases geometrically across the electrode gap, but electrons originating at the cathode are 'more valuable' because they have more opportunity for ionizing collisions since they must traverse the entire distance of the electrode separation. This process is referred to as a Townsend avalanche [10]. Plasmas may also be initiated using high intensity laser pulses or other energetic electromagnetic waves.

The curve shown in Figure 4 is representative of a Paschen curve, and it shows how breakdown voltage varies with *pd* scaling, which is the product of *p*, the gas pressure* in the electrode gap, and *d* the electrode gap spacing. The notions of a 'breakdown voltage' and '*pd* scaling' are briefly introduced here and will be elaborated upon in Section 2.2. The breakdown voltage is the voltage at which the plasma transitions from a non self-sustaining dark discharge to a self-sustaining glow discharge, and *pd* scaling is a Knudsen based similarity parameter that describes how collisional a plasma is. All gases have some *pd* at which the breakdown voltage is a minimum. This usually corresponds to a *pd* of ~1 torr cm and a breakdown voltage in the 100-1000 V range. For *pd* > 1000 torr-cm the breakdown mechanism shifts from electron avalanche to streamer breakdown. Our sparks follow both Paschen and Meeks breakdown.

Plasmas are complex substances – they consist of neutrals, ions and electrons, – and each of these constituent species has the ability to store energy in different internal

---

* Although pressure is used in many plasma scaling parameters, it is really *n*, the neutral particle number density, which is the physical property of interest. Pressure and number density are related by an equation of state, and when plasma scaling parameters are tabulated using *pd* scaling as opposed to the more fundamental *nd* scaling a reference temperature must be specified.

modes. Internal modes of energy storage are translational, rotational, vibrational and electronic, and each of these modes has a temperature associated with it that describes the energy distribution function of that storage mode in a given species. Molecular species have all energy modes available whereas atomic have translational and electronic storage modes. Electrons only have translational energy storage. When heat is applied to a bulk volume, as is the case with thermal ionization, energy is uniformly added to all species and modes, meaning that $T_{trans} = T_{rot} = T_{vib} = T_{elex} = T_i = T_e$. This is a thermally equilibrated system. However, when an electric field is applied to a gas, energy is preferentially transferred to electrons and ions due to their non-zero charge meaning it is possible that $T_{trans} << T_{e,i,}$ and therefore, the plasma is thermally non-equilibrated. As accelerated particles collide with neutral species and excite various energy storage modes within them, the bulk system tends towards thermal equilibrium. Spectroscopic techniques can be used to estimate the temperatures of the various modes and determine if the plasma is thermal (equilibrium) or non-thermal (non-equilibrium). Thermal plasmas are often used for high power applications such as cutting or welding metal, whereas non-thermal plasmas are more useful for lighting and chemical processing since energy is stored in modes that are beneficial to their specific applications, electronic and vibrational, respectively. The spark-type plasmas used in the experiments described in this dissertation were all initiated using electron impact by applying pulsed external DC E-fields. Our sparks are non-equilibrium, though they can transition to high temperature.

2.2 Breakdown using DC external E-fields

The characteristic voltage-current curve for a DC discharge in Figure 5 shows the three classes of DC discharges: dark (Townsend) discharge, glow discharge and arc discharge. Moving in the direction of increasing current, a voltage decrease occurs as the plasma transitions to the next class due to a shift in the source of electrons. The electron sources available at the higher current modes provide more electrons than the sources at the low current modes. Therefore, a smaller potential drop is required across the plasma to maintain discharges at larger currents. As the plasma shifts to high current modes electron number density increases and the plasma generally tends towards equilibrium.

Prior to applying voltage there already exist some electrons in the discharge gap. the only existing electrons are those few seed electrons caused by background radiation, and they are always present in steady state concentrations on the order of 1000 cm^{-3} [10]. As the applied voltage increases, the background electrons begin to move under the influence of the electric field and generate a small non self-sustaining current < 1 nA. New electrons are not created by electron impact ionization at low applied voltages (weak E-fields). For a period, further voltage increase does not correspond to an increase in current because no new electrons are created, and this voltage span is called the saturation regime because while the E-field is strong enough to move the seed electrons, it is not strong enough to accelerate them to speeds sufficient for ionization and thus the current is 'saturated.' Beyond the saturation regime, the E-field becomes strong enough to sufficiently energize electrons for impact ionization, and electron avalanching begins, the Townsend geometric multiplication from Figure 4. Corona discharges occur in this

regime and have a variety of applications and are used in copiers/printers, ozone generators, and air scrubbing.

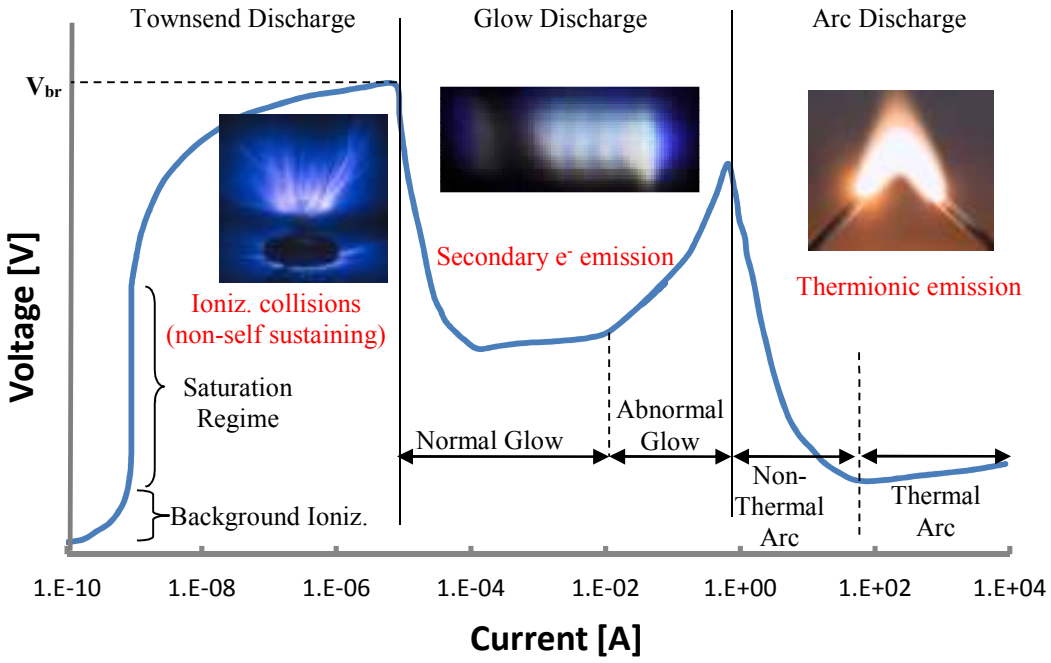

Figure 5. Voltage-current characteristics of DC discharges. V_{br} denotes breakdown voltage.

Once the breakdown voltage is achieved, the discharge transitions from corona discharge to glow discharge. Glow discharges are self-sustaining and have a cold cathode which emits electrons due to impacting energetic ions, and therefore the primary source of electrons shifts from background radiation to secondary electron emission (SEE) at the cathode. Initially, the glow discharge is in a 'normal' mode. In normal glow

mode, the voltage across the plasma is roughly constant as is the current density. Current density and plasma voltage are constant in the normal. The current in the normal glow increases as the diameter of the discharge expands, and once the discharge fills the entire free electrode surface an increase in voltage is required to increase current. This increase in voltage marks the onset of the abnormal glow mode and the once cool electrode begins to warm. Glow discharges are commonly used for lighting, surface modification, and chemistry.

When the plasma current is ~1 A the discharge shifts from the cold cathode glow discharge to an arc discharge. The main characteristic of the arc discharges is a hot cathode. Because the cathode is very hot, electrons are able to overcome the electrode's material dependent work function, and electrons essentially boil off the electrode in a process called thermionic emission. Electrons may also be removed via field emission which is due to local fields induced by the presence of ions near the cathode pulling the electrons from the electrode surface. Thermionic and field emission may occur simultaneously in process called thermally enhanced field emission. Due to the high temperatures associated with arc discharges, electrodes must be made from materials with high melting points such as tungsten or carbon. Due to the extreme temperature found in plasma arcs, they are often used for thermally intensive processes such as welding and cutting.

2.3 Continuous DC discharges and the load line

For a continuous DC discharge, it is possible to control the plasma mode by varying external circuit parameters, and many external circuits can be modeled as shown in Figure 6.

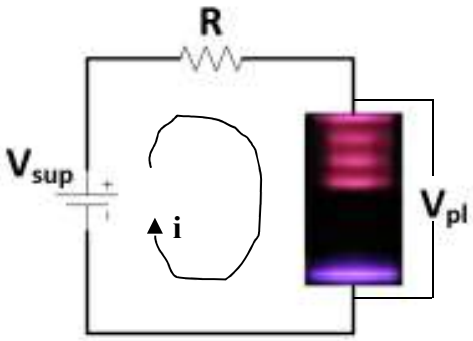

Figure 6. Circuit model for a continuous DC plasma discharge.

In this circuit a voltage source is connected to an electrode gap through a resistance R in series and supplies current i. The voltage source supplies voltage, V_{sup}, and the corresponding voltage drops are across the resistor, $V_{res} = iR$ and across the plasma, V_{pl}. Applying Ohm's Law and Kirchoff's Voltage Law to the circuit gives Equation 2 which defines the load line.

$$V_{sup} = iR + V_{pl} \tag{2}$$

The load line can superimposed upon the characteristic V-I curve for a continuous DC discharge, and the intersection of the two curves shows potential operating points of the plasma and determines what type of plasma will exist in the intra-electrode spacing. The load line can be sketched by marking a point on the y-axis at voltage of V_{sup} and connecting it to a point on the x-axis equal to i, the circuit current, with a straight line whose slope magnitude is equal to the plasma resistance. Here the choice of circuit resistor resistance and applied voltage both serve to control the current through the circuit and thus dictate in what regime the plasma will exist. The load line may cross the V-I curve in multiple locations and the plasma response is sensitive to the circuit's history. That is, if a plasma is suddenly ignited and is not current limited, then breakdown will occur rapidly and the plasma will almost immediately transition to an arc discharge. If the circuit current were then reduced by increasing circuit resistance, the plasma would gradually transition to a glow discharge.

2.4 Pulsed DC discharges

The DC circuit shown in Figure 6 can be modified so that the plasma and/or down current load sees pulses of voltage/current. This modified circuit is shown in Figure 7. In this circuit a power supply charges a capacitor C through a ballast resistor R_{bal}. A spark gap, SG, is connected down current and in parallel with the capacitor. When power is first applied to the circuit, charge accumulates in the capacitor and the voltage across the capacitor rises. Once fully charged, the voltage across the capacitor is the same as that provided by the power supply and no more charge accumulates in the

capacitor. If the capacitor voltage is above the spark gap's breakdown voltage, V_{br}, which is dictated by physical, geometric and material conditions at the spark gap, the capacitor discharges through the spark gap and can provide large current in brief intervals since it releases its stored charge in a relatively short time as compared to the capacitors charging time constant, $\tau = R_{bal}C$. Pulsed waveforms through the spark gap are load dependent and loads are, in general, complex and consist of resistive, capacitive and inductive components. Therefore, loads that have higher impedance tend to reduce peak amplitudes and broaden time dependent waveforms.

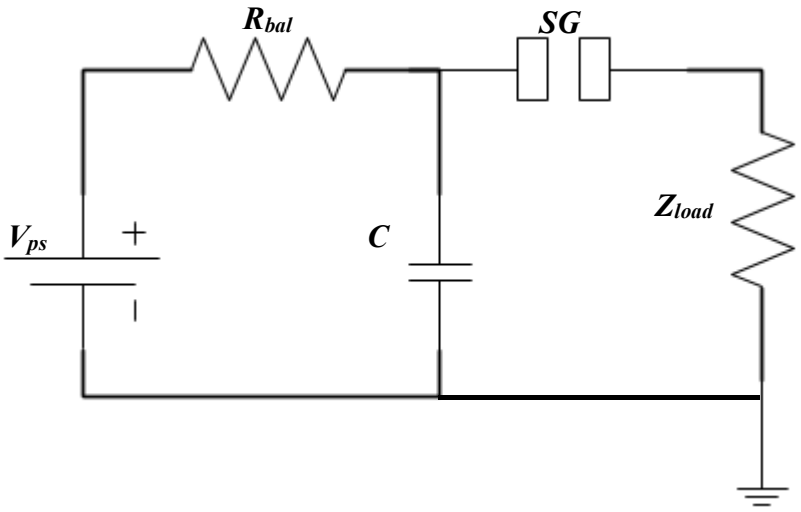

Figure 7. Pulsed DC circuit.

All real power supplies suffer from a power output limitation. Electrical power output is the product of the output voltage and current, and the maximum power output is a fixed quantity. Therefore, a real power supply provides finite current at a given voltage, and the max output current would decrease if the output voltage were increased. Pulsed DC circuits provide a means to temporarily allow high discharge currents by rapid switching in the spark gap. When the voltage across the spark gap is lower than the breakdown voltage the spark gap acts as an open switch with infinite resistance and no charge can be transferred. Once the spark gap breakdown voltage is achieved, a conductive path is formed and the spark gap can be modeled as a closed switch. With the switch closed, the charge stored in the capacitor is transferred through the spark gap to the load, and as was previously mentioned the electrical characteristics of the load will affect pulsed waveform peak and full width half max (FWHM).

2.5 Streamer breakdown mechanisms

Streamer breakdown was first described by Meek and Loeb in the 1940s [11] [12]. A new breakdown mechanism was required to account for experimentally observed discrepancies to Townsend's theory applied to atmospheric pressure discharges – especially those with >1 cm electrode spacing. Observations countering Townsend's theory and promoting the need for an explanation of a new breakdown mechanism include 1) time lags of atmospheric sparks were <100 ns, which is far faster than the time required, ~10 μs, for low mobility ions to cross the gap; 2) an apparent lack of independence of the secondary electron emission coefficient, which is a strong function

of cathode material; and 3) images indicating breakdown through long thin filaments of an erratic zigzagging nature [11], whereas Townsend breakdown is transversely uniform.

Although both Townsend and streamer breakdown processes are rooted with electron avalanching, the distinguishing characteristic of streamer breakdown is the development of locally distorted E-fields at the head and tail of an avalanche. Due to mass differences, electron mobility dwarfs ion mobility, and electrons quickly pass newly born ions. In this way the front of the avalanche is comprised of mostly negative charge and the tail of the avalanche is composed predominantly of ions. This charge separation creates local E-fields which can significantly change breakdown dynamics, and this effect was not considered by Townsend in his breakdown theory. The macroscopic effect of locally enhanced E-fields is that lower voltage is required for breakdown as compared to that predicted by *pd* scaling.

Photoionization and electron impact ionization are both significant in streamer breakdown. In air energetic electrons in the avalanche head are capable of electronically exciting nitrogen species to such a degree that photons released during relaxation are energetic enough to cause ionization. However, unlike electron impact ionization, photoionization is not spatially confined to the immediate vicinity. Photons are emitted in random directions and may cause ionization outside of the primary avalanche body. When local E-fields caused by space charge grow to of the order of the applied external E-field, secondary avalanches are drawn into the primary avalanche as opposed to drifting in the direction of the external E-field.

2.6 The thermal instability

Post breakdown transients can affect discharges in a variety of ways. One of these transients that affect constant pressure glow discharges in particular is a thermal instability called the ion overheating instability [10], and it causes the conductivity of the plasma column to change by initiating a positive feedback loop that increases the electron number density. The causal mechanism is described symbolically in Equation 3, and it can be initiated by change at any intermediary step.

$$\delta n_e \uparrow \rightarrow \delta(jE) \uparrow \rightarrow \delta T \uparrow \rightarrow \delta N \downarrow \rightarrow \delta(E/N) \uparrow \rightarrow \delta T_e \uparrow \rightarrow \delta k_i \uparrow \rightarrow \delta n_e \uparrow \qquad (3)$$

Upon breakdown the electron number density (n_e) increases, and the population of charged particles is proportional to the amount of current the plasma can conduct. Assuming a constant electric field (E), increases in current density (j) causes additional volumetric heating (jE) resulting in hotter gas temperatures (T). As the gas heats it slightly expands and the neutral number density (N) correspondingly decreases. With decreased number density, the mean free path in the electric field increases allowing charged particles, particularly electrons, to attain higher speed and thus have increased characteristic energy (T_e). Because ionization rate, (k_i) is a strong function of T_e, ionizing collisions are more frequent and thus n_e increases in a positive feedback loop. This instability is stabilized by either gas cooling [10] (gas temperature reaches steady-state) or reduction of the electric field [13]. The thermal instability is more severe at higher current density discharges and higher gas pressures. Characteristic time scales of the

instability are dependent on gas heating times, gas cooling times and also external circuit response time. Circuit response time refers to the rapidity at which capacitive discharge occur. In atmospheric microscale glow discharges instability time scales are on the order of MHz [13]. The estimated thermal instability time scale for the high pressure switching experiment is likely on the order of 10 GHz and is mainly due to increased discharge pressure. Because the instability time scale is fast relative to discharge duration (~10 ns), large $\frac{dn_e}{dt}$ results in fast discharge rise times. The instability should be taken advantage of if the objective is to reduce pulse duration, but care should be taken to prevent the plasma from transitioning to a stable mode.

3. HIGH VOLTAGE KHZ PLASMA SWITCH*

3.1 Introduction to pulsed plasma and applications

Pulsed plasmas are a type of pulsed power that can switch supplied electrical energy in order to drive a load. Pulsed power systems of any type must first store energy for a period of time and then release that stored energy over a comparatively short time scale. Therefore, in pulsed plasma applications the peak power of a given pulse is much greater than that which is continuously supplied by the power source, but energy is still conserved in the system at large. Energy may be stored mechanically (flywheels, springs, compressed air, thermal reservoirs), chemically (batteries, energetic materials), and electrically (electrostatic fields, magnetic fields). Some of these storage media are more amenable to pulsing than others. For example, although a fly wheel stores energy, it is impractical to pulse such a system, and without the use of other system components, it is not possible to increase the power output of the flywheel. Considering chemical potentials, energetic materials can 'pulse' power in a very limited sense. For example, a mass of nitroglycerin, which is sensitive to physical shock, will shift equilibrium states when disturbed and in the process release considerable energy. The problem with this storage mechanism is twofold. For one, the nitroglycerin will 'pulse' once, and after that there is no more nitroglycerin because it has undergone a chemical shift. After a single use the energy source is consumed in its entirety and must be replenished. Second, the

* The work presented in this chapter will be submitted for publication with the working title *"Plasma switching of 10 kV at 20 kHz"*

release of this energy is not well controlled. In applications such as mining and demolition, precise control of energy release is not as important as the position of detonation or its timing.

Storing energy in electrostatic and magnetic fields provides more precise control over energy release as compared to mechanical and chemical storage media. Energy can be stored in capacitive elements (electrostatic fields), and it can also be stored in inductive elements (magnetic fields). These elements can be directly implemented into circuits and magnitudes of capacitance and inductance are controlled by sizing these passive circuit elements. Some stray capacitance and inductance is always present in any real electrical circuit and may be negligible depending on the application. Equations 4 and 5 relate stored potential to basic circuit parameters for capacitive and inductive elements, respectively.

$$E_{cap} = \frac{1}{2} C V^2 \tag{4}$$

$$E_{ind} = \frac{1}{2} L I^2 \tag{5}$$

where, E is the stored energy, C is circuit capacitance, V is voltage, L is circuit inductance, and I is current. Using these equations, engineers can design circuits to deliver specific amounts of energy to a load. Although energy can be stored in magnetic fields, these fields tend to resist changes in current and therefore slow the rate at which energy (effectively, charge) is transferred. In this work inductance is viewed as a

hindrance and is not considered as a viable storage mechanism. The rate at which capacitive energy is released is largely controlled by inductance and resistance, whether intended or parasitic, inherent in the pulsing circuit and the load itself. Thus, if 1 joule of energy stored in a capacitor is released in 1 nanosecond, the pulsed power is 1 gigawatt, which is far greater power output than is achievable from continuous use of conventional power supplies. The pulsing frequency (or discharge frequency, both terms are used interchangeably in this work) of capacitive discharge circuits is limited by the current available from the power supply and any resistance between the power supply and the storage capacitor, and it is by this pulsing limitation that energy is conserved in the pulsed system.

Pulsed plasma research is still a relatively young field, and continued discovery of their uses drives advancement. In addition to the two specific applications investigated in this dissertation – microscale dense plasma focus, and plasma actuator for flow control – pulsed plasma systems have found use in a variety of other applications including, but not limited to, biological treatment [1] [2] [14] [15] [16], chemical treatment of gases/liquids [3] [4] [17] [18] [19], and materials processing [5] [6]. In the biological applications, pulsed plasmas can be used for decontamination of surface bacteria, mitigation of algal blooms, electroporation for food processing, and even self-destruction of melanoma. Pulsed plasmas can be used for environmental remediation by removing NO_x from flue gas, breaking down volatile organic compounds, and reducing other pollutants from effluent gases/liquids. Also, pulsed plasmas can be used for

materials processing as is done with the spark sintering of alumina, or in ion implantation of steels to increase surface hardness.

There are several aspects of pulsed power systems that are crucial to their operation/utility, and therefore impose limitations on system performance. In this discussion an arbitrary pulsed power system will be conceptualized as being comprised of four different components/processes: a driving energy source, an energy storage medium, a pulse shaping component/switch, and the load. One of the most important parameters in any system is its power to size ratio, and this becomes increasingly relevant with the push to make these platforms portable. Laboratory pulsed power sources range in size from ~1000 cm^3 to several thousand m^3, but they are surprisingly similar with respect to their power density which is within the range of 1-10 GW_{pk}/m^3 [20]. Advances in dielectrics and capacitors will have the most impact on maximizing energy density, provided that a suitable driving source is available and already integrated into the mobile platform.

Rapidly switching high voltage in a controlled manner is the main function of pulsed power systems, so in order to advance this technology, systems must switch higher voltages more rapidly and reliably than that of previous generations. Two types of switching mechanisms are commonly employed in pulsed power systems, and they can be classified as belonging to one of two groups: 1) solid-state devices and 2) gas phase discharges. Each group has its benefits and drawbacks. Solid state devices, of which MOSFETs are the most common, are well-controlled and may rely on complicated circuit topologies to achieve desired output voltage waveforms [21] [22] [23]. Although

the waveforms produced are high quality and approach idealized square wave pulse shape, solid state switches are limited in the range of voltages they can reliably switch because of dielectric weaknesses internal to the transistor. Most of the MOSFET switches are capable of voltages up to 1 kV [22] [24] [25] at 1 kHz pulsing frequencies, and some research has shown that arrays of IGBT are capable of pulsing 20 kV at a nominal 30 kHz and up to 400 kHz for short durations [26] because pulsing is mainly limited by unit cooling capabilities. In addition, the use of semiconductors as a switching mechanism may imply the use of digital logic such as CMOS circuits, and these devices have shown susceptibility to radiated EMI [27]. Spark gaps, however, are not susceptible to EMI because they do not rely on digital logic components. Therefore, gas phases switches are able to hold high standoff voltages, pulse high current, and operate in electronically harsh environments.

Plasma physics govern the spark gap discharges that are used in pulsed power applications. Plasma is a high energy state of matter that is essentially an electrical charge transporting gas. Behaviors governing plasma dynamics can be taken advantage of and used to tune pulsed power systems for their desired effect whether it be surface modification or fusion studies. Plasmas also make excellent switches since they cannot be damaged by high pulsed energy. The gas in the discharge gap switches between a conductive and non-conductive state without permanent damage ever occurring to the gas. In fact, self-healing (as well as energetic release) processes require very short time scales which are the areas of interest in many high energy physics applications. This is

unlike most conductors that eventually degrade from thermal cycling. This switching resilience is fundamentally important to pulsed power systems.

Spark gap switching offers an alternative to solid-state switches. Work undertaken by Rahaman, et al [28] investigated rapid discharges using a spark gap circuit similar to the one used in this work, and they were able to switch 800 V at repetition rates in the MHz range. Although these frequencies are 100× higher than those sought in this experiment, pulsed voltages are reduced by a factor of 10× and thus limit the scope of viable loads. One of the attractive features about spark gap switches is that they can hold >100 kV [29] and transfer large currents without being damaged. Pulsing frequency is primarily limited by the power supply, spark gap recovery time, and mode transitions resulting from thermal instabilities in the switch discharge region.

There also exist secondary effects that may have unwanted consequence on system behavior. These secondary effects include electrode degradation/contamination and thermal management in the discharge zone. Unless electrodes are constructed of hard materials like tungsten, discharges will erode electrodes at potentially unacceptable rates, and after extended use changes in spark gap spacing will become significant and alter breakdown characteristics. If the supplied voltage is not adjusted for the increased spark gap distance a complete cessation of pulsing is inevitable. Moreover, even if voltage is adjusted to compensate, the as-designed energy per pulse may also affected and may no longer be suitable for the intended application. Degradation of graphitic and tungsten electrodes is compared in the high voltage kHz switch section of this work.

Contamination of the electrodes is also a potential issue, especially if pulsing occurs in a reactive discharge environment, such as one that contains oxygen. Because the pulses are very energetic and occur in a reactive environment, there is the possibility of unwanted chemistry occurring at the electrodes. Oxidation can cause insulating layers to form on the electrodes, adding unwanted resistance to the spark gap. The immediate consequence of this is that stronger electric fields are required for switching, thus changing pulsing characteristics. For this reason, inert gases such as helium are excellent candidates for gas phase switching.

Electrode degradation and contamination may occur in concert. Consequences of this may be severe and in the limiting case would halt pulsing altogether. Consider the following - energetic pulses gradually erode soft electrodes, and during this ablation process the electrode material is vaporized and deposited elsewhere. Deposition along surfaces in the vicinity of the electrodes can entirely change discharge characteristics by providing unintended paths to electrical ground. This is especially problematic for discharges occurring along a dielectric surface because the conductive vaporized material will collect and eventually short circuit the high resistance spark gap.

Temperature increase at the electrodes and in the spark gap can alter discharge behavior as previously discussed via thermal instability. Each pulse imparts energy to the gas thus heating it and causing it to expand. Lower density regions increase the reduced electric field and electron temperatures increase as does electron number density. Joule heating and collisional processes can cause higher temperatures at the electrodes. As pulsing frequencies increase, thermal energy accumulates more rapidly in

the electrodes and local temperatures rise. As the electrodes heat, electron generation can shift to a thermionic mode which is a stable non-pulsing discharge that requires lower breakdown voltage. For these reasons, careful material selection, adequate thermal management, and prudent circuit design are necessary to avoid thermal instability.

Designing adequate heat removal can be complicated because very often good conductors of heat are good conductors of charge, so mechanisms relying on conduction are generally out of the question. Temperatures and densities of the gas are usually not great enough to make radiative heat transfer an attractive solution, so convection is an attractive mode for heat rejection. High gas flow rates maximize convective coefficients and promote lower temperatures. An alternative is to have electrical discharges occur in liquid. Previous research has shown that it is possible to achieve nanosecond rise rates of ~10 kV pulses immersed in liquid [30]. At lower pulsing frequencies, discharges in liquids should be capable of maintaining lower temperatures due to increased fluid medium density.

There are also practical physical limitations to spark gap discharges. For one, average discharge power cannot exceed that provided by the power source. Naturally, this limits pulse energy or pulse frequency if the other is held constant. Secondly, in the absence of pulse shaping, the quality of the pulsed waveform relies heavily on how well it is matched to the load and to the extent that parasitic components of the connecting circuit have been minimized. Another limitation to rapid spark gap discharges is that good load matching between switch and load is unlikely. Because these switches do not generate ideal square waves where power is constant and either ‘on’ or ‘off,’ load

matching during the rise and fall periods would require electrical characteristics of the load to change on a time scale similar to that of the rise and fall rates. Loads that are not well matched will be less efficient since a portion of the incoming pulse will be reflected, and this reflection (inefficiency) can be observed in circuit ringing.

3.2 Dissertation objectives

The objective of these experiments is to achieve reliable 20 kHz switching of 10 kV using a spark gap and pulsing RC circuit. Relays, conventional transistors or otherwise semi-conductor materials are not robust enough to operate at these voltages and pulsing frequencies. The plasma switch design evolved over three generations, and the operation and pulsing characteristics of each is discussed. The first generation was designed to be easily configurable with respect to gas fill pressure, gas convection in cross flow, electrode gap spacing, electrode material/geometry, and external circuit components. These features made Gen1 convenient for determining general system behavior. The Gen2 was designed to investigate effects of convection along the discharge direction. The Gen3 swtich incorporated the configurability of Gen1 with the axial convective gas flow of Gen2, and it was also designed to reduce stray capacitance and inductance to provide faster switching, shorter pulsing, and delayed thermal instability. Plasma switches were predominantly DC pulsed, but some early experiments investigated using AC power sources. The DC systems are discussed first in the order they were developed, and then AC pulsing circuits are described. Available AC hardware (power supply and transformer) was insufficient to meet the desired pulsing

characteristics of 10 kV at 20 kHz. EMI mitigation and electrode degradation are also characterized. Additionally, a DC ns-pulsed DBD load is powered by the plasma switch and its performance is characterized using Lissajous analysis. Such a switch is capable of driving a load in environmental conditions that would normally encourage the plasma to transition to a stable discharge mode. Successful development of high performance gas phase switches will enable other high voltage pulsed applications in unfavorable environments.

3.3 Experimental setup

In general, a customizable load circuit is electrically connected to the low voltage side of the plasma switch in the pulsing circuit. Power supply current and voltage are set to near maximum values. Supplied current was limited to a maximum of 40 mA by the power source. The power supply charges a 440 pF capacitor, C_1, through the ballast resistor, R_{bal}, which was constructed of 20 10 MΩ resistors rated for 16 W each, allowing total power of 320 W. Resistor terminals were soldered to flexed copper strips that supported the resistor array above an acrylic baseplate to allow flow across a majority of the resistors' surface area. Sustained supplied currents higher than 25 mA cause overheating in R_{bal}, but forced convection of ambient air across R_{bal} helps mitigate this risk and facilitates prolonged high current testing. This was an issue for long duration experiments performed on the Gen3 transistor. When the voltage at C_1 reaches the breakdown potential a discharge is initiated in the primary spark gap. The capacitance of C_1 must be large enough to destabilize a continuous discharge and force

pulsing, but it should not be so big as to resist changes in the external electric field which would cause thermal instability. In general, the load side of the primary spark gap consisted of a resistor connected to ground in parallel with a DC pulsed DBD discharge that grounded through a shunt.

The pressure vessel is purged and filled to a predetermined pressure and a needle valve is used at the gas outlet to control and maintain flow rate. Pressure was monitored at the gas cylinder regulator and at a pressure gage downstream of the pressure vessel near the gas outlet. Waveforms for load voltage, V_{load}, were measured with respect to ground using a PVM-4 (80 MHz; 50Ω; 40/60 kVDC cont/pulsed) North Star high voltage probe connected to a 2 GHz LeCroy Waverunner 204 MXi oscilloscope for data acquisition. Discharge frequency, f_{dis}, FWHM and rise/fall times were determined from acquired voltage waveforms. Current was determined by measuring the voltage drop across a shunt resistor located between the DBD load and electrical ground. Experiments were performed under both short (ms) and long (mins) time scales to examine operational stability.

3.3.1 Gen1 DC switch

The first generation, Gen1, switch and pulsing circuit are pictured in Figure 8 and the corresponding circuit diagram is shown in Figure 9. Gen1 transistor was housed in a single block of 152 mm x 152 mm x 76 mm acrylic with 26 mm wall thickness and could hold internal pressures of 15 atm without significant leakage. The total pressurized volume was 500 cm^3, and pressure in the system was measured by the gas cylinder

regulator and a pressure gage near the gas outlet (not shown in Figure 8). All circuit diagrams describe the power supply used, passive elements, and voltage measurement locations. The breakdown voltage V_{br}, is the pulsed voltage to the transistor, and the load voltage, V_{load}, is the pulsed voltage to the load down current of the transistor. Current measurements were made using a shunt between the DBD and ground, and V_{shunt} is indicated where applicable.

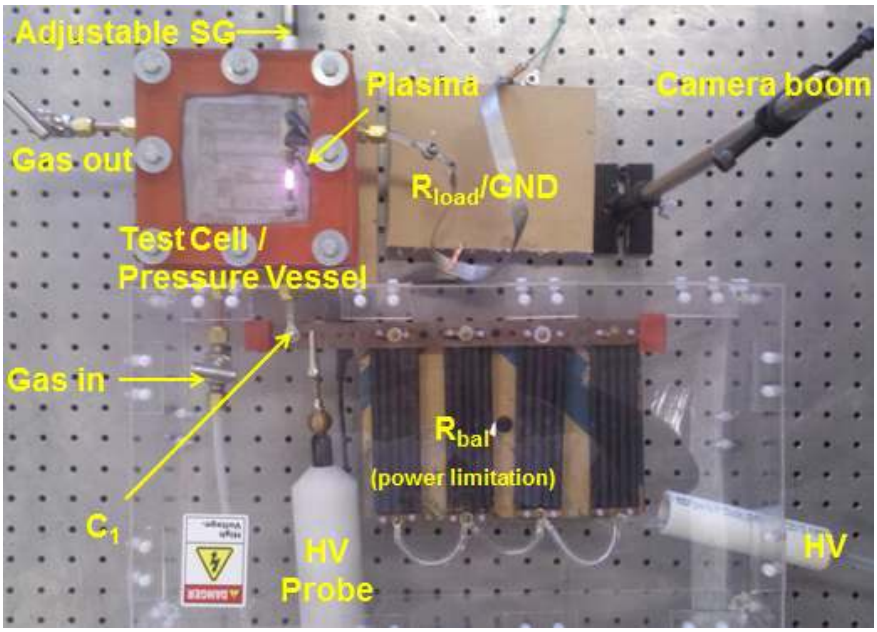

Figure 8. Gen1 switch showing pressure vessel and pulsing circuit.

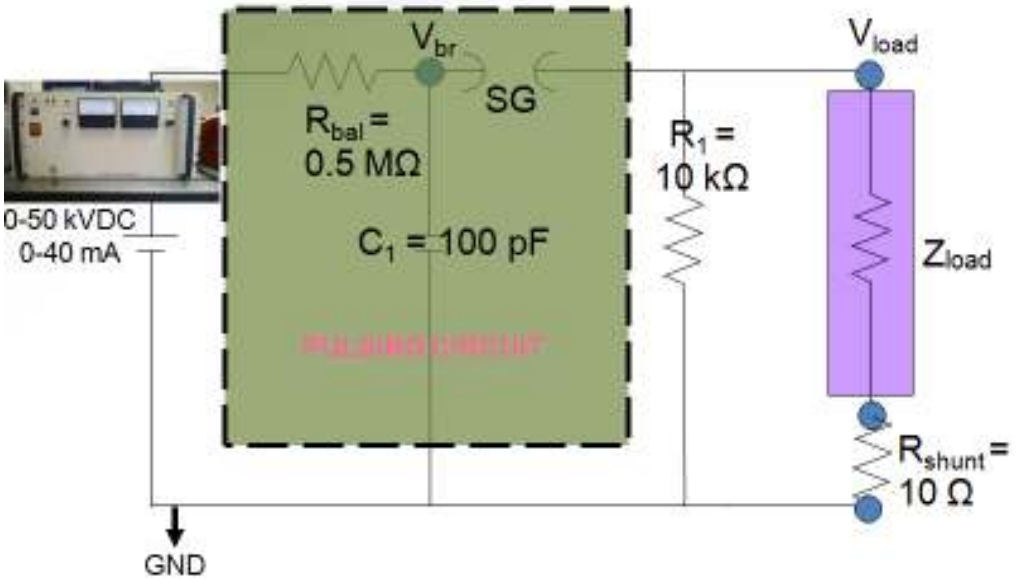

Figure 9. Circuit diagram of Gen1 switch. Values of passive elements were varied, and those shown are representative.

The power supply is a 2 kW Glassman Series LT DC power supply capable of supplying up to 40 mA at 50 kV where both output voltage and current may be independently controlled. The power supply output connects to an isolating ballast resistor in the pulsing circuit, and the pulsing circuit also contains a primary capacitor, C_1, and a variable distance spark gap, *SG*, which is housed in the pressure vessel. These components are common throughout generations.

The ballast resistor consists of twenty 10 MΩ resistors connected in parallel, and each resistor is rated for 16 W, allowing sustained power dissipation of 320 W. With an equivalent resistance of R_{bal} = 0.5 MΩ, sustained current as high as I_{ps} = 25 mA can be applied without overheating R_{bal}. The low voltage side of R_{bal} is connected to the spark gap via high voltage feed-thru on the pressure vessel, and primary capacitor C_1 is

connected to ground in parallel with the spark gap. Typical values of C_1 are on the order of 100 pF to prevent the discharge from becoming stable while still maintaining high discharge frequency and supplied energy. Corona dope or silicone end caps were applied to high voltage conductor segments having small radii of curvature in order to minimize coronal current leaks. For user safety HV_{in}, R_{bal}, and C_1 are located behind a 5 mm thick acrylic barrier to prevent unwanted contact with high voltage components.

The Gen1 vessel was open on the top face and sealed by compressing a 3 mm thick silicone gasket between the acrylic block and a 26 mm thick acrylic lid. The lid is fastened to the vessel using (8) 4" long ¼"-20 thru-hole bolts equally spaced about the vessel's perimeter. Electrical and gas feed-thrus are made using compression fitting adapters that secure to the pressure vessel walls via thru-holes tapped for ¼" NPT. Electrical feed-thrus are solid conductors with insulation rated for 60 kV, and gas feed-thrus are fitted with needle valves for flow control. Gas fill purity is ensured by repeated filling and purging of the pressure vessel prior to use and by continuous gas flow through the pressure vessel.

The electrodes used in Figure 8 are round tipped size 10 and size 8 brass screws on the anode and cathode, respectively. The cathode is held by a ceramic standoff mounted to a ½"-40 screw that passes through the pressure vessel wall. The screw, which was custom made on the lathe for very fine thread pitch, displaces the cathode by 0.6 mm/rotation, and the spark gap has a maximum separation distance of 260 mm. Electrode connections were designed such that various electrode geometries and materials could be investigated. A close up image of the spark gap region in Figure 10

shows how electrodes were secured as well as how air is directed through the spark gap. Spark gap separation distance is measured using digital image analysis. A boom mounted Nikon D90 digital camera with a macro lens images the spark gap, including the high voltage electrode of known diameter. Spark gap distances were calculated using image scaling.

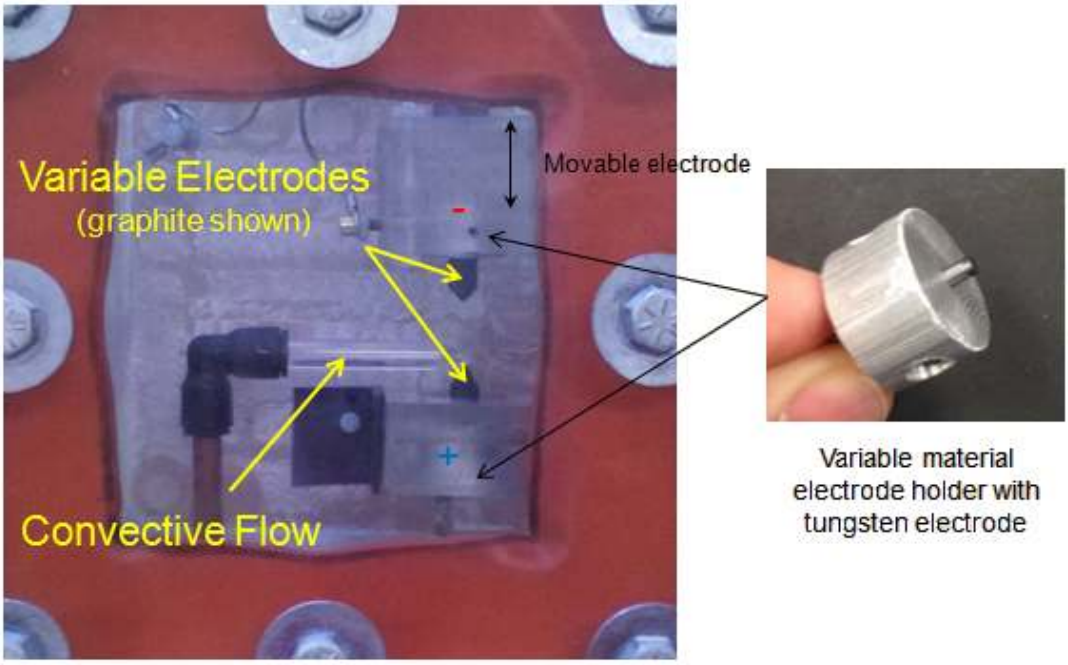

Figure 10. Close up image of Gen1 switch showing electrode holders and convective flow.

The gas inlet was directed such that a jet of high pressure gas would flow perpendicular to the discharge so that convective effects on the discharge and electrodes

could be investigated. This feature is also shown in Figure 10. Gas flow rate and chamber pressure were controlled using a needle valve on the gas outlet.

The load used for all generations was a DBD plasma in parallel with resistor R_1. A schematic of the DBD is shown in Figure 11 along with an image of the discharge. The DBD plasma was generated between a ½" diameter copper cylinder and an aluminum plate which was connected to ground through a shunt resistor. A 1/16" thin quartz disc and a 1 mm air gap separated the copper tube and aluminum plate. Air gap distance is adjusted using a micrometer precision linear traverse stage. The DBD plasma is modeled as a complex load, Z_{load}, having capacitive and resistive elements. Lissajous characterization of the DBD is discussed in a following section.

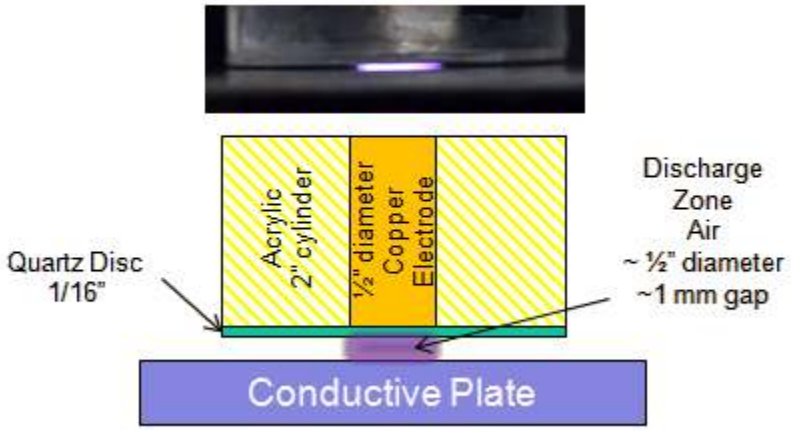

Figure 11. Image (top) and schematic (bottom) of DBD load used in all experiments.

3.3.2 Gen2 DC switch

An annotated image of the second generation transistor is shown in Figure 12, and approximate dimensions of the pressure chamber are shown in Figure 13. The external circuit was similar to that used in the Gen1 transistor, and the cell was constructed by compressing a 6" long glass tube of ¼" wall thickness with flanges for commercially available sanitary fittings. A metal guard surrounded the glass tube for safety in the event of an overpressure failure. Gas and electric feed-thrus were similar to those used in Gen1, and although rotameters were initially installed to measure flow rates, the flow rate was too large to be measured.

The Gen2 design was driven by the desire to investigate effects of convection along the axis of the discharge from anode to cathode, from cathode to anode and from both cathode and anode. Figure 12 shows the arrangement used for investigating simultaneous convection from anode and cathode. To investigate the other two flow patterns, the valve in Figure 12 was replaced with a T-fitting and valves were installed in lieu of rotameters. Large stray inductance is inherent in this design since relatively long lengths of solid conductor spanned the distance of the sanitary T-fittings on both ends of the pressure vessel. Gas and electrical paths were joined inside the pressure vessel using plastic T-fittings which occasionally resulted in unwanted breakdown to the inner sanitary fitting walls. Another issue with this generation was that spark gap adjustment was difficult to precisely and repeatably control.

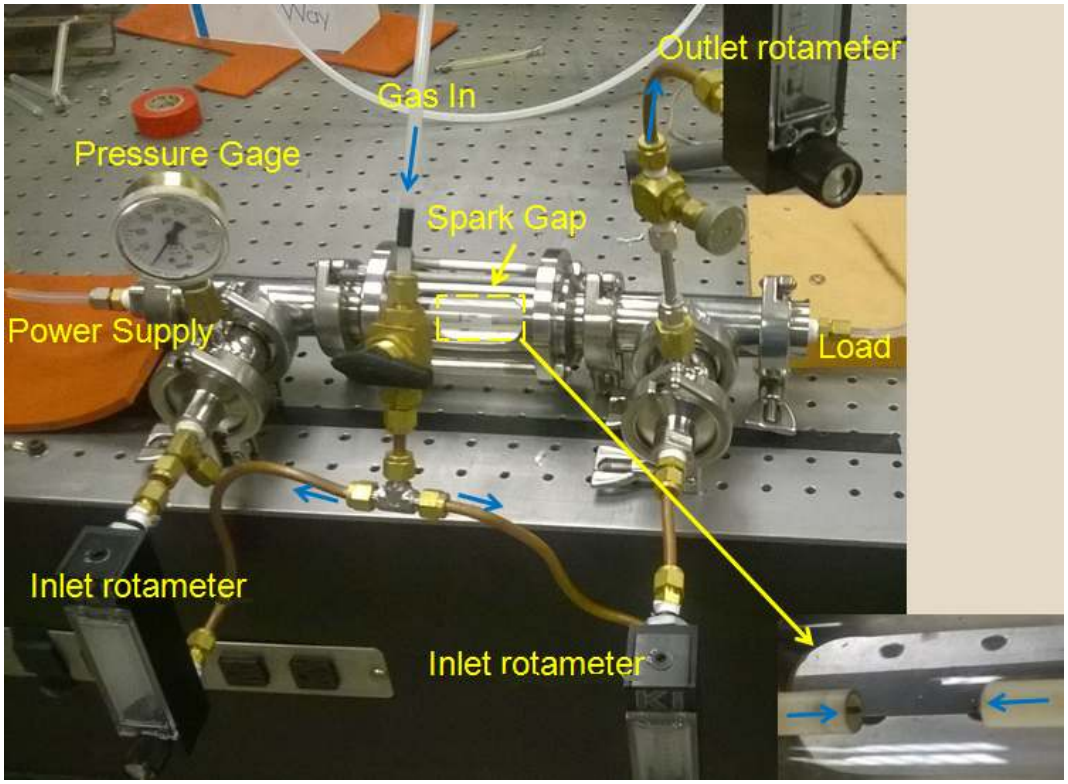

Figure 12. Annotated image of Gen2 switch used for investigating convection parallel to discharge.

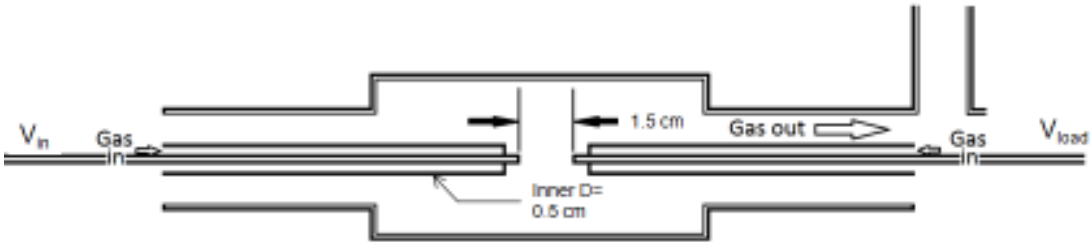

Figure 13. Approximate dimensions of Gen2 pressure vessel and spark gap.

3.3.3 Gen3 DC switch

The Gen3 switch was compactly designed for low stray inductance. An annotated image of the Gen3 switch is shown in Figure 14. Since a primary objective of this design was to create ns duration pulses, the load side of the external circuit is slightly modified from that used in Gen1 & Gen2 with the difference being the inclusion of a second variable distance spark gap down current from the primary spark gap. A circuit diagram for the Gen3 switch is shown in Figure 15. The values of the circuit parameters given in Figure 15 are representative and were varied between experiments. For example, in some tests the load side did not include a spark gap and R_1 = 1 kΩ.

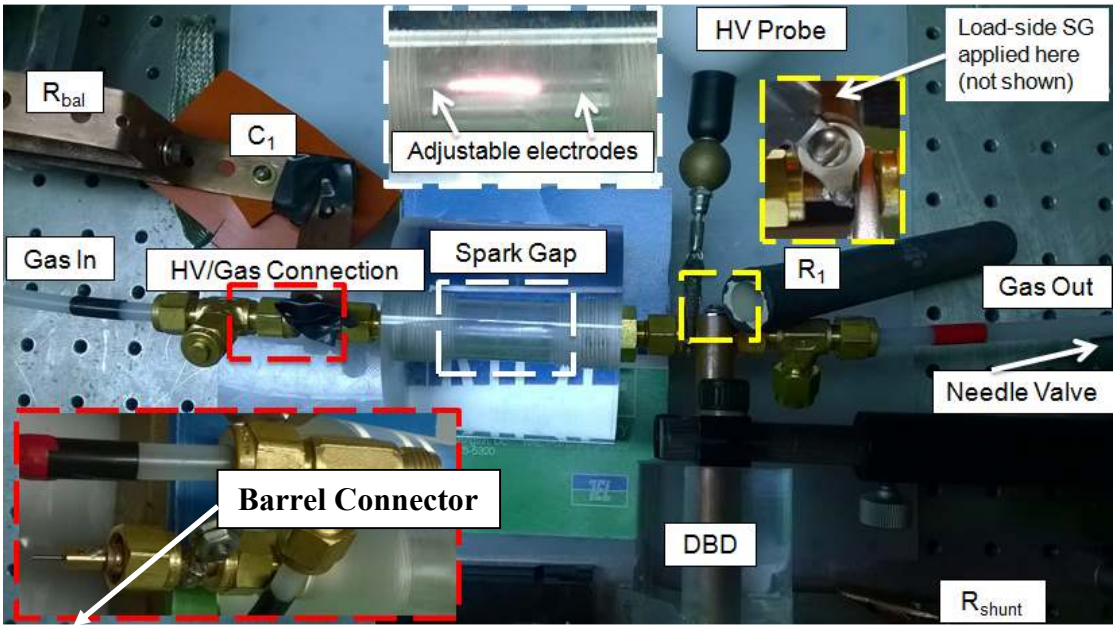

Figure 14. Annotated image of low inductance Gen3 switch.

Notable features of this design are the inclusion of a secondary variable spark gap and its compactness. The secondary spark gap (not shown in Figure 14) is connected to ground in parallel with R_1 and the DBD load. The spark gap limits voltage peaks and rapidly diverts current such that pulse widths of < 10 ns are regularly observed. Conductive paths down current from the ballast resistor are minimized and either large diameter or flat strip geometries are used to minimize inductance and help decrease discharge pulse width.

Electrical and gas feed-thrus were combined by installing brass barrel connectors inside ¼" copper tubing to which high voltage is applied. A set screw is used to secure the electrodes within the barrel connectors, and spark gap distance is determined by the following geometric relation in Equation 6

$$D_{SG} = \ell_1 + \ell_2 + \ell_{BC2BC} - L_{anode} - L_{cathode} \tag{6}$$

where, D_{SG} is the desired spark gap length; ℓ_1 and ℓ_2 are the protrusion lengths of the anode and cathode, respectively, from the barrel connector in the direction opposite the spark gap; ℓ_{BC2BC} is the distance between barrel connector ends; and L_{anode} and $L_{cathode}$ are the lengths of the anode and cathode, respectively. In this way a desired D_{SG} is attained by adjusting ℓ_1 and ℓ_2.

The pressure vessel is a 3" long cylinder with 3" diameter, and an on axis hole was drilled for ¼" NPT to ¼" tube compression fittings. Chamber pressure is estimated using gas cylinder regulator pressure as well as a pressure gage on the gas outlet. An

alumina tube of 3/8” OD and 1/16” wall thickness was placed within the on-axis hole to protect the acrylic from overheating. One drawback of this design is the close proximity of the alumina to the electrodes which encourages surface breakdown.

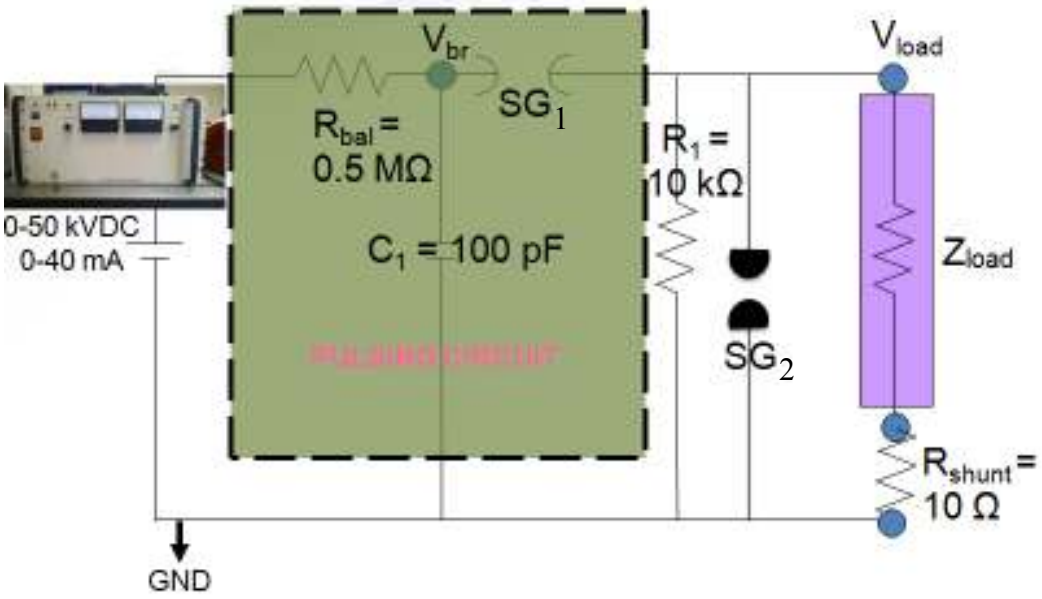

Figure 15. Circuit diagram of Gen3 switch.

3.3.4 AC switching

Each transistor generation was tested using an AC power supply in addition to pulsed DC. Exploration into AC operation was motivated by two primary factors. For one, system efficiency is improved by removing R_{bal}. Since R_{bal} was 0.5 MΩ and power supply I_{rms} and V_{rms} were 40 mA and 35 kV, respectively, much of the input power went to heat generation. The other reason was that since AC waveforms are bipolar, two

discharges would occur for each cycle. The two AC circuits used in experiments are shown in Figure 16 and Figure 17. The first is powered using a 120 VAC 60 Hz variac and transformer, and the second was powered using a commercially available AC plasma driver.

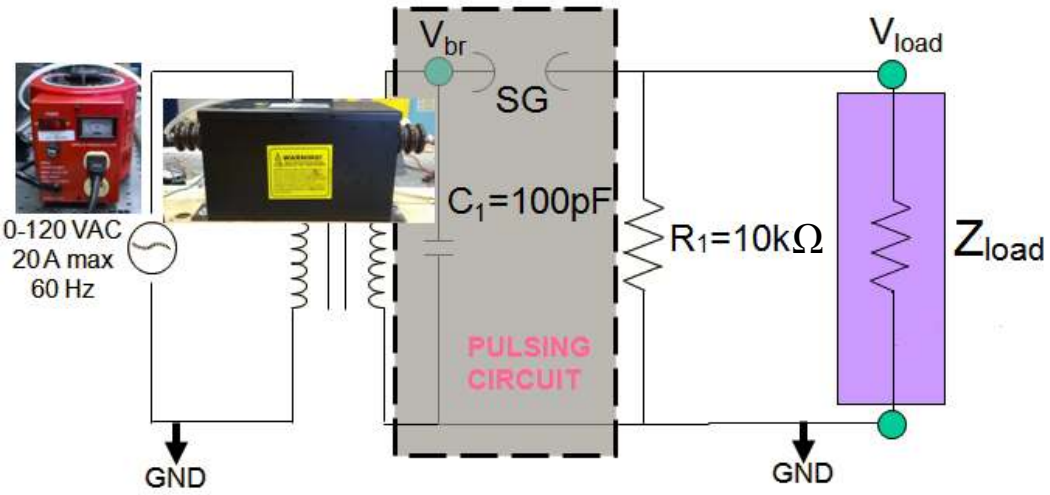

Figure 16. AC pulsing circuit diagram. Variac and transformer used to supply high voltage.

The 120 VAC with transformer setup provided roughly 6000 VAC to the pulsing circuit at 120 Hz as measured from peak to trough, both of which were insufficient for project goals. Frequency dependent transformer gain is shown in Figure 18 for the transformer pictured in Figure 16 (black transformer) and for a second transformer (white transformer – *not pictured*) that was readily available in the Plasma Experimental and Diagnostics Lab. The black and white transformers have respective peak gains of

300 and 100 at 1 kHz, and the gain drops rapidly at higher frequencies. The plasma driver had insufficient power to deliver the desired pulsing.

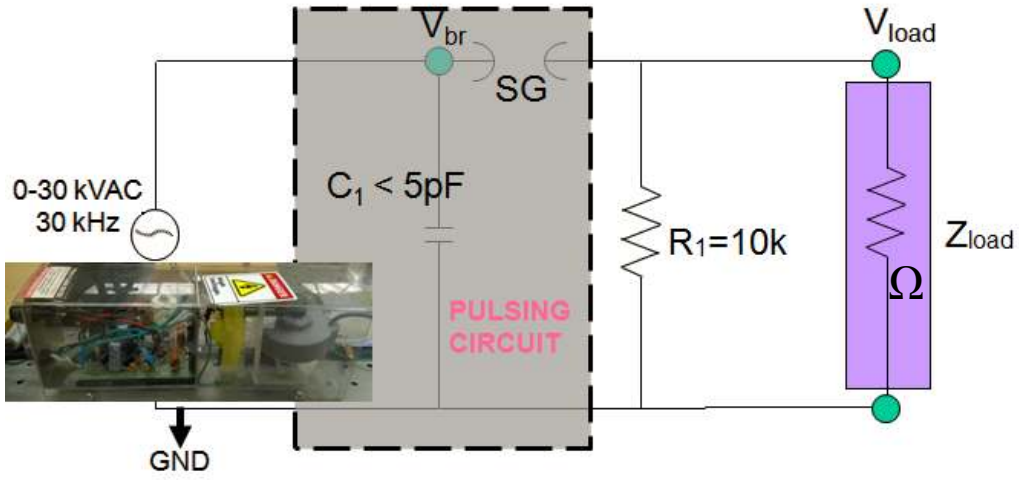

Figure 17. AC pulsed circuit. High voltage supplied by a 30 kV 30 kHz commercially available plasma driver.

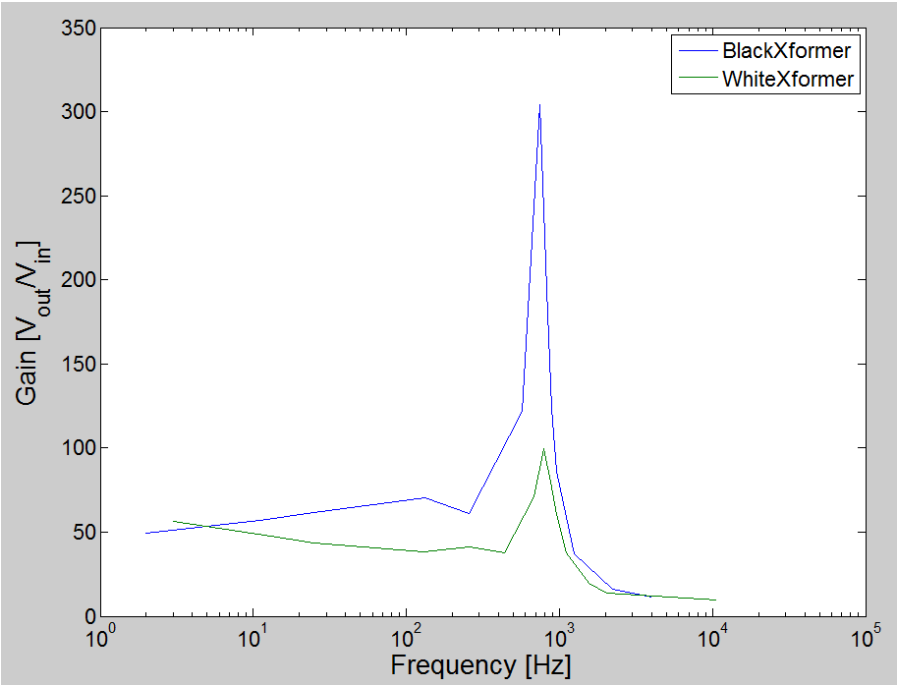

Figure 18. Frequency dependent transformer gain for two different transformers.

3.4 Results

Each of the previously discussed transistors was tested for ms time scales under a variety of load side circuit conditions specifically tailored to their generation. The load voltage is the voltage between the DBD and ground. Voltage and pulsing characteristics were assessed as gas type, gas pressure, electrode material, electrode geometry and convective conditions were varied.

A summary of notable results from selected experiments of each generation are provided in Table 1 and are described with respect to important operating parameters. A more detailed presentation of the results follows. AC pulsing has not yet been achieved at the desired conditions and their results are not included below.

Table 1. Voltage and pulsing characteristics of plasma switches over a variety of experimental conditions.

Gen#	Elec. Mat.	P_{He} [psig] (d [mm])	Flow Rate [SLPM]	Flow Dir*	V_{load} [kV]	f_{dis} [kHz]	FWHM [ns]	Parallel Load
1	Graph	260 (12.4)	est, 10^2-10^3	X	11.2±0.3	22.8±0.6	1000	10k DBD
2	Tung	225 (15)	est, 10^2-10^3	A2C	23.0±1.4	12.2±1.4	30**	10k DBD
3	Tung	200 (18.5)	480	A2C	9.0±2.8	27.2±7.5	137±4	500 DBD
3	Tung	200 (18.5)	720	A2C	10.9±4.1	25.1±8.7	15±2	3.5mm SG DBD
3	Tung	80 (30)	200	A2C	9.9±0.9	19.6±1.6	914±38	10k DBD

* – X, cross-flow; A2C, anode to cathode
** – Possibly due to unintended breakdown within transistor.

3.4.1 Gen1 DC results

The first experiments investigated pulsing characteristics of an unloaded system (R_{load} = 0 Ω) on ms time scales. Variables such as gas type, gas fill pressure, electrode material, spark gap distance, and capacitance were controlled and breakdown voltage (V_{br}, as shown in Figure 9) was recorded as discharge frequency was increased. These results are shown in Figure 19. This data shows that helium is a good candidate for gas fill, and it also shows that choice in electrode material may prevent undesirable mode changes.

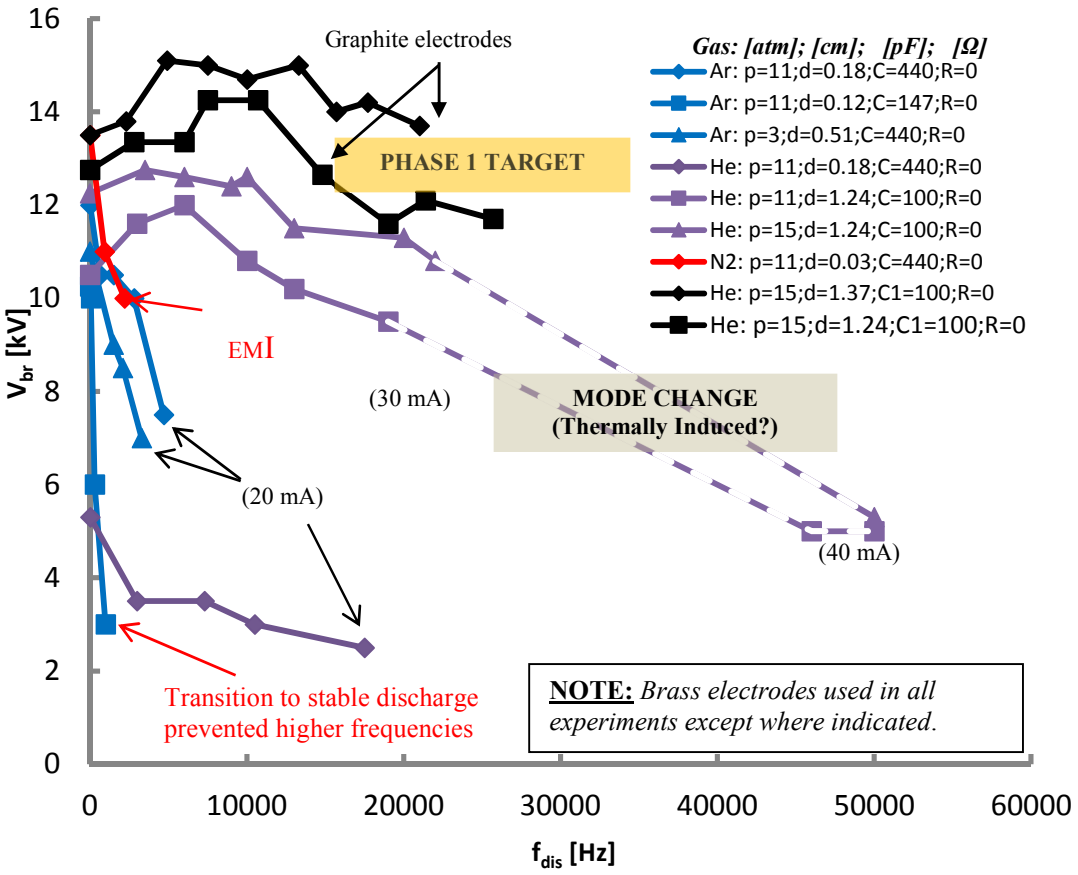

Figure 19. Breakdown voltage and discharge frequency in preliminary parameter space testing of Gen1 switch. Gas type, gas pressure, spark gap distance, capacitance, and electrode material are examined. High pressure helium with graphite electrodes provides best pulsing characteristics.

The next experiment investigated if convection across the spark gap altered pulsing characteristics to the plasma switch. Experimental results and conditions are described in Figure 20. Helium flow rate was not directly measured, but a ΔP between the gas cylinder regulator and a pressure gage on the gas outlet was used to ensure consistency. For this trial the pressure difference between the cylinder regulator and the

outlet pressure gage was ΔP=10 psig. The spark gap distance between the graphite electrodes was d=1.24 cm, and rms current was intentionally kept low to avoid over-heating. This experiment showed that convection encourages higher voltage breakdown. This experiment also demonstrated the existence of two pulsing modes which were observed in all subsequent experiments. With a cold cathode and cold gas, gap breakdown is relatively difficult. As the gas and electrodes increase in temperature, breakdown becomes easier. This leads to lower voltage breakdown, and since low voltage operation requires less energy, breakdown occurs more rapidly. It was not unusual to see a 10 kV load voltage pulsed at 20 kHz transition to a 5 kV voltage pulsing at 40 kHz. These two modes are termed 'high voltage mode' and 'low voltage mode.' The high voltage mode is preferred for applications requiring higher pulsed energy due to the $\sim V^2$ dependence. As previously mentioned these data were collected from operation on ms timescales. A characteristic curve of breakdown voltage versus pulse frequency was generated from long duration experiments in the Gen3 switch and is presented in that section.

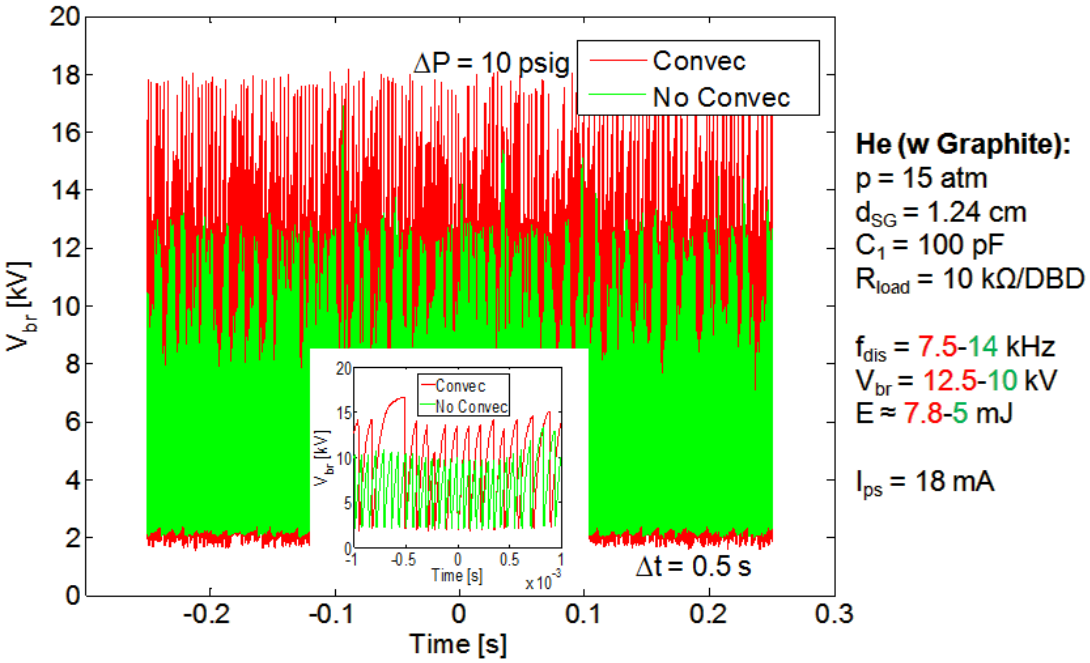

Figure 20. Gen1 plasma switch breakdown voltage with and without cross flow in the spark gap.

The load voltage data displayed in Figure 21 was collected using brass electrodes without convection. The average voltage and discharge frequency were 10.5 kV and 7.5 kHz, respectively. Similar data were collected for the same conditions but using graphite electrodes instead. With graphite electrodes average load voltages were 10 kV, but pulsing frequency increased to 14 kHz. This is due to the graphite electrodes' ability to delay the transition from pulsed discharge to stable discharge at higher currents, and hence higher currents were achievable. Increased load resistance has the effect of increasing voltage down-current of the switch. The resistance impedes charge transfer and consequently higher voltages are attained. Voltage fall times were observed to increase with greater load resistance, and this is for the same reason that increased

voltages are observed with higher impedance loads. These trends are observed throughout subsequent experiments.

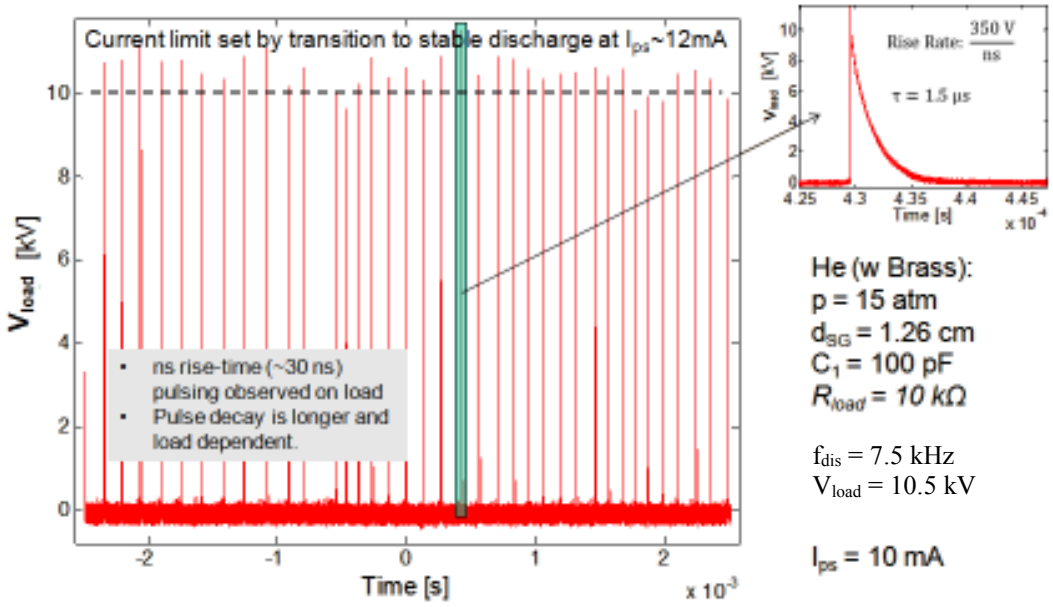

Figure 21. Gen1 load voltage using brass electrodes.

Figure 22 shows load voltage using graphite electrodes and convected helium. Convection delays transition to stable discharge and higher power supply rms currents and pulsing frequencies are available. In the plot shown below V_{load} = 11 kV was able to be switched at f_{dis} = 23 kHz due to the increased current delivered by the power supply and the plasma delaying mode transition. Pulse characteristics are similar to those without convection, having time scales on the order of μs.

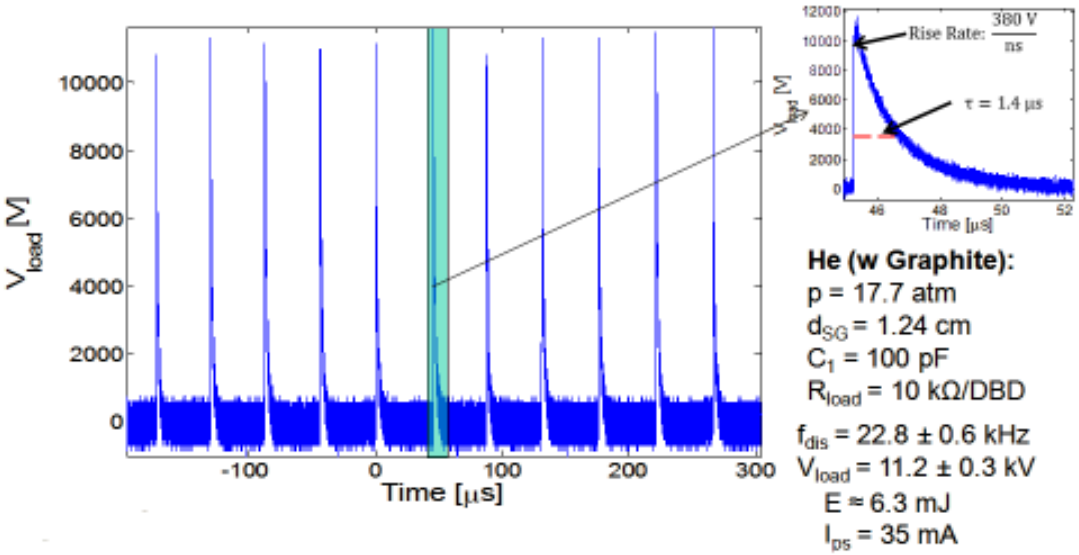

Figure 22. Gen1 load voltage using graphite electrodes with convection - best results for short time scale.

3.4.2 Gen 2 DC results

The Gen2 switch was developed to investigate the effects of convection along the spark gap as opposed to flow across it as was done in Gen1. The plot in Figure 23 shows the load voltage for axial flow originating from the anode in the Gen2 switch with steel electrodes. This plot shows 23.4 kHz switching of 8.3 kV. This operation is characteristic of the Gen1 switch, but there is a pronounced difference in the pulse shape. With axial flow, the decay constant was 200 ns as opposed to 1400 ns, and this motivates the use of on-axis convection to achieve nanosecond duration high voltage high frequency pulses. A comparison of axial and cross-flow convection is given in Table 2. This is not an even comparison as there are significant differences between the experiments. Known differences in experimental conditions include inconsistent

pressures (240 v 260 psia), loads (1 kΩ v 10 kΩ) and electrode materials (steel v graphite). Nevertheless, the difference in pulse decay makes axial convection attractive for continued investigation.

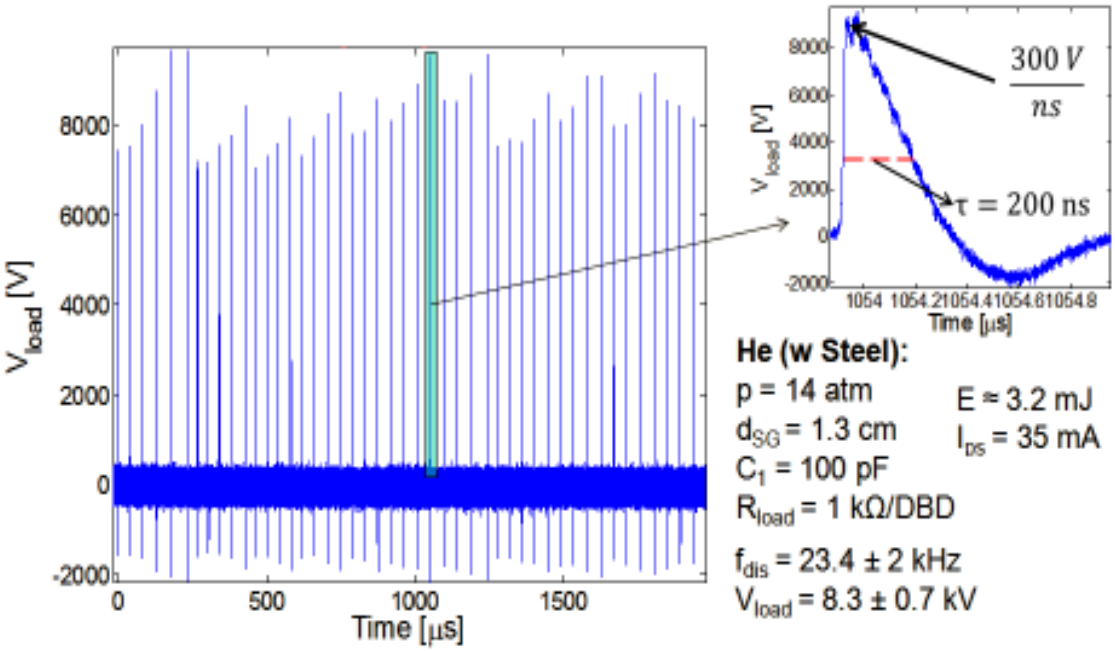

Figure 23. Load voltage with axial flow originating from the anode in Gen2 transistor.

Table 2. Comparison of transistor performance using axial and cross flow convection. Gen2 testing had a load of 1 kΩ in parallel with DBD as opposed to the 10 kΩ in parallel with DBD used in the Gen1 switch.

Convection Orientation	**V_{load} [kV]**	**f_{dis} [kHz]**	**V_{rise} rate [V/ns]**	**Decay Constant [ns]**	**Pulse Energy [mJ]**	**He pressure [psia]**	**d_{SG} [cm]**
Axial, Gen2	8.3±0.7	23.4±2.0	300	200	3.2	240	1.3
Cross, Gen1	11.2±0.3	22.8±0.6	380	1400	6.3	260	1.3

Experiments were then performed to determine the effects of axial convection source, i.e. from anode to cathode, or cathode to anode with 40 mA of supplied current to a 100 pF storage capacitor. The primary difference in flow direction is related to the relative temperature of the electrodes. Because of ion impingement, the cathode is higher temperature than the anode and flow originating from the cathode would be warmer as it entered the spark gap. Data from these experiments are presented in Table 3. Each experiment used tungsten electrodes in 225 psi helium with a spark gap distance of 15 mm. The load in all trials was a 10 kΩ resistor in parallel with the DBD. In the condition with flow originating at the anode, pulse frequency was 12 kHz, and pulsed voltage was >20 kV with a decay constant of 40 ns. The energy input was 26.5 mJ/pulse. Therefore, conservation of energy suggests that reducing the voltage at the load would allow for higher pulse frequencies. This specific trial is anomalous in that the decay constant is so short considering the use of a 10 kΩ resistor in the load. It is possible that undetected and unintended breakdown within the chamber resulted in such rapid charge dissipation.

Table 3. Gen 2 flow direction experiment using tungsten electrode in 225 psi He with C_1 = 100 pF, d_{SG} = 15 mm with 10 kΩ/DBD load.

Flow Source	**V_{rms} [kV]**	**I_{rms} [mA]**	**V_L [kV]**	**E_{in} [mJ/pulse]**	**τ_{pulse} [ns]**	**V_{rise} rate [V/ns]**	**f_{dis} [kHz]**	**I_{peak} [A]**
Anode	39	40	23.0±1.4	26.5	40	700	12.2±1.4	26.7±2.9
None	33	40	14.4±0.9	10.4	1600	180	19.6±2.3	3.3±0.9
Both	34	40	10.7±1.2	5.7	1500	200	23.9±2.9	1.9±0.5
Cathode	29	40	10.4±0.4	5.4	1700	170	23.4±1.1	2.0±0.2

Further experiments with axial flow using lower R_1 (500 Ω) yield lower V_{load} (~7 kV) since charge is transferred more rapidly, but the benefit is that pulse width is reduced to 200 ns.

3.4.3 Gen3 DC results

Experiments in the Gen3 transistor focused on pulse shaping and switch performance during operation lasting 10s minutes. Much data were collected over the course of long duration tests, a more representative description of pulsing characteristics could be realized. A MATLAB script was used to locate voltage peaks from data files and determine peak voltage, pulse frequency and FWHM. Characteristic voltage v frequency trends are plotted in Figure 24.

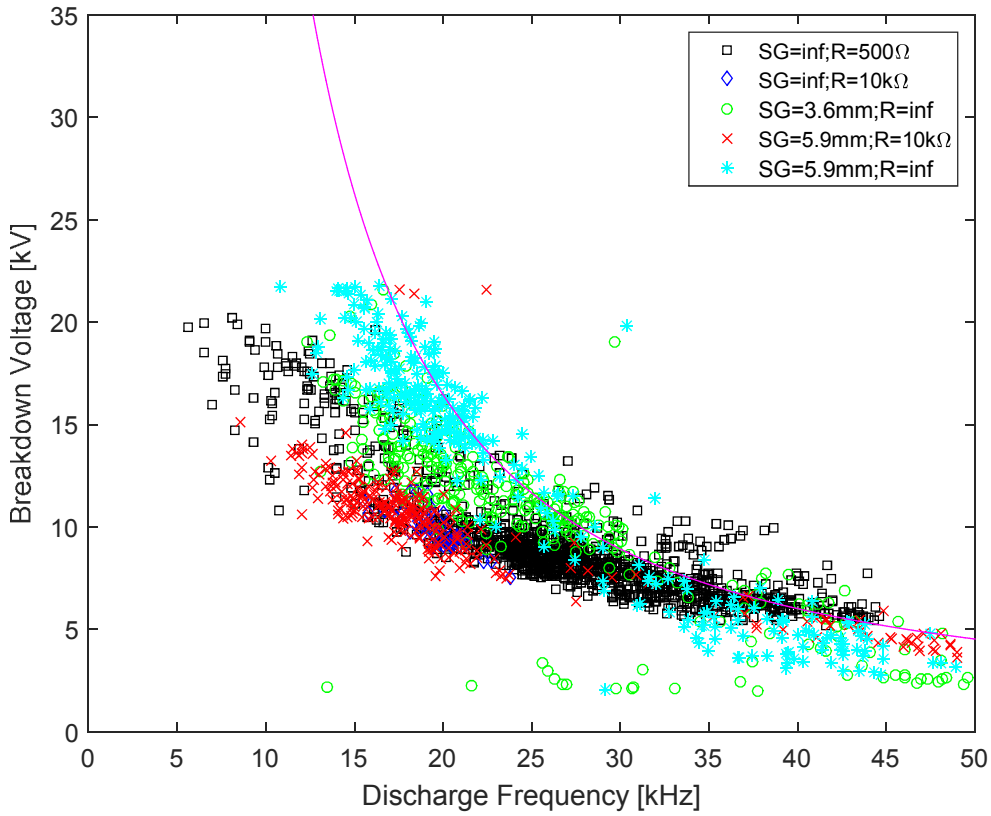

Figure 24. Characteristic voltage response to discharge frequency for all long duration runs in Gen3 transistor.

The voltage-frequency data shown in Figure 24shows a distinct trend of decreased breakdown voltage at higher discharge frequency. Assuming steady state operation, a characteristic curve relating switched voltage to discharge frequency can be derived for this trend by applying conservation of energy to the circuit relating rms power from the power supply to power consumed by the ballast resistor and power transferred by the switch. This relation is shown in Equation 7

$$V_{br} \approx \frac{1}{f_{dis}} \frac{2(V_{rms} I_{rms} - I_{rms}^2 R_{bal})}{C} \left(\frac{1}{V_{max}(1 - \exp[-\tau f_{dis}])} \right) \quad (7)$$

where, V_{br} is breakdown voltage, f_{dis} is discharge frequency, V_{rms} is rms power supply voltage, I_{rms} is rms power supply current, R_{bal} is ballast resistance, C is applied capacitance, V_{max} is maximum power supply voltage, and τ is the $R_{bal}C$ time constant. Equation 7 neglects inefficiencies in load matching as well as the voltage drops across the plasma, and is therefore more representative of the voltage up current of the plasma switch. The term in the denominator on the right had side relates discharge frequency to a characteristic capacitance charging time. V_{max} is used in this charging term because this is the voltage the capacitor would attain after several τ. This characteristic curve can be used to estimate voltage drop across the plasma switch by comparing predicted breakdown voltage to the voltage measured down current of the switch. This curve may also be parameterized for power supply rms and maximum voltage and current and circuit capacitance to help determine operating conditions that shift the circuit specific characteristic curve shown in Figure 24 to regions where higher voltages are accessible for a given discharge frequency.

Long duration Gen3 experiments are summarized in Table 4. Mode transitions were observed in all experiments except Run 5, which stayed in the high voltage mode. FWHM values are reported based on algorithm output for consistency. However, for runs using a second spark gap FWHM values are known to be high due to an error in the FWHM algorithm. Very often FWHM is less than 10 ns with a standard deviation less

than 1 ns. This is conservatively based on manual inspection of the data. Manual investigation showed 7.2±0.3 ns FWHM.

Table 4. Comparison of pulse characteristics for long duration tests in Gen3 transistor: μ±1σ as indicated. A DBD plasma was present on the load side of the transistor for all runs.

Run	*1*	*2*	*3*	*4*	*5*	*5sub*[2]
P_{He} [psig]	200	200	200	200	125	80[3]
Q [SLPM]	480	720	720	720	360	200[3]
SG_1 [mm]	18.5	18.5	18.5	18.5	30	30
SG_2 [mm]	Inf	5.9	5.9	3.5	Inf	Inf
R_1 [kOhm]	0.5	10	Inf	Inf	10	10
V_{load} [kV]	9.0±2.8	10.0±2.8	13.0±5.8	10.9±4.1	13.3±4.0	9.9±0.9
f_{dis} [kHz]	27.2±7.5	21.4±9.9	24.9±9.6	25.1±8.7	18.8±5.0	19.6±1.6
FWHM [ns]	137±4	18±18[1]	619±3330[1]	556±3145[1]	772±112	914±48
Sample Size	1264	267	306	333	135	48[2]

(1) Issue in algorithm causes high mu and sig; confirmed by manual inspection and elaborated upon in following section. **Typ 7±1 ns**

(2) Subset of Run 5 due to sudden loss of pressure

(3) Best estimate due to sudden loss of pressure

The first run lasted 30 minutes with waveforms collected every 20 s. The characteristic voltage/frequency behavior is generated from the data shown in Figure 25, Figure 26 and Figure 27 describe load voltage, pulse frequency and FWHM throughout Run 1. The data in these plots show considerable variation as is evident by large standard deviations, which can be as high as 50% of the mean in some samples. It is difficult to determine if pulsing characteristics show evidence of time dependence since data acquisition was performed manually and not strictly controlled in a temporal sense,

but is it assumed that the volume of individual short time samples are representative of continuous operation.

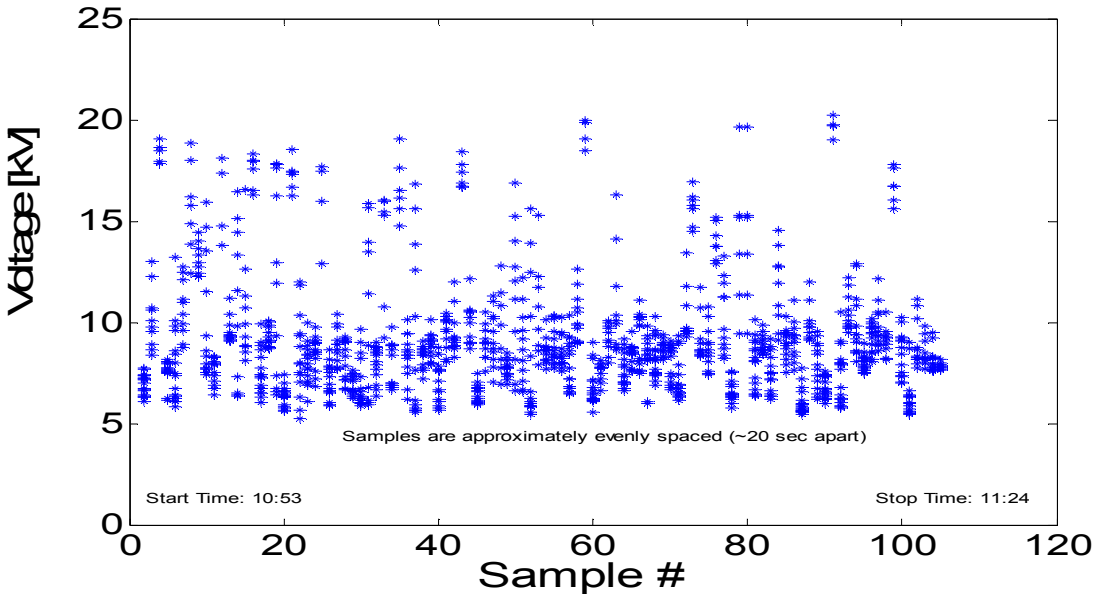

Figure 25. Pulsed voltage throughout long duration experiment Run1 (as described in Table 4), in Gen3 switch

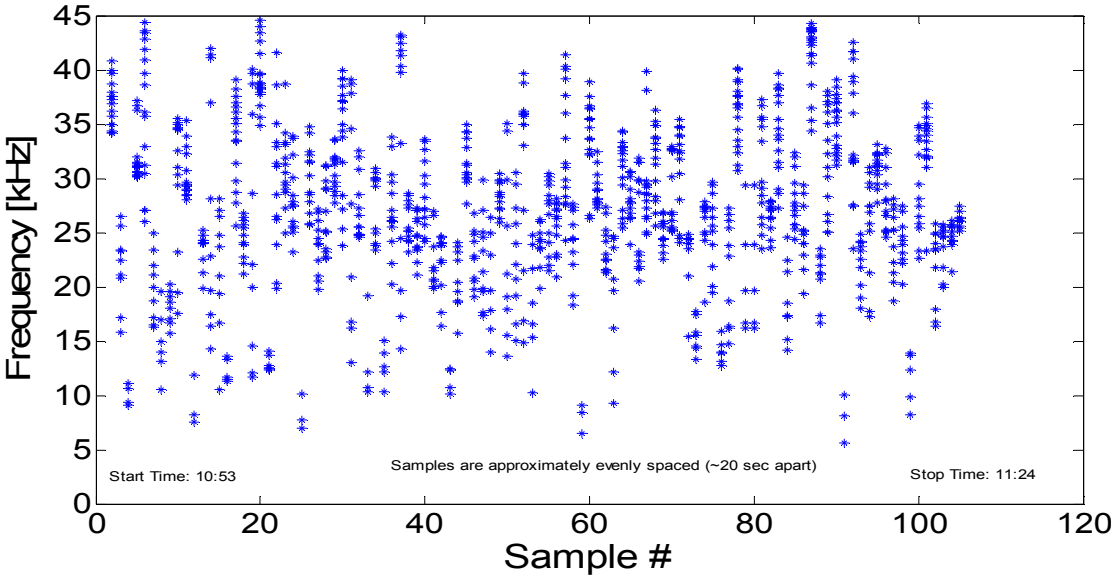

Figure 26. Pulse frequency throughout long duration experiment Run1 (as described in Table 4), in Gen3 switch.

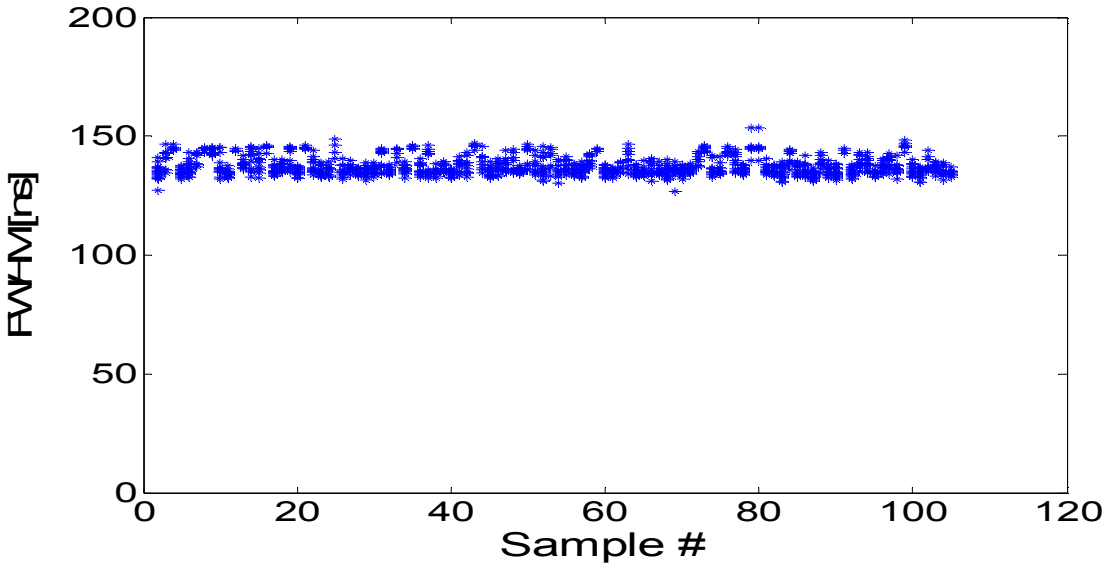

Figure 27. FWHM throughout long duration experiment Run1 (as described in Table 4), in Gen3 switch.

The FWHM for Run1 showed good consistency. This reduction in FWHM is due to the use of small R_1 and compact design of the Gen3 transistor that minimizes stray inductances that resist the rapidly switched current. Applying a spark gap on the load side has a significant impact on pulse width. The spark gap limits peak voltage and encourages rapid voltage fall times. Full width half max times <10 ns are regularly observed but can also be in the range of 10-50 ns when a second spark gap is used, whereas without it FWHM times are in the range of 100-1000 ns or longer, depending on R_1. Using small R_1 reduces FWHM, but it also reduces the pulsed voltage, by providing a relatively easy path to ground. In trials where the load contains only a spark gap in parallel with the DBD, FWHM standard deviations are 1-5× greater than the mean. This is an issue with the algorithm used to determine FWHM, which occasionally calculates FWHM to be in excess of 20,000 ns due to the position of the pulse in the wavetrain. Manual inspection of the data showed that FWHM was in the range of 10-100 ns and often less than 10 ns.

An extreme example of the FWHM algorithm issue is illustrated as follows. The FWHM data in Figure 28 is from Run 4 which uses a load side spark gap. This figure shows that FWHM values are very small compared to the circled outliers that can be seen in Samples 1 and 26. These extreme outliers have FWHM > 10,000 ns. Figure 29 shows the voltage waveform of Sample 26 in Run 4, and all pulses have FWHM < 10 ns as determined by manual inspection.

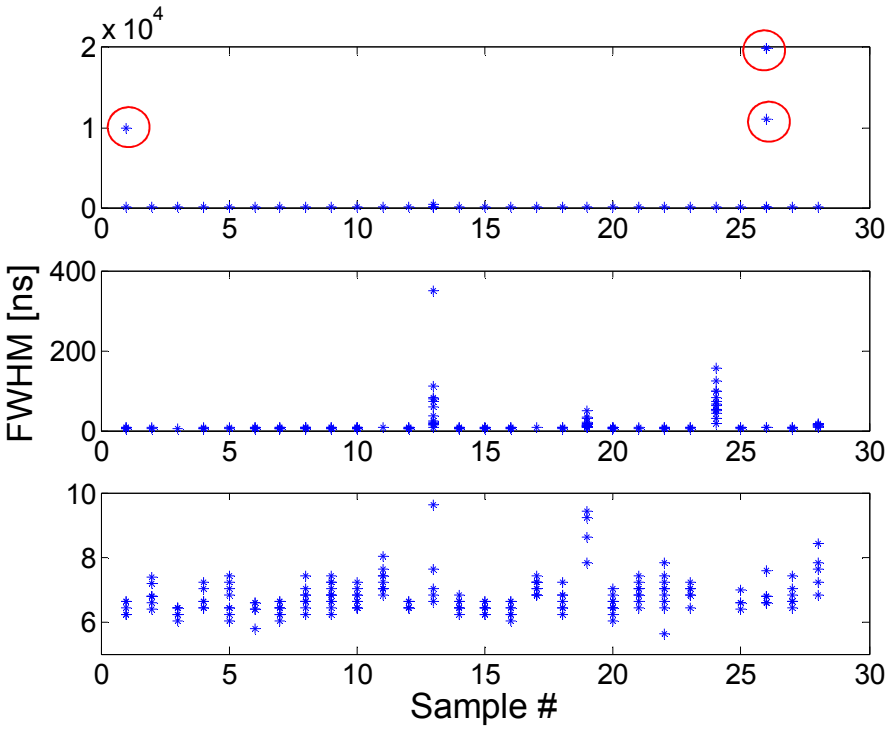

Figure 28. FWHM calculations for each sample in Run 4. Extreme outliers are circled in red. Ignoring known outliers, FWHM is shown to generally fall in the range of 7±1 ns.

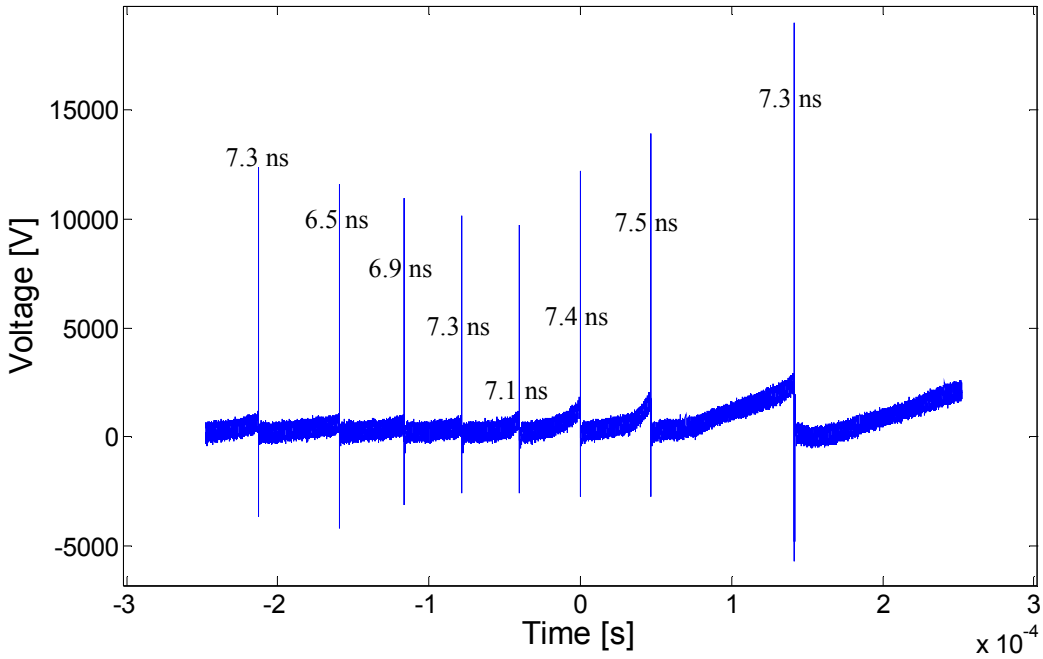

Figure 29. Voltage waveform of sample #26 from Run 4 showing that pulse FWHM << 10,000 ns. Manual check confirms FWHM < 10 ns in all pulses.

FWHM times reported in Figure 28 show a nearly even distribution with the exception of a few samples. Transitions to the low voltage mode can cause miscalculations in FWHM as baseline voltages are high compared to peak voltages. High baseline voltages make it difficult to find an accurate time difference for pulses. In Figure 28, it is shown that nearly all samples are well behaved except 13, 19 and 24 where FWHM appears to be in the 5-200 ns range. Some of these points are real, but some of them are inflated. Sample 24 waveform is shown in Figure 30 as an example of how complications arise during calculation of FWHM. In this figure, the max voltage is normally around 2 kV. At half this maximum voltage, the waveform is essentially at a baseline state where strict numerical application of FWHM becomes an issue.

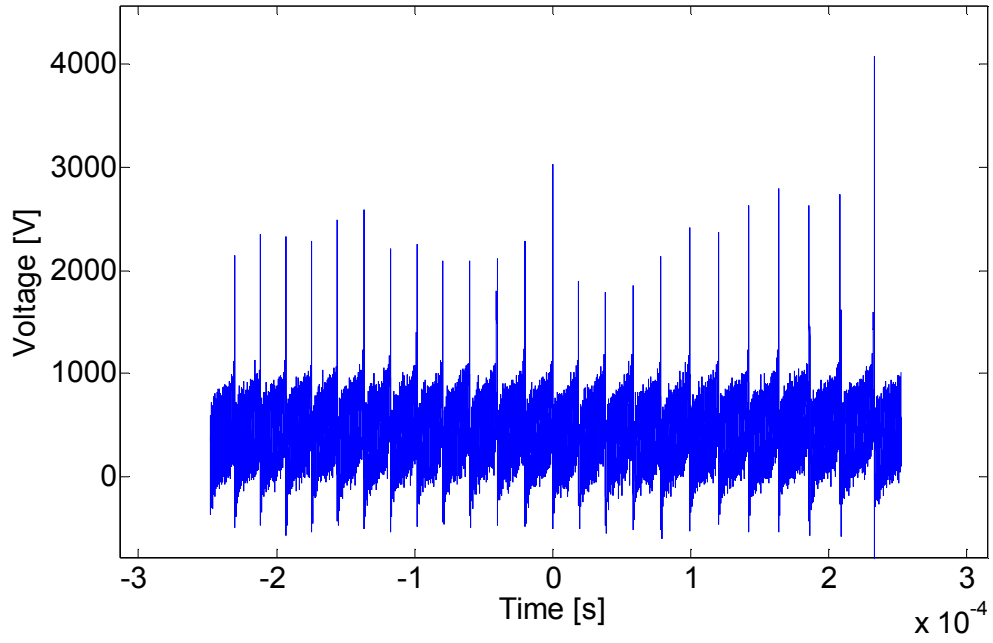

Figure 30. Voltage waveform of sample #24 from Run 4 showing low voltage mode pulsing. FWHM calculations become inaccurate in this mode because near baseline voltages are approximately equal to half of peak voltages.

3.4.4 AC results

Both the Gen1 and Gen2 switches were tested using AC power supplies – variacs and plasma drivers. Pulsing characteristics were insufficient for the objective of this research. The waveforms generated using the transformer lacked the power to provide the required voltage at the desired pulsing frequency.

3.4.4.1 Gen1 AC results

The Gen1 plasma transistor was also tested using an AC power supply. An AC source would be more efficient since most of the supplied power would be delivered to

the discharge instead of dissipated as heat in ballast resistors which are a necessary requirement for pulsed DC discharges. AC sources are amenable to generating some plasma discharges such as DBDs, and they are capable of high frequency nanosecond discharges [31]. The circuits used in these experiments are the same as those shown in Figure 16 and Figure 17.

The variac/transformer circuit was not able to pulse fast enough as it is driven by the supplied frequency of 60 Hz, and no circuit elements are used to adjust this. Each half-cycle contains two pulses, a strong pulse followed by a weaker pulse of the same polarity. Bipolar pulsing was consistent, but the pulsed voltage ranged between 6-8 kVAC which was all the transformer was capable of supplying. A plot of this load voltage is shown in Figure 31.

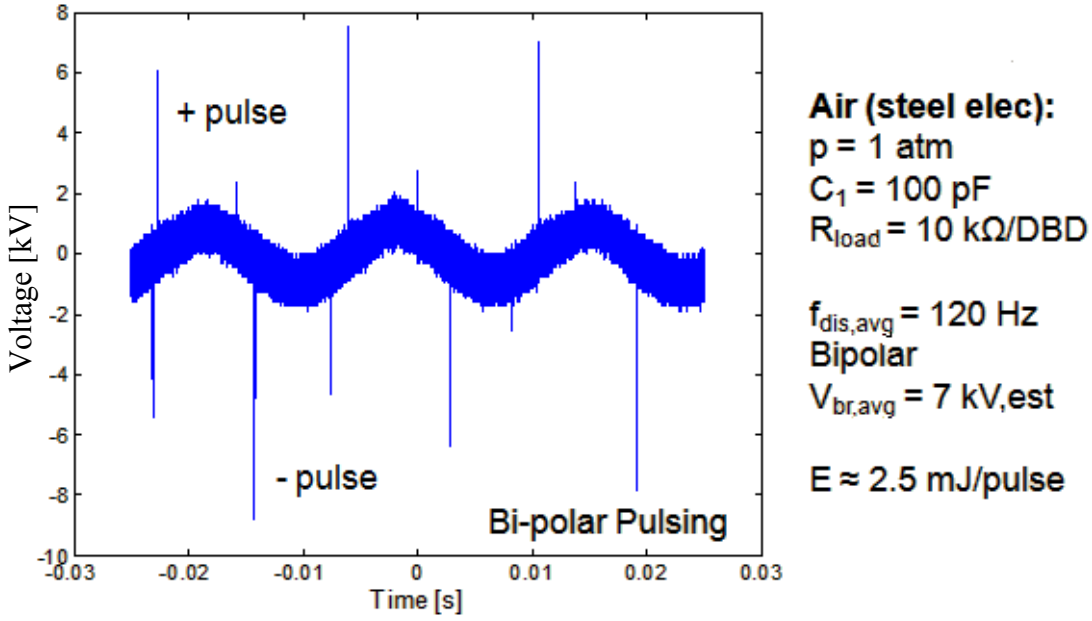

Figure 31. Load voltage of AC power applied to Gen1 transistor via variac and transformer.

A representative plot of the Gen1 transistor load voltage powered by the plasma driver is shown in Figure 32. Bipolar load voltages as great as 3 kV were observed but were on average 2.5 kV. Pulsing frequency was around 50 kHz. When convection was applied to this setup load voltages increased to 4 kV and pulsed at similar frequency. Bipolar discharges were observed throughout experiments using the plasma driver. In the final experiment, the load was changed to a 1 kΩ resistor in parallel with the DBD, and convection was not used. This experiment showed that the AC circuit as driven by the plasma driver did not appear load sensitive. The AC experiments are summarized in Table 5.

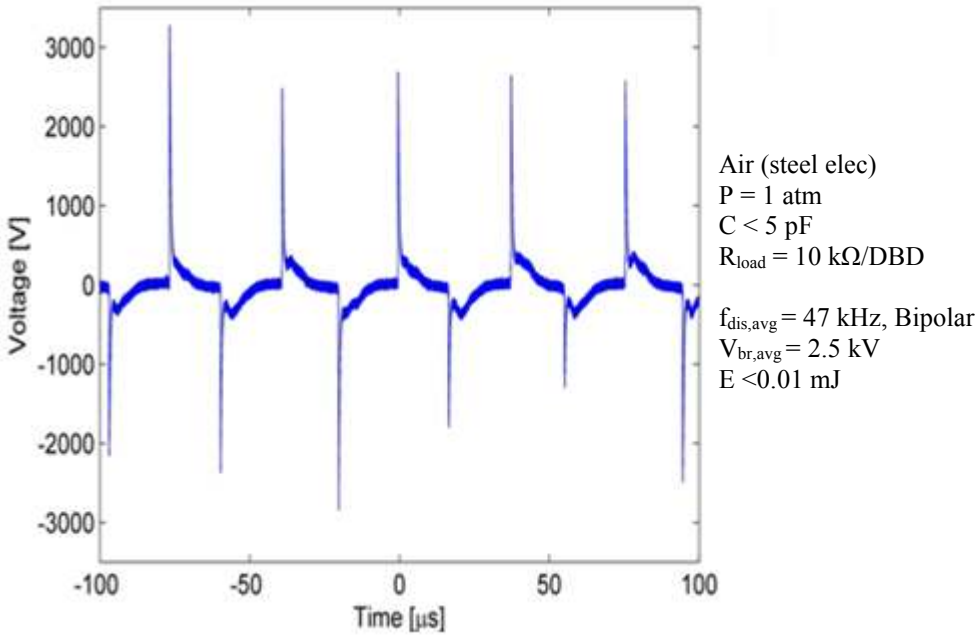

Figure 32. Load voltage of the Gen1 transistor using steel electrode with no convection as powered by AC plasma driver.

Table 5. Summary of AC pulsed circuits in Gen1 transistor.

AC Pulsed Circuit	V_{load} [kV]	f_{dis} [kHz]	Pulse Energy [mJ]
DBD; 1 kΩ; no conv	3.1±0.9	49.5±5.5	0.02
DBD; 10 k; no conv	2.4±0.5	52.4±4.0	0.04
DBD; 10 k; conv	4.4±1.0	48.5±6.4	0.05

3.4.4.2 Gen2 AC results

AC experiments with axial flow were unable to generate the desired high voltage high frequency pulses. Nitrogen gas at a high flow rate and helium at a lower flow rate were tested and 40 and 150 psig, respectively. In both tests the plasma driver was used to pulse a load of 1 kΩ in parallel with the DBD. Nanosecond load voltage pulses as high

as 10 kV at 12 kHz were observed, but discharges did not occur every half cycle. In helium at high flow rate, 2 kV was pulsed at 50 kHz with discharges occurring every half cycle. These experiments indicate that helium recovers quickly from rapid discharges, possibly due to it larger thermal capacity, but remains low voltage while discharges in nitrogen provide high voltage pulses at lower frequency due to its longer recovery rate.

3.4.5 Conclusions

In general, 20 kHz pulsing of 10 kV has been achieved although occasional transition to a low voltage mode is present and consistent operation remains a challenge for future work. The three generations of switches allowed for the methodical exploration of switch operating space in order to identify important operating conditions for high voltage high frequency application on both short and long operational time scales. Although challenges in operation remain, this work shows that gas phase switching can be used at kHz frequency for 10 kV switching. Such a switch will enable to use of other pulsed plasma applications in environments where discharges may tend towards a stable non-pulsing mode.

The Gen1 switch was helpful for determining an effective parameter space in which to operate with respect to the effects of convection, electrode material and circuit elements. Results were then compared with the Gen2 transistor in which directed gas across the transistor spark gap were varied. Both Gen1 and Gen2 transistors were operated with AC current, but readily available AC power sources were either unable to

provide the needed discharge frequencies or provide sufficient power to continue their investigation as a useful alternative to DC pulsing. The Gen3 switch examined system behavior over longer time scales and found that under the current operating conditions, there is a tradeoff between consistent pulsing and short pulse duration. Operation of 10 kV at 20 kHz has been achieved with relatively high load side impedance, but pulse FWHM is 900 ns. Using a second spark gap reduces FWHM to 10 ns and pulses are still on average above 10 kV and 20 kHz, but their operation is inconsistent as indicated by standard deviations that can be as much as 50% of the mean value.

Ideally, gas phase switching will expand in use to 50 kV pulsed at 100 kHz frequency. The general idea to achieve this is that transition from a neutral gas to a highly conductive plasma and back to a neutral gas needs to be done 1) rapidly, 2) repeatedly and at 3) high voltage. The rationale to attain each of these is described in detail below.

Switching is done at high voltage by relying on a cold cathode, secondary electron emission dominated, Paschen scaled (pd = const) method of breakdown. For higher voltages the breakdown is actually a modified Townsend breakdown at large electrode spacing with potential leader propagation similar to Meek breakdown criteria. A cold cathode, without thermionic electron emission, is necessary as this ensures high voltage breakdown and minimizes transitions. Active cooling of the cathode is already necessary and will continued to be required at high power operation. Because of the high pressure operation the cathode spot sizes are small and have characteristics times of cooling shorter than the time between pulses. However, cooling of the cathode is needed

so that bulk temperature does not significantly increase with time. This was done in this work with convection of the discharge gas over the cathode, and this method may be practical in further experimentation and with optimized cathode geometry. Another consideration in long gap breakdown is that dielectric surfaces nearby do not act as breakdown conduits; the gas-surface-gas breakdown mechanism is lower voltage than a gas only breakdown. This will be accounted for in the design of the larger gaps.

Both rapid ignition of the plasma and rapid quenching of the plasma are needed. The rapid ignition is needed so that the rise time on the voltage pulses is fast enough. Rapid quenching is needed so that the electron and charged particles from the discharge are no longer present at the time of the next sequential firing. Both of these processes are determined by collision frequencies, and operation of the spark gaps at high pressure ensure both rapid ignition and quenching. Characteristic frequency for ionization instabilities are proportional to n^2. Similarly characteristic frequency for three body recombination increases with pressure. Also characteristic sizes of the discharges decrease with pressure so that diffusion of charged particles to lower plasma density regions is faster. Ignition collisional dynamics at 200 psi were sufficiently fast that the rise time was circuit inductance limited and not limited by plasma dynamics. Voltage fall times were equally fast and pulsing frequencies as high as 0.5 MHz have been achieved at 1kV with smaller gaps indicating that charged particle quenching is sufficiently fast to achieve 100 kHz.

Shot to shot repeatability of the switching process is a major concern as experimentation scales to higher powers and frequencies. In general there are three

discharge modes identified in Phase 1. 1) cold gas – cold electrode, 2) warm gas – cold electrode, and 3) warm gas – hot electrode. The electrode temperature refers to whether secondary electron emission or thermionic emission provides electrons for the breakdown process. Secondary electron emission and glow mode is preferred. The gas temperature refers to whether the subsequent discharge sees the warm gas channel from the previous discharge. Although the electrons may have recombined the warm gas channel can result in a lower gas density region and lower breakdown voltages. In this research significant mode changes from ~12 kV breakdown to ~6 kV breakdown were noted and associated with transitioning from a cold gas mode to a warm gas mode. There is a mode change to warm gas mode because of the thermal instability onset when the gas channels warm; however there is a stable operation in the warm channel mode because a new steady state temperature (1000-2000 °C above ambient) is achieved. Because the discharges are high pressure microplasmas with small radii and rapid radial thermal diffusion, the warm gas mode steady state temperature is still below the hot electrode temperature associated with arc transition where electron generation is dominated by thermionic emission. High rates of convective flow through the channel increased the probability of cold gas mode operation. Either warm or cold gas mode operation is allowable so long as the plasma is a microplasma and sufficient convection is available to have a steady state. In this work both warm gas and cold gas operating modes were explored. Future design operating conditions will likely be in a warm-gas/cold cathode operating mode. The warm gas mode of operation may actually be more stable than the cold-gas mode sought in these experiments.

3.5 Electrode degradation

Electrode erosion for graphite and tungsten electrodes was studied. Electrodes were imaged using a microscope or macro lens before and after prolonged use. Tungsten electrodes were nearly unaffected by extended use whereas the graphite electrodes were visibly eroded and eroded at a rate of approximately 200 μm/10^6 pulses. Before and after use images of tungsten and graphite electrodes are provided in Figure 33 and Figure 34, respectively. Experimental results from the electrode longevity tests are summarized in Table 6.

Table 6. Tungsten and graphite electrode erosion rates after extended use.

Electrode Material	**Electrode**	**Elec. Erosion Rate [μm/10^6 pulses]**
Tungsten	Anode	Not detectable
Tungsten	Cathode	6
Graphite	Anode	211
Graphite	Cathode	211

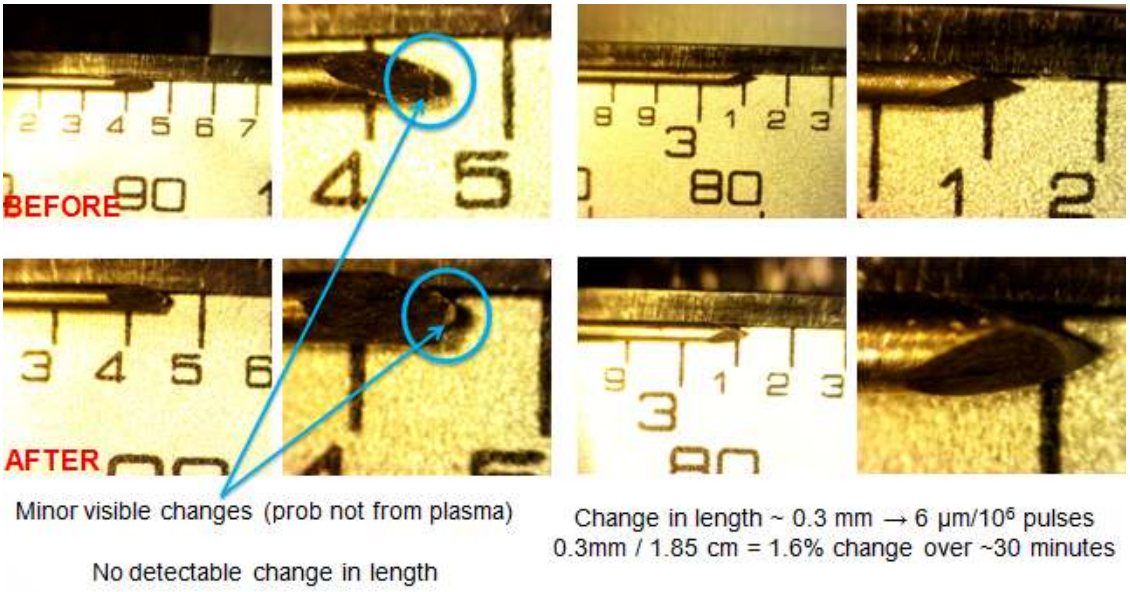

Figure 33. Tungsten electrode wear. Pre and post use images for anode and cathode. Electrode wear determined by microscopy.

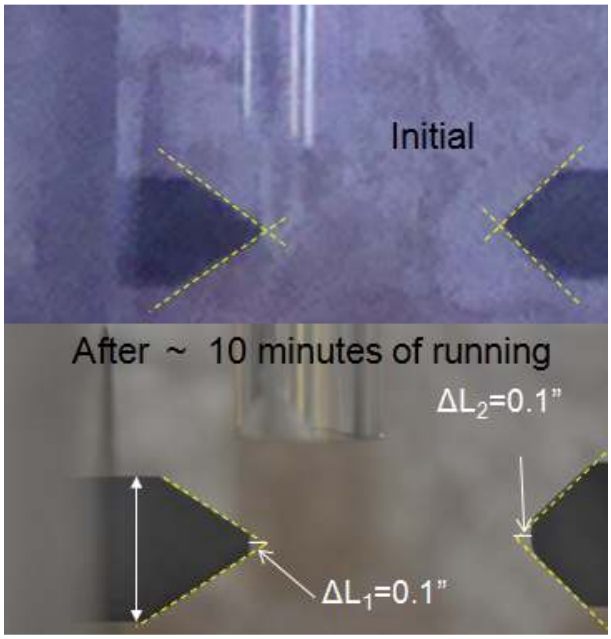

Figure 34. Graphite anode and cathode images pre and post use.

3.6 DBD load characterization

The load characteristics, namely capacitance and time dependent resistance, of a small Dielectric Barrier Discharge (DBD) load are determined based upon time resolved voltage and current measurements in the DBD circuit. The general methodology is first applied to a DBD powered by a sinusoidal varying high voltage. For this condition the analysis method and expected results are generally well known for comparison. This condition was used to 'debug' the analysis method and determine necessary data post-processing procedures. Surface charging of the dielectric have yet to be taken into account, but results are still relevant. The method was then applied with some minor modifications to measurements of the load characteristics for the same DBD powered by a unipolar (positive) ns-pulsed high voltage.

3.6.1 Load characterization theory – Lissajous plots

The voltage to the DBD was measured between the points marked V_{load} and GND in Figure 35, and the voltage across the shunt resistor was measured between V_{shunt} and GND. Both voltage waveforms were captured by an oscilloscope sampling at 5 GHz for a period of 200 μs providing 1 million samples that span approximately 4.5 power supply cycles. The high frequency, 5GHz, sampling is essential providing 200 ps per data point to accurately capture the nanosecond duration current pulses. The total current passing through the DBD, I_{tot}, is calculated by dividing V_{shunt} by R_{shunt} in accordance with Ohm's Law. However, the total current is comprised of two components – displacement currents (to C_{airgap}) and real currents (through R_{plasma}) – both of which have their own

associated impedances as governed by Ohm's Law. Displacement currents originate from the time varying E-field of the capacitance of the system, and the real currents are the result of charged particles' translational motion. By Kirchhoff's current law, the sum of these two currents must be the total current leaving the DBD and seen by the shunt, i.e. $I_{tot} = I_{disp} + I_{plasma}$. The resistance and capacitance of the DBD load can be experimentally determined by careful examination of the two voltage traces. Calculating the total resistance of the DBD is straightforward, and is found by application of Ohm's Law – $R_{tot} = V_{load}/I_{tot}$.

Before the displacement and real currents can be separated, it is necessary to determine the capacitance of the system. It should be noted that capacitance is dependent on electrode geometry, i.e. $C \sim A_{surf}/d$, and this consideration is important when applying the following results to subsequent experiments. The capacitance is experimentally determined by examining the relationship of accumulated charge and voltage. The accumulated charge, q_{acc}, is the time integrated I_{tot} signal. The capacitance of the DBD load is then the average slope given by the plot of q_{acc} v V_{load}, since $C = q/V$. The displacement current is then calculated as $I_{disp}=C(\mathrm{d}V_{load}/\mathrm{d}t)$, and $I_{plasma}=I_{tot} - I_{disp}$. Currently, the plasma resistance is determined using Ohm's Law – $R_{plasma} = V_{load}/I_{plasma}$. The following paragraphs will apply the aforementioned techniques to a real data set corresponding to the set up just described with AC sinusoid voltage application.

3.6.2 Sinusoidal driven DBD experimental setup

The objective of the following analysis is to characterize the complex impedance of an atmospheric DBD (dielectric barrier discharge) plasma driven by a sinusoidal voltage waveform. A diagram of the circuit is shown in Figure 35. A RF power supply is connected to a DBD configuration shown schematically as the capacitance of the quartz, C_{quartz}, in series with the capacitance of the air in the DBD gap, $C_{airgap,}$ in parallel with the non-constant resistance of the plasma, R_{plasma}, in the DBD gap. Since the plasma is low density the permittivity of the ambient air and ionized air have no significant difference. An AC power source (10 kV; 24 kHz) was used in this setup for convenience as the DBD response to AC inputs is well known. The same DBD configuration was used as the load in pulsed power experiments, where both AC-ns pulsed and DC- ns pulsed inputs will be used. Those results are still under analysis but, based upon preliminary results the type of input signal does not have major effect on the impedances of the DBD load.

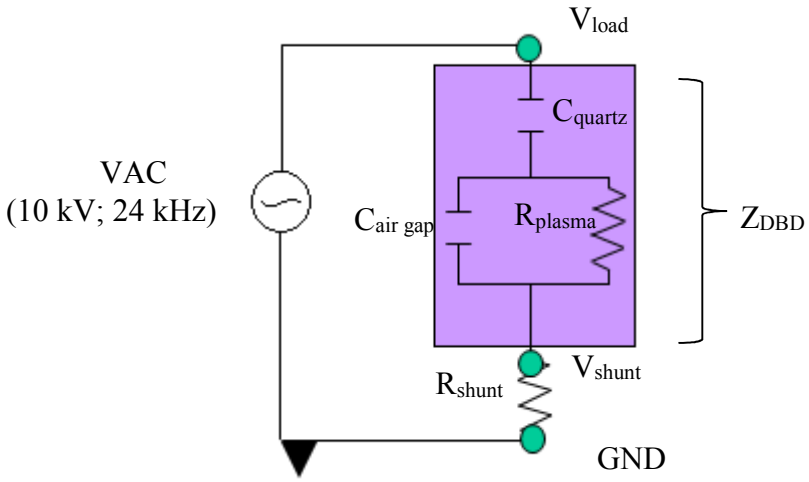

Figure 35. Circuit representation of complex impedance of a DBD load powered by sinusoid voltage. The complex impedance can be simplified as an equivalent resistance given by Z_{DBD}.

The AC power supply and DBD plasma are the same as those shown previously in Figure 17 and Figure 11, respectively. The power supply is commercially available (AmazingOne), and the DBD was fabricated in house by inserting a 0.5" diameter copper rod along the axis of a 2" diameter acrylic cylinder. One end of the acrylic cylinder was covered by a 2" diameter quartz disc with a thickness of 1/16", serving as the dielectric barrier. The other end was left open for electrical connections, namely the HV connection and voltage probe lead. The low voltage side of the DBD was a conductive plate which was located approximately 1mm below the dielectric barrier in atmospheric air. The shunt resistor, R_{shunt}, connected between the plate to ground.

3.6.3 AC DBD characterization

The voltage traces for V_{load} and V_{shunt} are shown in Figure 36 and Figure 37, respectively. The V_{load} signal contains high frequency noise causing the time derivative of V_{load} to oscillate unrealistically between large positive and negative values. Therefore, it is important to smooth the V_{load} signal as cleanly as possible while still preserving its characteristic features. In this instance a piecewise 3rd order polynomial fit over 1000 points was used (MATLAB function 'smooth' with sgolay method, 1000 points, and order 3). [***Note***: In later analyses it was found that a less aggressive smoothing worked equally well].

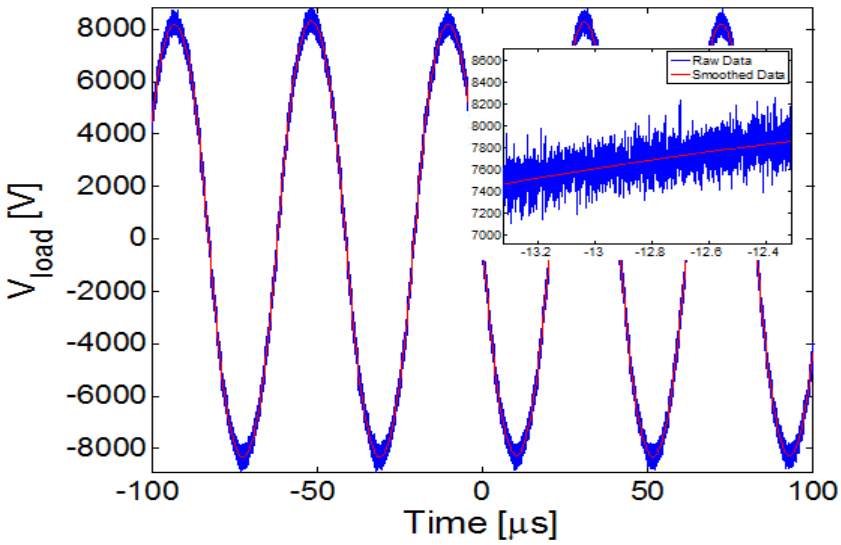

Figure 36. DBD voltage signal, V_{load}, showing raw and smoothed data. The inset shows that the signal features were preserved while removing rapid oscillations in the time rate of change of V_{load}.

The V_{shunt} signal also required smoothing in order to reduce noise, but in this instance there are important voltage spikes, which correspond to current spikes, that occur during positive and negative cycles. These spikes must be preserved because they are representative of charge transfer, which is an important characteristic of the DBD load. Another feature that must be preserved is the lower amplitude oscillation which is characteristic of displacement currents. A piecewise linear fit over 50 points was used (MATLAB function 'smooth' with 'moving average' method, and 50 points). The V_{shunt} data contains a DC offset which must be subtracted out due to the integration used in the analysis procedure. This DC offset is characteristic of the oscilloscopes analog to digital (AD) conversion and typically is on the order of several bits and is only an issue when integrating signals. This offset correction is accomplished by subtracting the mean of either the smoothed or raw signal from all values in the signal, and the resulting trend is shown in Figure 37 as 'Smthd/Corr Data.' By subtracting the mean, an assumption is made that over longer time scales, 200 μs in this case, the net charge accumulation in the DBD is zero, this is probably a reasonable assumption. The waveform of the total current, I_{tot}, through the DBD is determined from the smoothed and corrected V_{shunt} waveform using Ohm's Law and the value of the shunt resistance (in this case 822 Ω) and is plotted in Figure 38. Noticeable in Figure 38 is the sinusoidal varying current which corresponds to the displacement current and the short duration current spikes which correspond to the conductive plasma breakdowns.

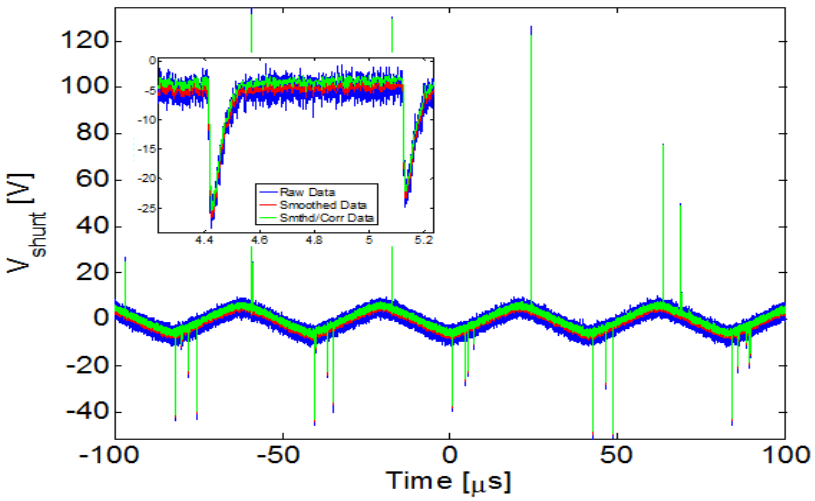

Figure 37. 822 Ω shunt resistor voltage signal, V_{shunt}, showing both raw and smoothed waveforms. Smoothing has been used to reduce signal noise while maintaining important signal characteristics as is shown in the inset. The corrected data included the removal of a slight DC offset in the voltage measurements.

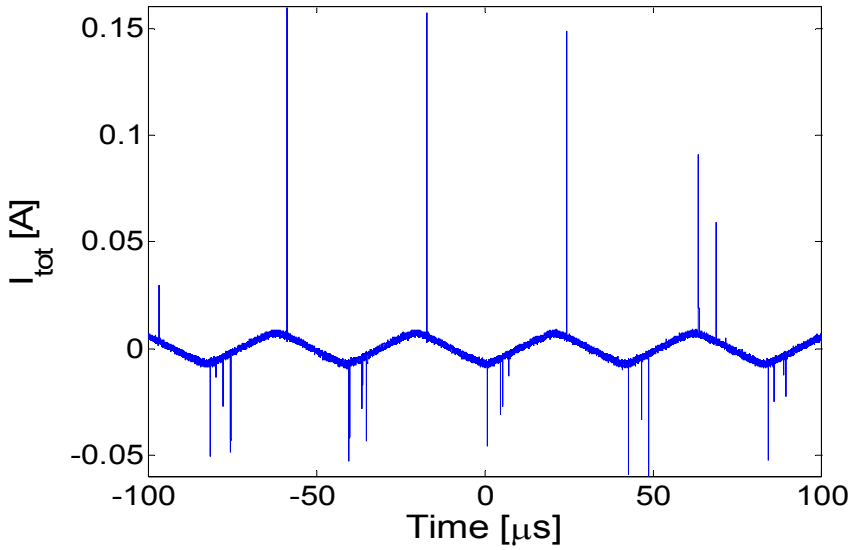

Figure 38. Smoothed and corrected waveform for total current, I_{tot}, passed through a DBD plasma.

The net charge accumulation, Q, is determined by time integrating the I_{tot} trace. Because this is an AC driven DBD plasma, the net charge accumulation should oscillate about 0 on long time scales. This is the basis of the assumption made when correcting for the current DC offset. The charge accumulation is shown in Figure 39. In this case for the raw data, the charge accumulation continually increases during the time interval. The precise reason for this is yet unclear. It is possible that this is due to a slight variation in the oscilloscope A-D offset (it is also possible that charge accumulation on short time scales over a few cycles is non-zero). Analysis is made assuming that the offset is due to the A-to-D and can be ignored (and subtracted). Using a 2^{nd} degree polynomial fit, a charge offset was removed using the same method described for the V_{shunt} waveform. The corrected charge accumulation is plotted along with the charge accumulation in Figure 64. Although the corrected charge accumulation still contains a slight upward trend, it is an improvement upon the original.

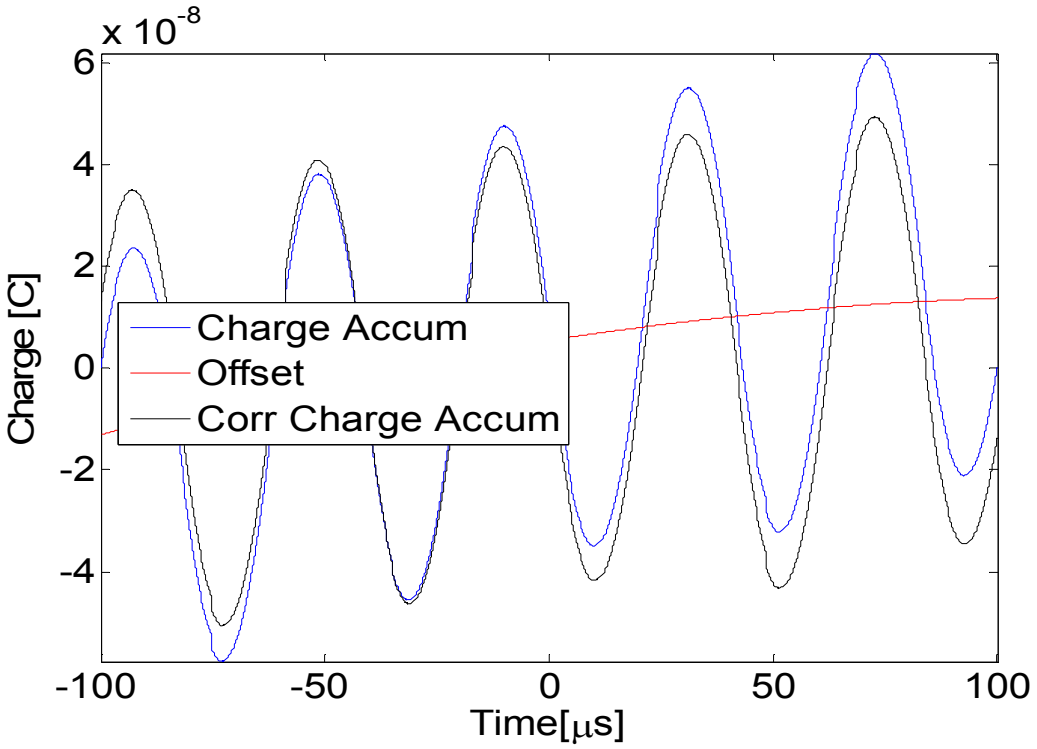

Figure 39. Charge accumulation as calculated from time integrated current waveform. A 2nd degree polynomial was fit to the curve and subtracted as an offset. The result is plotted as 'Corr Charge Accum.'

A comparison of the voltage on the DBD load, current through the DBD load, and charge accumulation on the lower electrode are normalized in Figure 40. As can be seen charge largely follow voltage and this is indicative of the capacitive nature of the discharge system ($Q=CV$). Charge does not follow voltage only at the specific instances of the current spikes due to breakdown of the air dielectric in the DBD plasma.

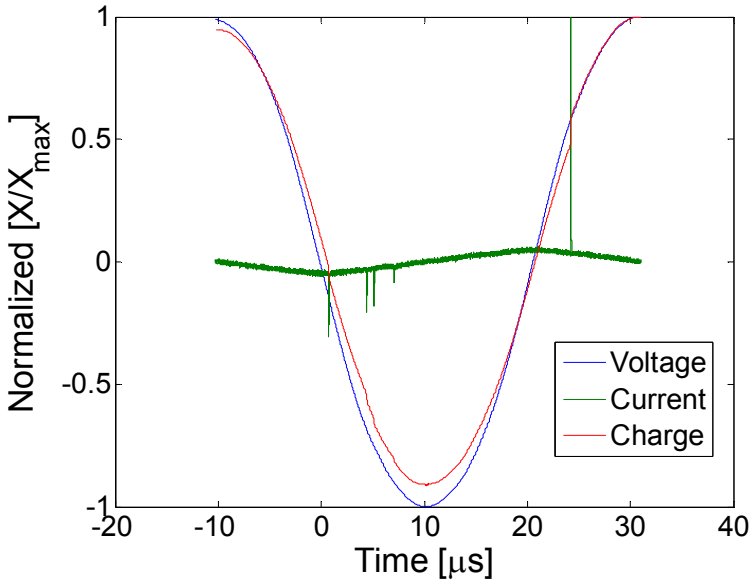

Figure 40. Comparison of normalized V_{load}, I_{tot} and Q traces.

The displacement current, I_{disp}, of the load is calculated using Equation 8

$$I_{disp} = C\frac{dV_{load}}{dt} \tag{8}$$

where, I_{disp} is the displacement current, C is the capacitance of the load given by the slope of the linear least squares fit to the Q v. V_{load} curve, V_{load} is the voltage across the load, and t is time . In determining C, the following analysis examines only one charge/discharge of the power cycle, but the analysis can be expanded to include all data points in the domain and the end result remains very nearly unchanged. A plot of Q v. V_{load} and the linear fit (by least squares) indicating the average capacitance is shown in

Figure 41 for the voltage cycle spanning -10 μs < t < 30 μs. At t = -10 μs, the voltage is at its peak and beginning the discharge cycle. The path taken in Figure 41 is counterclockwise beginning at the top right. The majority of this trace is capacitive, however, charge discontinuities occur during the current pulses. In this case there are three current pulses on the voltage falling portion of the cycle and one on the voltage rising portion of the cycle.

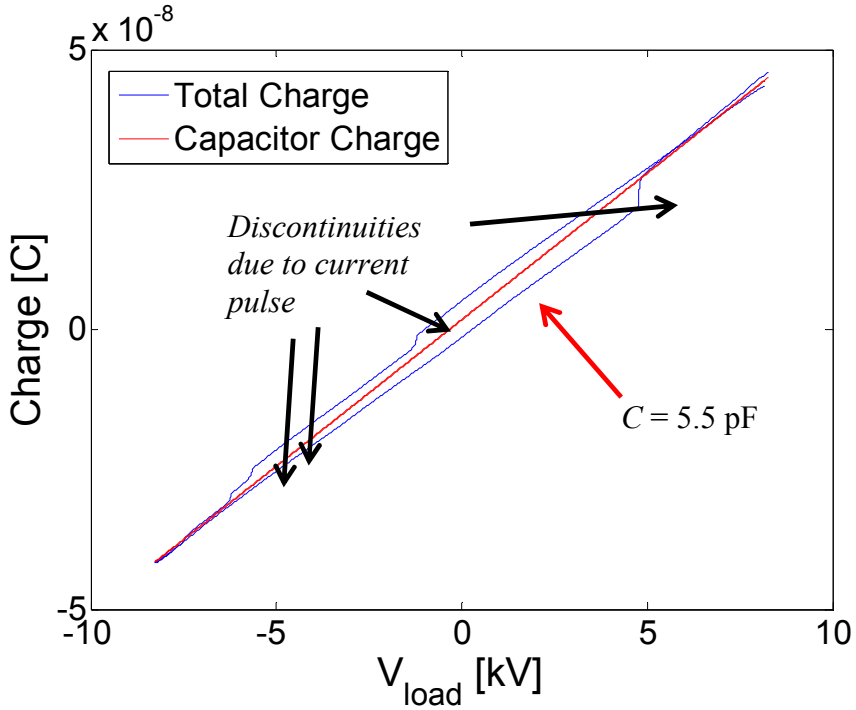

Figure 41. Lissajous analysis of DBD load capacitance based on the slope of a linear least squares fit (shown in red). C = dQ/dV = 5.5 pF.

Determining the displacement current requires knowledge of both the system capacitance and dV/dt. The time derivative of V_{load} was calculated using a 1st order central difference algorithm from the measured V_{load}. V_{load} as well as dV_{load}/dt are plotted together in Figure 42. Although apparently a sine wave, inspection of the derivative reveals slight variations in the derivative of the voltage due to the current spikes through the DBD (i.e. dV/dt is not a perfect cosine wave).

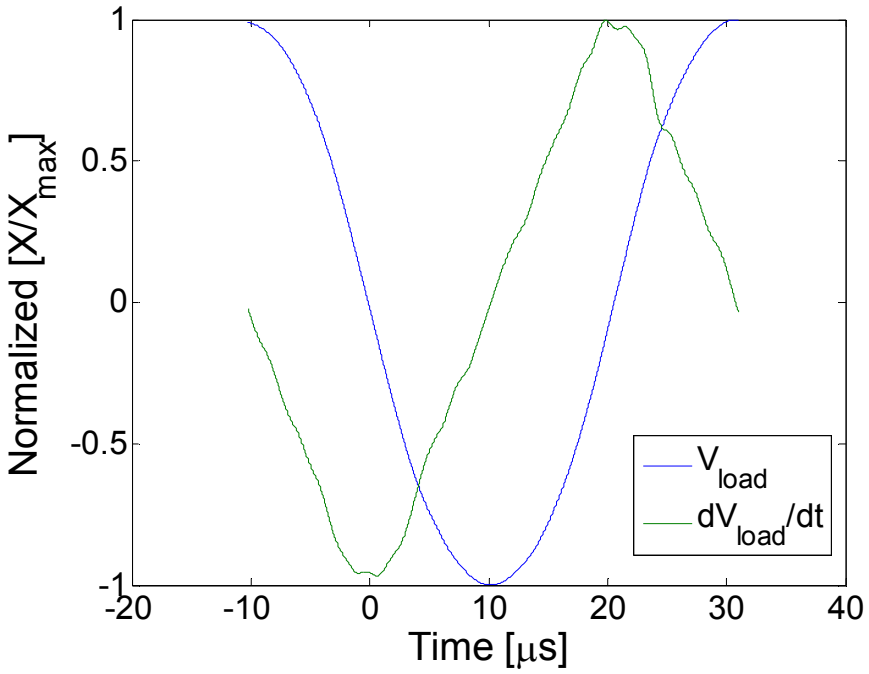

Figure 42. Normalized comparison of V_{load} and the time derivative of V_{load}. The derivative is 90° out of phase with V_{load} as expected, showing that the displacement current will lag behind voltage in mainly a capacitive nature.

Having determined both C and the time derivative of V_{load}, it is now possible to determine the current and resistive components of the plasma in the DBD load. First, the displacement current is calculated using $C = \frac{dV}{dt}$. The displacement current can be subtracted from the total current to give the plasma current. The three currents, I_{tot}, I_{disp}, and I_{plasma} are all shown in Figure 43. The plasma current is used to determine the plasma resistance by Ohm's Law. Ohm's Law states that the plasmas resistance, $R_{plasma} = V_{load}/I_{plasma}$. There are some analysis challenges in doing this ratio. As is evident in Figure 43, the current is very small (on average zero) and has a low signal to noise ratio at all times except during the spikes. Luckily the current spikes are the features of interest. For this reason R_{plasma} is only calculated when the absolute value of current is above a threshold of 5 mA, and if the current was less than the threshold value then a large resistance $R_{load} > 100$ MΩ is assumed. The plasma resistance is plotted as a function of time in Figure 44. As is seen in the figure during the current pulses of the DBD plasma the resistance drops to below 100 kΩ for about 50 ns, and has a minimum of about 35 kΩ for about 10 ns. During both the positive and negative halves of the voltage cycle there are at least one and sometimes several short duration conductive plasmas. The initial current pulse on all 9 half cycles shown has a relatively consistent minimum resistance of about 35 kΩ. When there are subsequent current pulses (for all of the negative cases and one of the positive cases) the plasma is significantly (a factor of 4 to 10) less conductive than during the first current pulse. Attention at this point should only be paid to the first plasma pulse on each half cycle. That the resistance is different on the subsequent cycles is due to a miscalculation of the voltage in these cases due to

charge buildup on the quartz dielectric. The asymmetry in the positive and negative half cycles is due to the asymmetry of this DBD configuration, a quartz dielectric only covers the top electrode.

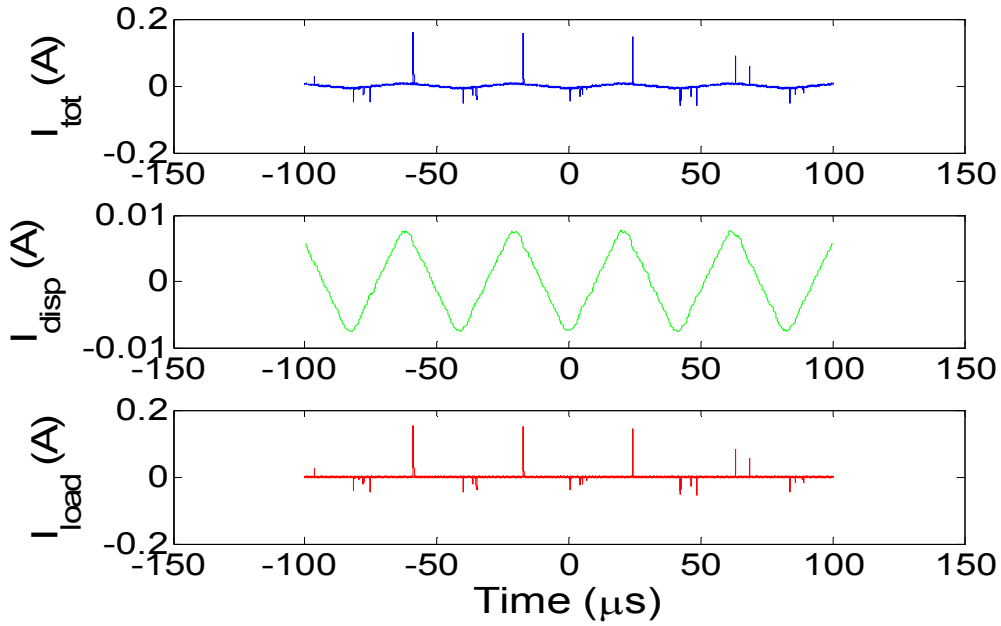

Figure 43. Current traces for I_{tot}, I_{disp} and I_{load} over entire time domain. The total current is the sum of the displacement and load currents. The y-axes are not constant.

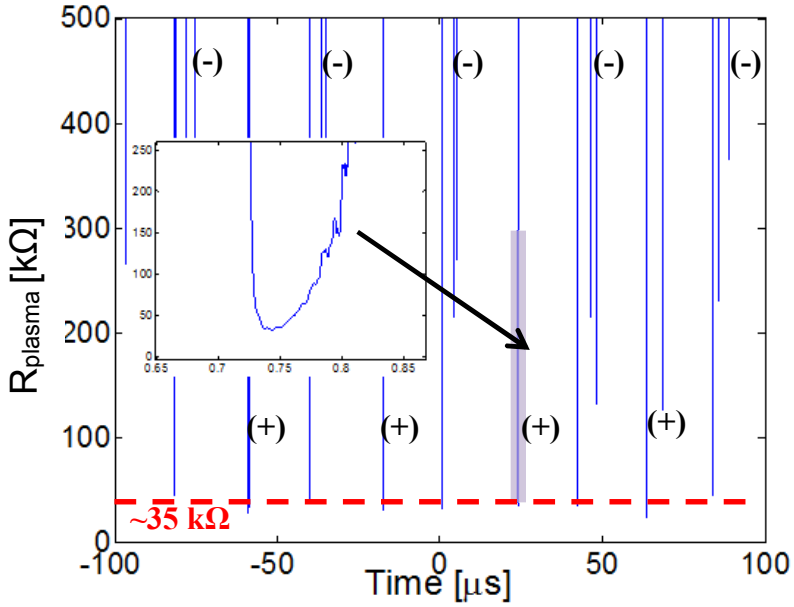

Figure 44. Time history of plasma resistance. The initial discharge typically has a minimum resistance of ~35 kΩ while subsequent discharges (generally only in the negative cycle) have minimum resistances in excess of 150 kΩ.

Some interesting characteristic can be studied by plotting the plasma resistance as a function of plasma current or voltage. Figure 45 shows a plot of how resistance varies with current. Key features of this plot are somewhat intuitive. As the discharge approaches its peak current, the plasma resistance asymptotically approaches some minimum value, and then as the discharge is quenched, the resistance increase to infinity. Furthermore, the resistances during the positive and negative cycles are easily discernible, and are qualitatively similar. The first discharge pulses follows the same resistance trace, subsequent ones do not, but do follows a parallel trace. A better understanding of this and perhaps a collapse onto one another of some of the curves may occur as we take into account the quartz dielectric surface charging.

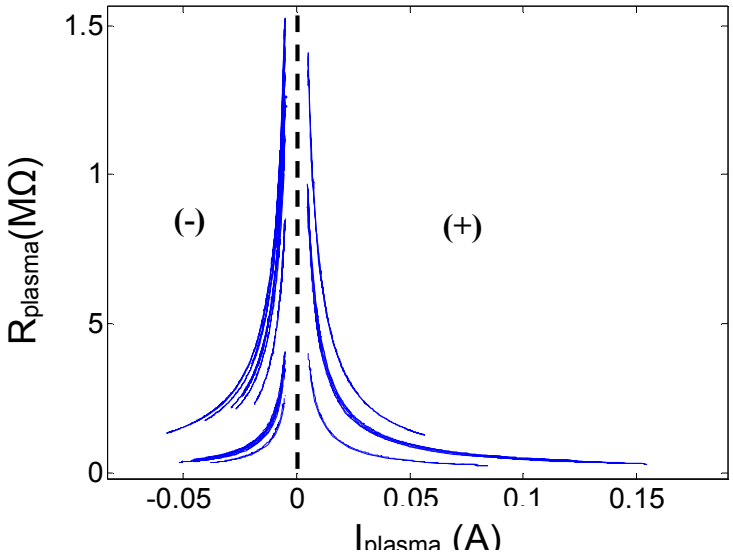

Figure 45. Variation of DBD resistance with plasma current. Resistances from positive and negative cycles are distinguishable. The plasma resistance rapidly increases as the current approaches 0 A. Note that resistances at low current were filtered out, so the very high resistance regime is not shown.

The plasma resistance is plotted as a function of V_{load} in Figure 46. V_{load} represents the breakdown voltage at which the DBD plasma was initiated. The supposedly more accurate R_{plasma} are those reaching down to 35 kΩ. These indicate a breakdown voltage of about 4600 V on the positive half cycle and about -2kV on the negative half cycle. These will be revisited as we consider surface charging on the quartz dielectric.

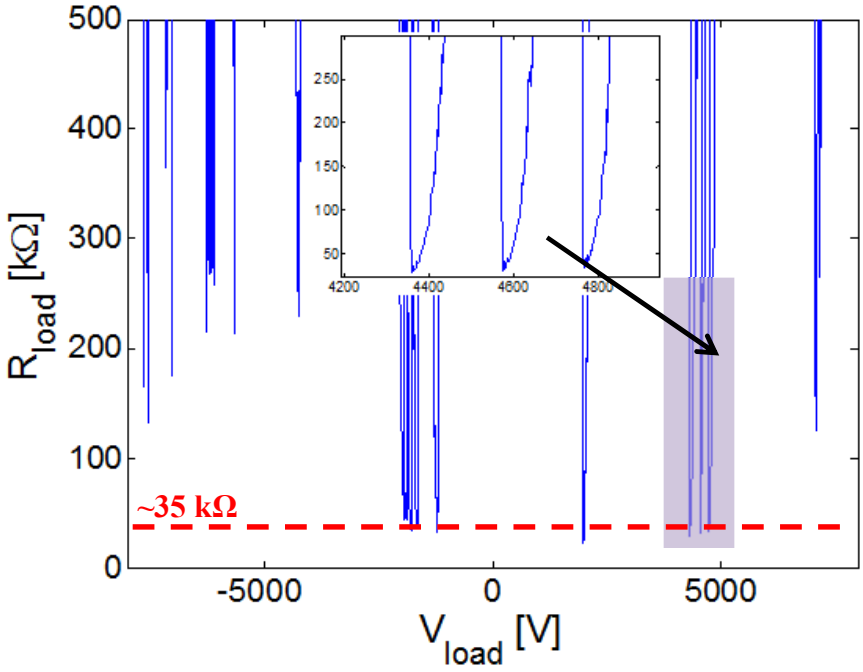

Figure 46. Variation of plasma resistance with respect to load voltage.

3.6.4 DC ns-pulsed experimental setup

After the DBD was characterized using the AC sinusoidal plasma driver, experiments were conducted with the DBD load driven through the pulsing circuit. A complete circuit diagram is shown in Figure 47.

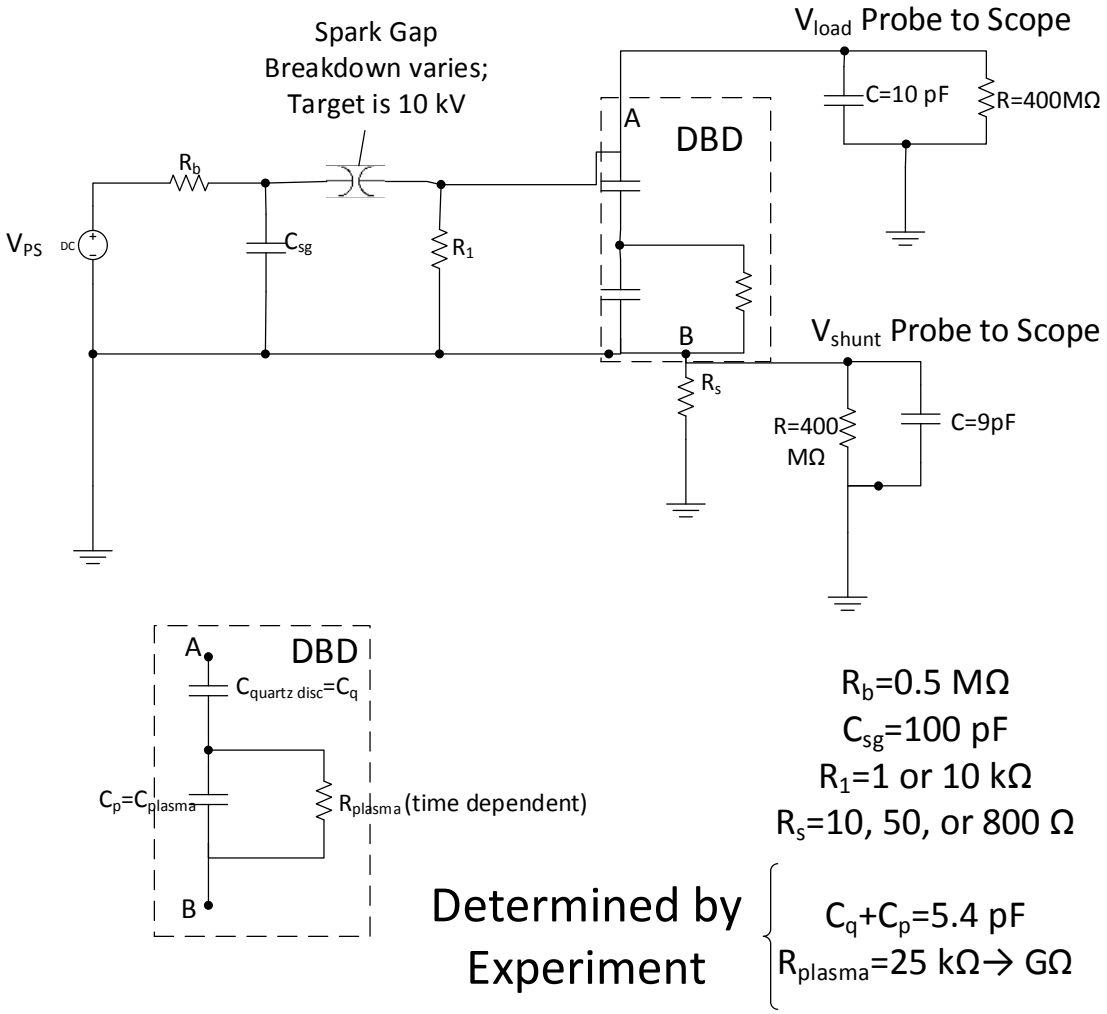

Figure 47. Circuit diagram for DC ns-pulsed experimental setup with DBD load.

This pulsing circuit featured a 1.5 cm spark gap in a pressure chamber. The pressure chamber was filled with Helium at various pressures from 150 to 240 psig. The circuit was powered by a 0-50 kV DC power supply, with a ballast resistor to limit current and protect the power supply. A 100 pF capacitor is part of the pulsing circuit and provides the energy required for DBD formation, and resistor R_1 was added to prevent charge accumulation on the load. The DBD configuration including the probes is

the same as used from the AC sinusoidal characterization. The exception to this is that a 10Ω shunt resistor was used. The input impedances of the diagnostic probes are shown in Figure 47 as we are considering if they too should be included in the circuit model used for estimating the load characteristics. Also potentially necessary to include are stray inductances (0 to 5 nH, typ.) in the wiring and circuit elements.

3.6.5 Monopolar DBD characterization

The theory used for characterizing the load is unchanged for the DC experiments but several minor modifications had to be made to the analysis algorithm. One important change was the time response on the probes had to be more accurately synchronized since both current and voltage change rapidly. Two dissimilar voltage probes are used to collect V_{load} and V_{shunt}. The cables lengths between probe and oscilloscope are different for the probes. The V_{shunt} cable length was approximately 1 m, and the V_{load} cable was 5 m in length. Because of the rapid nature of the ns-discharge, delays resulting from different cable lengths must be considered. To determine the delays that the length difference would cause the probes were both connected to a function generator and the delay measured on the oscilloscope. Voltage traces from the function generator are shown in Figure 48, showing a delay of 18.8 ns between identical input signals. Comparison shows the ÷1000 V_{load} probe lagging the ÷10 V_{shunt} probe by 18.8 ns. This delay was used to synchronize the signals.

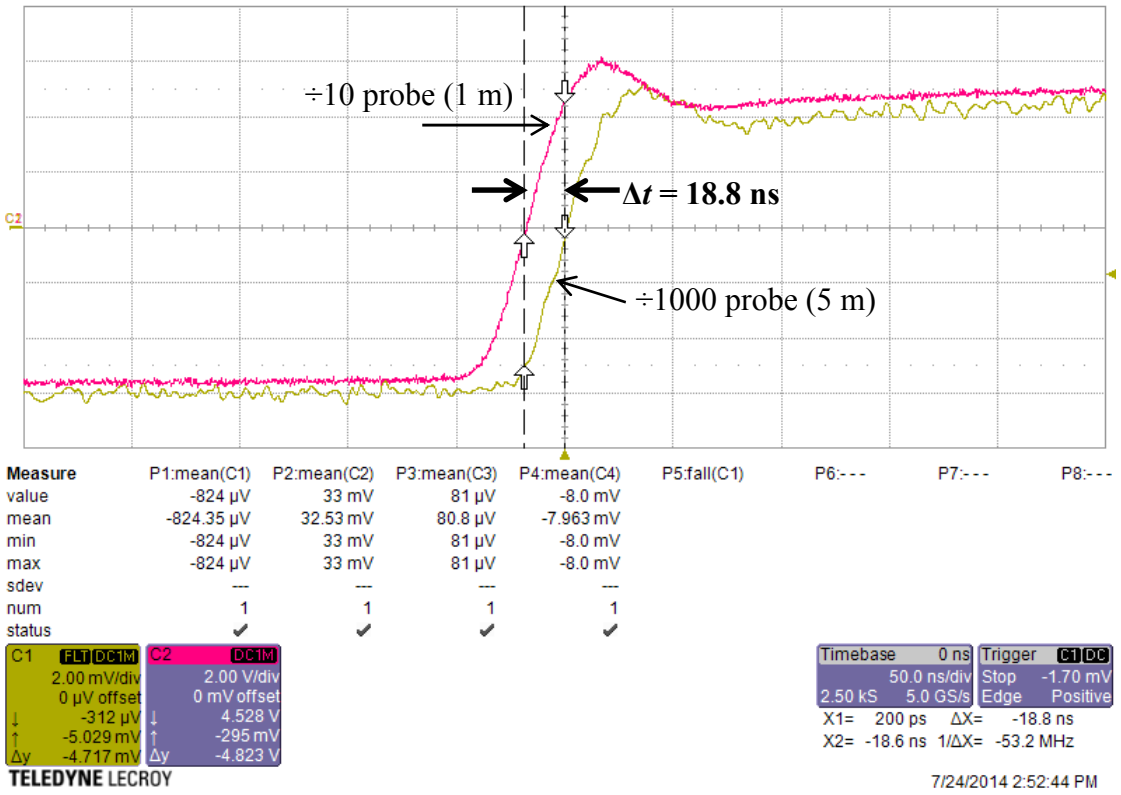

Figure 48. Voltage traces of pulses produced by function generator. The delay is shown to be 18.8 ns.

The load voltage was again smoothed to numerically determine $\frac{dV}{dt}$ to calculate displacement current. Both raw and smoothed data are shown in Figure 49. Due to rapid transience less aggressive smoothing was used. Specifically, a piecewise linear fit over 50 points was used (MATLAB function '*smooth*' with '*moving average*' method over 50 points). As seen in Figure 49, and unlike the AC voltage trace, the pulsed DC voltage is not sinusoidal, and features large voltage spikes. To preserve these spikes, less smoothing was applied to the voltage data, and a central difference method was used to

calculate the derivative of voltage with respect to time. Derivative values were smoothed with the same function parameters to determine displacement current.

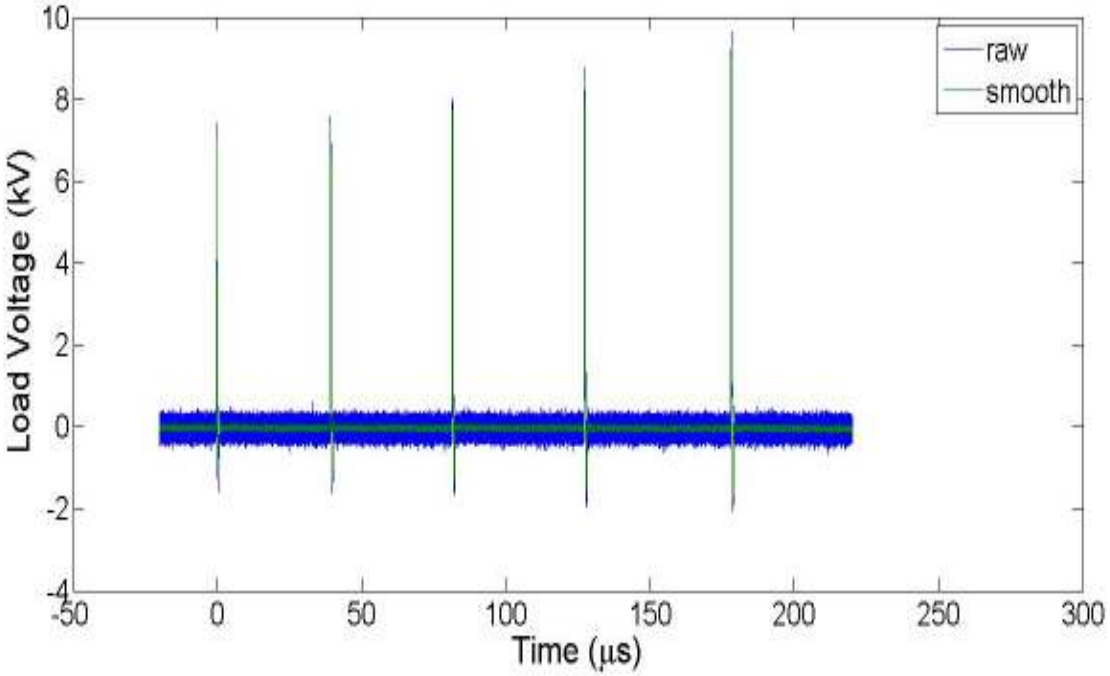

Figure 49. Raw and smoothed load voltage. Less filtering was applied to preserve the voltage spikes.

For the DC ns-pulsed case V_{shunt} measurements were treated the same way as for the AC data. First an offset was removed under the no net charge accumulation assumption and I_{avg} = 0 mA over the 250 μs sample period. The current offset was found and corrected in the same way as for the AC circuit. Mean V_{shunt} was calculated and subtracted from the data. The shunt voltage was smoothed using the previously mentioned '*smooth*' function in MATLAB. Figure 50 shows V_{shunt} before and after

smoothing. The resulting signal was then divided by the R_{shunt} to give total current and integrated to give charge. As in the case of the sinusoidal AC DBD the charge after integration was not zero between each cycle. Again it is assumed that this is not a real physical effect, but rather is an artifact of the AD process. To remove this erroneous charge an additional correction (as in the AC sinusoidal case) was applied to the charge by fitting a high order polynomial to the data and subtracting it, resulting in charge data that more closely resembled the expected behavior of the DBD with zero net charge between each cycle. The initial and corrected charge plots, along with the applied polynomial, are shown in Figure 51.

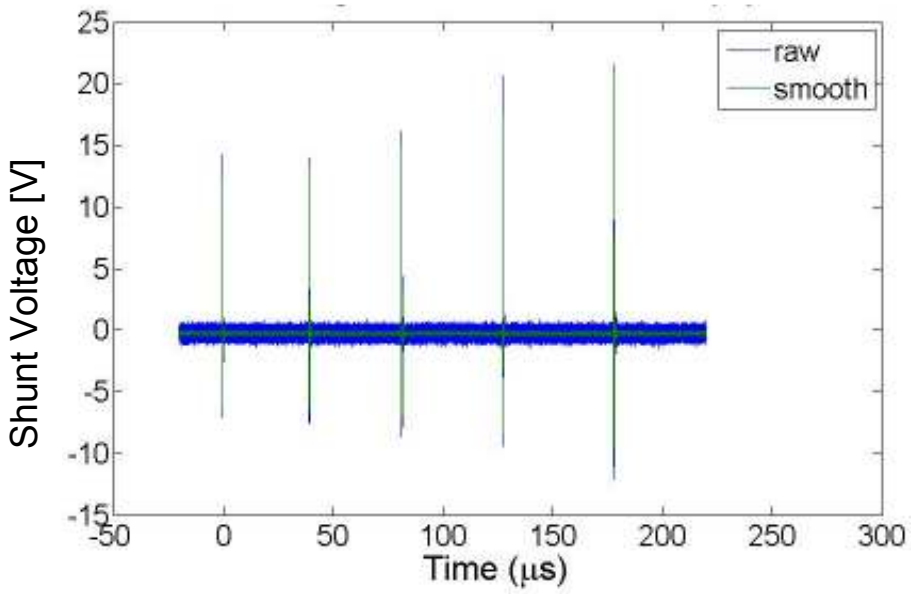

Figure 50. Raw and smooth voltage data across current shunt. As for AC current, less smoothing was applied to preserve information about current spikes.

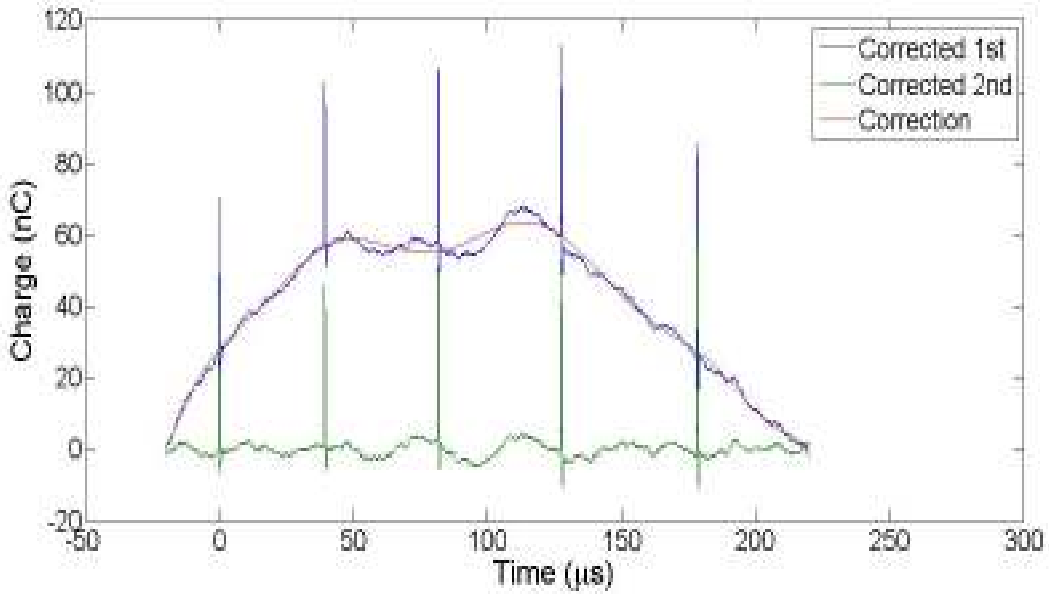

Figure 51. Charge plots showing initial charge plot and correction.

Using the corrected charge and the V_{load} signal, charge was plotted against voltage to create a Lissajous plot for a single pulse. The plot is shown in Figure 52 and indicates the voltage rising ($dV/dt>0$) and voltage falling ($dV/dt<0$) parts of the pulse as well as linear fits whose slopes correspond to C_{load} during the voltage fall and rise. The capacitance of the DBD gap is determined by a linear fit of charge vs. voltage. The linear potion of the voltage rise (<6kV) is probably most accurate for determining capacitance, and the capacitance determined from this is similar to (if not identical) to that determined for the sinusoidal driven DBD. The same capacitance is to be expected since the geometry of the DBD system did not change.

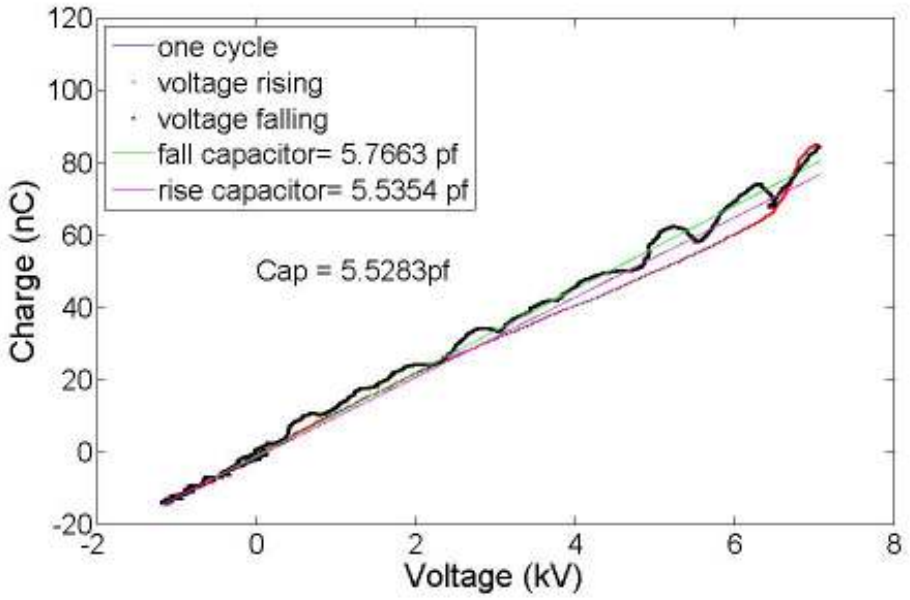

Figure 52. Lissajous plot of charge vs. voltage indicating capacitance during fall and rise of pulse.

Displacement current was again calculated using $I = C\frac{dV}{dt}$ and then subtracted from the I_{shunt} to give the I_{plasma}, which is plotted in Figure 53. The validity of some of the trends features is questionable. First, as calculated, the displacement current is larger than the total current indicating negative current through the plasma. This may not be a real effect, but rather an artifact of some neglected elements of the circuit, possibly EMI. When the voltage is rapidly changing $\frac{dV}{dt}$ on the diagnostic probes may become significant. This was not taken into account in this analysis.

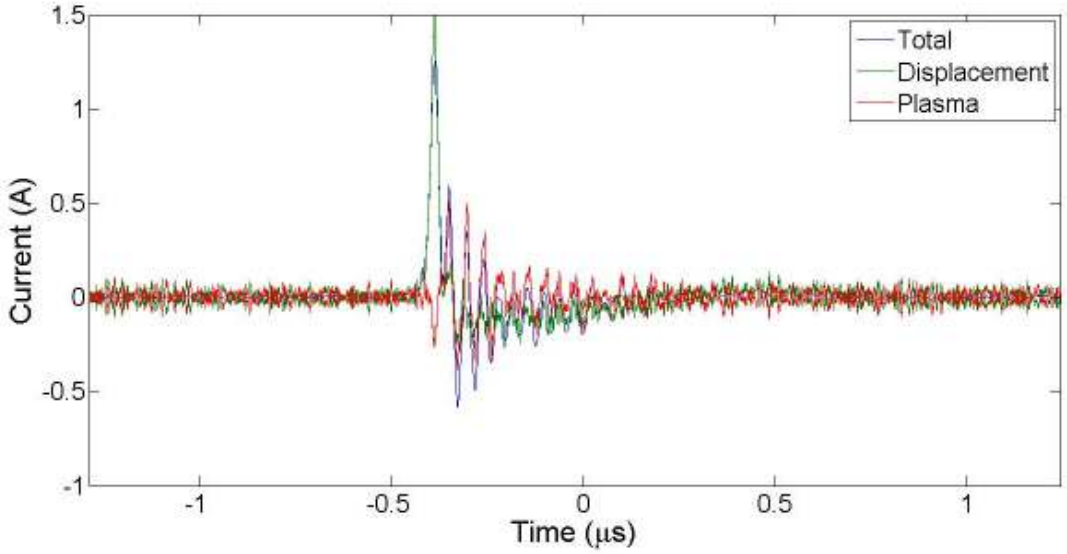

Figure 53. Plots of total current, displacement current, and plasma current for one pulse.

The plasma resistance was calculated using an oversimplified model. This was done as before by dividing the DBD voltage by the DBD current during pulsing, the plasma resistance was obtained. As in the AC analysis, plasma resistance drops sharply as current is initiated, then rises back to practically infinite values as the charge on the load drops. Resistance is plotted against time in Figure 54. The resistance plot shows intervals of negative resistance during pulses which is unrealistic. These intervals may occur because of $\frac{dQ}{dt}$ oscillations from displacement currents in the diagnostic probe that have not been taken into account. Calculated resistances are similar to those observed for the sinusoid AC driven DBD.

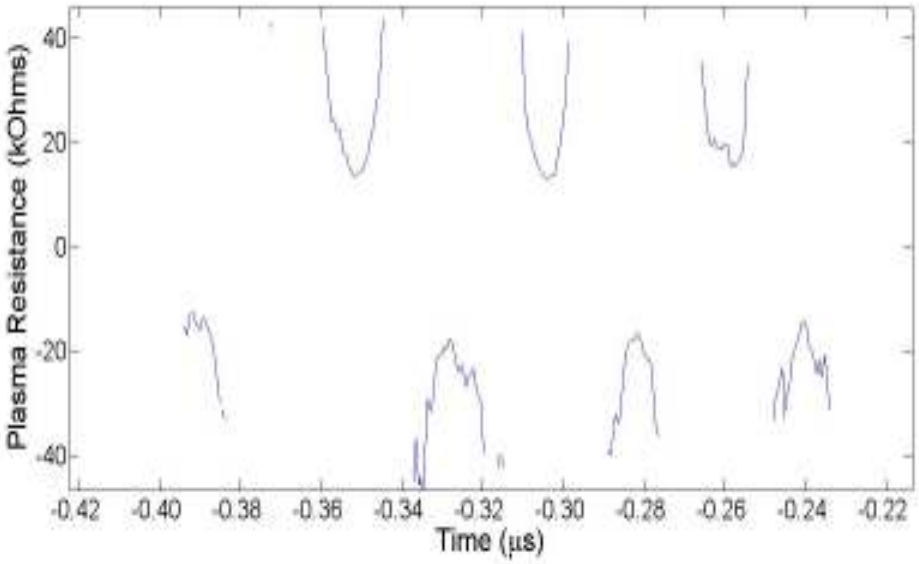

Figure 54. Calculated plasma resistance shows intervals of negative resistance corresponding to oscillations in current.

3.6.6 Conclusions

The DBD load has been characterized in terms of its capacitance and resistance using a simplified model of the DBD and plasma circuit. Capacitance was determined from Lissajous plots and was used to separate displacement from direct currents, and the direct currents were used to calculate the plasma resistance. The analysis method was first applied to a DBD powered by a sinusoidal AC power supply, and then it applied to a DBD driven by a ns-pulsed DC power supply. Smoothing variations in the analysis algorithm are discussed. The capacitance and resistance of the DBD load was determined by two independent time dependent data sets. The first data set was of the voltage across the DBD, and the second was the voltage drop across a shunt resistor to determine total current. Post-processing of the data from the DBD powered by the two

different sources were in good agreement and showed that the capacitance of the DBD load is approximately 5.5 pF and the minimum resistance is in the range of 15-40 kΩ. The data and analysis model is still being examined in an effort to identify faults and useful trends and other relationships.

3.7 EMI mitigation

EMI is an undesirable side effect of all pulsed power systems, and steps should be taken to either reduce EMI emission or bolster EMI resilience. EMI emission from DC pulsed circuits with various cable lengths, cable orientations, and shielding presence was measured. In these experiments, EMI was measured using a monopole antenna connected to an oscilloscope and monitoring voltage transients during pulsing events. Means and standard deviations were recorded for large sample sizes (n>1000) of the antenna peak to peak voltage. Results were compared and best practices for EMI reduction were determined. Properly grounding the oscilloscope and removing 'unintended antennas', in this case a voltage probe, reduced EMI detected by the oscilloscope by a factor of 4. The investigation concluded that EMI could be reduced by more than 50% by shielding all high voltage components as opposed to when components are unshielded.

3.7.1 Experimental setup

The DC pulsed circuit used for generating EMI is described in Figure 55. The power supply was capable of 7.5 mA at 40 kVDC, and a ballast resistor of 3 MΩ

isolated it from the pulsed circuit which contained a 100 pF door-knob type capacitor connected in parallel with a spark gap of 3 mm in ambient air. The oscilloscope was situated 150 cm away from the pulsing circuit. RMS values for power supply current and voltage were 1 mA and 5 kV and were held constant. Conductors L_1 and L_2 were independently manipulated.

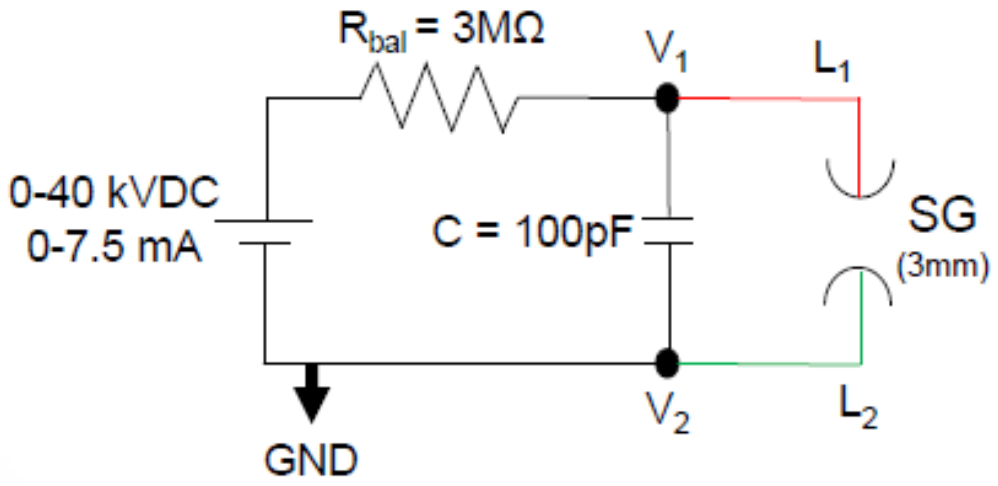

Figure 55. Pulsed DC circuit in ambient air used for generating EMI detected by an antenna.

Lengths of conductor, L_1 and L_2 were varied to determine effects of conductor length, geometry and orientation. Long (96”), medium (44”) and short (12”) lengths of round stranded conductor were investigated and their orientations, as described in Figure 56, were varied. A short length of flat grounding strap was also tested.

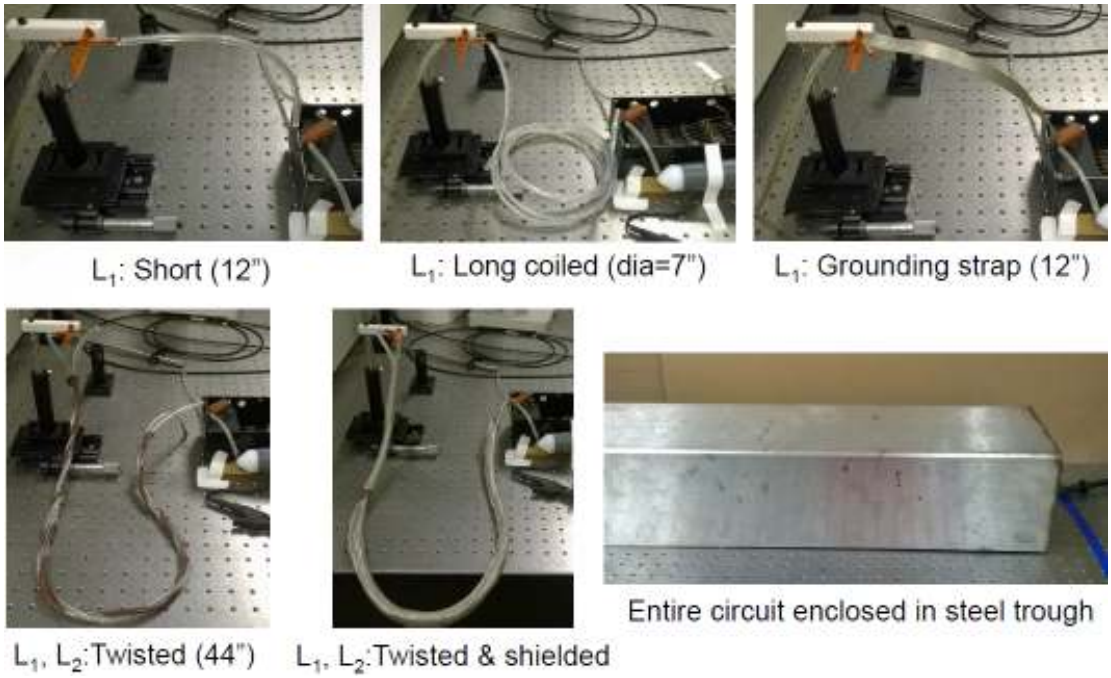

Figure 56. DC pulsed discharge circuit variations used in assessing EMI reduction.

Radiated EMI was detected using a 30.5 cm long 1 mm diameter monopole antenna connected to an oscilloscope as shown in Figure 57. If the antenna length is taken as λ/4, the quarter-wavelength, then this antenna is best suited for frequencies of 2.5 GHz. Conducted EMI generally has an upper frequency limit of 30 MHz and was not considered in this experiment.

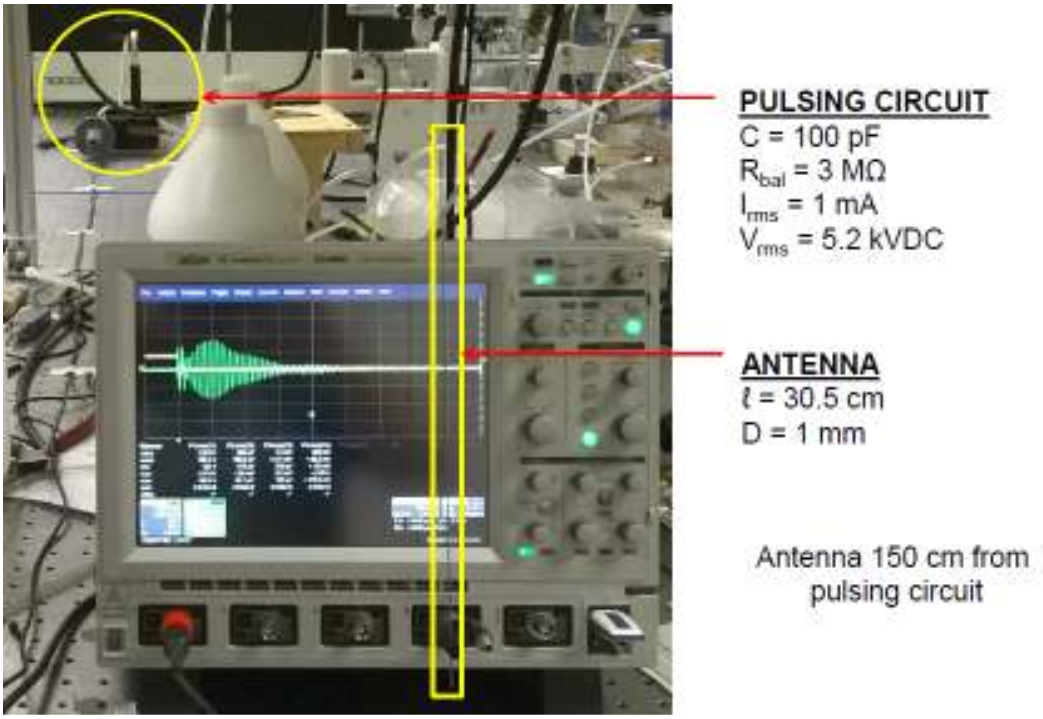

Figure 57. EMI reduction experimental setup showing antenna in scope Ch4 and DC pulsed circuit parameters. The high voltage probe in Ch1 is connected to the pulsed circuit and the oscilloscope is not well grounded.

3.7.2 Results

EMI was reduced by more than 50% when the pulsed circuit and HV leads were surrounded by a conductive trough shaped shield as shown in Figure 58. Although not shown in this figure, foil was used to fill air gaps between the trough and grounded optical table. When the trough covered all HV components, the peak to peak voltage detected by the antenna was 353±22 mV. When shielding was not used peak to peak voltage was 925±121 mV. Antenna voltage responses to the varied circuit/shielding/grounding configurations are provided in Table 7 and Table 8.

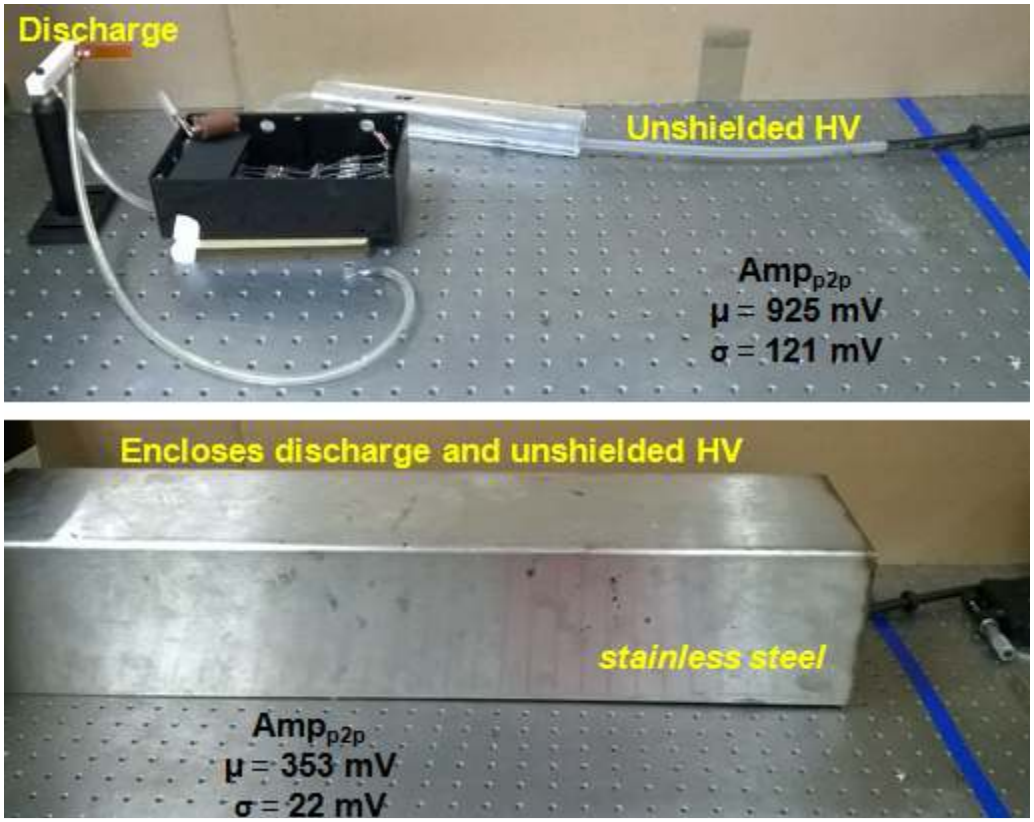

Figure 58. Unshielded and shielded HV components.

Table 7. Peak to peak voltage on monopole EMI detecting antenna connected to an ungrounded oscilloscope with unintended antenna (HV probe). Oscilloscope ungrounded with high voltage probe connected.

PULSED CIRCUIT CONDUCTOR CONFIGURATION	L_1 *[in]*	L_2 *[in]*	EMI_{avg} *[mV]*	EMI_{max} *[mV]*	EMI_{std} *[mV]*
Long (7" coil dia)	96	12	1170	1420	83
Long ('S' pattern)	96	12	1610	2380	257
Medium (Hanging 'U')	44	44	1690	2330	213
Twisted	44	44	1890	2530	213
Long (Hanging 'U')	96	12	2190	2720	177
Flat (ground strip)	12	12	2440	3210	257
Short	12	12	2960	3730	257
Medium (gnd strap shld)	44	44	3220	4150	310
Twisted (gnd strap shld)	44	44	3330	4050	240

Table 8. Peak to peak voltage on monopole EMI detecting antenna connected to a grounded oscilloscope with no unintended antenna (HV probe). Oscilloscope grounded with high voltage probe disconnected.

PULSED CIRCUIT CONDUCTOR CONFIGURATION	***L1 [in]***	***L2 [in]***	***EMI_{avg} [mV]***	***EMI_{std} [mV]***
Short w Trough & Foil (all HV)*****	12	12	353	22
Short w Trough/Foil; PS GND (all HV)*****	12	12	420	35
Short w Trough (all HV)*****	12	12	502	37
Short w Trough (DC Pulse)*****	12	12	573	53
Short w Trough/Foil (DC Pulse)*****	12	12	583	73
Long w Trough	96	12	647	71
Short w Trough	12	12	840	91
Long	96	12	901	157
Short	12	12	925	121
Short*****	12	12	951	133

**** Pretzel knot in HV-side wire to prevent contact with trough wall.***

3.7.3 Conclusions

The data shows that voltages were nearly three times higher when the oscilloscope was not well grounded and was connected to a high voltage probe measuring the pulsed voltage. The high voltage probe could have caused EMI increases in two ways. Physically connected components introduce conducted EMI in addition to radiated EMI. Also, the long length of the HV cable serves as an unintended second antenna, and because of the length difference it would be sensitive to EMI of different frequencies. Long L_1 and L_2 appeared to induce less EMI than short cables, and surrounding them with grounding straps, which were intended for shielding, caused greater EMI. The geometry of the conductor did not appear to have a significant impact, as flat conductors and round wire conductors of the same length caused similar EMI.

Twisting L_1 and L_2 did not have a significant effect on EMI reduction. The most important effects in reducing EMI were complete shielding of all HV components and limiting unnecessary EMI components (conducted and excess antennas).

4. MICROSCALE DENSE PLASMA FOCUS*

The dense plasma focus (DPF) is a device that uses strong magnetic fields caused by high pulsed currents to rapidly compress gas at the anode tip and generate a high temperature plasma. In optimized devices compression is so great that pulsed fusion reactions occur, releasing energetic neutrons and x-rays. The dense plasma focus was invented in the mid-1950s by N. Filippov and then independently by J. Mather in the 1960s. Since its invention, the dense plasma focus has found use as an 'on-demand' source of energetic particles and as a convenient experimental apparatus to study complex plasma dynamics.

4.1 Introduction to dense plasma focus devices

The DPF is a coaxial plasma discharge device with a central anode, outer cathode electrodes and one open end. DPF devices are capable of generating regions of dense high temperature plasma by rapidly pulsing current between the anode and cathode in a low pressure environment. Current densities in DPF devices are sufficiently high that self-induced magnetic fields dominate the dynamics of the plasma. The magnetic fields can localize and confine the energy release to a region near the anode tip. While these effects are brief, usually lasting only nanoseconds, plasma densities can be greater than

---

* Reprinted with permission from "Dynamics of two microscale DPF devices" by W. Pollard, A. Duggleby & D. Staack, 2015. J. Phys D: Applied Physics, 49(5), pages 1-12, Copyright 2015 by IOP Science.
DOI - http://dx.doi.org.ezproxy.library.tamu.edu/10.1088/0022-3727/49/5/055201

10^{19} cm^{-3} and ion temperatures on the order of 1 keV can be achieved [32] [33] [34] [35].

Because they are so effective at creating highly energetic compressions, DPF devices are used as sources of x-rays and neutrons as well as generators for ion and electron beams [35]. DPF devices have been tested across a wide range of energies and sizes from the larger devices, ~10 cm in diameter, which may consume energy on the order of MJ, to the smaller devices, <1 mm in diameter, which operate at less than 1 J. The most well studied DPFs are those in the United Nations University/International Centre for Theoretical Physics Plasma Fusion Facility (UNU/ICTP PFF) network. These DPF devices were constructed by the Asian-African Association for Plasma Training. The UNU/ICTP PFF network consists of at least six similar DPF devices all of which operate on the order of 1 kJ [36]. Given the wide array of capabilities, it is not surprising that DPF devices have found an equally wide array of practical and theoretical applications. Such applications are materials processing [37] [38] [39] [40] [41] [42] [43] [44], neutron generation (creation of radioisotopes, neutron imaging, equipment calibration, fast neutron activation analysis) [45] [46] [47] [48] [49] [50] [51], x-ray generation (radiography, microlithography) [52] [53] [54] [55] [56] [57], fusion research [58] [59] [60] [61], object detection (active interrogation) [62] [63], and even medical applications [64].

DPF devices generally come in two geometric variations based on the aspect ratio of the anode length to its diameter, ℓD. Mather-type configurations have anodes that are longer than they are wide such that $\ell D > 1$ where a ratio in the range of 5-10 is

typical. The other type of configuration is the Filipov type where $\ell D < 1$ [34]. There are several ways in which the cathode may be situated around the anode. For one, the anode and cathode may be configured as coaxial cylinders with a dielectric interface between the two at one end. In a slight modification to the coaxial arrangement, a squirrel cage setup is one in which the anode is surrounded by a set of evenly spaced cathode pins equidistant from the anode axis. In yet another arrangement, the anode is insulated by a dielectric and left to protrude from a conductive surface that is cathode. This last anode/cathode arrangement was used in our experiments. The last two configurations have open cathodes which allow for radial expansion and prevent plasma flow stagnation at the cathode surface and thus improve the quality of the device [33].

The operation of a DPF device can be divided into three distinct phases. The first phase is the initial breakdown. During this stage, the voltage applied to the central anode reaches the breakdown voltage which is controlled by environmental and geometric conditions as well as insulator properties. The second phase is the rundown phase during which the current sheath is accelerated by $\mathbf{j}\times\mathbf{B}$ forces to the end of the anode, and a parabolic current sheath develops. The current sheath is both a propagating ionization wavefront and the motion of ionized gas moving in the direction of the anode tip and is different from a plasma sheath which is more similar to a fluidic boundary layer. The vertex of the parabolic current sheath is located at the exposed tip of the anode, expanding in the direction of the cathode, and ideally the sheath development is azimuthally symmetric. Finally, in the pinch phase these same $\mathbf{j}\times\mathbf{B}$ forces acting around the central electrode tip cause a concentration and confinement of the plasma to the tip

of the anode. Elevated temperatures and plasma densities occur during the pinch phase and are maximized when the circuit is timed to peak current as the sheath reaches the anode tip, collecting and pushing gas into this region by the **j**×**B** forces in the so called snow plow effect. A significant portion of the confined plasma may escape along the axis, and very intense pinches do not always occur given this geometry. Other deficiencies are asymmetric breakdown phases resulting in **j**×**B** forces not leading to compression at the tip [33], or poor timing of current peaking during the end of the rundown phase [34].

DPF devices of various sizes tend to share similar derived parameters, and they are useful as guidelines in the design of DPF devices. The PF-1000, one of the largest DPF devices, operates above 1 MJ and has an anode radius of 6.1 cm whereas the PF-50J is by comparison one of the smaller devices, operating with 50 J and a 0.15 cm anode radius [65]. The anode radius, a, can be used to predict the size of the pinch which is assumed to be cylindrical having a radius of ~0.12a, length of ~0.8a and a volume of V_p=0.036a^3. Even though the operating energies, E, of these devices can differ by 4 orders of magnitude, their energy density (ED) parameters, given by ED=28Ea^{-3}, differ by less than one order of magnitude. In optimized devices the energy density parameter is on the order of 10^{10} J m^{-3}. Another important scaling quantity is the drive parameter (DP), which is given by $DP = I_0\, p^{-1/2}\, a^{-1}$, where I_0 is the peak current and p is the environmental filling gas pressure. The drive parameter is typically in the range of 65-95 kA mbar$^{-1/2}$ cm^{-1} for all optimized DPF devices, and it controls the radial and axial plasma velocities. Devices of similar drive parameters, have comparable characteristic

velocities and temperatures [66]. Furthermore, during the rundown and pinch phases both the current sheath's radial and axial velocities, v_r and v_a respectively, are proportional to the drive parameter and in the range of ~1-2.5 × 10^5m s^{-1}. The microscale DPFs investigated in this research have characteristic velocities of ~1-4 × 10^4 m s^{-1}.

Since focus devices are effective in generating high energy particles, scaling laws for neutron and x-ray production are of practical importance. Experimental and numerical results of neutron yield, Y, in deuterium seem to follow scaling that suggests $Y \sim I_{pinch}^{3.3-4.5}$ [65] [67]. X-ray emission is highly gas dependent and has been found to scale as $E_{xray} \sim I_{peak}^{3.2-5.5}$ [34] [67]. Considerable numerical analysis for neutron and x-ray scaling has been conducted by Lee and is evident in the success of his 5 phase model, which shows good agreement with experiments involving low inductance Mather type focus devices with E >1 kJ [68] [69].

A motivation for building lower energy devices - those with small anode radii - is so that rapidly firing radiation sources may be investigated. Rapid firing radiation sources tend to be smaller and are thus more portable. Furthermore, since they are rapid firing devices, they can maintain sufficient flux of high energy particles. Such devices may be amenable for fieldwork involving substance detection [46] [70]. Researchers led by L. Soto have pioneered the miniaturization of the DPF device. They have shown evidence of pinch in the PF-50J (E=50 J, a=6 mm) and also in the nanofocus (NF) device (E=0.1 J; a=0.8 mm) using optical techniques and voltage/current waveform analyses [71] [72] [73]. Using a proportional ^{3}He counter, they were able to show neutron emissions on the order of 10^4 neutrons per shot in the PF-50J device.

In their work on the PF-50J, Moreno et al captured highly time resolved images of the rundown phase, the pinch, and even the lifting of the pinch off of the anode [72]. They note how the evolution of the current sheath is the same in this device as it is in those that operate at energies several orders of magnitude higher. However, in their work on the very smallest DPF, the nanofocus (a=200 um) device [71], a full description of the current sheath's evolution is absent. Energy density and drive parameters for the nanofocus have been calculated as 3×10^{11} J m^{-3} and 126 kA mbar$^{-1/2}$ cm^{-1}, respectively.

In this paper, temporally resolved dynamics of two small protruding Mather-type microscale DPF devices are explored. Previous work with microscale devices has done an excellent job demonstrating and characterizing miniaturized DPF operation, but little attempt has been made to capture and describe the entire lifetime of microscale pinch phenomena in terms of their characteristic features. This work serves to fill in these gaps with the hopes that it will lead to a better understanding of the pinching process which will result in more reliable operation of smaller devices. Advantages of miniaturizing these devices are explained shortly. This work also helps to bridge understanding of larger low pressure pinches and more recent moderate energy density sources with novel applications like high pressure microplasmas. A secondary contribution of this work is to further validate DPF operation at micrometer length scales. The larger of the two operates with a=550 μm and stored energy of E~2 J. The second device operated with similar energy but had anode radius of a=100 μm. Miniaturized DPF devices are of interest because efficiency of high energy neutron production may scale as a^{-3} assuming Knudsen and DPF scaling parameters are maintained. As a decreases, operation at

increased pressure is required to maintain scaling, and since maintaining symmetry is an important factor in ensuring effective pinching, close examination of breakdown and rundown phases is necessary. Plasma dynamics were visualized using the plasma visible luminescence and a nanosecond gated ICCD camera. Sequential 50 ns exposures at 100 ns intervals spanning 1 μs were captured from the onset of breakdown through the post pinch expansion. Images were collected and compared for a test matrix of three pressures and three operating voltages. Breakdown asymmetries, rundown features and luminous intensities were evaluated from the images and scaling parameters were also compared to those in the literature. Both devices are among the smallest DPFs tested. Their small size makes convenient the analysis of pinch dynamics using several thousand repetitious firings. Both devices were operated in helium, and neither neutron nor x-rays were sought. Observed microscale dynamics indicate promise for applications to rapid firing neutron sources organized in microscale arrays. Optimization of the current setup is still required.

4.2 Dissertation objectives

This research investigates operation of a microscale DPF powered by gas phase switching. Typically these devices are operated individually at low pulsing frequencies. Because the neutron generation efficiency scales with a^{-3} there is motivation to explore DPF devices with small characteristic lengths. The drawback to this approach is that the absolute number of neutrons generated per pulse decreases as size is reduced. Therefore, the proposed use would be to operate 1000s of microscale DPF devices at kHz

frequencies to attain a practically usable flux of energetic particles. This experiment shows that pinching behavior continues to occur as low as 100 μm anode radius. As the size of the devices decrease, it is important to maintain Paschen scaling for breakdown processes and therefore higher pressure operation (still below atmospheric in these experiments) is required. The gas phase switching research discussed in the prior chapter has shown that it is capable of maintaining this high frequency high voltage operation.

4.3 Experimental setup

Two protruding type anode cathode assemblies were used in this experiment, and they are shown in Figure 59. The larger of the two assemblies shown in Figure 59(a) had a copper wire anode with a=550 μm insulated by an alumina sleeve having OD=2400 μm and a 5 mm square copper block cathode. The alumina insulator extended 7 mm beyond the cathode backplane, and the anode extended 3 mm beyond the alumina.

The anode of the smaller assembly shown in Figure 59(b) was a tungsten wire of a=100 μm radius insulated by an alumina tube with OD =500 μm. A copper block was again used for the cathode. The insulator in the smaller system protruded 4.5 mm from the cathode, and the tungsten anode extended 2.3 mm beyond the alumina. The electrode housing shown behind the cathode contains electrical connections, and it was designed so that the insulator protrusion length was adjustable. Set screws were used to secure the alumina insulator. Electrode assemblies were mounted in and electrically grounded to a vacuum chamber backfilled with helium at flow rates such that chamber pressures were

in the range of 50-190 torr. Industrial grade helium flowed continuously through the vacuum chamber to maintain purity.

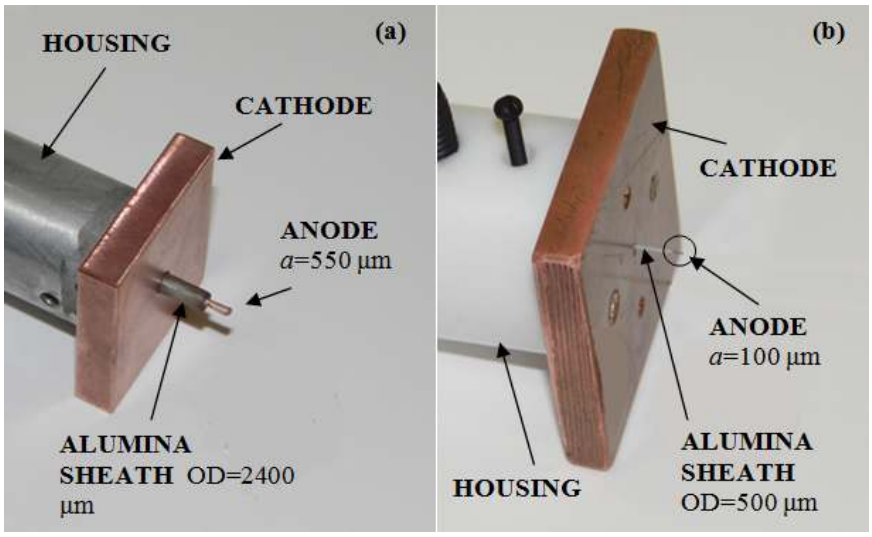

Figure 59. DPF anode cathode assemblies. (a) a=550 um, (b) a=100 um. These are among the smallest DPF anodes tested to date.

To power the DPF, a high voltage DC power supply was connected through a 20 MΩ ballast resistor to a variable length spark gap in parallel with a 100 nF primary capacitor. The variable length spark gap controlled voltage across the primary capacitor. Down-current of the spark gap, two 10 nF low inductance secondary capacitors were connected in parallel, providing 20 nF of equivalent capacitance, and the secondary capacitors were connected in parallel with the DPF electrode housing. The DPF connects to ground through the vacuum chamber. Self-inductance in the circuit down-current of

the spark gap was measured using an LC meter as 1100 nH, which is high in comparison to other DPFs where inductance is typically on the order of 10-100 nH [34]. The DPF device was fired at a rate of 0.5 Hz, limited by the RC circuit and the current supplied by the DC power supply. A schematic of the experimental setup is shown in Figure 60 and an annotated image is shown in Figure 61.

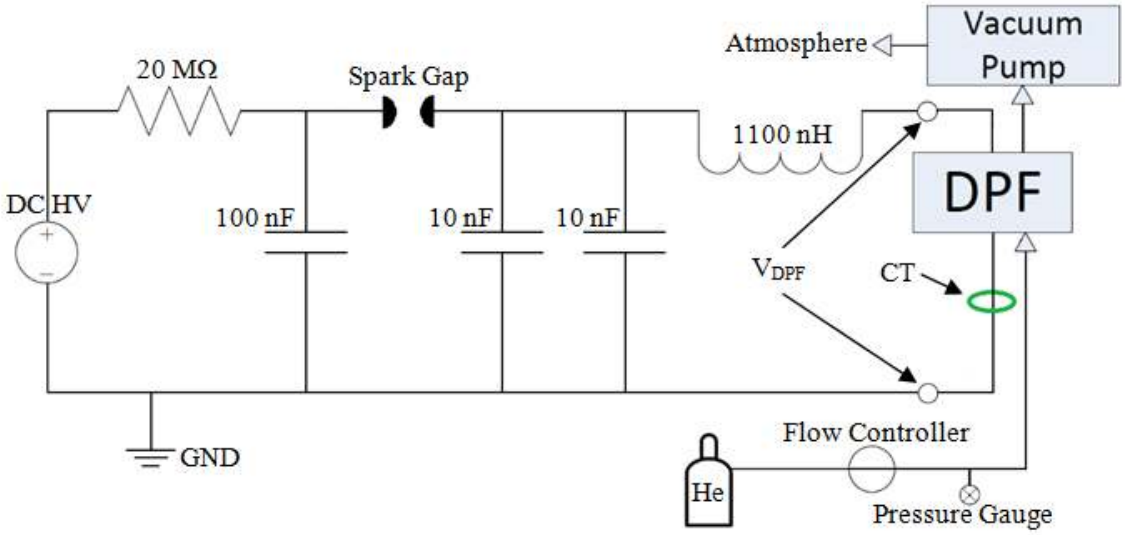

Figure 60. Annotated schematic of experimental setup showing pulsing circuit, gas regulation and electrical measurements.

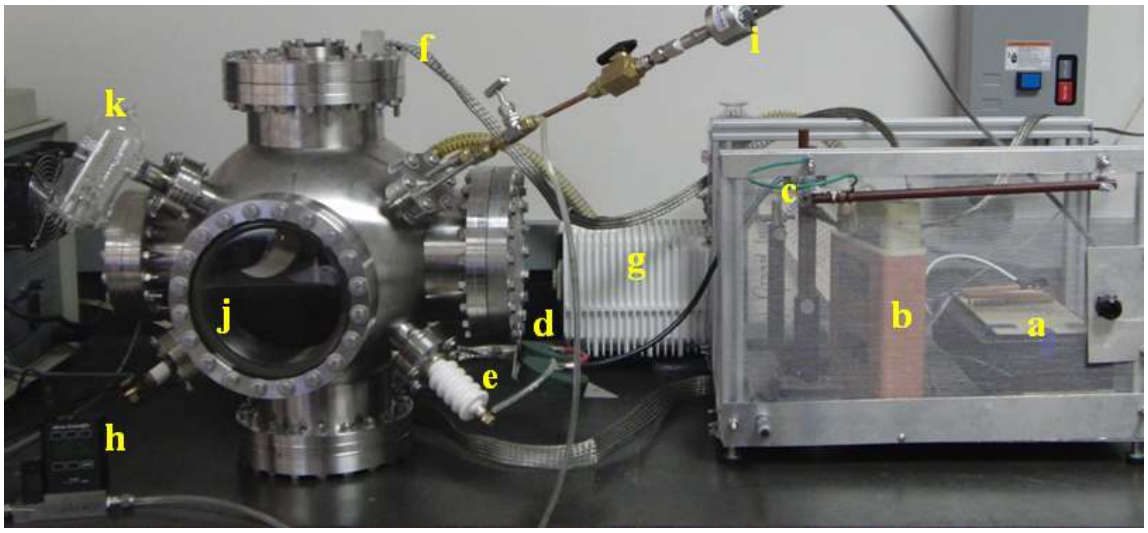

Figure 61. DPF experimental setup. Power supply not pictured. Annotated components are as follows: (a) 20 MΩ ballast resistor, (b) 100 nF primary capacitor, (c) variable spark gap (occluded),(d) two 10 nF secondary capacitors wired in parallel, (e) high voltage feedthru, (f) ground connection (current transducer not shown), (g) vacuum pump, (h) gas flow controller, (i) pressure gauge, (j) optical port. Note: the ionization pressure gauge (k) was not used in the experiment

Images were collected using Stanford Computer Optics 4-picos ICCD camera through a glass optical port on the vacuum chamber. The light was filtered by the vacuum chamber window and camera spectral response. The camera responds to light in the 200-900 nm band, but the window is glass and removes some of the ultraviolet. The acquired light is roughly in the 300-900 nm spectrum. EMI from breakdown in the spark gap was detected by a 5 cm antenna and used to trigger image acquisition in order to avoid cable delays. Internal gating delays are inherent in the ICCD and are specified by the manufacturer as 75 ns.

DPF voltage and current were measured as indicated by Figure 60 on a DPF anode/cathode assembly similar to those shown in Figure 59(a). The anode/cathode

assemblies used while measuring voltage and current had a shorter anode insulator protrusion length. Changing the protrusion length alters the rundown time which is important for peak power timing. Therefore, the electrical signals presented are similar to those of the anode/cathode assembly used during optical analysis. Voltage and current signals were acquired via a LeCroy 204MXi Waverunner oscilloscope triggered by voltage rise. Voltage was measured using a North Star PVM-4 40 kV voltage probe, and current was measured using a Pearson M#101 current transducer (CT). A 50 ns time integrated image is shown in Figure 62 of the anode/cathode assembly used for electrical diagnostics 700 ns after spark gap firing. Similar visible features are apparent upon comparison of the image in Figure 62 to those used for dynamic analysis to be presented in the following section. Voltage and current signals of the DPF pictured in Figure 62 are provided in Figure 63. Presented traces are believed to be representative of DPF operation regimes examined in these experiments. Waveforms in Figure 63 show a peak voltage of 17.3 kV with rise time ~300 ns and peak current of 3.5 kA with a rise time ~350 ns and FWHM ~1 μs. Circuit ringing was observed in both signals and dissipated after 15 μs. Power delivered during the pinch process was calculated from voltage and current signals and is shown in Figure 64. As will be shown in later figures, peak power is delivered after 300 ns, which is approximately the end of the rundown phase.

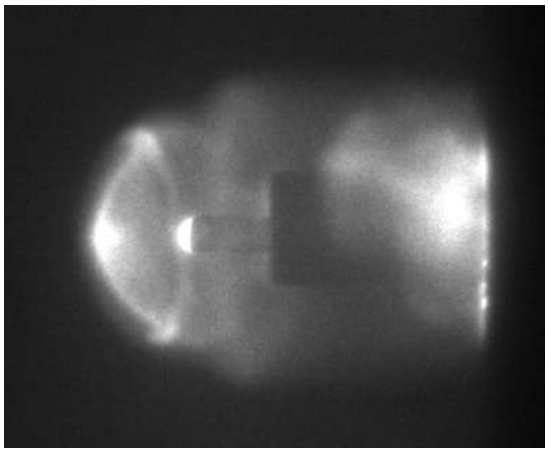

Figure 62. DPF (a=550 μm) firing in 130 torr He at 17 kV. This image was collected using a 700 ns trigger delay and a 50 ns integration time. Subsequent voltage and current traces were collected from this individual firing.

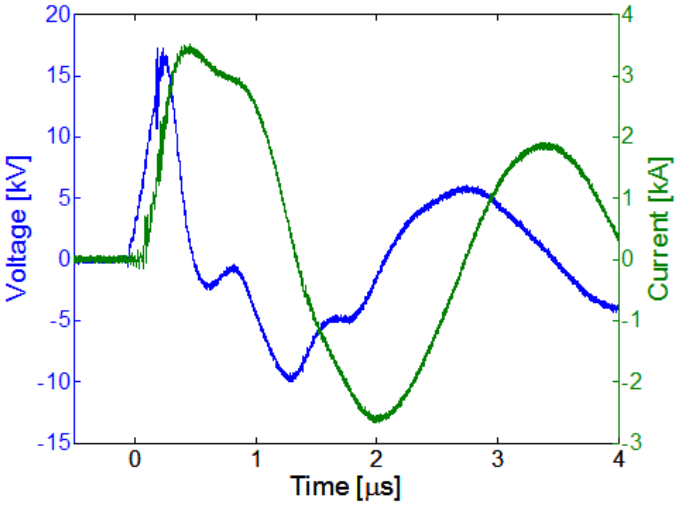

Figure 63. Voltage and current characteristics of DPF (a=550 μm) firing in 130 torr He. Voltage and current rise times are 300 and 350 ns, respectively.

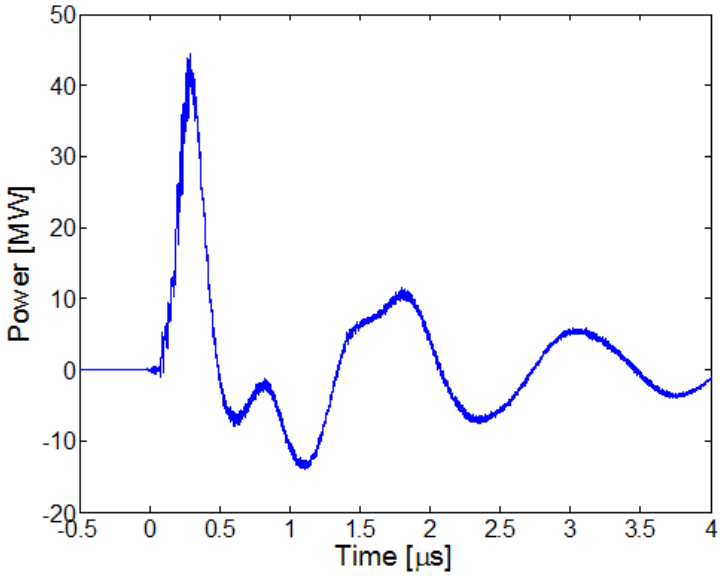

Figure 64. Power delivered during pinch process corresponding to voltage and current waveforms shown in Figure 63. Peak power is delivered around 300 ns, which is approximately the end of the rundown phase.

For the 550 μm anode, two sets of images were taken for each of nine test conditions which are described in Table 9 with respect to gas fill pressure and peak voltage. The first set of images from the 550 μm anode configuration was taken with relatively high gain so that features were visible throughout the breakdown, rundown, pinch, and post pinch phases. Gain was held constant throughout a test condition but was adjusted between conditions to enhance visible features. Adjusting gain allowed for improved visualization of pinch dynamics but hindered luminous intensity assessment since pixel intensities were often saturated.

Table 9. Test condition matrix for the a=550 um DPF.

Condition	1	2	3	4	5	6	7	8	9
P_{He} [torr]	50	50	50	125	125	125	190	190	190
V_{DPF} [kV]	10.1	13.5	18.9	10.1	13.5	18.9	10.1	13.5	18.9
I_{DPF} [kA]	2.3	2.3	2.3	2.9	2.9	3.2	3.7	3.8	3.8

The second set of images from the 550 μm configuration was taken with a gain such that no images were saturated, and this level was held constant for all test combinations in this set. The purpose of this image set was to detect local regions of relative intense brightness and to allow for cross condition peak intensity comparisons. All images in both sets were taken with an integration time of 50 ns, and collected in delay increments of 100 ns from 0 to 1000 ns providing 11 images for each experimental condition. Intensely bright regions correspond to high energy and high plasma density. Regions of intense brightness at the anode tip are indicative of a pinch event, and in some cases evidence of a pinch can only be observed optically because electrical signals do not show the characteristic dip in the d*I*/d*t* trace accompanied by a simultaneous voltage spike [74] [75].

For the *a*=100 μm DPF only one set of saturated images was captured, and the test matrix for these experiments is given in Table 10. Images were taken at combinations of two pressures and two DPF voltages. Using an image integration time of 100 ns and a delay between images of 100 ns 11 images were captured between 0 and 1000 ns, similar to the case of the 550 μm anode DPF. ICCD gain was set sufficiently

high such that features were visible throughout the pinch process. An unsaturated comparison was not made for the smaller DPF.

Table 10. Test condition matrix for the a=100 μm DPF.

Condition	b	c	d	e
P_{He} [torr]	85	85	150	150
V_{DPF} [kV]	4.7	9.4	4.7	9.4
I_{DPF} [kA]	0.7	0.9	1.8	1.8

4.4 Results

Figure 65 shows two typical images of a discharge. The image in Figure 65(a) shows the 550 μm DPF during the rundown phase, and the image in Figure 65(b) shows how the plasma develops after the pinch occurs. These images were taken with high gain and portions of the images are saturated as is indicated by the regions of bright white color. Geometries of the devices visible in these images are the anode, the alumina dielectric, and the cathode plane. Also apparent are several characteristic features of the plasma, more clearly understood from later results but introduced here. First is the current sheath, which surrounds the alumina and runs down towards the anode tip. The pinch occurs when the sheath reaches the anode tip at approximately 300 ns, and an intensely bright region is present at the anode tip during the time of the pinch. Peak power is delivered around this time as shown in Figure 64. Second are radially

expanding spherical (at the tip), and cylindrical (along length of anode and dielectric) shock fronts of the higher temperature plasma region expanding into the cool background. The expanding spherical shock front is termed the 'bubble.' Third is an apparent slug of plasma which has been ejected from the pinch region. Lastly, a build-up of plasma is observed flowing against the cathode wall.

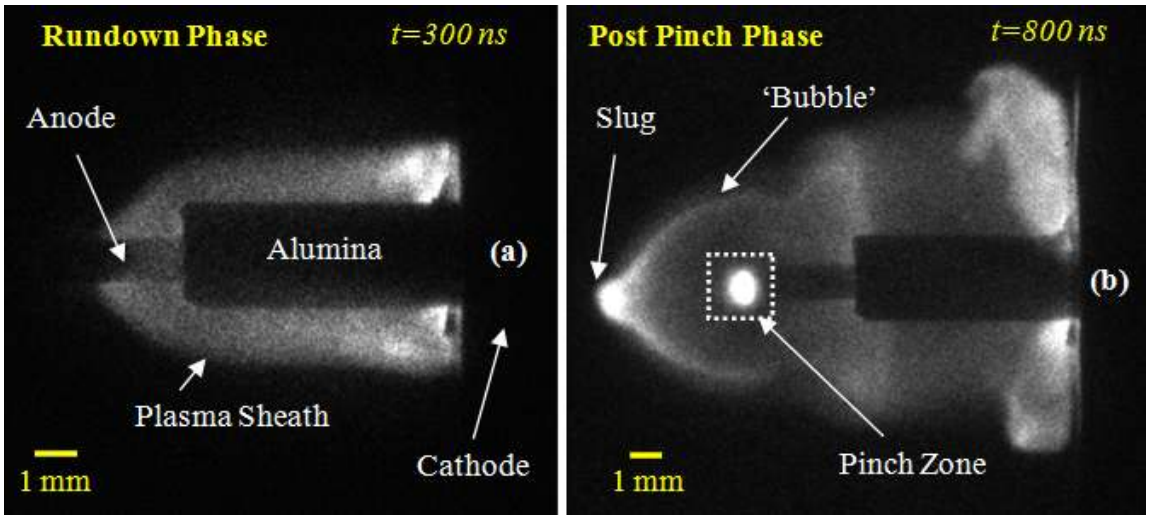

Figure 65. Annotated images of pinch process showing characteristic features in the a=550 μm DPF used for optical diagnostics in pinch dynamic analysis. (a) Rundown phase, (b) Post-pinch phase.

A multi-exposed image of a single pinch event under condition *5* as described in Table 9 is shown in Figure 66. Individual images each have an exposure time of 50 ns, and using a delay of 300 ns between images, several images from a single pinch event were captured and then combined with one another. This image is representative of how

the pinch evolves in a single firing. A false color set of the saturated images showing the dynamics of the pinch evolution under all nine conditions for the 550 μm DPF is provided in Figure 67. Each image in Figure 67 was taken from separate firings of the DPF. As such, the images are qualitative representations of one pinch. By examining plasma slug locations in Figure 67 it is clear that each image is from separate firings. For example, at t=1000 ns in condition *3*, the slug is shown moving towards the bottom right of the image, whereas at the previous time the slug is observed moving to the top right. Regions that are pink in color indicate brightness saturation. An unsaturated set of images for condition *5*, indicated as *5*', is included in Figure 67 for comparison of relative brightness intensities. The condition *5*' images show the pinch, which is circled by a dotted yellow line, as being far more luminous than any other area in the field of view. In fact, the anode tip is approximately 30× brighter than any other area in the field of view as is demonstrated in Figure 68. This is determined by comparing relative intensities after subtracting background from the signal. Therefore, the energy density at the anode tip is much greater than any surrounding area. The range of drive factors for conditions *1-3*, *4-6*, and *7-9*} are 5-8, 3-5 and 3-4 kA $mbar^{-1/2}$ cm^{-1}, respectively, which are <10% of the typical range of 65-95 kA mbar $mbar^{-1/2}$ cm^{-1}, setting an expectation for radial and axial sheath velocities less than those of optimized devices.

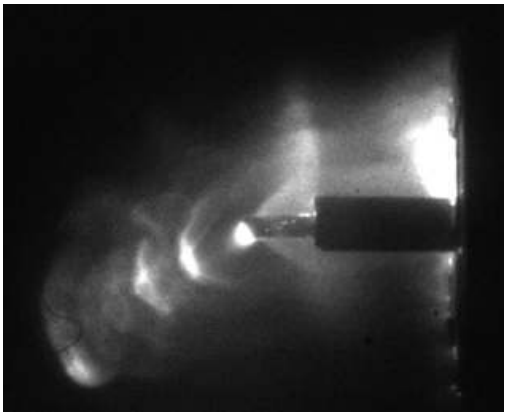

Figure 66. Multi-exposed image of a single firing of the 550 μm DPF. Individual images have exposure times of 50 ns, and the delay between images is 300 ns.

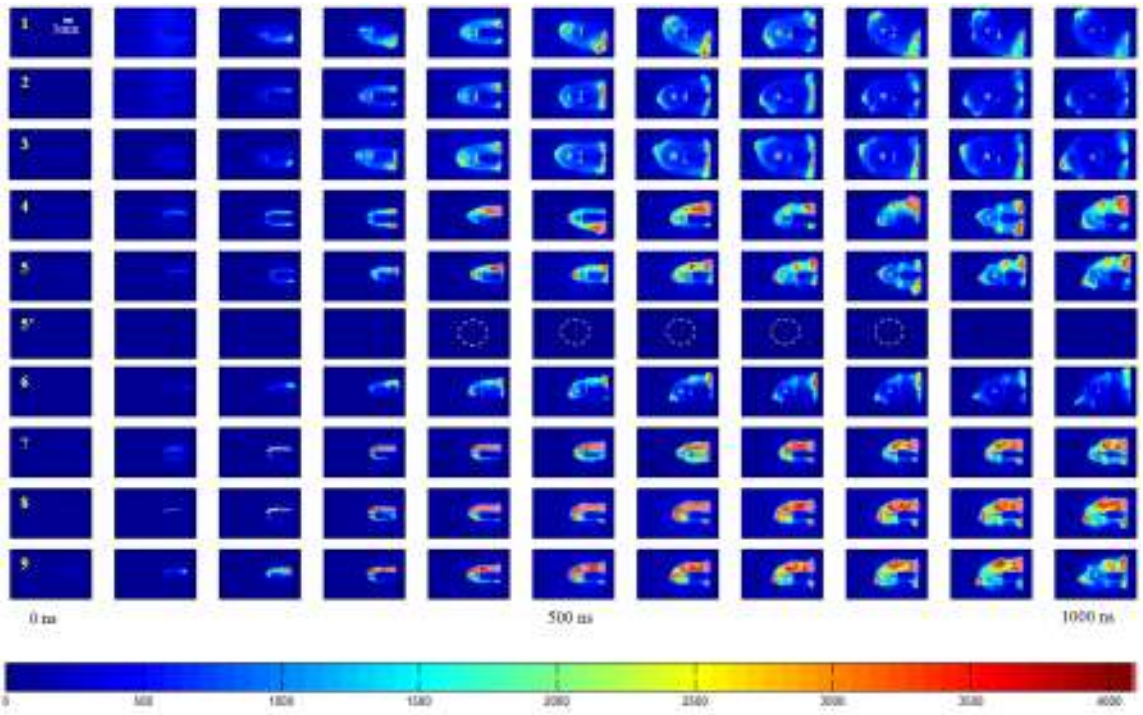

Figure 67. Saturated ICCD images of the 550 μm DPF. Saturated areas are shown in pink. All test conditions are shown. Image sequence 5' shows the corresponding unsaturated ICCD images. The unsaturated pinch area is indicated by the broken circle.

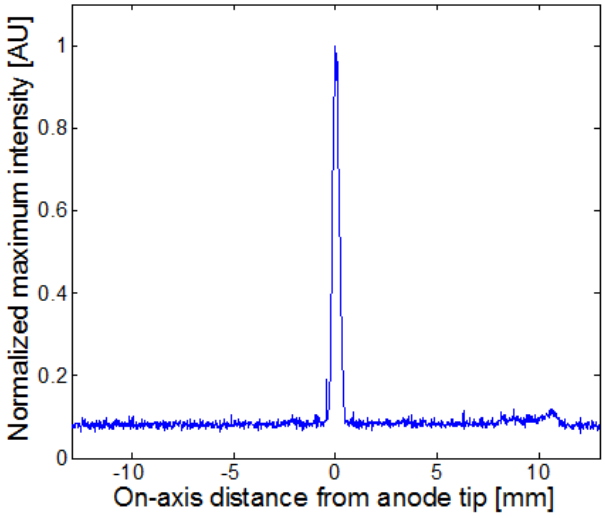

Figure 68. Normalized column-wise maximum brightness intensity for unsaturated condition 5' at t=500 ns. The pinch at the anode tip is 30× brighter than surrounding areas. The cathode is located at +11 mm.

Timing of the image sequence begins at breakdown in the spark gap and is initiated by detection of EMI through an antenna. After the discharge in the spark gap, initial breakdown occurs between the DPF anode and the cathode, and a thin current sheath forms around the alumina. The sheath accelerates towards the anode tip, expanding radially, and the pinch occurs when the sheath reaches the anode tip and **j**×**B** forces compress the plasma to high temperature and pressure. Initial concerns of whether or not the bright spot indicated a pinch were quelled by the observation that the presence of a bright spot at the anode tip was sensitive to gas pressure for the same applied voltage, so pinching and non-pinching conditions were easily discernible at similar input energy. If the anode spot was due to heating it should be present in all conditions with similar input energies. In these image sequences the pinch is observed after 300 ns in all

cases. Subsequent images show how the plasma returns to quiescence after the pinch. These images indicate that pressure has a more pronounced effect on breakdown/rundown symmetry than does energy input.

4.4.1 550 µm anode results

Two distinct trends are evident in the saturated images of the 550 µm anode DPF shown in Figure 67. The first is that as pressure increases, the current sheath becomes more confined to the anode axis and tends towards asymmetry. Lower pressure conditions show the current sheath appearing diffuse, and as pressure increases the breakdown is more closely confined to a preferred side of the dielectric/gas interface region. Higher pressure conditions show breakdown occurring most strongly in the region above the anode. This could be a result of imperfect anode geometry. Small deviations from a perfect coaxial arrangement can encourage bias in the breakdown direction due to stronger electric fields. The second trend evident is that at increased energy input (higher voltage) the presence of the slug feature becomes more pronounced. At t=600 ns in all high voltage conditions (*3, 6 & 9*), the slug is prominent even though it is smaller in size as compared to its lower energy counterparts. The slug is most likely composed of gas being squeezed out in the axial direction during the compression process. The slug departure angle can be as much as 70° off the axis, but since the images are from individual firings, it is not clear whether or not the slug's trajectory is influenced by **B**-fields.

Dynamics of the features described in Figure 65 are plotted alongside the unsaturated peak intensity of the brightness in Figure 69. Since these images are captured at a common gain, luminous features of relatively weaker pinches are undetectable, but this is necessary for consistent comparison. During the initial rundown phase, peak intensity maintains low levels in all conditions. Generally, peak intensity increases as the current sheath travels toward the anode tip, reaching its maximum as the sheath approaches the anode tip. In low voltage conditions *1, 4*, & *7* there is little variation in luminous intensity throughout the pinch, and furthermore, in these same conditions there are no sudden changes in luminous intensity. This is most likely due to filtering caused by ICCD gain selection since DPF features are similar across all conditions indicating similar behavior. For most all other conditions the rise time of luminous intensity is about 200 ns. That the rapid increase in luminous intensity occurs simultaneously with the sheath's arrival at the anode tip likely indicates the occurrence of a pinch as previous research has demonstrated [74] [75]. From event to event luminous intensity appears to vary by 25% due to initial asymmetry or shot to shot variation. As this is an unoptimized DPF, the pinching occurs over longer time scales than those typically reported for small-scale DPF devices [71] due to slower peak current rise times which are due to higher inductance in the external pulsing circuit. The energy densities for the 10, 13 and 19 kV conditions are 2, 3 and 6×10^{11} J m^{-3}, and this is reflected in Figure 69 by row-wise comparison of luminous intensity.

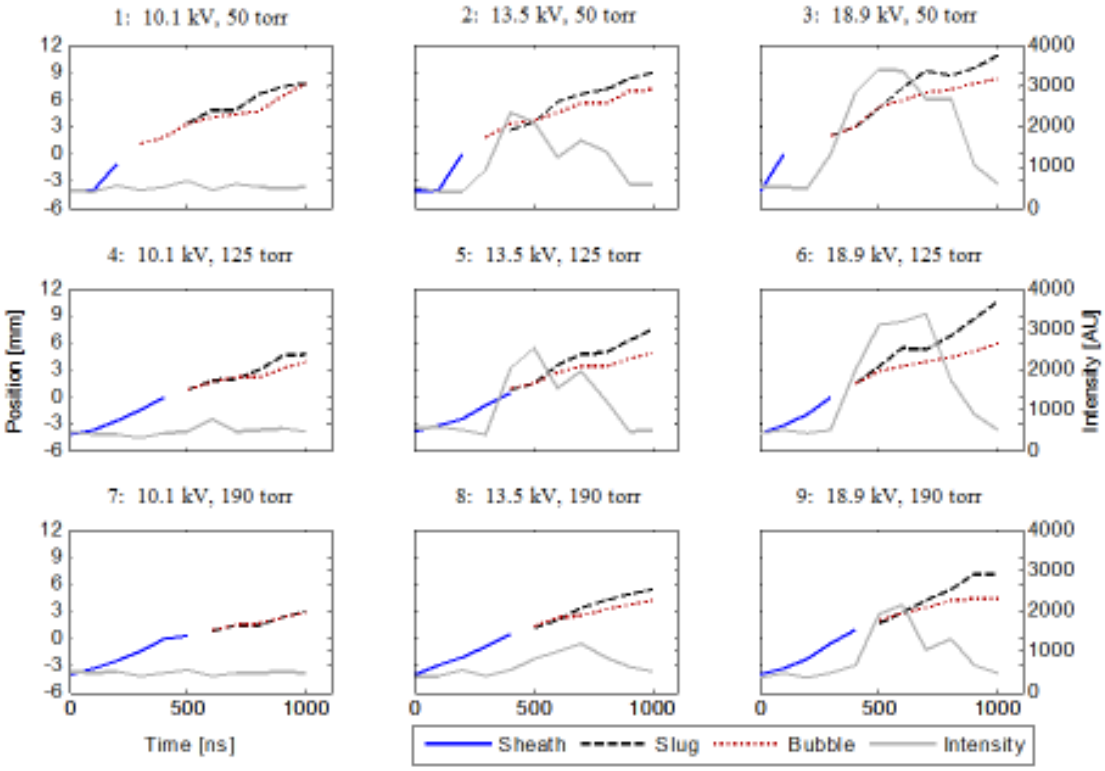

Figure 69. Spatial evolution of plasma in 550 µm DPF device plotted with peak brightness intensity from unsaturated images. Positions are relative to the anode tip. Experimental conditions are provided above individual plots.

The sheath, bubble and slug velocities are indirectly shown in Figure 69 as the slopes of the position profiles. Sheath velocity has a maximum of ~40,000 m s^{-1} under condition *3* (19 kV/50 torr) and minimum of ~8,000 m s^{-1} under condition *7* (10 kV/190 torr). Because drive parameters are roughly 10% of the lower limit of the idealized range of 65-95 kA $mbar^{-1/2}$ cm^{-1}, reduced sheath velocities are expected, especially at increased pressure. Generally, the sheath velocity is greater than both the bubble and slug velocity

with this effect being most pronounced in condition *3*. Average sheath velocity decreases as pressure increases and increases as input energy increases.

Average velocity data for the features is summarized in Table 11. Slug velocities show similar response to pressure and input energy and is observed to range between 5,000-15,000 m s^{-1}. The slug velocity is proportional to the input energy and inversely proportional to pressure. Both of these observations are consistent with drive parameter scaling. Slug velocities are determined assuming straight-line displacement from the anode tip, and as such they are a minimum value as any curvature in the trajectory is neglected. No correlation is observed with input energy and average bubble velocity, which ranged from 4,500-9,500 m s^{-1}, but bubble velocity decreases with increasing pressure as the higher density retards plasma expansion.

Table 11. Summarized average velocity data for features observed in the a=550 μm DPF.

Condition	Pressure [torr]	Voltage [kV]	Drive Param $\left[\frac{kA}{cm\sqrt{mbar}}\right]$	Avg Vel [m/s]		
				Sheath	*Bubble*	*Slug*
1		10.1	5	14,920	9,423	8,992
2	50	13.5	6	20,375	7,680	10,586
3		18.9	8	41,470	9,143	12,703
4		10.1	3	10,187	5,931	7,624
5	125	13.5	4	10,985	6,647	11,036
6		18.9	5	13,153	7,378	15,299
7		10.1	2	8,439	4,741	5,285
8	190	13.5	3	11,068	5,726	8,794
9		18.9	4	12,271	4,764	10,907

Bubble expansion could be due to either thermal expansion (neutral sound speed) or ambipolar diffusion (ion sound speed). Since no data were collected for either electron or ion temperatures, it is not possible to say that this is an equilibrium plasma, and therefore the driving factor of the bubble's velocity remains unclear. The bubble expands with some characteristic velocity, and from that a characteristic temperature of either emitting neutrals or electrons can be estimated. The characteristic temperature can be estimated using the relation $V_{rms} = \sqrt{3k_B T/m_{ion}}$, where V_{rms} is the measured characteristic root mean square speed, k_B is the Boltzmann constant, T is the characteristic temperature and m_{ion} is the mass of a helium ion. Characteristic temperatures for the 50, 125, and 190 torr conditions are thus in the range of 0.28-1.25 eV. At higher pressures there is less energy per unit mass resulting in lower characteristic temperatures. If expansion is thermally driven, then this is an ion temperature and representative of an equilibrium plasma. On the other hand, if the expansion is driven by ambipolar diffusion, then this is an electron temperature and represents a non-equilibrium plasma.

4.4.2 100 μm anode results

Saturated images from the 100 μm anode DPF are shown in Figure 70, and as was done for the images in Figure 67, images in Figure 70 were taken from individual firings of the DPF and are therefore only representative of average behavior. Again the ICCD was triggered by breakdown in the spark gap to minimized cable delays. The image sequences show sheath formation at breakdown between anode and cathode

followed by sheath advance towards the anode tip where it undergoes radial expansion. The pinch appears to occur around 500 ns based on the position of the current sheath. Because the images are saturated, comparisons of light intensity during the process are not possible. However, symmetry is assessed and velocities of characteristics described in Figure 65 are examined. As compared to the images in Figure 67the images in Figure 70 show spatially consistent sheath and bubble development with a high degree of axial symmetry. This is especially noticeable in conditions *c* & *e* where the process is nearly symmetric. Energy density parameters of this device are 6.2×10^{12} and 2.5×10^{13} J m^{-3} for the 5 and 9 kV conditions, respectively, which are 2-3 orders of magnitude greater than energy densities found in optimized devices of larger diameter. The bright region at the anode tip is larger than the anode diameter, and the actual energy density may be lower than that determined by calculation based on electrode geometry alone. The Figure 70 images show that the pinch radius is about 5× larger than the anode radius which would make the energy density comparable to optimized devices.

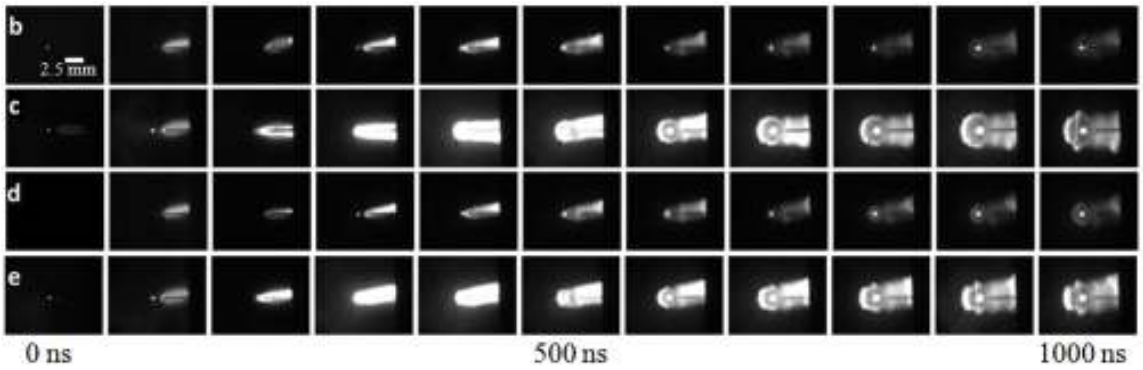

Figure 70. Saturated images of the 100 μm DPF. The test condition letter is given in t=100 ns images.

Several qualitative observations can be made from the images in Figure 67. The first observation is the absence of a slug in all conditions. Second, axial symmetry is improved with higher energy input. Third, bubble presence becomes more distinct and appears at earlier times at higher energy input. In conditions *c* and *e* the bubble is well defined at *t*=600 ns, whereas the bubble is present, but not as distinct, at *t*=900 ns for the *b* and *d* conditions. Fourth, a small point of intense light is noticeable in the pinch region at the anode tip. This bright point is also visible in the saturated images of the 550 μm DPF and hints at pinching. Lastly, the dynamics of the 100 μm DPF do not appear to respond to increased pressure. Comparison of conditions *b* to *d* and *c* to *e* do not reveal significant qualitative variation.

Average velocity data for the 100 μm DPF is summarized in Table 12, and dynamics of the 100 μm DPF under the four conditions are plotted in Figure 71. For the 100 μm DPF, pressure and energy input have very different effects on the sheath and bubble velocities as compared to the 550 μm DPF. The 100 μm DPF sheath velocity

ranges between 3,200 m s^{-1} for condition *d* and 5,500 m s^{-1} for condition *e*, and the drive parameters are 5 and 13 kA $mbar^{-1/2}$ cm^{-1} respectively. The drive parameters for conditions *b* and *c* are 6 and 17 kA $mbar^{-1/2}$ cm^{-1} and remain 10-25% of the idealized range, and the sheath velocities are 10% of optimized DPFs. Sheath velocity appears to be sensitive only to energy input at these pressures, whereas with the larger DPF sheath velocity was sensitive to both energy input and pressure. The bubble velocity of the 100 μm DPF ranges from 1,600-2,300 m s^{-1} and is only sensitive to energy input in the high pressure condition. Using the same analysis as described for the *a*=550 μm anode, characteristic temperatures for the 100 μm DPF were in the range of 0.04-0.09 eV. Bubbles are visible in all conditions of the 100 μm DPF, but the most pronounced bubbles are seen in condition *c* and *e*. The bubbles become noticeable at *a*=500 ns and eventually deform most likely to shock interactions, and features observed here have been observed in prior work on larger devices [76].

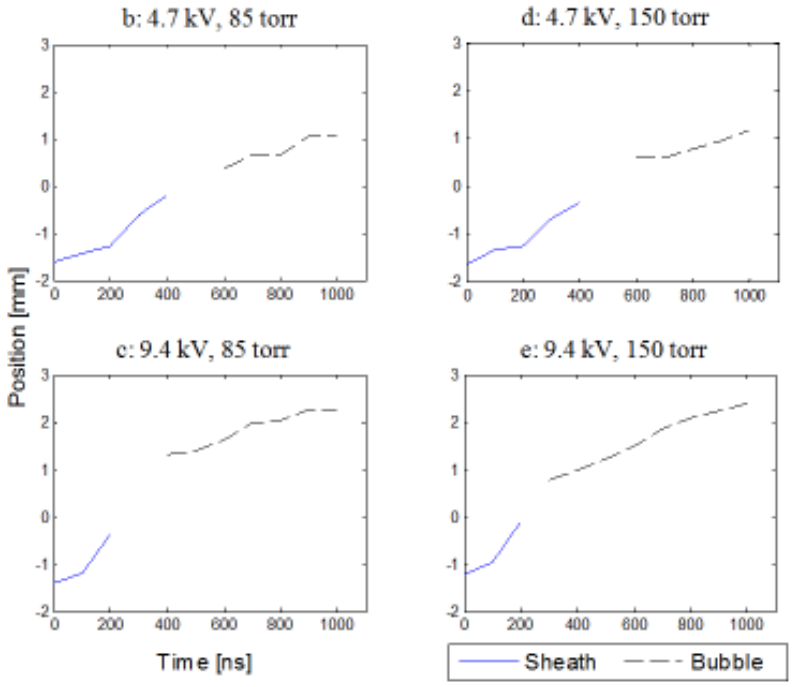

Figure 71. Spatial evolution of plasma in 100 μm DPF device. Position is given relative to the anode tip. Experimental conditions are provided above individual plots.

Table 12. Summarized average velocity data for features observed in the a=100 μm DPF.

Condition	Pressure [torr]	Voltage [kV]	Drive Param	Avg Vel [m/s] *Sheath*	*Bubble*
b	85	4.7	6	3,514	1,695
c	85	9.4	17	5,160	1,605
d	150	4.7	5	3,225	1,488
e	150	9.4	13	5,504	2,310

4.5 Conclusion

Dynamics of two relatively high pressure <5 J Mather type microscale DPFs, one with an anode radius of 550 μm and the other with radius of 100 μm, have been compared both qualitatively and quantitatively by examining event symmetry, light intensity and velocity characteristics. Small sizes were investigated because such DPF systems may be portable, operate at high frequencies, and be capable of operating in parallel. Relatively high pressure was investigated to achieve Knudsen number scaling (in this context equivalent to Paschen scaling) similar to typical devices. Adjusting pressure (*pa* range from 1–3 torr-cm) can help maintain breakdown dynamics, initial symmetry, and final pinch symmetry. Though not optimized, typical rundown and pinch phases were experimentally observed at high pressure and small size. Generally, these results indicate that high pressure and small size should be further explored. Particularly considering, as introduced in this paper but not addressed experimentally, efficiency of neutron production may scale as a^{-3} when Knudsen and typical DPF (drive parameter and yield) scaling are maintained. Pressure may introduce collisional losses but can be optimized and addressed by faster timing and reduced inductances potentially achievable at small size.

As mentioned both devices showed characteristic DPF behavior. Regions of intense brightness at the anode tip coincident with peak power output indicate that the device is pinching, and the luminous intensity of the pinch was 30 times greater than that of the surrounding area. As expected pinch luminosity increases with drive parameter, but only when the breakdown is symmetric. Measured sheath velocities were negatively

correlated with pressure and positively correlated with input energy, and bubble and slug velocities, while generally lower than the sheath velocity, were seen to decrease with increasing pressure. The DPF with 550 μm radius showed considerable spatial variation in both the rundown and pinch phases and appeared more symmetric at the middle pressure with breakdown being contracted at higher pressure, and initially diffuse breakdown and slug ejection off axis at lower pressures. The 100 μm device was notably more symmetric at these high pressures.

Compared to optimized DPF devices of larger diameter in lower pressure operation, gas pressures are two orders of magnitude higher, the DPFs in this study had energy densities as much as 100 times greater, and the drive parameter was a factor of 4–12 below that considered to the be standard range for pinching (65–95 kA $mbar^{-0.5}$ cm^{-1}) [34]. This likely resulted in the reduced observed sheath velocities. It should be noted that efficient pinching can occur outside this range of drive parameter [34] [71] and this range is not an absolute rule. Maintaining symmetry appears, in part, to be related to Knudsen scaling which is controlled by gas pressure and anode geometry, and an additional constraint of DPF operation may be that devices should strive to operate near but to the right of the Paschen minimum (*pa* range 1–3 torr-cm).

5. PLASMA ACTUATORS FOR FLOW CONTROL*

In the early 1900s, the Wright brothers of Kitty Hawk, North Carolina in USA pioneered airplane development and had the first successful manned test flight of a controlled fixed wing engine powered airplane. By 1905 they had caught the attention of the world with flights lasting over 30 minutes and covering distances of 20 miles. By the First World War, airplanes had been sufficiently developed as to make them reliable platforms of attack and surveillance. Jet powered aircraft was developed by the Germans in the 1930s, and in 1947 the XS-1, developed in the United States, broke the sound barrier. Fixed wing aircraft are continually evolving, and new technologies create opportunities for increased speed, stealth and performance.

The following research investigates the use of a novel plasma actuator that can be applied to the surface of a NACA 0012 airfoil in order to improve its performance by delaying stall. The NACA 0012 airfoil is similar to those used for tail wings on airplanes and for rotor blades on helicopters. Delaying stall increases the amount of lift an airfoil can generate and reattaching separated flow can reduce drag. Both of these have several benefits. For one, the amount of available lift determines how small of a turning radius the aircraft can handle, thus improving the aircraft's maneuverability. Another benefit is that the stall speed, which is the minimum speed an aircraft can travel without

* This work will be submitted for publication as two distinct papers. The working titles are "*Characterization of synthetic jets from a slotted spark plasma actuator for flow control*" and "*Changes in drag on a spark actuated NACA 0012 airfoil from stalled conditions.*"

descending, decreases as lift increases. Another way to look at this advantage is to consider that more lift can be generated for the same airspeed, allowing an increase in payload. Drag reductions directly improve fuel economy and thus reduce operating costs.

5.1 Background

Before describing the details of this research project, background information is required in several subject areas. Fluid mechanics and aerodynamics are essential to understanding the physical mechanisms of operation, and a brief explanation of actuators follows. Finally, plasma actuators are discussed within the context of current research.

5.1.1 Fluid dynamics

Knowledge of fluid dynamics is critical to understanding flight mechanics, and the central theme in fluid dynamics is the determination of the velocity field. A fluid is any substance that experiences a continuously increasing deformation when a shear force is applied to its surface, and the rate of deformation is usually proportional to the shear stress. A fluid's resistance to deformation is its viscosity, and it is due to friction between molecules in the fluid as they translate past one another. Fluids can be classified based upon their responses to shear stresses. Assuming no time dependence, if the shear rate is proportional to the shear stress, the fluid is Newtonian, and if there is a nonlinear relation between shear rate and shear stress, then the fluid is Non-Newtonian. Water and air are examples of common Newtonian fluids, whereas blood and quicksand are Non-

Newtonian fluids that experience shear thinning and shear thickening, respectively. Shear thinning refers to a decrease in a fluid's apparent viscosity, and shear thickening refers to an increase in a fluid's apparent viscosity. There is another class of fluids called Bingham plastics which are fluids that can support a finite amount of shear stress before beginning to flow, and an example of this class of fluids is toothpaste. By contrast, a solid is any substance that experiences a finite deformation that is proportional to an applied shear stress. The distinction between liquids and gases is that while both will flow to take the shape of their containers, only gases allow changes in their density, making them compressible, whereas liquids are considered incompressible. Under certain conditions, namely in flows where the gas velocity is less than 100 m/s at atmospheric conditions, gases can be analyzed as though they are incompressible. All real fluids are viscous and compressible to some degree. The working fluid in this research is air, which is a Newtonian fluid and is considered incompressible because of the relatively low velocities used in this work.

The first consideration when investigating fluid behavior is whether or not the fluid can be modeled using continuum mechanics, which deal with continuous masses, as opposed to statistical mechanics, which is used to analyze discrete bodies. In continuum mechanics properties are not allowed to be undefined or discontinuous at any point in space. The Knudsen number, $Kn = \lambda/\ell$, is used to determine the validity of the continuum assumption, and if it is <<1 the continuum assumption is valid. Assuming an average hard shell diameter of 350 pm, the mean free path for air at standard temperature and pressure (T = 298 K, p = 101 kPa) is approximately 70 nm. Therefore, characteristic

length scales of 7 μm, which are several orders of magnitude smaller than those in this actuator research, maintain $Kn = 0.01$, validating the continuum assumption.

Analysis of fluid behavior must maintain consistency with fundamental conservation laws of mass, momentum and energy, and these laws are expressed mathematically in their differential form in Equations 9-13. These three equations assume that the fluid behaves as a continuum.

Mass:
$$\frac{\partial \rho}{\partial t} + \nabla \cdot (\rho \mathbf{u}) = 0 \tag{9}$$

Momentum:
$$\rho \frac{\partial u}{\partial t} + \rho(\mathbf{u} \cdot \nabla)\mathrm{u} = \nabla \cdot \left[-p\boldsymbol{I} + \mu(\nabla \mathrm{u} + (\nabla \mathrm{u})^T) - \frac{2}{3}\mu(\nabla \cdot \mathbf{u})\mathbf{I} \right] + \mathbf{F} \tag{10}$$

Energy:
$$\rho C_p \frac{\partial T}{\partial t} + \rho C_p \mathbf{u} \cdot \nabla \mathrm{T} = \nabla \cdot (k \nabla \mathrm{T}) + Q + Q_{vh} + W_p \tag{11}$$

$$Q_{vh} = \mu \left(\nabla \mathrm{u} + (\nabla \mathrm{u})^T - \frac{2}{3}(\nabla \cdot \mathbf{u})\mathbf{I} \right) : \nabla \mathrm{u} \tag{12}$$

$$W_p = \frac{T}{\rho}\left(\frac{\partial \rho}{\partial T}\right)\Big|_p \left(\frac{\partial p_A}{\partial t} + \mathbf{u} \cdot \nabla p_A \right) \tag{13}$$

where, ρ is density, t is time, $\boldsymbol{u}$ is velocity, p is pressure, $\boldsymbol{I}$ is the identity matrix, μ is dynamic viscosity, $\boldsymbol{F}$ is a body force, C_p is the constant pressure specific heat, T is temperature, k is thermal conductivity, Q is external heating, Q_{vh} is viscous heating, and W_p is work. In equations 2-4 both the dynamic viscosity and the thermal conductivity are strong functions of temperature, and variations of these physical properties are accounted for using Sutherland's Law, which calculates temperature dependent fluid

properties using reference values of the property at a reference temperature. Sutherland's Law is shown in Equation 14

$$\Omega = \Omega_{ref}\left(\frac{T}{\mathrm{T}_{\Omega,\mathrm{ref}}}\right)^{1.5}\frac{T_{\Omega,\mathrm{ref}} + S_{\Omega}}{T + S_{\Omega}} \tag{14}$$

where, Ω is the property of interest, and S_{Ω} is the Sutherland constant and has units of temperature.

The conservation of mass equation states that the mass per unit volume at some location in space changes in time as mass is convected in and out of that volume. If the fluid is assumed incompressible then the equation for conservation of mass reduces to the form shown in Equation 15.

$$\nabla \cdot \boldsymbol{u} = 0 \tag{15}$$

The expression for momentum conservation shown in Equation 10 is the famous Navier-Stokes equation, and it is applicable to all fluid flows. This equation shows that the time rate of change of momentum in a control volume and the momentum convected into and out of that control volume are balanced by pressure forces, viscous forces and body forces acting on that control volume. This is a complicated non-linear partial differential equation, and the non-linear LHS convective term, $\partial_j\left(\rho u_j u_i\right)$, gives rise to turbulent phenomena. If the Navier-Stokes equation is to be applied to turbulent flows then the Reynolds-averaged Navier-Stokes (RANS) equation, which takes instantaneous

values of the parameters and decomposes them into a time-averaged component and an oscillating component, must be used. If the incompressible assumption is made and the fluid is Newtonian, then Equation 10 can be simplified as shown in Equation 16.

$$\rho \frac{\partial u}{\partial t} + \rho(\mathbf{u} \cdot \nabla)\mathrm{u} = -\frac{\partial p}{\partial x} + \mu \nabla^2 \boldsymbol{u} + \boldsymbol{F} \tag{16}$$

Equation 16 can be further simplified by including the following additional assumptions: 1) the flow is at steady-state, 2) the fluid is inviscid, and 3) the fluid is examined along a streamline, which is a curve that traces the velocity vector of a flow. The result is Bernoulli's principle, which is also a form of energy conservation, and it is provided in Equation 17.

$$\left(\frac{p_2}{\rho} + \frac{u_2^2}{2} + g z_2\right) - \left(\frac{p_1}{\rho} + \frac{u_1^2}{2} + g z_1\right) = 0 \tag{17}$$

where, g is the acceleration of gravity and z is height. With mechanical energy being comprised of kinetic energy and potential energy, the principle states that the mechanical energy of a fluid is constant between two points on a streamline in a flow field.

Two consequences of this relation are of particular importance to this research. For one, if it is assumed that $z_1=z_2$, then it is apparent that if the streamline velocity increases, then the pressure must decrease. This has practical implications with regards to flow over an airfoil and lift generation. Secondly, again assuming that $z_1=z_2$, if the

fluid is brought to rest, the relation shows that there will be a corresponding increase in pressure. The total pressure in a flow is the sum of the static and the dynamic pressure, where the static pressure is the pressure exerted on an element due to its surroundings, such as a volume of water below a water column, and the dynamic pressure is caused by fluid motion. When a streamline impacts a surface there is a point called the stagnation point where the fluid velocity goes to zero. Streamlines and the stagnation point are illustrated in Figure 72.

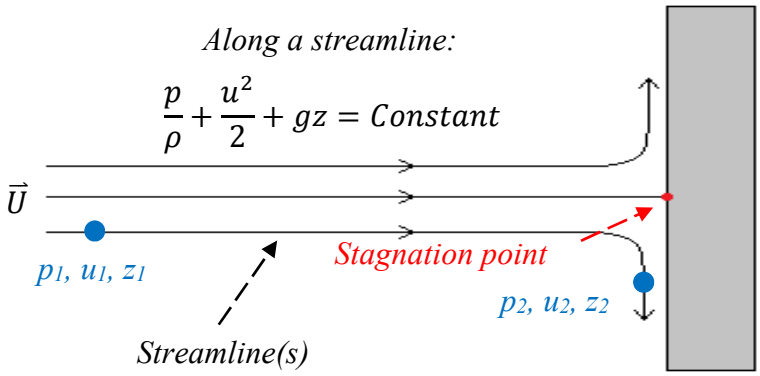

Figure 72. Streamlines and stagnation point in steady incompressible inviscid flow normal to a flat plate.

At the stagnation point, the kinetic energy of the fluid is converted entirely into pressure. Measuring the dynamic pressure is useful because it provides an inexpensive reliable straightforward velocity measurement. It is because of these reasons that this technique is often used to measure the airspeed of aircraft as well as wind tunnel speeds.

The conservation of energy equation shows that the time rate of change of energy in a control volume and the energy convecting into and out of that volume are balanced by heat transfer, viscous dissipation and work energy. In non-reacting flows changes in energy manifest themselves as changes in temperature and mechanical energy. The energy equation is required for compressible flow analysis, but it is not necessary for determining the velocity field of an incompressible fluid. Additionally, an equation of state may be required to provide a relation between the fluid's thermodynamic properties of temperature, pressure and density for compressible flow analysis. There are many different equations of state - the choice of which is often dictated by the nature of the system and the desired accuracy. The classical ideal gas law is a commonly used equation of state, and it is given in Equation 18. Other equations of state include the virial equation of state and Van der Waals equation of state.

$$p = \rho RT \tag{18}$$

Fluid flow regimes can be quantized by their Reynolds number, $Re = \frac{u\ell}{\nu}$, where u is velocity, ℓ is a characteristic length and ν is fluid viscosity. This non-dimensional ratio is a measure of the flow's inertial forces to its viscous forces. Flows that are inertially driven have large *Re* and are typically turbulent, having vortices and chaotic eddies; whereas low *Re* flows are dominated by viscous forces and tend towards laminar behavior with smooth streamlines. The Reynolds number can be calculated for either internal flow, like that through a channel, or an external flow, like that over the surface

of an object. For internal flows and external flows the laminar to turbulent transitions occur at Re=2000 and Re=10^5, respectively. Flows over flat plates and airfoils are examples of external flows, and important features in this type of flow are shown schematically in Figure 73 and are described in the following paragraphs.

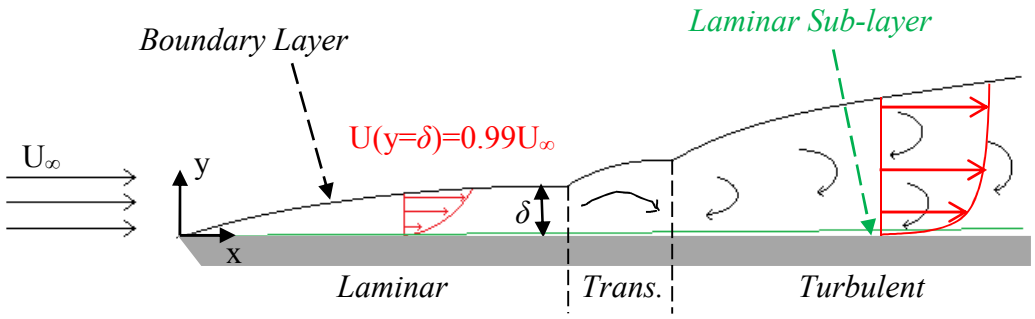

Figure 73. Flow over a flat plate showing boundary layers and laminar to turbulent transition. NOTE: Velocity profiles in red are not to scale.

Because all real fluids are viscous, a thin layer develops along solid-fluid and fluid-fluid interfaces at high Re flows that confines important viscous effects. This region is called the boundary layer and was first described by Prandtl in 1905. The boundary layer is characterized by steep velocity gradients in the direction normal to the interface plane. The gradients arise due to friction between particles, and the no-slip condition assumes that fluid particles in direct contact with a solid interface have zero velocity. The velocity of the fluid in the boundary layer increases with distance from the interface until the velocity at some distance δ, the thickness of the boundary layer, from the interface is 99% of the freestream velocity. The thickness of the flat plate boundary

layer depends on whether or not the flow is laminar or turbulent. In general, higher *Re* results in thinner (smaller δ) boundary layers. For flow over a flat plate, laminar and turbulent boundary layer growth scale with $Re^{-0.5}$ and $Re^{-0.2}$, respectively, and the full equations are given in Equations 19 and 20. Airfoil boundary layers in these experiments remain laminar and have thickness of $\delta_{x,lam}$ = 2.3 mm.

$$\delta_{x,lam} = \frac{4.91x}{\sqrt{Re_x}} \tag{19}$$

$$\delta_{x,turb} = \frac{0.382x}{Re_x^{0.2}} \tag{20}$$

Boundary layer behavior and thickness evolve with distance as is shown in Figure 73. The boundary layer is laminar at low *Re*, but the boundary layer will transition and ultimately become turbulent as *Re* increases. In the laminar boundary layer region all mass and momentum transfer occurs between thin adjacent layers. Since each layer is only influenced by those neighboring it and the velocity is zero at *y*=0, this gives rise to the gradual curve of the velocity profile in the laminar region. The turbulent boundary layer is characterized by mixing throughout the region and particles are no longer only influenced by neighboring layers. This gives rise to a nearly top-hat velocity profile and because the velocity gradients are so large near the wall, large shear stresses exist. There exists a very thin laminar viscous sub-layer adjacent to the solid-fluid interface. This layer exists because of the no-slip condition. At arbitrarily small *y* the velocity approaches zero, thus reducing *Re* and tending towards laminar characteristics.

If an adverse pressure gradient develops it is possible for the boundary layer to detach from its surface, and this phenomenon is called separation. For flow over a flat plate, the flow will remain attached so long as $\frac{\partial p}{\partial x} < 0$, meaning that pressure forces in the boundary layer are in favor of a velocity in the positive *x*-direction. As the pressure gradient increases, the boundary layer velocity profile is retarded near the interface. If the pressure gradient becomes positive then flow reversal can occur resulting in separation. The separation point is defined as the point along the surface where the velocity and shear stress are both zero. Figure 74 shows the evolution of a velocity profile throughout the separation process.

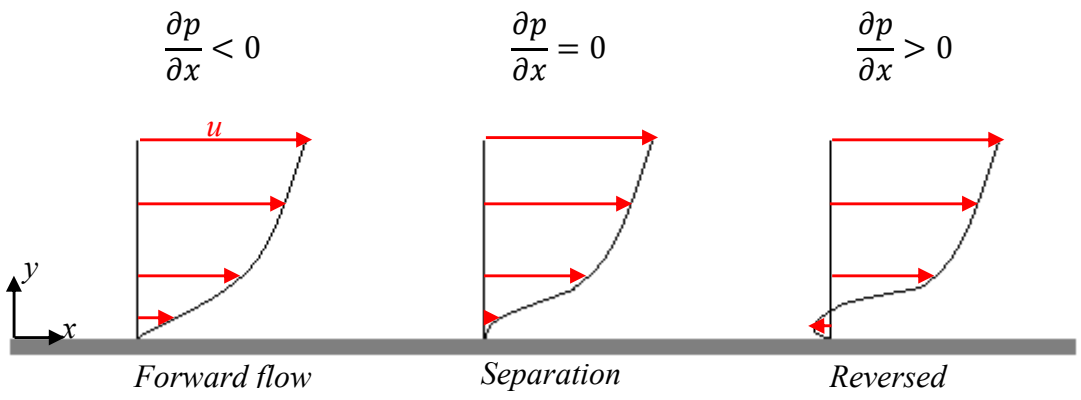

Figure 74. Representation of velocity profile with a separating boundary layer in flow over a flat plate**.**

For external flows, *Re* is typically based on distance past the front edge of a surface. Therefore, *Re* is proportional to the distance downstream of the front edge of the surface. Near the front edge the flow will be laminar, but the flow will transition to

turbulent at some point down the surface. Flow over an airfoil is also an external flow and is shown in Figure 75. Just like flow over a flat plate, flow over an airfoil can detach, causing flow reversal, which leads to reduced performance. Delaying the onset of separation over an airfoil has tremendous benefits, and it is possible to overcome the adverse pressure gradient by applying a small momentum flux directly to the boundary layer to prevent flow reversal.

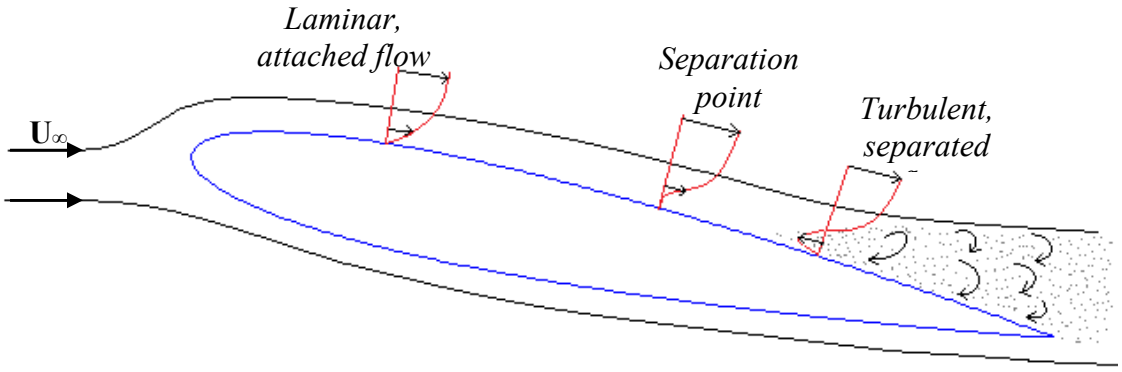

Figure 75. Flow over an airfoil showing viscous boundary layer velocity profile and flow detachment with the resulting wake.

5.1.2 Flight mechanics

Nomenclature commonly used in aerodynamics is illustrated in Figure 76, and these terms are elaborated upon in the following paragraphs. Within a flow stream the only ways information can be exchanged between the flow and an object in the flow are through *pressure forces* and *shear forces*. Pressure forces always act perpendicular and towards the surface of a body while shear forces always act parallel to a body's surface.

The surface considered in this research is a NACA 0012 airfoil which is the cross sectional shapes of a particular wing. Airfoils are carefully designed to communicate with the flow field so that specific pressure and shear distributions result during an anticipated set of flight conditions. Pressure and shear distributions on an airfoil vary with *Re* and the airfoil's *angle of attack* (AoA), which is the orientation of the airfoil relative to the direction of the flow, and is represented by the symbol α.

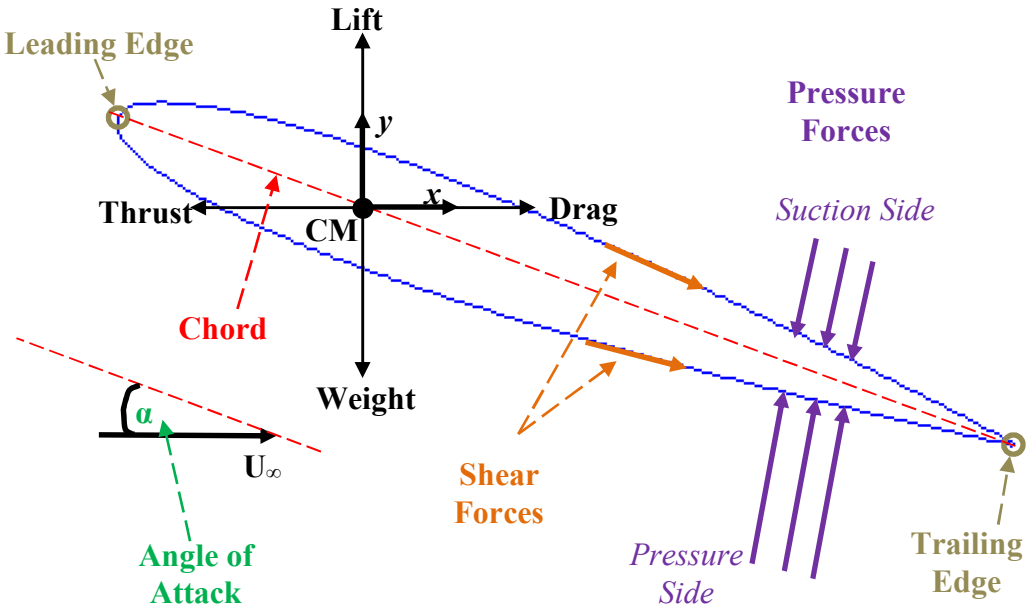

Figure 76. Illustration of NACA 0012 airfoil with common aerodynamic nomenclature labeled.

The upper surface of an airfoil is the *suction side*, and the lower surface is the *pressure side*. Relative to the pressure side, the suction side is characterized by faster

flow and lower static pressure. The front of the airfoil, as seen by the fluid flow stream, is called the *leading edge*, and the tail of the airfoil is called the *trailing edge*. The length of a straight line connecting the leading edge to the trailing edge is the *chord*, *c*, of the airfoil. Many dimensions are expressed in terms of percent of chord length. Some airfoils are symmetric about the chord line and others are not. Cambered airfoils are those that are asymmetric about the chord line. The camber line traces out the collection of points from leading edge to trailing edge that are equidistant from the suction and pressure sides of the airfoil. For symmetric airfoils the camber line and the chord line are the same. The shape of an airfoil is often provided in the airfoils numerical designation. For example, in the NACA 4-digit naming convention, the first number represents the degree of camber as a percentage of the chord length; the second number tells the location of maximum camber in tenths of chord length; and the last two digits specify the maximum thickness from suction side to pressure side of the wing as a percentage of chord length. Therefore, the NACA 0012 airfoil has no camber (symmetric) and a maximum thickness of $0.11c$. Other airfoil naming conventions are used but their descriptions are beyond the scope of this research.

There are four forces acting on an airfoil's *center of mass* (*CM*) that must be considered for flight applications, and those forces, which are depicted in Figure 76, are *lift*, *weight*, *thrust* and *drag*. Center of mass on a NACA 0012 airfoil is located at $x/C = 0.25$. This research focuses on the lift and drag forces generated by an airfoil and how they can be improved by delaying flow separation from the airfoil. It is common practice to express lift and drag as the non-dimensional coefficients of lift and drag by

normalizing the forces by the quantity $\frac{1}{2}\rho_\infty U_\infty^2 CS$, which is the effective pressure in the flow field. Using lift and drag coefficients standardizes comparison for airfoils of different geometries.

Although simplistic in nature, plots of lift and drag coefficients at different *Re* versus the airfoil's AoA provide valuable insight to the performance capabilities of an airfoil. Coefficients of lift and drag for a NACA 0012 airfoil at different *Re* are given in Table 13 over an angle of attack ranging from 0 to 20 degrees [77]. Plots of these data are shown in Figure 77 and Figure 78 showing AoA dependencies of the coefficients of lift and drag, respectively. In general the lift coefficient is an odd function of AoA and the drag coefficient is an even function of AoA.

Table 13. Lift and drag coefficients of a NACA 0012 airfoil at four different Re for 0 < α < 20°.

α [deg]	Re = 10 000		Re = 160 000		Re = 360 000		Re = 1 000 000	
	C_L	C_D	C_L	C_D	C_L	C_D	C_L	C_D
0	0	0.0337	0	0.0103	0	0.0079	0	0.0065
1	0.083	0.0338	0.11	0.0104	0.11	0.008	0.11	0.0066
2	0.1534	0.0343	0.22	0.0108	0.22	0.0084	0.22	0.0068
3	0.2009	0.0351	0.33	0.0114	0.33	0.0089	0.33	0.0071
4	0.2003	0.0359	0.44	0.0124	0.44	0.0098	0.44	0.0078
5	0.0328	0.0351	0.55	0.014	0.55	0.0113	0.55	0.0091
6	-0.1413	0.046	0.66	0.0152	0.66	0.0125	0.66	0.0101
7	-0.1142	0.058	0.746	0.017	0.77	0.0135	0.77	0.011
8	-0.0703	0.072	0.8274	0.0185	0.8542	0.0153	0.88	0.0119
9	-0.0215	0.086	0.8527	0.0203	0.9352	0.0167	0.9661	0.0134
10	0.0311	0.101	0.1325	0.0188	0.9811	0.0184	1.0512	0.0147
11	0.0848	0.117	0.1095	0.076	0.9132	0.0204	1.1097	0.0162
12	0.1387	0.134	0.1533	0.134	0.4832	0.0217	1.1212	0.018
13	0.1928	0.152	0.203	0.152	0.2759	0.0222	1.0487	0.02
14	0.2468	0.171	0.2546	0.171	0.2893	0.106	0.8846	0.0222
15	0.3008	0.19	0.3082	0.19	0.3306	0.19	0.7108	0.0245
16	0.3548	0.21	0.362	0.21	0.3792	0.21	0.606	0.128
17	0.4079	0.231	0.42	0.231	0.4455	0.231	0.5906	0.231
18	0.4606	0.252	0.4768	0.252	0.5047	0.252	0.603	0.252
19	0.5121	0.274	0.5322	0.274	0.5591	0.274	0.6334	0.274
20	0.5838	0.297	0.587	0.297	0.612	0.297	0.6716	0.297

In Figure 77 several trends relating lift to α and *Re* are observable. First, considering that the NACA 0012 is a symmetric airfoil, it is not surprising that $C_L(\alpha=0°)=0$ because the velocity field is the same on the suction side as it is on the pressure side, and therefore no lift can be generated. This is the *zero lift angle of attack.*

Cambered airfoils, due to their asymmetry, have negative zero lift angle of attack, meaning that the leading edge of the airfoil is pitched slightly downward, and the more camber present in an airfoil, the more negative is the zero lift angle of attack. Conversely, for a given *Re*, there is a maximum C_L. Since the lift force must equal aircraft weight in order to maintain altitude, knowing $C_{L,max}$ allows prediction of the minimum velocity, the *stall speed*, an aerial vehicle can travel without descending uncontrollably, and it is given by the expression $U_{stall} = \sqrt{\frac{0.5\ W}{C_L \rho C S}}$. The lift coefficients match that predicted by inviscid flow airfoil theory where the slope of the lift line is given as $\frac{dC_L}{d\alpha} = 2\pi$, and this is why the lift lines fall on top of one another. However, the theory does not allow for prediction of $C_{L,max}$ because of the dominating viscous effects at higher AoA.

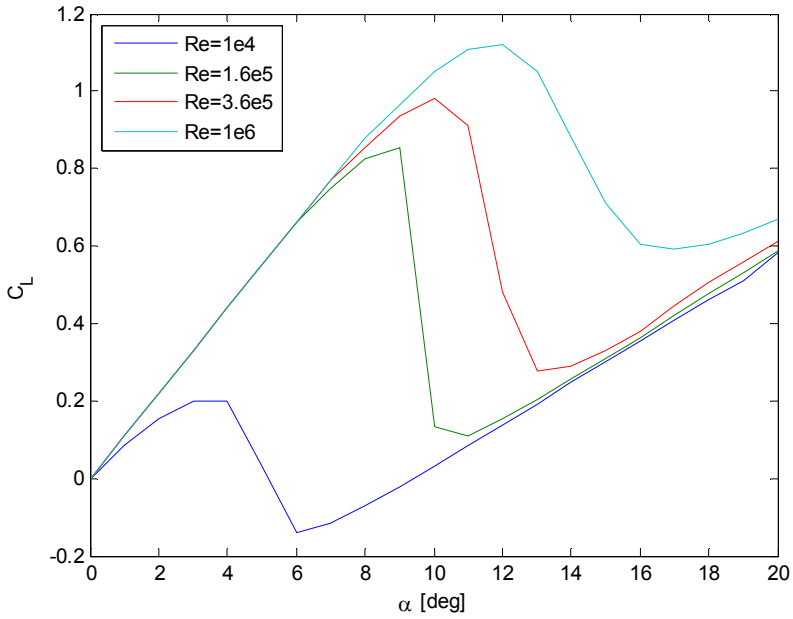

Figure 77. Lift coefficient as function of Re and α for NACA 0012 airfoil.

Next, at a given *Re*, C_L increases with α to a point, and then drops off sharply, and the AoA at which this occurs is called the *stall angle*. This dramatic reduction in lift is the result of flow separating from the airfoil due to the development of an adverse pressure gradient sustaining a separation bubble, and this consequently reduces the amount of lift the airfoil can generate because of the disruption to the velocity field. Airfoil stall will be discussed in a later paragraph.

It is also noticed that maximum C_L increases with *Re*. Flows tend towards turbulence as *Re* increases, and this delays the onset of separation allowing higher AoA to be maintained without stall and thus achieving larger coefficients of lift. As is implied by the *Re* dependency, this behavior is entirely due to viscous effects around the airfoil.

One of the main goals in airfoil design is to delay stall so that higher effective AoAs can be achieved allowing more lift. To this end airfoils have been outfitted with retractable high lift mechanisms such as leading edge slats and trailing edge flaps, and they are easily visible in their extended positions on the wings of commercial aircraft during take-off and landing procedures, where high lift and low stall speeds, respectively, are of primary concern. These devices alter the flow around the airfoil to effectively overcome the development of an adverse pressure gradient. This is also the goal for the airfoil surface mounted actuator described in this research.

The dependency of the drag coefficient on α and Re for a NACA 0012 airfoil is shown in Figure 78, but first some explanation of the various types of drag is warranted. For subsonic velocities, drag on an airfoil is comprised of three unique components – *form drag*, *skin friction drag*, and *induced drag*. The form drag arises due to the geometry of an object. Larger objects naturally have a more extensive cross section than thin objects, and that increases resistance. Furthermore, in order to keep form drag to a minimum, any changes to the cross section should occur gradually so that streamlines remain as smooth as possible and separation is avoided. Skin friction is due to the fluid shear stress on the surface of a body, so as one might expect, the skin friction drag is proportional to the total surface area of the airfoil exposed to the flow, also referred to as the *wetted surface*. Since shear stress is proportional to the velocity gradient in the direction normal to the airfoil surface, the skin friction drag does not usually contribute significantly to the overall drag at subsonic speeds. The sum of the form drag and the

skin friction is termed the *profile drag*. Profile drag is felt by both the theoretical infinite span wing and the real wing of finite span.

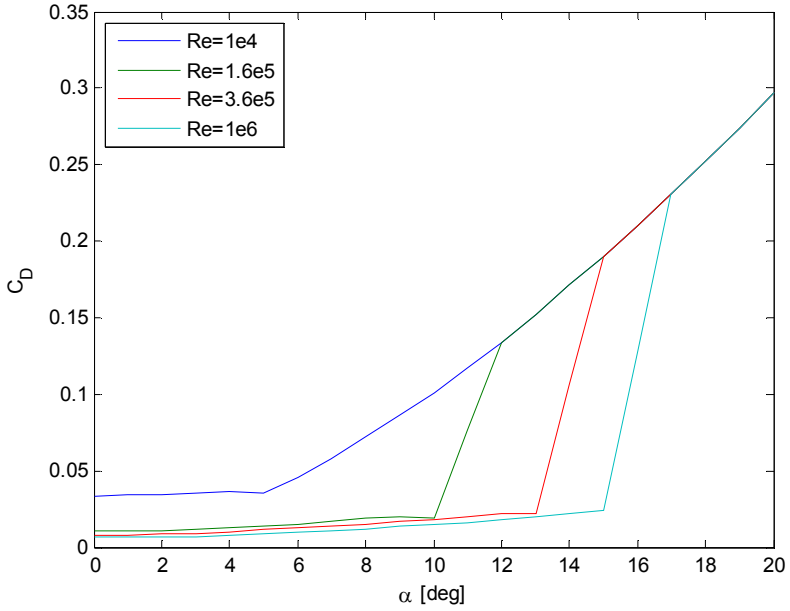

Figure 78. Drag coefficient as function of Re and α for NACA 0012 airfoil.

Induced drag is a finite wing effect and it is also called 'drag due to lift' because it is associated with the pressure imbalance between the suction and pressure sides of a wing that is responsible for lift generation. Since the pressure is greater on the pressure side of the airfoil, the air on the bottom has a tendency to leak out laterally around the wing tips and up to the lower pressure suction side of the airfoil. This causes outward and inward spanwise velocities on the pressure and suction sides, respectively, which combine with the chordwise freestream velocity and the combination of the two

components creates a trailing vortex at the wingtip. The vortices add a downward component to the freestream velocity called *downwash*. Downwash has the effect of creating a tilted relative wind velocity and creating an effective angle of attack that is less than the geometric angle of attack. Since the lift generated by a wing acts perpendicular to the relative velocity and downwash has the effect of tilting the velocity downwards, the lift no longer acts in a purely upwards direction, and it has a component acting in the 'drag' direction. This is shown Figure 79. The horizontal component of the tilted lift vector is the induced drag, and while it cannot be eliminated, it can be reduced by altering wing geometry.

The drag coefficient shown in Figure 78 represents profile drag only because in the experimental setup from which the data was collected the airfoils were outfitted with walls on the wing tips preventing downwash, and consequently induced drag, from occurring. In all cases, the drag is initially very small and increases gradually up to a point just past the AoA at which maximum lift occurs. Beyond this point, the drag increases rapidly and converges along a single line for all *Re*. The sudden change in the drag coefficient is due to boundary layer separation, and as such it is most heavily influenced by the form drag component. By overcoming the adverse pressure gradient that develops in the boundary layer, more lift can be generated as higher α become attainable, and the drag forces can be prevented from rising so sharply. Forces applied on an airfoil have lines of action coincident with a point called the *center of pressure* and these loads can cause moments about the leading edge of an airfoil. This is an important consideration when mounting an experimental airfoil inside a wind tunnel.

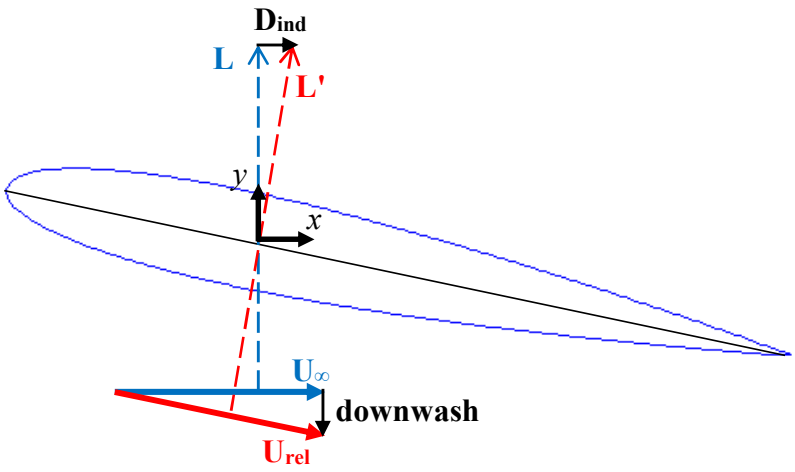

Figure 79. Change in lift line of action as a result of downwash for a finite wing and the resulting induced drag component. Infinite wing components shown in blue, and finite wing components shown in red.

Both Figure 77 and Figure 78 make it clear that boundary detachment has severe effects on airfoil performance, and when the boundary layer separates at high AoA and lifting forces drop rapidly as drag forces increase, the airfoil is in a *stalled* condition. There are two main categories of stall, and they are differentiated based on the *x/C* location at which the flow separates. A *leading edge stall* is one where separation occurs near the leading edge and proceeds to cover the suction side of the airfoil, and because of this global stall phenomenon the lift coefficient drops suddenly. This is also referred to as a hard stall. Leading edge stall is often associated with 'thinner' airfoils having NACA xx10 - xx16 designation, including the NACA 0012 which is the subject of this

research. The other type of stall is *trailing edge stall*, and in this type of stall separation begins near the trailing edge and gradually moves towards the leading edge if α continues to increase. Since the area affected by the separation is initially small and increases with α trailing edge stall occurs much more gradually than does leading edge stall, and for this reason, it is also called soft stall. It is interesting to note that for two airfoils with the same camber, the thinner airfoil will generally have a higher $C_{L,max}$. However, in the case of extremely thin airfoils this does not hold true. For airfoils with a thickness of approximately 2% chord length, there is a substantially reduced $C_{L,max.}$. Therefore, it is important for an airfoil to have some thickness but not too much.

5.1.3 Description of actuators

An actuator is a device that takes a relatively low power signal and converts it to either a mass flow or a mechanical potential [78]. Actuator input signals are often either electrically driven or pressure (hydraulic/pneumatic) driven. In this way actuators can be thought of as having the opposite functionality of a transducer, such as a thermocouple, which takes some potential and converts it to a calibrated electrical signal. Common examples of actuators include motors and audio speakers.

Components of an actuator fall under two distinctions – 1) the energy controller, and 2) the energy converter [78]. The energy controller usually takes the form of a secondary power circuit or amplifier that is controlled by the low power input signal. Using an audio speaker as an example, the energy controller is the amplifier as it takes a relatively low power transient input voltage and increases it prior to sending it to the

speaker. The energy converter in the speaker consists of a fixed position permanent annular magnet surrounding a coil of wire. The coil is connected to the amplified electrical signal and is secured to a cylindrical driver attached to a diaphragm. Variations in the amplitude and polarity of the amplified signal cause the driver to oscillate in the magnetic field of the fixed permanent magnet, resulting in the controlled diaphragm motion responsible for the pressure waves our ears interpret as sound. A speaker system is shown schematically in Figure 80. In this set up the amplifier is the energy controller and the electromagnet created by the coiled wire is the energy converter.

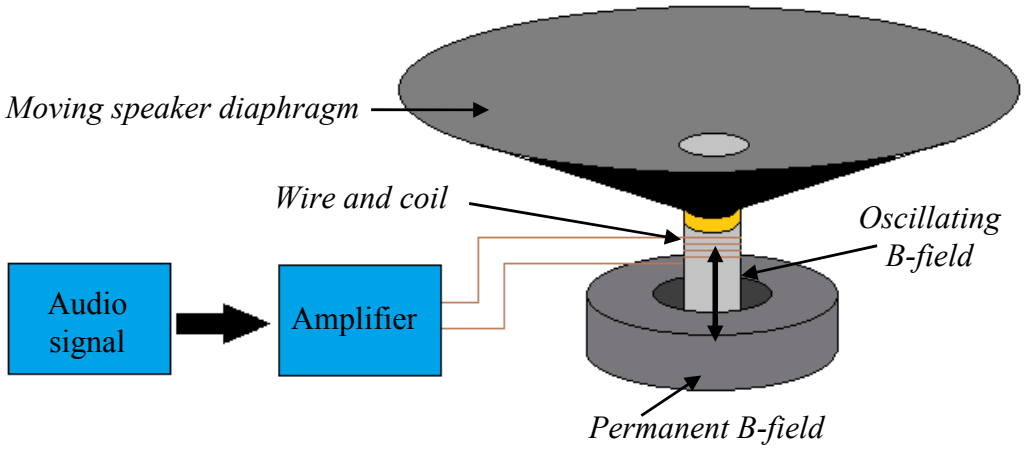

Figure 80. Diagram of a commonly used actuator system (audio speakers).

Due to their mechanism of operation, actuators are amenable to control systems, although they are not necessarily required. Their activation can be triggered by a

transducer operating point falling outside of its operating range, or they can be manually activated as the operator sees necessary. Well understood processes rely on actuators' responses to transducers and feedback loops, so in this way intelligent systems are automated and allowed to operate with a high degree of reliability. However, other actuators may be powered cycled as desired without relying on feedback loops, as is the case with audio speakers.

This research investigates the use of a plasma actuator to delay stall on a NACA 0012 airfoil by creating multiple small jets of air along the suction side of the airfoil. The jets point in the direction of the trailing edge, and are used to overcome the adverse pressure gradient that develops as flow separates from the airfoil. Overcoming the adverse pressure gradient allows the airfoil to achieve a greater angle of attack by reducing the form drag. Currently, there are no intelligent control schemes in place for actuator ignition, and it is manually activated by powering on a high voltage power supply.

The actuator housing is a machinable ceramic and contains a cylindrical cavity with electrodes on opposite ends and an on-axis slot. A representation of the plasma actuator is shown in Figure 81. A plasma is generated in the cavity that can be modeled as a square wave volumetric heating function. The rapid heating causes a steep rise in temperature and a corresponding increase in pressure. The air in the cavity is allowed to expand and issue forth from the on-axis slot, creating a small short lived jet with a velocity of ~100 m/s. The nearly instantaneous heating of the air in the cavity is possible due to the use of a plasma. No other heating mechanism can repeatedly provide such

temperatures rises in a nondestructive fashion. This method can be thought of as resistive heating where the air in the cavity is the wire which is heated to destruction and immediately repairs itself.

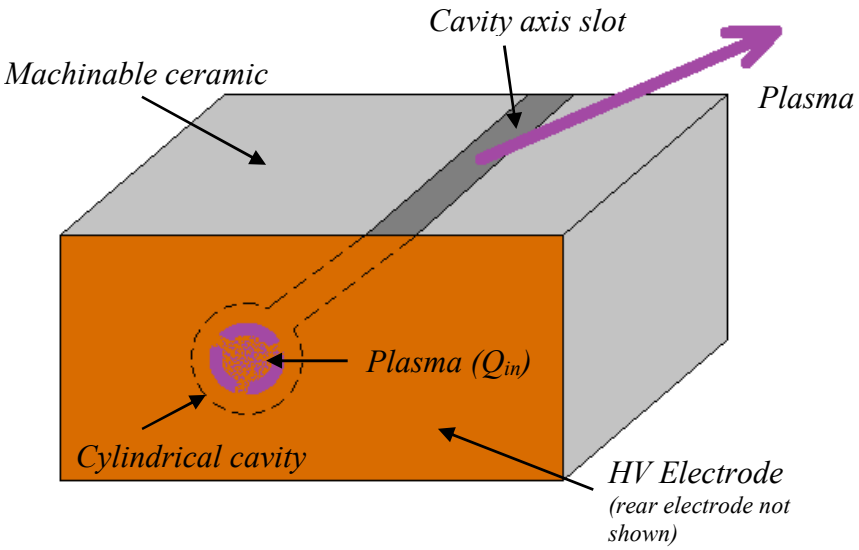

Figure 81. Schematic of plasma actuator showing important features.

5.1.4 Plasma actuators

Actuators are integral components in mechanical control systems. They convert electrical input to mechanical output, and they are therefore crucial in the areas of mechatronics and intelligent systems [78]. Using plasma actuators for flow control offers several advantages over their fluidic and moving surface counterparts, but plasma actuators also have their disadvantages [79]. Among the advantages are high jet velocity,

wide operating bandwidth, mechanical simplicity (no moving components), and amenability to control schemes. Additionally, plasma actuators are convenient because they are zero net mass flux systems. This refers to the fact that the working fluid, ambient air, is naturally replenished, negating the need for storage/transport of high pressure fluids or combustibles. For this reason, these plasma driven jets are commonly referred to as 'synthetic jets' in the literature.

Plasma actuators are amenable to control schemes due to their electric nature and capable of pulsing high velocity jets at kHz rep rates without using moving parts. Since these devices are zero net mass flux, the working fluid is naturally replenished eliminating the need for pressurized vessels and/or combustible materials. Plasma actuators do suffer from EMI generation and susceptibility to clogging. EMI is especially problematic in spark type actuators due to the nature of the discharge process, and jet channels may become obstructed with foreign debris.

Over the past decade, plasma actuators have received considerable attention for their flow control capabilities in a variety of applications. They have been investigated for reducing skin friction drag in hypersonic flows [80] and also in jets promoting mixing and noise mitigation [81] [82]. They have also shown promise reducing turbulence in low to moderate *Re* from bluff bodies (*Re* <30,000) [83] and boundary layer reattachment on low pressure turbine blades (10^4<*Re*<10^5) [84]. The actuator that is the subject of this research is intended for use in boundary layer reattachment on a NACA 0012 airfoil at *Re* >10^6.

Boundary layer separation over an airfoil, whether it is a turbine blade, airplane wing or a helicopter rotor, limits the performance of the system. Lifting-line theory shows that the lift coefficient is proportional to the angle of attack (AoA) [85], but practically limited by the onset of stall, which is dependent on AoA, *Re* and airfoil shape. For many symmetric airfoils the onset of stall is often observed in the 8-12° AoA range [77]. As AoA increases, an adverse chord-wise pressure gradient develops and the flow begins to detach from the airfoil surface. Unless the adverse pressure gradient is addressed, incoming air molecules are obstructed and pushed from the airfoil suction-side surface, creating a stall bubble. Past the stall angle a decrease in lift is accompanied by a corresponding increase in drag. The role of actuators in this context is to energize the boundary layer and mitigate adverse pressure gradients, thus delaying stall and improving performance by providing enhanced maneuverability, greater payload capacity, increased vehicle range and reduced stall speeds [86].

Two fundamentally different plasma actuators have been studied for boundary layer reattachment - the dielectric barrier discharge (DBD) and the spark discharge. The DBD actuator has been well studied and reviewed in the literature [87] [88] [89] [90]. A high voltage source applies a sinusoidal electric field between two asymmetrically placed conductors, one of which is exposed on the surface and the other embedded in the dielectric. Voltages and currents typically fall in the ranges of 3-10 kV and 0.1-10 mA, respectively, with frequencies in the 0.05-50 kHz range. Plasma densities of 10^{11} cm^{-31} and electron temperatures of a few eV are common [87]. The alternating waveform has positive and negative half cycles. During the negative half cycle electrons are easily

pushed from the exposed electrode and collected by the dielectric surface. A space charge develops that temporarily reduces the electric field, quenching charge transfer. When the polarity of the field switches to the positive cycle, electrons are pulled in bursts from the dielectric surface and return to the exposed electrode. Electrical and optical diagnostics have shown spatial and temporal variations in the DBD plasma structure as well as impacts of electronegative chemical species on discharge lifetimes [91].

The DBD actuator is recognized for its ability to reattach separated flows by velocity addition in the near wall region, but it has its limitations. Experiments have shown that DBD actuators replicate the effects of leading edge slats and trailing edge flaps by increasing AoA up to 8° past the stall angle and increasing the lift to drag ratio by 350% at *Re* 2.5×10^5 with as little as 2 W power input [92] [93]. Their utility under dynamic conditions has also been demonstrated and results suggest optimum control schemes at various airfoil pitching modes [94] [95]. In order for a DBD actuator to achieve maximum reattachment effectiveness, it should be located near the point of separation [96]. Although clever combinations of linear and annular DBD arrays can be used to increase their effectiveness and affect the flow field at large and not just the near wall region [97] [98]. DBD actuators remain limited in their application to general aviation, where *Re* $\sim10^7$, due to their low jet velocity which is typically around 5 m s^{-1} [87].

Spark type plasma actuators, referred to as “SparkJet” by its creators, were pioneered by Grossman, Cybyk and VanWie at Johns Hopkins University [86], and a

description of their operation follows. Spark type actuators are DC pulsed discharges ignited within a dielectric cavity having an opening on one end, usually opposite the electrodes. The mechanism of actuation can be divided into three distinct stages: 1) Energy input, 2) Mass ejection, and 3) Cavity recovery. Prior to electrical breakdown the gas within the cavity is at some reference temperature and pressure. Upon breakdown energy is rapidly transferred to the gas in the cavity in a constant volume process via rapid joule heating which causes elevated temperature and pressure. The sudden pressure increase creates a jet by expanding the cavity gas through the opening in the dielectric housing. During this period residual thermal energy in the cavity is convected away via the jet and conducted away via cavity wall interaction. After a short time, cavity pressure falls below reference as mass is ejected and the cavity simultaneously cools. The relatively higher pressure surrounding gas then fills the cavity, cooling it further and prepping the actuator for subsequent discharge. Limitations to the process include the efficiency with which electrical energy is transferred to thermal energy in the gas and the cooling rate of the cavity after the discharge.

Parametric CFD studies on spark type actuators indicate great promise for separation control in high speed flows. Predictions estimate jet velocity in excess of 500 m s^{-1} which is much higher than those attainable by DBD actuators [99]. Other CFD studies examined effects of cavity volume, orifice diameter, and energy input on recovery stage time scales, which are in the range of 300-2000 μs, after discharging into both quiescent air and a fully developed supersonic boundary layer with results indicating the potential to penetrate a *Ma*=3 cross-flow [100] [101]. Emphasis on

recovery time is crucial to understanding operating limits in terms of pulsing frequency because thermal energy has less time to dissipate at faster discharge rates. Pulsing too rapidly leads to diminished mass in the cavity and potentially less available impulse for future jets. Other relevant findings from these preliminary studies showed that for constant cavity volume, jet velocity increased with increased energy input and increased orifice diameter. The first result follows first law expectations. The second result indicates that viscous effects can dominate nozzling effects at the exit plane, making the investigation of various exit plane geometries worthwhile. Fast discharge times allow more time for cavity recovery, and since recovery time is somewhat controlled by orifice size, actuators can be tuned to specific applications [101].

Experimental studies of spark type actuators have demonstrated their effectiveness [102] [103] [104] [105]. In quiescent 35 torr air with 30 mJ/pulse energy input, a jet velocity of 250 m s^{-1} was measured, and a maximum pulse rate of 5 kHz was achieved, believed to be limited by insufficient cavity recovery time. In these experiments jet velocity was found to be current dependent and independent of pulsing frequency and orifice geometry. A ten-fold increase in current improved jet velocity by only 30%. Material selection for the cavity also showed some effect on jet velocity. When boron nitride was used instead of MACOR higher jet velocities were observed, and this is thought to be due to the higher thermal conductivity of boron nitride [102]. Using schlieren imaging the plasma jet was observed to penetrate 1.5 boundary layer thicknesses into a *Ma*=3 cross-flow. Other observations showed displacement of separation shocks both downstream and upstream of the actuators indicating a shift of

potentially undesirable oscillation frequencies that may couple with structural resonance. In a similar experiment a glow discharge plasma actuator was used with comparable average input power of a spark type actuator [106]. Although high speed flow actuation was possible using the sparking actuator, no such actuation was observed in the case of the glow actuator. It should be noted that glow discharges are not exactly the same as DBD discharges, but the microdischarges in a DBD have similar properties to those of transient high pressure glow discharges [107]. Experimental estimates of spark actuator efficiency as defined by energy input, cavity pressure rise and jet velocity are in the 20-30% range [108] [109].

Characterization of sparking plasma actuators is important because synthetic jet properties are excellent indicators of the actuators potential to affect flow. Jet velocity and impulse are two of the most important actuator properties for determining effectiveness, and a few different groups have sought to experimentally and/or computationally determine these quantities [110] [111] [112] [113]. Jet velocities into ambient air from single low frequency (~1 Hz) pulses have been measured using schlieren and PIV and range from 50-500 m s^{-1}. Direct comparison of jet velocities is usually not appropriate due to variations in actuator geometry and discharge energy, but even still some of these previously mentioned works are comparable in these respects and still show order of magnitude jet velocity differences. Some results are contradictory with respect to jet response to pulsing frequency and input energy. Miniature thrust stands have been described to measure these relatively small jet impulses [110] [114], but work in this area has yet to reach the maturity of experimental velocity

measurements. However, the ultimate goal of actuators is to reduce drag and/or increase lift on an airfoil. Thus, it is important to not only characterize actuator performance based on a single spark, but also to experimentally test the effectiveness of an array of such actuators on a real airfoil surface.

Much of the computational and experimental research into sparking actuators has been aimed at characterizing jet velocity, momentum/thrust generation, and the plasma discharge, but this investigation is unique in that it demonstrates that sparking plasma actuators are capable of affecting flow over a real surface, such as airfoils. Parametric studies of various actuator geometries and operating conditions report jet velocities in the 100-500 m s^{-1} range [110] [112] [115] [116] [117] [118], but direct comparison of these results is often hindered by these various testing conditions. Experimental approaches to characterize jet momentum and/or thrust have used laser interferometry [111], pendulum thrust stands [114] [118], and integrated pressure distributions [117] with measured impulse bits of 1-5 μN-s. Spark plasma actuator efficiency has been defined in terms of cavity pressure [113] rise and impulse generation [114] with respect to capacitor energy deposition and the calculated efficiencies were 25% and 6%, respectively. While such individual characterization is important, the number of actuators required along the airfoil has a more direct impact on power consumption.

Among the first to investigate sparking actuator on an airfoil for drag reduction is the PLASMAERO project undertaken by Onera and CNRS/LAPLACE laboratory [119]. This project used a span-wise array of 20 equidistant actuators positioned at $x/C = 0.32$ on a NACA 0015 airfoil having chord of 500 mm and span of 1200 mm. Angle of attack

was 10-13.6°. A turbulent airfoil boundary layer was tripped using carborundum dots, and chord based Reynolds number was $6\times10^5 < Re < 1.2\times10^6$. At discharge frequencies of 2 kHz, actuator jet velocity and duration were 200 m s^{-1} and 150 μs, respectively. The 2-component PIV technique and an array of pressure taps were used to interrogate a region perpendicular to the airfoil suction surface mid-span between $0.55 < x/C < 1.0$, and results showed a 19% drag reduction based on the size and position of the separated flow region.

5.2 Dissertation objectives

The experiments discussed in this chapter demonstrate that gas phase switching is suitable to for powering a plasma actuator for flow control and that the sparking plasma actuator can be used to successfully control boundary layer separation and thus alter aerodynamic forces on an airfoil. One objective of this research is to characterize a slotted orifice spark type plasma actuator in terms of its jet velocity, impulse bit generation and steady-state operating temperature. First, a commercially available CFD package is used to investigate actuator geometries that generate jets with higher velocity for a given energy input. Two actuators were fabricated based on the aforementioned computational results, and schlieren imaging is used to visualize the jets from these actuators and experimentally determine their jet velocities under different operating conditions – namely energy input and pulsing frequency. Another set of six actuators is then fabricated and tested on a custom thrust stand to characterize actuator impulse bit generation with respect to geometric variations. These geometric variations will be

elaborated upon in the impulse bit measurement section. These same six actuators are then thermally imaged to investigate actuator temperature response to both input power and geometry. The slotted orifice used in these experiments is distinct from circular orifice actuators discussed in previous work, and for applications requiring wide lengths (relative to orifice diameter) of actuation, slotted actuators may be a more amenable geometry since jets issuing from circular orifices are spatially constrained by their cavity geometry.

The other main objective of this research is to use optical monitoring of load cell deflection to directly measure drag forces on an actuated NACA 0012 airfoil operating under stalled conditions. Because of strong EMI generated during sparking, the utility of lift/drag measurement systems that rely on sensitive circuitry is limited, and methods relying on pressure taps or optical measurements are more amenable to these relatively harsh electrical conditions. Traditional methods of suspended masses were used to simulate and calibrate drag forces on a sting. A high resolution digital camera monitored sting deflection through a microscope, and in this way drag forces acting on the airfoil were determined in static wind tunnel conditions while the actuator was power cycled. Local boundary layer separation and attachment were qualitatively assessed using an array of small colored tufts on the suction side of the airfoil. This provides data for important whole airfoil integration of actuators.

5.3 Thermodynamic analysis of a single pulsed jet

A first order analysis of the transient nature of the spark actuator is included to provide better insight to the physical mechanisms of operation and determine which system parameters are of particular interest. This analysis follows that described in previous work [86]. The actuator cycle can be divided into three distinct processes. First, energy is rapidly input to a fluid inside a control volume. Air is the working fluid and initially it is at standard conditions. Energy deposition is so rapid that it can be assumed a constant volume process and the temperature and pressure within the control volume quickly rise. The second process is the expulsion of the high temperature high pressure fluid from the control volume through an orifice creating a high velocity jet. Whether directly (momentum injection) or indirectly (vortical entrainment of air in the freestream), this jet energizes the boundary layer and has the potential to overcome adverse pressure gradients that cause separation. Finally, pressure in the control volume drops to ambient conditions. However, temperature inside the control volume may still be higher than ambient. These conditions dictate that the mass now inside the control volume be less than prior to energy input. As the control volume cools and maintains ambient pressure, the mass in the control volume approaches the initial amount. Equation 21 describes conservation of energy applied to the actuator and is as follows

$$\iiint \dot{q}\rho dV - \iint \dot{q}'' dS - \iint P\vec{\boldsymbol{U}} \cdot d\vec{\boldsymbol{S}} = \iiint \frac{\partial}{\partial t}\left[\rho\left(e + \frac{U^2}{2}\right)\right] dV + \iint \rho\left(e + \frac{U^2}{2}\right)\vec{\boldsymbol{U}} \cdot d\vec{\boldsymbol{S}} \tag{21}$$

where, $\dot{q}$ is specific power (heat) addition, ρ is fluid density, V is volume of the control system, $\dot{q}''$ is heat flux, S is surface area, P is pressure, U is fluid velocity, t is time and e is specific internal energy. The volume the control volume is assumed to be the cylindrical cavity in Figure 81. Similarly, the control surface for the heat flux term is the internal surface area of the cylindrical cavity and the surface area appearing in the dot product is the surface area of the orifice through which the jet exits. In this analysis it is assumed that flow within the control volume is 1-dimensional, and the conservation of energy equation reduces to the form given in Equation 22.

$$\frac{d}{dt}(e\rho V) = \dot{Q} - \dot{Q}'' A_s - \dot{m} h_t \tag{22}$$

Since energy input is assumed 1) to occur on times scales very short in comparison with those associated heat lost through the surface and mass flow from the control volume and 2) to be constant in time, the temperature rise of the fluid in the control volume can be determined using Equation 23 and assuming standard initial conditions.

$$T_2 - T_1 = \frac{\dot{Q}}{c_v \rho_1 V} \tag{23}$$

The corresponding pressure rise in the control volume can be determined by applying an equation of state. In this analysis, the ideal gas law is used and shown in Equation 24 below

$$P_2 = \rho_1 R T_2 \tag{24}$$

where, R is the gas constant for the working fluid (air). This calculation concludes the analysis for the first process in the actuator power cycle.

The second process is modeled as an isentropic expansion of the gas in the control volume, and no energy is input to the system. If heat transfer modes are ignored, then the control volume's only energy loss is through flow work from the escaping gas, and the energy balance reduces to Equation 25 below

$$\frac{d}{dt}(e\rho V) = -\dot{m} h_t \tag{25}$$

where h_t is the enthalpy of the gas.

Prior to this process, energy was rapidly input at constant volume causing large temperature and pressure increases. During this process of mass ejection, the flow is choked, since $P_2 > 1.893 P_{amb}$, for most of the jet's lifetime. As mass is ejected the

pressure in the control volume will drop and the flow will ultimately become unchoked. Equations 26 and 27 use isentropic and choked flow assumptions to determine the mass flow rate and duration of the choked flow portion of the process.

$$\dot{m} = \frac{\sqrt{\frac{\gamma}{R}}\left(\frac{\gamma+1}{2}\right)^{-\left(\frac{\gamma+1}{2(\gamma-1)}\right)} P_2 A_{orifice}}{\sqrt{T_2}} \tag{26}$$

$$\Delta t = \frac{V}{\sqrt{\frac{\gamma}{R}}\left(\frac{\gamma+1}{2}\right)^{-\left(\frac{\gamma+1}{2(\gamma-1)}\right)} \gamma R A_{orifice}\sqrt{T_2}}\left[\left(\frac{P_2}{P_1}\right)^{\frac{\gamma-1}{2\gamma}} - 1\right] \tag{27}$$

In the above equations γ is the ratio of specific heats. In actuality, the time of mass ejection will be longer than that calculated using Equation 27 because this only accounts for mass ejected during the choked flow condition. As the pressure inside the control volume drops over this time period, the temperature will also drop, but temperature and pressure will not equilibrate with the surrounding atmosphere at the same time. However, assuming an isentropic expansion, the temperature at the end of the process is determined using Equation 28.

$$T_3 = T_2\left(\frac{P_{amb}}{P_2}\right)^{\frac{\gamma-1}{\gamma}} \tag{28}$$

During the third and final process, the cavity continues to cool at constant pressure as heat is convected from the gas to the chamber walls where it is conducted away. If a lumped capacitance system is assumed and internal convection is the limiting mode of heat removal from the control volume then the gas temperature will decrease exponentially with a time constant τ as described in Equation 29 below

$$T(t) = (T_3 - T_1)\exp\left[\frac{t}{\tau}\right] + T_1 \tag{29}$$

and τ is defined in Equation 30 which can be used to solve for the convective heat transfer coefficient, h.

$$\tau = \frac{c_v \rho V}{h A_{surface}} \tag{30}$$

At this point it is possible to estimate a characteristic time for the cavity to return to ambient conditions. This is determined by dividing the change in internal energy of the control volume required to bring the gas back to ambient temperatures by the rate at which heat is removed via convection to the control volume walls. The characteristic time, t_{char}, is calculated in Equation 31 below.

$$t_{char} = \frac{\rho_3 V(e_3 - e_1)}{h A_{surf}\left(T - T_{surf}\right)} \tag{31}$$

This is a first order analysis intended to highlight the fundamental processes of a spark type plasma actuator operation cycle. In reality the processes are far more complex as a result of transience, spatial gradients, non-ideal processes and variable thermos-physical properties. A more rigorous analysis is best handled using CFD solvers. However, although the aforementioned approach is simplified, useful insight can be gained from the first order analysis. For example, the third process during which the control volume cools imposes some limitations on the peak performance of spark type actuation. If the sparking rate is faster than the characteristic cooling time, t_{char}, then the control volume will gradually heat to some equilibrium temperature above ambient conditions and as a result hold a reduced mass of working fluid which will have deleterious consequences with respect to mass ejection and momentum flux. Therefore, these devices are expected to have some practical upper limit for sparking frequency. Similarly, it is apparent that the control volume should be constructed of a material that is a dielectric yet is an effective heat conductor so that heat removal from the control volume is not limited by conduction through the walls.

5.4 Modeling the actuator using COMSOL

The actuator was modeled in COMSOL and results were used to guide fabrication of actuators for experimental testing. Specifically, various ratios of throat width to cavity diameter were examined to determine ratios that provide high velocity jets. The model mesh was refined to the point where the solution differed by less than 5% difference from the next coarse mesh. As such strict grid independence was not

sought, and the model does not converge in the presence of strong gradients and large transience. This limitation is imposed by available computational power. Therefore, while the model is known to be quantitatively inaccurate, it is expected to be reliable from a qualitative standpoint.

5.4.1 Model overview

Computational results were generated using the compressible 2D laminar high Mach number flow model available in the COMSOL multi-physics software package. A portion of the domain is shown in Figure 82, and it is divided into two material regions. The grey region is air at standard conditions, and the blue area on the bottom represents the actuator body. In this model air at standard conditions initially flows above the actuator top surface from left to right with velocity of 100 m s^{-1} while the air within the actuator body is initially quiescent and also at standard conditions. Regarding the ambient air portion of the model, the left side boundary condition had constant velocity of 100 m s-1 while the top and right sides had P = 1 atm. The actuator body is comprised of a circular cavity and a rectangular throat enclosed in a dielectric (MACOR) material. The actuator cavity has diameter of 1 mm, but the plasma is generated within a concentric discharge region having diameter 0.8 mm. The plasma discharge was modeled by inputting energy to the actuator at a rate of 5 mJ/pulse with an assumed cavity depth of 4 mm. Energy was added in the model by having a 100 ns duration step function heat source within the discharge region. With respect to the image in Figure 82, the plasma discharge in the cavity is perpendicular to the image plane. The hot high

pressure gas created by the plasma in the cavity expands through the slotted throat and issues into the free stream. The slot has length and width of 1.3 mm and 0.3 mm, respectively, and it intersects the free stream at an angle of 35°. The model was run several times exploring the impact of the actuator aspect ratio (*AR*), which is defined here as the ratio of throat width to cavity diameter, on actuator performance. Aspect ratio was varied by holding the cavity diameter constant and varying throat width. Important parameters to be examined include 1) exit velocity, 2) mass flux, 3) duration of mass ejection, 4) cavity refill time, and 5) flow structure.

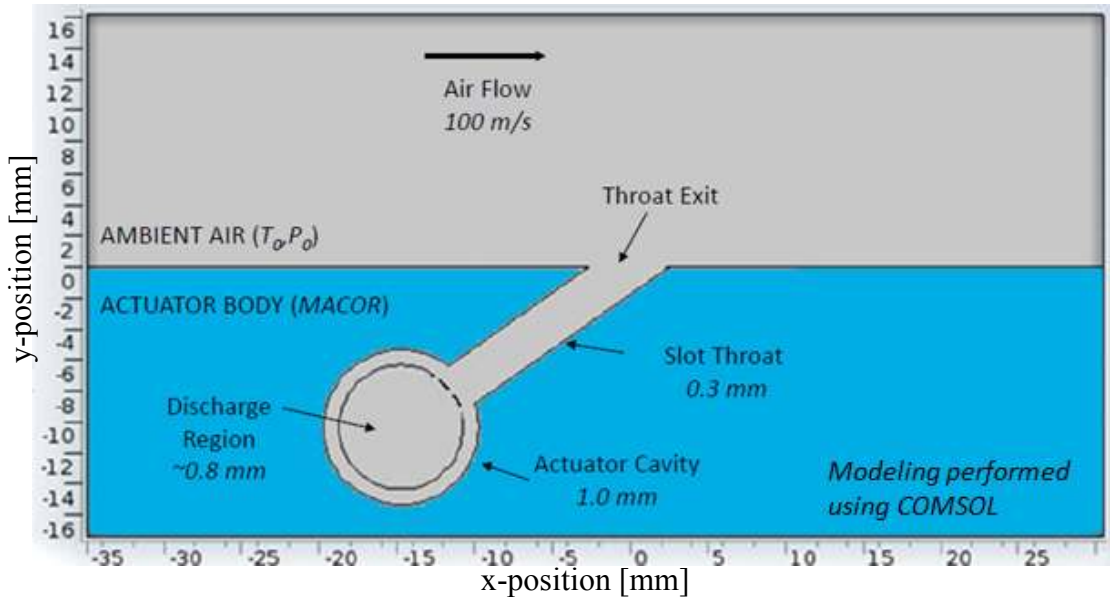

Figure 82. Representative geometry for improved plasma actuator. Ambient air flow is from left to right. The air/actuator interface is shown by the black horizontal line at y = 0. The gap in the air/actuator interface marks the location of the throat exit.

The model was processed on a Win7-SP1 workstation with an i3-2100 3.1 GHz processor and 8 GB of RAM and simulated 1 ms of real time with data stored every 0.1 μs. In the actuator cavity and near wall regions grid spacing was less than 10 μm. Grid spacing was relaxed at increasing distances from the actuator body. Computational time steps were chosen by the solver and were smaller at times where large gradients existed. A energy of 5 mJ/pulse was chosen because higher energy input caused large spatial and temporal gradients that caused solver issues.

5.4.2 Parametric study

The geometry of the new actuator suggests that certain scaling parameters could be important considerations for optimum actuator operation. One of these parameters is the aspect ratio (*AR*), $AR = D_{throat}/D_{cavity}$, where, D_{throat} is the width of the slot throat and D_{cavity} is the diameter of the actuator cavity. Jet velocity and mass flow across the throat exit were examined using the CFD model in two studies: 1) as functions of the throat size (Figure 83 - Figure 86) and 2) as a function of cavity diameter (Figure 87 & Figure 88). In the first method, the *AR* was adjusted by varying D_{throat} while holding D_{cavity} constant, and in the other method, the *AR* was adjusted by varying D_{cavity} while holding D_{throat} constant. Results are presented with respect to *AR*, though another important scaling parameter is the cavity diameter to discharge diameter ratio, which is constant in the first study and varies in the second study.

Figure 83 shows the model predicted mass flow across the throat exit for various values of *AR* maintaining D_{cavity} = 1.0 mm. Three distinct regions are visible in these

plots and the following physical interpretation of the fluid flow. In the first region, a sharp pulse is apparent in the mass flow, and corresponds to the flow pushed directly out of the throat by the initial shock wave generated by the plasma discharge. As this initial mass flow decreases a weaker longer duration outflow is evident as a knee on the curve, and this knee marks second region. This is physically interpreted as outflow from the high pressure cavity/plenum by shock reflections within the cavity. The third region is where the actuator begins to refill, which is when $\dot{m}(t \approx 20\ \mu s) < 0$, and this region is characterized by the sinusoidal behavior of the mass flow across the actuator exit plane. Physically this represents the numerically observed vortices created as cooler denser air from the free stream swirls into the cavity and the warmer gas from the discharge swirls outs. The three distinct regions are noticeable for all values of *AR*. As *AR* increases the vertical behavior of the refilling process becomes more pronounced. Mass flow was predicted to increase as *AR* increased. However, because of the higher mass flow, the duration of mass ejection was shorter. These findings raise the question of whether or not it is better to design an actuator that is capable of ejecting more mass in a short time or if it is better to have an actuator that ejects mass more gradually over a longer period of time.

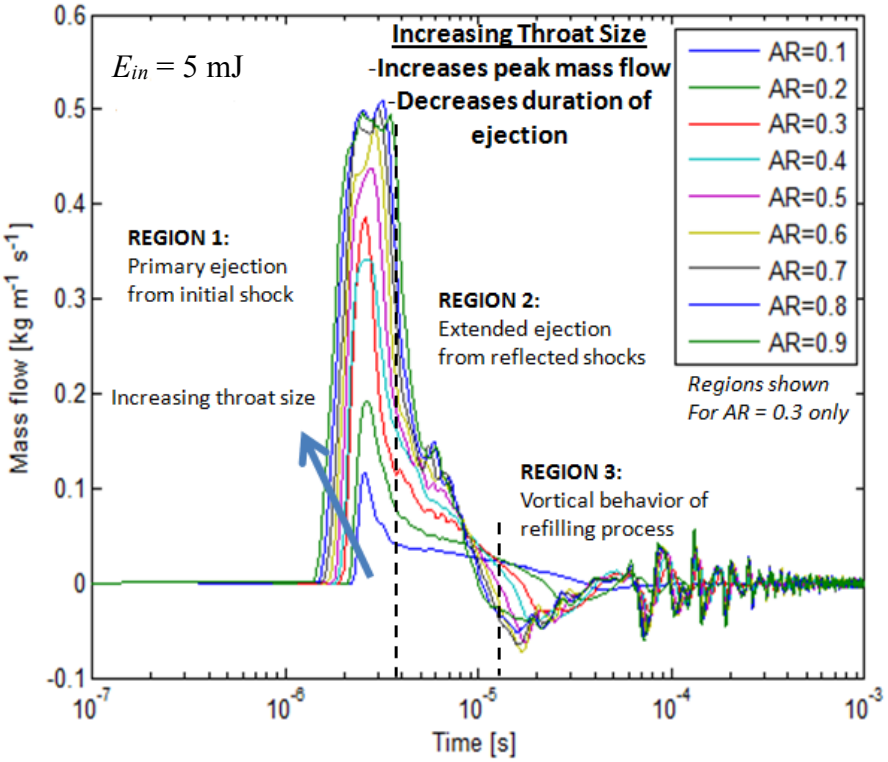

Figure 83. Mass flow across the throat exit when throat diameter is varied from 0.1 to 0.9 mm while maintaining D_{cavity} = 1.0 mm and constant input energy of 5 mJ.

In Figure 84 the jet velocity at the throat exit is examined as *AR* is adjusted by holding D_{cavity} constant. From Figure 84 it is shown that *AR* has a distinct effect on jet velocity. This is expected since the actuator throat acts as a nozzle accelerating the flow. When the throat width is small jets tend to have high velocity, and when the throat is wide, the jet velocity is reduced. However, if the throat is too small the flow may lose energy due to the very narrow slot. The model predicts a maximum velocity of 600 m/s at *AR* = 0.3 and a minimum velocity of 225 m/s for *AR* = 0.9.

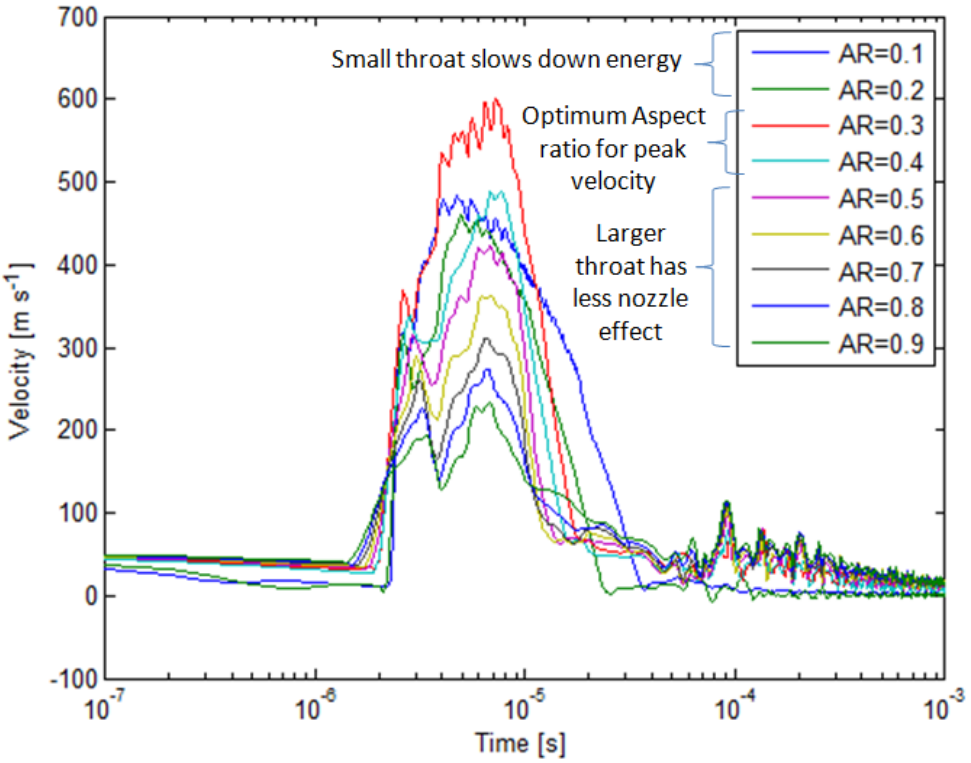

Figure 84. Jet velocity at throat exit when throat diameter is varied from 0.1 to 0.9 mm while maintaining D_{cavity} = 1.0 mm. Same conditions as Figure 83.

Velocity and temperature profiles of the throat exit region were taken from the COMSOL model at times of 1, 10 and 25 μs for AR = 0.3 and AR = 0.9. These profiles are provided in Figure 85, respectively. In the profile images taken at t = 1 μs, expansion can be seen within the cavity. No mass has left the actuator, so this process is pre-Region 1. At t = 20 μs, the hot gas can be seen expanding through the throat exit. This is characteristic of Regions 1 and 2. The later profiles collected at t = 25 μs show cooler ambient air circulating into the relatively low pressure actuator cavity in the

refilling/cooling process that is characteristic of Region 3 (N.B. – Regions are described in Figure 83).

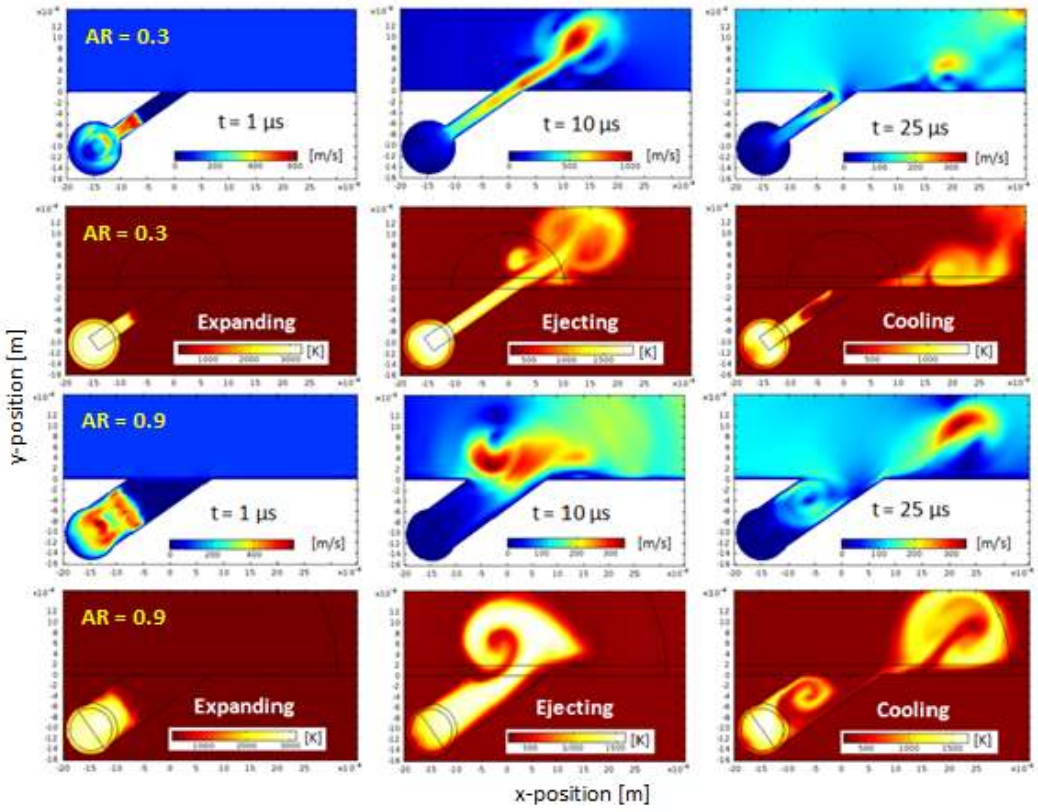

Figure 85. Velocity and temperature profiles in the throat exit region for (top) AR = 0.3 and (bottom) AR = 0.9. D_{cavity} = 1.0 mm in both cases.

Since the actuator is designed for repetitive use, it is necessary to investigate how the actuator cavity refills itself between pulses. The mass flow curves in Figure 83 were integrated over time to obtain the cumulative mass ejected from the actuator cavity, which is shown in Figure 86. A plot of the total mass ejected from the cavity, which is

the maximum of the integrated mass flow curves, as a function of *AR* is shown in the subplot of Figure 86. The initial peaks represent the amount of mass that is ejected from a single discharge. As the ejected mass issues forth from the actuator slot, a low density region in the actuator cavity slowly develops. After the hot gas has fully expanded out of the slot, ambient air rushes to fill the region in the actuator. Ideally, the filling process is complete prior to subsequent firing. The model predicts that *AR* = 0.3 and *AR* = 0.4 perform equally well in this regard. Both of these *ARs* refill in less than 1000 μs which implies that repetition rates of 1 kHz are feasible.

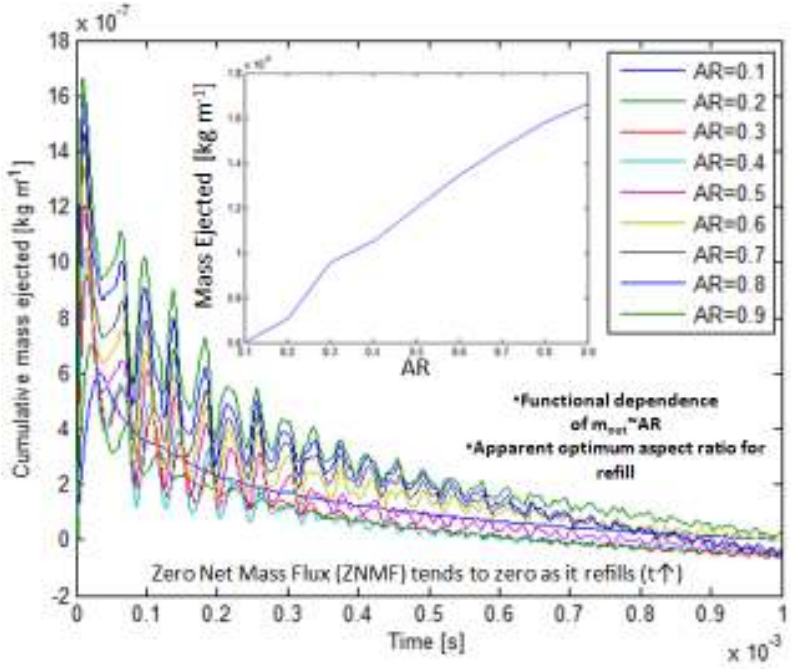

Figure 86. Cumulative mass ejected from a slot type plasma actuator with E_{in} = 5 mJ and varying throat width. The smaller plot shows the maximum mass ejected from the cavity as a function of AR. D_{cavity} = 1.0 mm. Same conditions as Figure 83.

Mass flow was also examined for *ARs* when D_{cavity} was varied while maintaining D_{throat} = 0.3 mm. These trends are shown in Figure 87. The model predicts similar behavior as that seen in Figure 86 where *AR* was adjusted by varying D_{throat}. Results are comparable for $AR_{cavity} = 0.2 = AR_{throat}$. In Figure 88 the cumulative mass ejected across the throat exit is shown. From this graph it can be seen that the larger cavity *ARs* do not refill as quickly as was previously shown in the case where D_{cavity} remained constant. These cavities are larger than in the first case and refilling times are longer. The fastest refilling occurs at the smallest cavity, *AR* = 0.24, where the refill time is about10 ms. Refill times of that length indicate repetition rates on the order of 100 Hz. Faster repetition rates may still be used, but the mass of air inside the cavity will be diminished upon a second firing. Ultimately, the cycle will become periodically steady with steady state temperature in the cavity above T_{amb}.

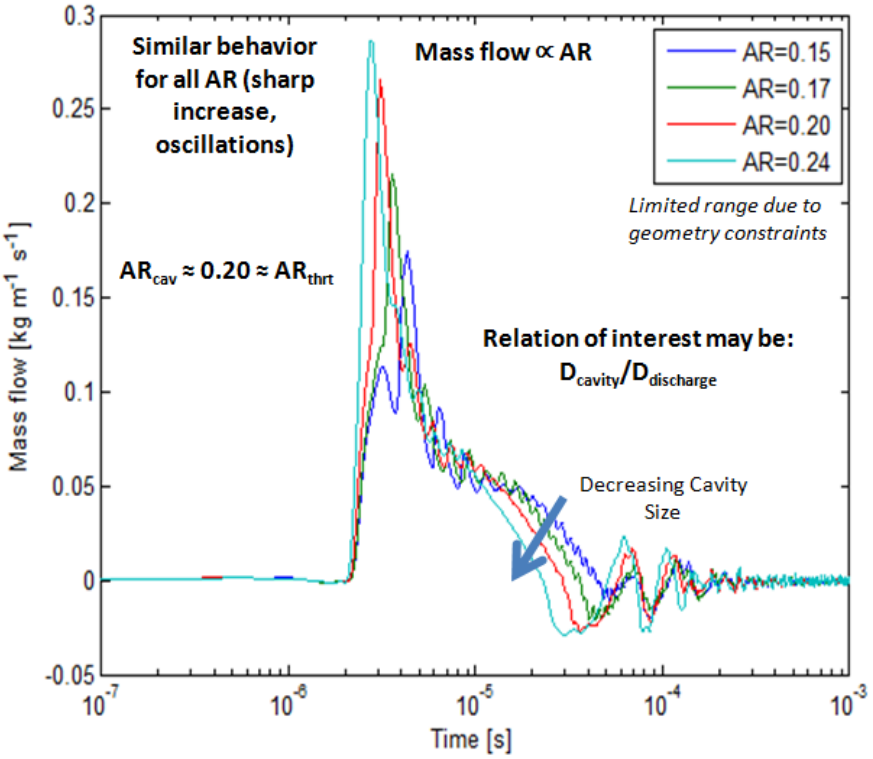

Figure 87. Mass flow across throat exit as a function of time with varying cavity diameter from 1.25 mm to 2 mm while maintaining D_{throat} = 0.3 mm and input energy of 5 mJ.

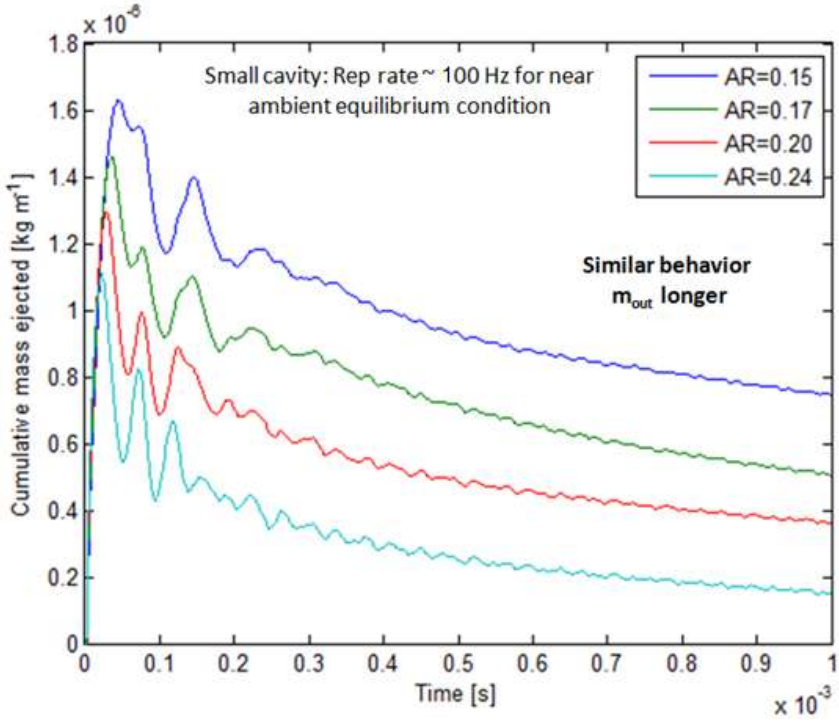

Figure 88. Cumulative mass flow for varying cavity diameter 1.25 mm to 2 mm while maintaining D_{throat} = 0.3 mm. Same conditions as Figure 87.

5.4.3 Determination of mass flow boundary condition

A functional form of the mass flow across the throat exit was desired for use as a boundary condition in the full airfoil simulation being performed by Lynntech. Assuming no variation in the *z*-direction, the mass flow per unit depth [kg $m^{-1} \cdot s^{-1}$] from the actuator was determined by calculating a line integral of the product (ρv), where ρ was the density and v was the velocity in the *y*-direction, across the throat exit. The corresponding data were subsequently analyzed in MATLAB, and an approximate fit to the model output was determined. Figure 89 shows the mass flow [kg $m^{-1} \cdot s^{-1}$] data from COMSOL plotted against the fit model.

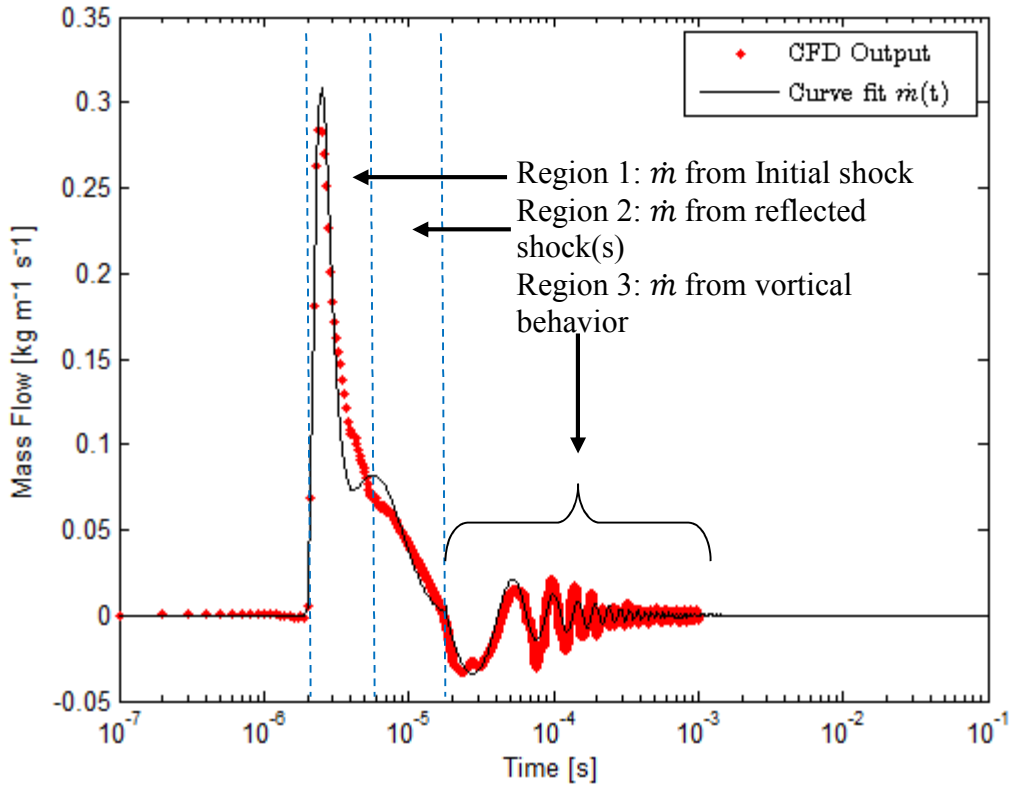

Figure 89. Overlay of MATLAB curve fit on COMSOL CFD output. AR = 0.3.

The fit model was created using a least squares fitting routine for the summation of three different functions, given in Equations 32-34, that account for the distinct regions that exist in our physical interpretation of the fluid flow. Eleven constants, $A - I$, t_1 and t_2, were used in the fitting routine, and they are provided in Table 14. The constants t_1 and t_2 serve to shape their respective functions as well as act as logical switches in Heaviside functions, represented by Φ_i ($\Phi_i = 1$ for $t \geq t_i$, and $\Phi_i = 0$ otherwise). The overall mass flow as a function of time is given in Equation 35.

$$\dot{m}_1 = B \exp\left[\frac{-(t-t_1)}{A}\right](t-t_1)^2 \tag{32}$$

$$\dot{m}_2 = D \exp\left[\frac{-(t-t_1)}{C}\right](t-t_1)^2 \tag{33}$$

$$\dot{m}_3 = E \exp\left[-\left(\frac{(t-t_2)}{F}\right)^I\right]\left[H + \sin\big(G(t-t_2)\big)\right] \tag{34}$$

Table 14. Curve fit constants for actuator mass flow as a function of time.

CONSTANT	*VALUE*
A	2.5802e-7
B	8.297e12
C	1.8602e-6
D	4.3821e10
E	-0.11248
F	6.9348e-6
G	1.3268e5
H	-0.028122
I	0.32785
$\mathbf{t_1}$	1.9741e-6
$\mathbf{t_2}$	1.8e-5

$$\dot{m} = \Phi_1\dot{m}_1 + \Phi_1\dot{m}_2 + \Phi_2\dot{m}_3 \tag{35}$$

5.5 Actuator fabrication

Three different batches of actuators were fabricated for different purposes. The first batch consisted of two different actuators having different aspect ratios and was used to experimentally investigate actuator jet velocity response to different aspect

ratios, energy inputs and pulsing frequencies. The second batch consisted of six different actuators of various geometry and was used to investigate momentum and thrust generation. These two batches were similar in that they were both constructed out of MACOR ceramic. The third batch of actuators was of a completely different design than the first two batches. The third batch was a strip type actuator wherein a series of spark gaps were placed on an alumina or mica substrate and partially covered with glass slides or mica. A more complete description of each style of actuator follows.

5.5.1 MACOR actuators for velocity measurement

Based upon the CFD design studies an initial test matrix of actuators to be for shadowgraph experiments was developed as shown in Table 15. Due to fabrication limitations, it was difficult to precisely machine ceramic actuators to specified AR= 0.3. Nevertheless, actuators have two sufficiently different aspect ratios for direct comparison. Varying these parameters will allow for validation and/or comparison to the jets observed in the modeling. Aspect ratios of 0.5 and 1.0 have been investigated.

Table 15. Actuator geometry for those used for jet velocity measurements.

Actuator	Cavity Diameter (mm)	Throat Width (mm)	Throat Slot Angle (deg)	Slot Length (mm)	AR
A	1	1	40	3	1
B	2	1	65	4	0.5

Some parameters may be modified depending on the constraints of the fabrications methods. Currently an easy-to-machine glass-mica ceramic (similar to MACOR) has been chosen as the material from which to build the actuator. Two mockup actuators with different geometries are shown in Figure 90. This ceramic is amenable to machining and has attractive electrical properties. If necessary, higher thermal conductivity boron nitride ceramics could also be used. Two different methods were used to fabricate actuators. The actuator on the left in Figure 90 was machined using a mill and angle parallels, the actual slot angle is 65° below the horizontal. The actuator was secured to the angle parallels and the throat was cut using a 1 mm diameter milling bit. Cuts were made in the direction of the actuator cavity. A 2 mm diameter through hole was drilled at the interior end of the throat for the actuator cavity. The throat length with this method is currently limited and non-uniform beyond 2 mm due to a tapered geometry of the milling bit. The acutuator on the right in Figure 90 was created using a single cut of a fine toothed saw-blade. This fabrication is easier but has less design variability, and issues with accurately matching the small feature sizes. The first fabrication method should be sufficient for the initial test matrix, though other machining techniques are also being investigated.

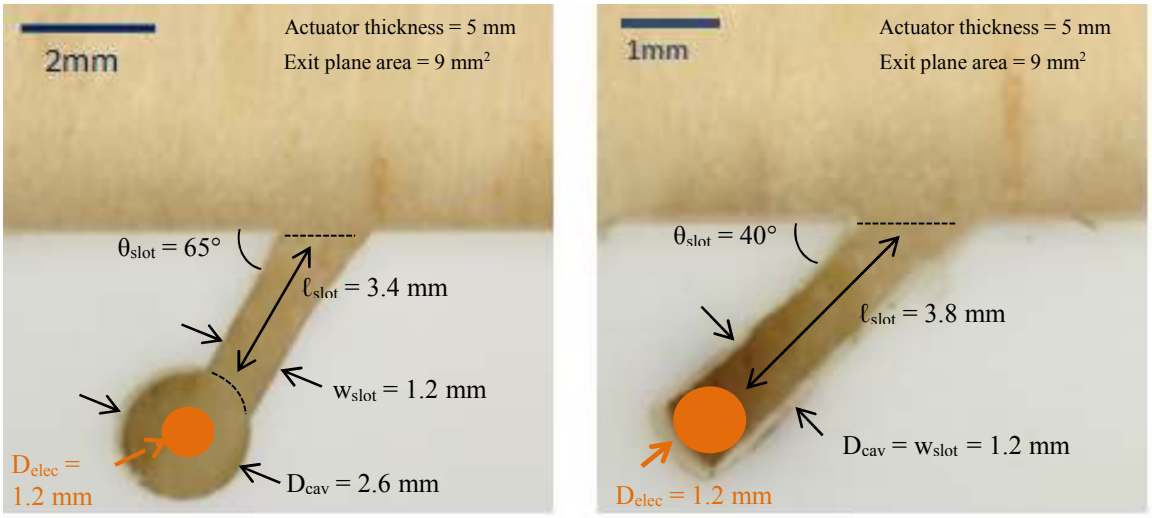

Figure 90. Actuator mockups for jet velocity measurement. (left) Actuator A (AR = 0.5) throat angle 65° below horizontal with circular cavity, (right) Actuator B (AR = 1.0) throat angle 40° below horizontal with rectangular cavity.

Additional geometries may be added to the test matrix to verify some of the optimizations predicted in the modeling. Such variations in actuator geometry are described in Table 16. Constant in these studies would be throat length, and fabrication materials. The discharge characteristics will also vary. Applied voltage will largely be determined by the inter-electrode spacing, and the corresponding breakdown voltage, which initially will be equal to the slot length. This breakdown voltage, though, is expected to have some variation with cavity diameter as in such cavities the breakdown is surface enhanced. The capacitance in the external circuit will be a easily changed and significant variable as it will largely determine the energy release (since breakdown voltage is fixed). Alternatively, gas phase switching can be used to overvoltage the spark gap in the actuator cavity and thus more directly control energy input.

Table 16. Considered actuator geometries**.**

Actuator	Cavity Diameter (mm)	Throat Width (mm)	Throat Slot Angle (deg)	Slot Length (mm)
1.1.1.1	2	1	45	3.175
2.1.1.1	1	1	45	3.175
1.2.1.1	2	2	45	3.175
1.1.2.1	2	1	15	3.175
1.1.1.2	2	1	45	12.25

5.5.2 MACOR actuators for momentum measurement

Six durable actuators have been fabricated based on a slightly modification of the test matrix outlined in the previous section. The general structure of the actuator, as shown in Figure 91, is a stack of five components 1) ceramic ground electrode holder, 2) mica sheet, 3) ceramic actuator cavity, 4) mica sheet, and 5) ceramic high voltage electrode holder. Large electrodes (used to prevent electrode overheating if thin wire were used) are mounted onto the electrode holders. Since the electrodes are larger than the cavity the mica sheets utilize pinholes as barriers to localize the discharge to the center of the actuator cavity. Two plastic fastening screws hold the assembly together.

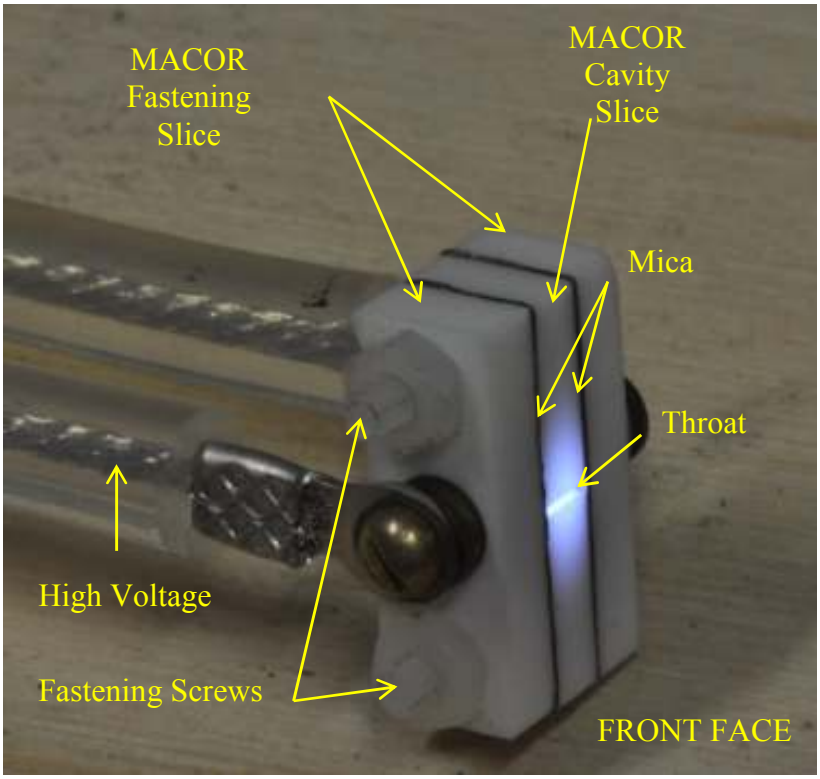

Figure 91. Annotated actuator for thrust measurements in operation.

The main body of each actuator is fabricated from MACOR which is a machinable glass-ceramic stable up to 1000 °C. It is a very good electrical insulator, and a generally poor thermal conductor. Boron nitride (BN) ceramics are preferable in this respect due to their high thermal conductivity (k_{MAC} = 1.46 W m^{-1} K^{-1}; k_{BN} = 30 W m^{-1} K^{-1}). MACOR is easy to machine and can be shaped using standard metal working tools. The fabrication process begins with a 53 mm x 17 mm x 7 mm *(nominal dimensions)* bar stock of MACOR. Three holes are drilled lengthwise into the stock, and the electrode/cavity hole is drilled along the lengthwise axis. Then larger fastening holes are drilled on either side of the center electrode/cavity hole. After the holes are drilled, three

slices that are perpendicular to the lengthwise axis are cut from the MACOR stock using a diamond saw. This is shown in Figure 92. Two slices are used to hold the electrodes and sandwich the actuator in place, and the third slice is the actuator cavity.

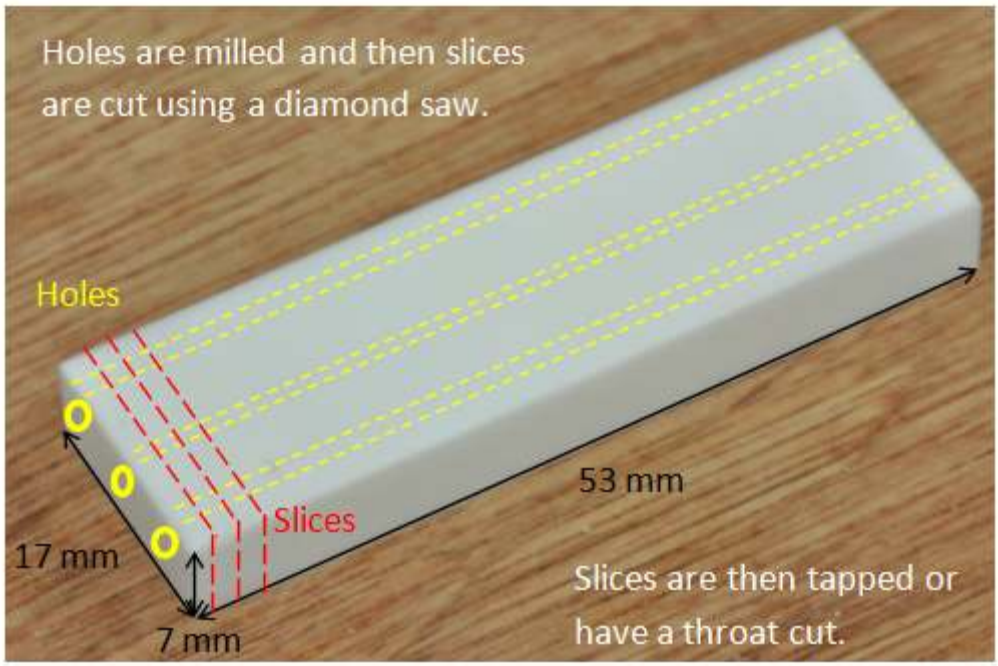

Figure 92. Actuator fabrication process. NOTE: Hole and slice sizes are not to scale.

The center hole for the electrodes on the fastening slices are tapped appropriately according to the desired center-hole diameter. For the actuators shown, the holes are tapped for either 2-56 (nominal cavity) or 0-80 screws (small cavity). The outer two holes are left as through holes with diameters of 2.32 mm. The actuator cavity slice is then secured in a lathe and the throat to the actuator cavity is cut using a thin diamond

blade. The MACOR slices are then stacked together separated by a 0.25 mm thick sheet of mica, referred to as the dielectric spacer. Holes with a diameter of approximately 0.5 mm are made in the mica sheet barriers. Because mica is a strong dielectric, these holes localize the discharge to the center of the cavity. Larger holes are also made in the mica at the location of the fastening holes. The actuator is assembled and nylon screws are used to secure the components. The actuator front and back faces are sanded flush to within less than 50μm, and brass screws connected to high voltage wire are attached to the tapped holes in the fastening slices. A fully assembled actuator in operation is shown in Figure 91. A list of all components is provided in Table 17.

Table 17. List of MACOR actuator materials.

COMPONENT	MATERIAL
Fastening/Cavity slice	MACOR bar stock
Dielectric spacer	Mica sheet
Fastening screws & nuts	Nylon screw (2-56)
Electrodes	Brass screw (var)

The six tested geometries are taken varying a single geometric dimension from a standard case. The standard actuator is labeled '*V*' (for vanilla), and all other actuators are labeled based on which of their dimensions deviates from the *V* actuator. The dimensions of interest, and subsequently the actuator names, are cavity diameter (D), slot length (ℓ), actuator width (W), slot thickness (d), and slot angle (θ). The dimensions of each actuator are provided in Table 18. For the θ actuator the angle slot length is

listed (the perpendicular slot length in parenthesis) mm), thus is has both a change angle and slot length. Images of the actuators are shown in Figure 93 (a) & (b). The aspect ratios d/D are generally lower than previously tested because of the expected increase in performance, and are within the range of $0.1 < AR < 0.2$, as this should give more nozzleing effect and longer duration high exit velocities.

Table 18. Actuator design matrix. Dimensions with (*) are not included in the tolerance calculation because it is the variable of interest.

Actuator Label	Cavity Diameter, D [mm]	Slot Length, ℓ [mm]	Actuator Width, W [mm]	Slot Thickness, d [mm]	Throat Slot Angle, θ [deg]
V	2.0	2.15	3.10	0.2	0
D	1.2*	2.27	3.11	0.2	0
ℓ	2.0	1.30*	3.08	0.2	0
W	2.0	2.27	5.82*	0.2	0
d	2.0	2.22	2.98	0.4*	0
θ	2.0	2.92 (2.07)	3.05	0.2	45*
Tolerance	1%	2.17 ± 0.10 (5%)	3.05 ± 0.07 (2%)	5%	±3°

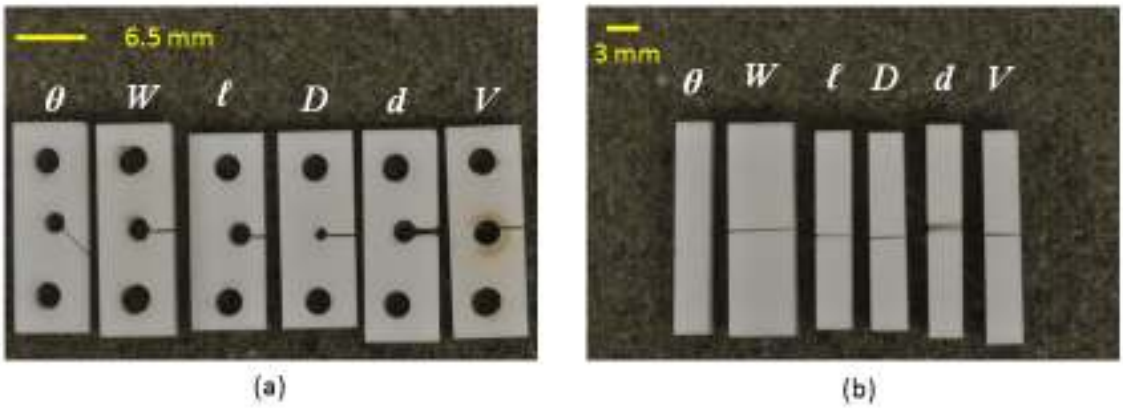

Figure 93. Side (a) and front (b) views of actuator cavities for those actuators used for thrust measurements.

5.5.3 Strip actuator used for wind tunnel testing

An actuator strip was implemented so that the affected flow zone would cover the entire span of the airfoil as opposed to the previous actuator design which consisted of a single discharge cavity in a MACOR housing that only covered a span of 6.4 mm. Preliminary wind tunnel testing showed that the previously designed actuators did not have sufficient spanwise influence. This style actuator allowed for testing a directed actuator jet using a glass cover as well as an undirected actuator jet if the glass cover were removed. Comparison of the two trials can be used to help determine dominant mechanisms of momentum injection interacting with the boundary layer. On the one hand, the boundary layer may be energized by direct momentum injection – that is, the jet itself is used to overcome adverse chordwise pressure gradients and thus reattach flow in stalled conditions. Or the boundary layer may be energized by vortical entrainment of ambient air outside the boundary (having velocity equal to the

freestream). A photograph of the actuator strip is shown in Figure 94 with the top image showing the actuator off and lower portion showing the actuator on. A schematic of the actuator strip with top and side view is shown in Figure 95.

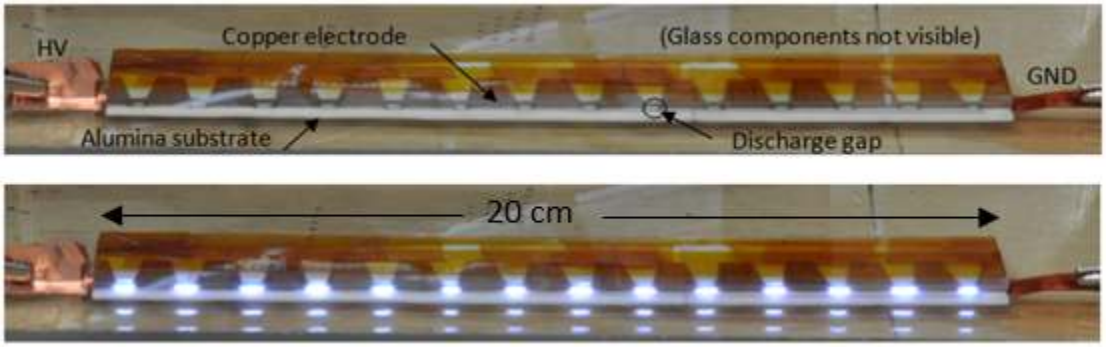

Figure 94. Picture of a 20 cm wide strip sparking plasma actuator. (top) unpowered, showing main components (bottom) powered showing spark discharges. This actuator is on an alumina substrate and has a glass top cover.

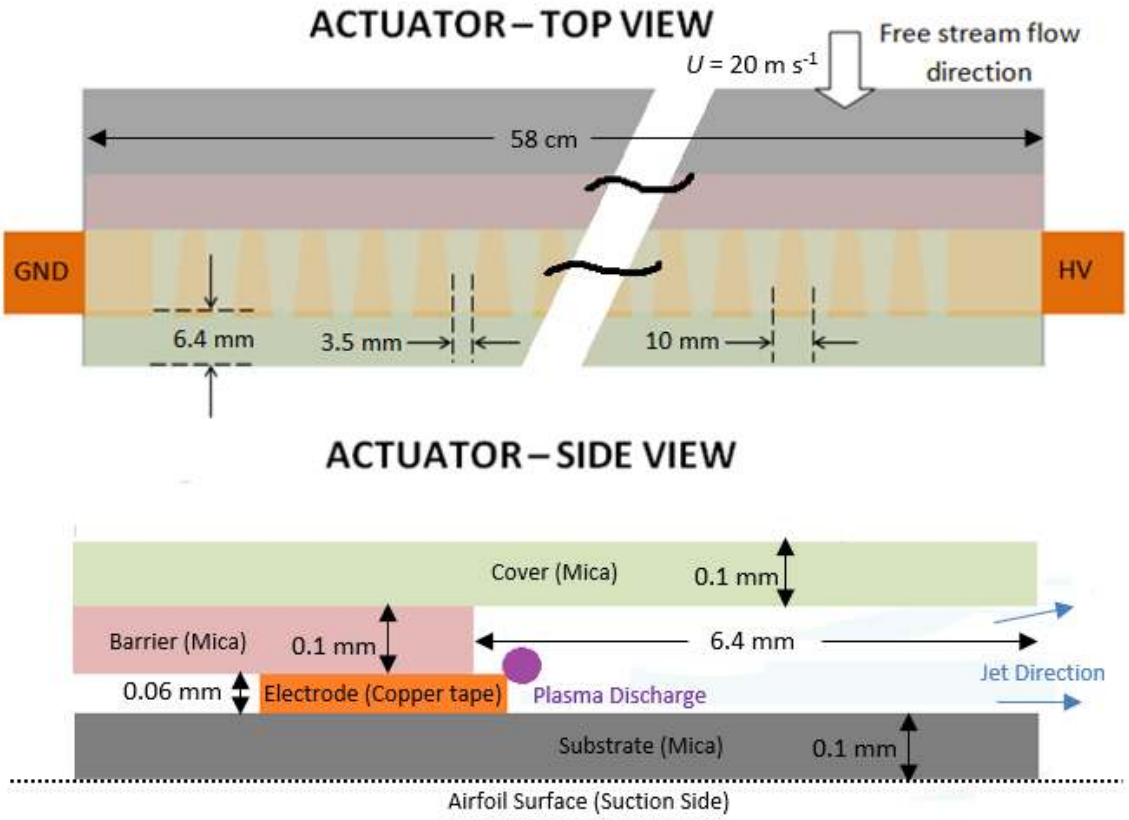

Figure 95. Plan sketch of the 58 cm strip actuator used in wind tunnel experiments. (not to scale)

As shown Figure 94 the actuator strip contains 14 discharge gaps (later this was reduced to 12 gaps, removing one at either end in order to reduce the required applied voltage) arranged in a straight line across a 1 mm thick alumina substrate having a span of 18 cm. High voltage and ground connections are made on either end of the actuator strip. The electrodes are made of 0.06 mm thick trapezoidal copper tape segments and are separated from one another with a discharge gap of approximately 3.2 mm. The electrodes are about 9.6 mm long thus about 25% of the airfoil span has an active plasma

discharge. The trapezoidal shape is used to encourage the breakdown location to be at the downstream side of the trapezoidal electrode. A 1 mm thick glass strip (microscope slides) covering the span of the actuator is placed directly above copper electrode/gap configuration in such a way that only the 0.5mm downstream end of each copper electrode protrudes. This barrier glass prevents the plasma from expanding upstream. A 0.1 mm thick glass strip (fabricated from microscope slide covers) is cantilevered above the 1 mm thick glass strip. This cover prevents the plasma from expanding outward and directs the gap flow downstream. The alumina substrate and glass strips enclose the discharge nodes on three sides, and the hot jet generated by the discharge is allowed to escape from the open end on the trailing face of the actuator. The plasma jets from are allowed to expand in the spanwise and downstream directions. The approximate location of the plasma discharges and direction of plasma expansion is indicated in Figure 95. It is estimated that from this geometry the jets emanate at a maximum angle of 8° relative to the airfoil surface. The lack of spanwise confinement allow for the emanated jet to be more uniform than the discharge spacing and for jets from adjacent discharges to overlap. The large volume of gas confined between the glass cover and substrate also lowers the specific energy input, a desirable design choice considering results from bench top testing. The large exit area allows for rapid refilling of the actuator with cold air. For operation on the airfoil the leftmost and rightmost discharge gaps were shorted using pieces of copper tape resulting in 12 discharge gaps across the actuator. The *x/c* location and number of discharges was in no-way varied or optimized during this phase of research, but twelve actuators was sufficient to see evidence of stall delay. Whether

fewer span-wise actuators could also work, or more actuators could work over a greater range of AoAs, or whether specific actuator spacing are beneficial are all interesting questions that will be addressed in subsequent research.

The actuator strip was secured to the top surface of the airfoil with the jet issuing at x/C = 0.5 (28.6 cm chord) without the strip being recessed, causing the flow to see a 2 mm high, 31.4 mm long bump (effectively a turbulator) on the airfoil. The sharp edges of the actuator were mitigated as much as possible by smoothing the leading face of the actuator with tape.

5.6 MACOR actuator thermal performance

Infrared images of the back face of the actuator were collected using a Fluke TiX series thermal imager. While the actuator was at room temperature, emissivity was set by matching IR temperature to that read by a K-type thermocouple and assumed constant over the temperature range observed. Pictures were acquired at regular intervals while the actuator was mounted to the thrust stand (described in the momentum measurement section), and the highest observed temperatures for a given image were recorded. All actuators were powered for 10 minutes with a 6 W power input to investigate geometric effects, and then the N actuator was tested under three power inputs– 1 W, 6 W, 94 W. Actuator power, P, was determined by the relation $P = \frac{1}{2} C V^2 f_{dis}$, where f_{dis} is the discharge frequency.

Temperature responses of the N actuator under varying load and of the six actuators of different geometry under a 6 W load are shown in Figure 96. Steady state

temperatures were reached around 300 s in all trials. The temperature data in Figure 96 can be useful for determining mass reduction in the cavity as the actuator heats as a result of increased duty cycle. At low power input, temperature increase is negligible. However, in the high power condition the actuator back face peak temperature reaches 550 K, and application of ideal gas law predicts a reduction in cavity mass of 47% as compared to the same actuator at standard conditions. The expectation of these thermal loads on actuator performance is that at such high pulsing frequencies, impulse bit generation should be reduced by nearly half. When comparing temperature response of the six actuators under a 6 W load, maximum actuator back face steady-state temperatures ranged 360-390 K and were highest for the D actuator (small cavity diameter) and smallest for the d actuator (wider throat). The D actuator likely had the highest temperature because the small diameter cavity provides less surface area for thermal interaction. The d actuator likely had the lowest temperatures due to the wider throat which is favorable to refilling/cooling processes.

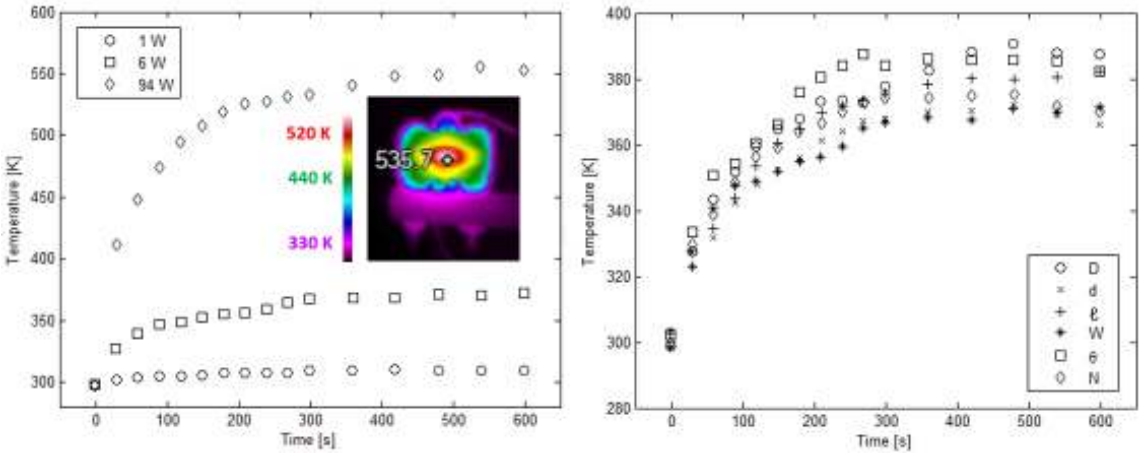

Figure 96. Back face temperatures ofthe (left) the V actuator at various thermal loads and (right) all actuators at 6 W input power.

Images of the *V* actuator after the thermal test are provided in Figure 97 (a)-(f). The actuator showed no indication of undue wear as a result of the high power input. Areas in close proximity to the electrodes, specifically in images (b) and (e), exhibit discoloration which is an indication of elevated temperature, but there is no damage to the structure. There was also no observed change in operation (i.e. breakdown voltage). Discoloration is believed to be due to evaporation of the electrode material during the pulsing, as can be expected (due to ion bombardment) this is more severe on the cathode biased electrode. The pin hole in the mica sheet appears to serve an additional benefit by confining some of the evaporated metal to the near electrode region and by preventing excessive coating of the cavity walls. To address similar issues in other microplasma systems we have used coatings of low evaporating (high melting point), non-oxidizing,

palladium or platinum-rhenium alloys on the electrodes to reduce this effect. Damage to the mica fastening holes is evident throughout but is not related to thermal stresses.

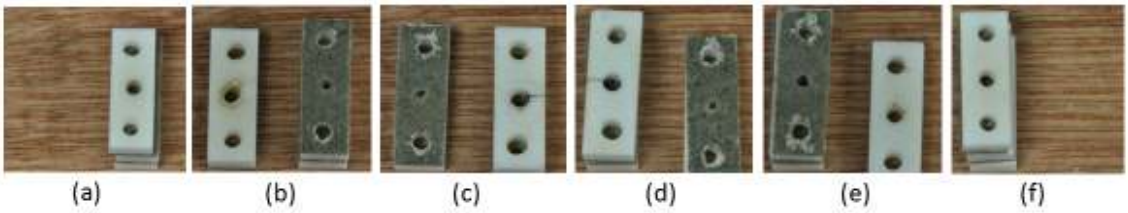

Figure 97. Actuator V components post thermal stress test. Areas in close proximity to the electrodes, specifically in images (b) and (e), exhibit signs of elevated temperature.

5.7 Measuring actuator jet velocity using shadowgraph

This section describes the experimental approach used to determine actuator jet velocity. Actuators were fired and emanating jets were visualized using shadowgraph techniques and captured using high speed imaging. Images were then analyzed to determine velocity of prominent features such as shocks and plumes. As predicted by CFD, a re-circulating flow pattern was observed at the end of the discharge cycle which simultaneously cools and refills the actuator cavity.

5.7.1 Flow visualization using shadowgraph/schlieren

Schlieren visualization is an optical technique that takes advantage of density gradients within a medium to image otherwise transparent phenomena. This phenomenon was formally acknowledged in the 16th century by Robert Hooke [120] as

he watched the stars, and then in the mid-1800s the phenomenon was used for quality control of large astronomical lenses [121]. In modern applications, this technique is often used in experiments to observe constituent species in a flow, shock waves, and thermal variations. Note that the flow fields in the aforementioned examples of imaging use all imply density gradients. A medium's index of refraction, *n*, is strongly related to its density, so as light passes through a medium of non-uniform density, individual light rays will deviate from their undisturbed paths by varying degrees. When projected on a screen or camera, the resulting image shows patterns of light and dark regions that correspond to density gradients in the flow field.

The refractive index of a material is defined as the ratio of the speed of light in a vacuum to the phase velocity of light in some medium, and it describes how much the light bends as it enters a new medium. Larger *n* means more refraction, and hence more deviation from the undisturbed path. Snell's law relates indices of refraction and angles of incidence at the interface of two mediums, and this relation is expressed in Equation 34 and shown graphically in Figure 98.

$$n_1 \sin\theta_1 = n_2 \sin\theta_2 \tag{34}$$

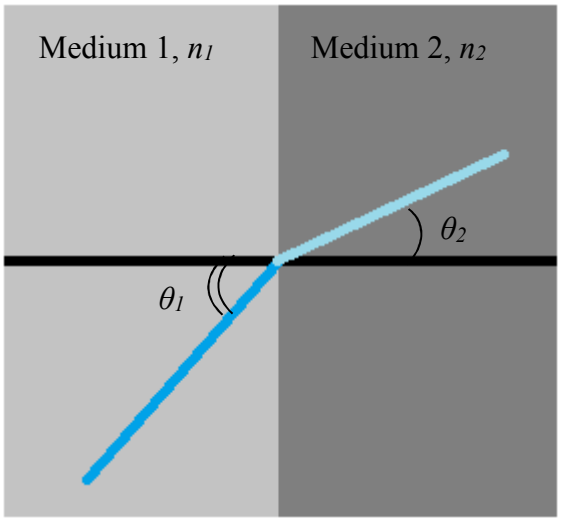

Figure 98. Graphical representation of Snell's Law. Medium 1 has index of refraction n_1 with the light beam is incident at θ_1, and medium 2 has index of refraction n_2 and the light enters at angle θ_2.

The index of refraction of a vacuum is defined as unity, and for most ordinary materials, n lies in the 1-2 range. Generally, n increases with density, but this is not always the case. In addition to density dependence, n is also a function of the wavelength (or frequency) of the incoming light. The result of the frequency dependence is the dispersion of polychromatic light such as when white light passes through a prism. Schlieren visualization systems all have the same basic components. Essential items for schlieren include a light source, components used to shape the light, a target to be viewed, an optical filter, and a screen or camera for viewing. Many different types of light sources can be used including arc lamps and lasers. The most important attribute of the light is that the rays passing through the test section be collimated. Lasers are inherently collimated, but usually the beam diameter is too small to serve as a test

section. Lens or mirrors can be used to reshape beams from a light source. If a laser is used as a light source, first the beam may need to be expanded such that the beam diameter is large enough to capture the interrogation region, and once the beam has undergone expansion, it must then be re-collimated. This process can be done using primary surface mirrors and/or lenses. The collimated beam is then passed through the test section where the light refracts according to optical density gradients. After passing through the test section the collimated beams and refracted beams are passed through another lens which focuses the light. The collimated beams concentrate at the focal point which the refracted beams do not pass through. An optical diaphragm (or knife edge) can be positioned directly at the focal point so that all refracted light, which is not focused at the focal point, is filtered. After the image is optically filtered, it is allowed to expand to fill an appropriate image plane. Images can be greatly enlarged and projected on a screen, or it may be desirable to enlarge the image only slightly so that it can be recorded by a camera. Design and fabrication of simple 2D schlieren systems can be found in the literature [122]. Modifications to schlieren system can be made to enhance focusing [123], increase sensitivity [124], add color [125], and interrogate 3D targets [126]. The image in Figure 99 shows a colorized schlieren image of a hot soldering iron in air. In this instance density gradients are the result of thermal variations.

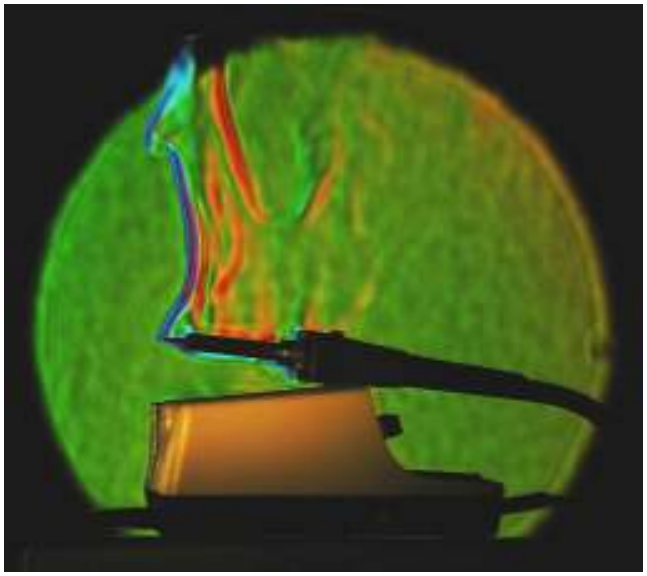

Figure 99. Schlieren image of a hot soldering iron. Visible patterns are due to density gradients arising from thermal variations. [Image from: https://en.wikipedia.org/wiki/Stealth_aircraft]

5.7.2 Experimental setup

Two actuators, one with $AR = 0.5$ and the other with $AR = 1.0$, were fabricated from MACOR ceramic bar stock. Rectangular slices of 5 mm thickness were cut from the bar stock and then material was removed to accommodate the actuator cavity and throat. Pictures of the actuators are provided in Figure 90 and dimensions are specified. The open sides of the cavity and throat were sealed with a mica sheet that had a hole with diameter of 1.2 mm on the axis of the cavity. Copper tape covering these holes was used as the electrode with electrical connections soldered to the tape. The holes in the mica served to control the diameter and position of the plasma discharge in the actuator cavity.

The actuator was pulsed by a high voltage DC power supply which charged a capacitive element through a 20 MΩ ballast resistor. Waveforms and circuit diagram are shown in Figure 100. Voltage and current signals were acquired using a NorthStar PVM-4 voltage probe and a Pearson M#5046 current monitor, respectively. Both signals were logged by a LeCroy 204MXi Waverunner oscilloscope. The high resistance isolates the power supply from the discharge process and simplifies analysis of the energy input. The actuator was connected in parallel to the capacitor, and capacitances of 1 nF and 0.33 nF were used to control energy input to the discharge. Since electrode spacing and initial cavity pressure were fixed conditions, breakdown voltage in the cavity was roughly constant at 8 kV. This combination of capacitors and breakdown voltage allowed testing the actuator with capacitively stored energies of 32 and 11 mJ, as determined using the relation $E = \frac{1}{2}C\mathrm{V}^2$, where E is the stored energy, C is capacitance and V is breakdown voltage. Actuator pulsing frequency was controlled by varying the power supply current and using an oscilloscope to monitor pulsing. Pulsing frequencies of 10 Hz and 500 Hz were tested. A summary of the test conditions is provided in Table 19.

Table 19. Actuator condition matrix for shadowgraph experiments.

Case	Actuator AR	Energy [mJ/pulse]	Frequency [Hz]
1	1.0	3.5	6
2	1.0	3.5	460
3	1.0	1.2	18
4	0.5	3.5	4

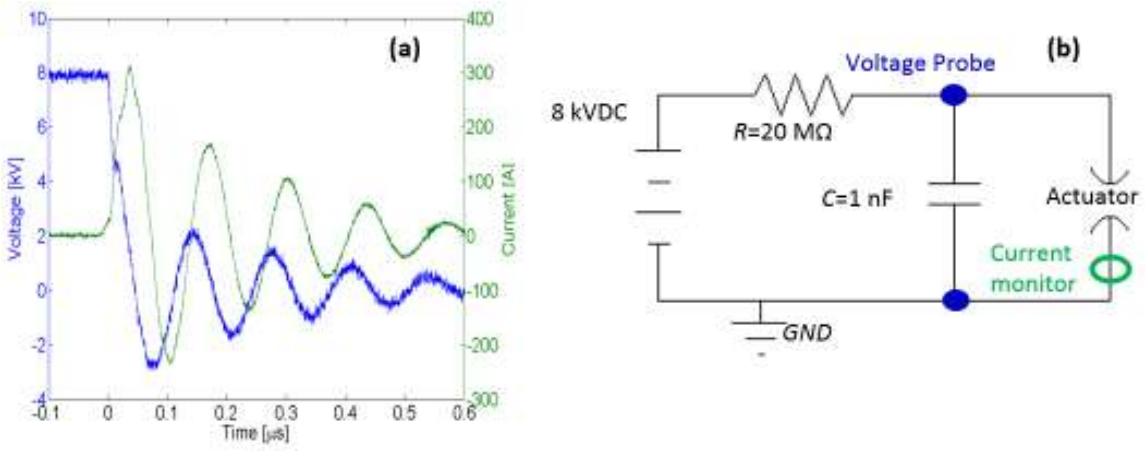

Figure 100. (a)Voltage and current waveforms. (b) Pulsing RC circuit used to drive plasma actuator. An 8 kVDC source charges a capacitor through a 20 MΩ ballast resistor. Capacitances of 1 and 0.33 nF were tested. Energy stored in the capacitor is discharged upon breakdown in the actuator, represented schematically as a spark gap.

Synthetic jets from the plasma actuator were visualized using the schlieren setup shown in Figure 101. A 300 mW diode laser with wavelength centered about 540 nm was used as the light source. Approximately 4% of the beam intensity was directed to the test section. The laser beam is reflected from both the front and the back face of the glass, so it was necessary to use a knife edge to clip one of the beams. The beam was expanded to a diameter of 22.4 mm and then re-collimated. This wider diameter collimated portion of the beam comprised the test section. After passing through the test section, the beam was focused and filtered using an iris diaphragm. The image was recorded using a high speed video camera capable of recording 525,000 fps with resolution of 128 x 48 pixels which corresponds to physical dimensions of 5.75 x 2.16 mm in this setup.

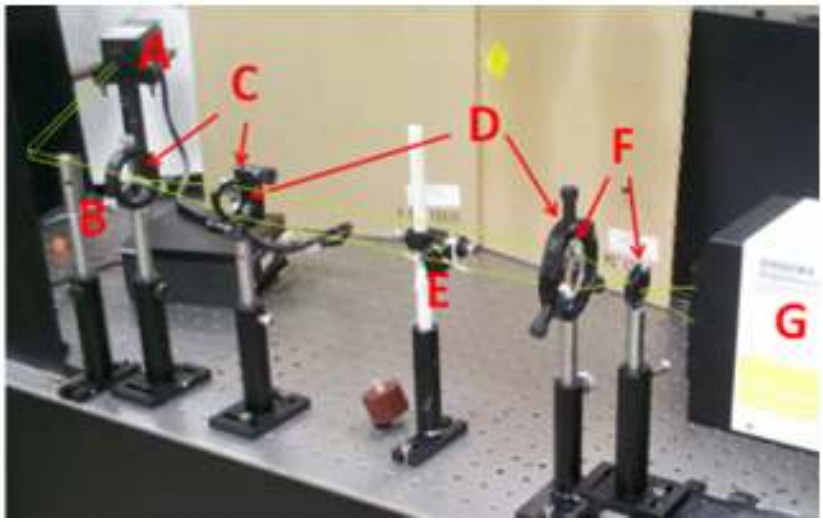

Figure 101. Schlieren setup for measuring actuator jet velocity. A) laser, B) beam obstruction, C) beam expansion and collimation, D) collimated test section, E) actuator, F) focal section with iris diaphragm and filter, G) camera.

5.7.3 Results and discussion of jet velocity experiments

A series of images from Case 1 is shown in Figure 102. The jet is formed shortly after breakdown when the air is rapidly heated in a near constant volume process causing a sudden pressure rise. The times shown in the figure are in reference to breakdown which is visible in the videos. After the plasma discharge, a shock wave, indicated at t = 4 μs, propagates down the length of the slot and expands upon exiting. Shortly thereafter, the high temperature high pressure air escapes, forming the primary jet which extends up to 2 mm beyond the throat exit plane. As gas escapes the flow switches from initially pressure driven to quasi-steady secondary mass flux (Region 2 in Figure 83) which is observed well after the initial jet as a sustained flow for 5-20 μs in some geometries. The oscillating flow associated with cavity refilling is then observed near the

exit at $t \sim 50$ μs. The intensity of this secondary flow was geometry dependent, being more prevalent at smaller AR. During the refilling and cooling process at $t > 300$ μs, weaker oscillations similar to those predicted by the modeling can sometimes be seen. Under the conditions investigated, the ejection/refilling process required less than 1 ms, which is comparable to the model.

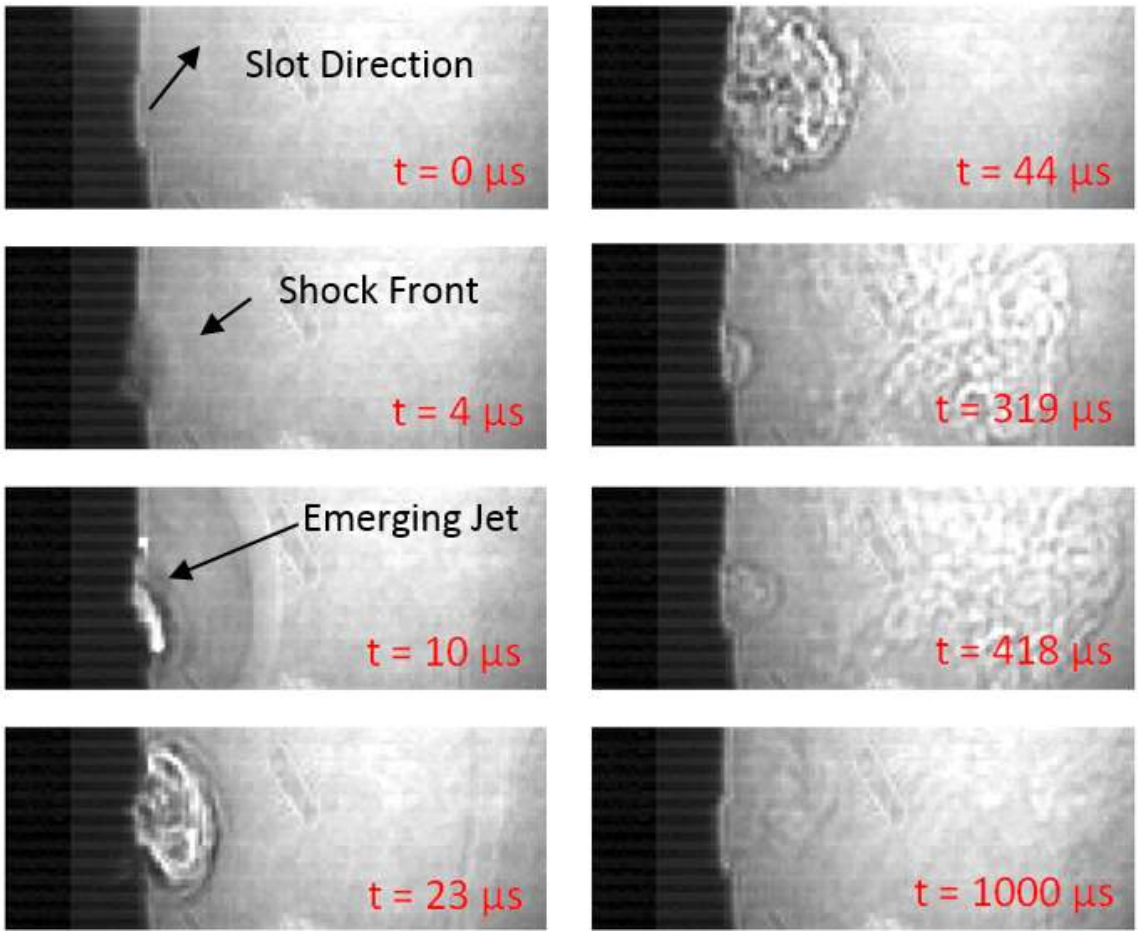

Figure 102. Annotated evolution of typical actuator jet from plasma initiation to quiescence. Observable features include shock front, primary actuator jet, and secondary buoyancy driven flow.

Figure 103 shows a series of images comparing the four experimental cases. Shock and jet positions are plotted in Figure 104 where time t=0 μs corresponds to discharge initiation and distance x=0 mm corresponds to the jet exit plane, with positive distance values in the direction of the expanding jet. The shock front and primary jet edge as shown in Figure 102 were used to determine average shock velocity, instantaneous jet velocity and average initial jet velocity from the images. Online supplemental material contains videos of the jets. Images collected at t > 40 μs were not used to determine characteristic velocities but are included in Figure 103 to show a return to a near quiescent state. Shock velocity was determined by measuring the radial shock expansion at two points in time – the first of these pairing is when the shock front first protrudes and the last was when the shock front approached the edge of the field of view. The instantaneous velocity of the jet was calculated by measuring the jet front displacement along the direction of the actuator throat between two subsequent video frames. The first frame was chosen as the one where the jet is first clearly observed to cross the throat exit plane. Time between images is 1.9 μs. Average jet velocity is determined from first and last observations of the jet. Velocity data is summarized in Table 20 and qualitative descriptions of the jets follow. In general, cases 1 & 4 and 2 & 3 were similar with respect to jet average velocity magnitude. Qualitatively, cases 2 & 3 were still similar, but cases 1 & 4 showed different shock and flow structures.

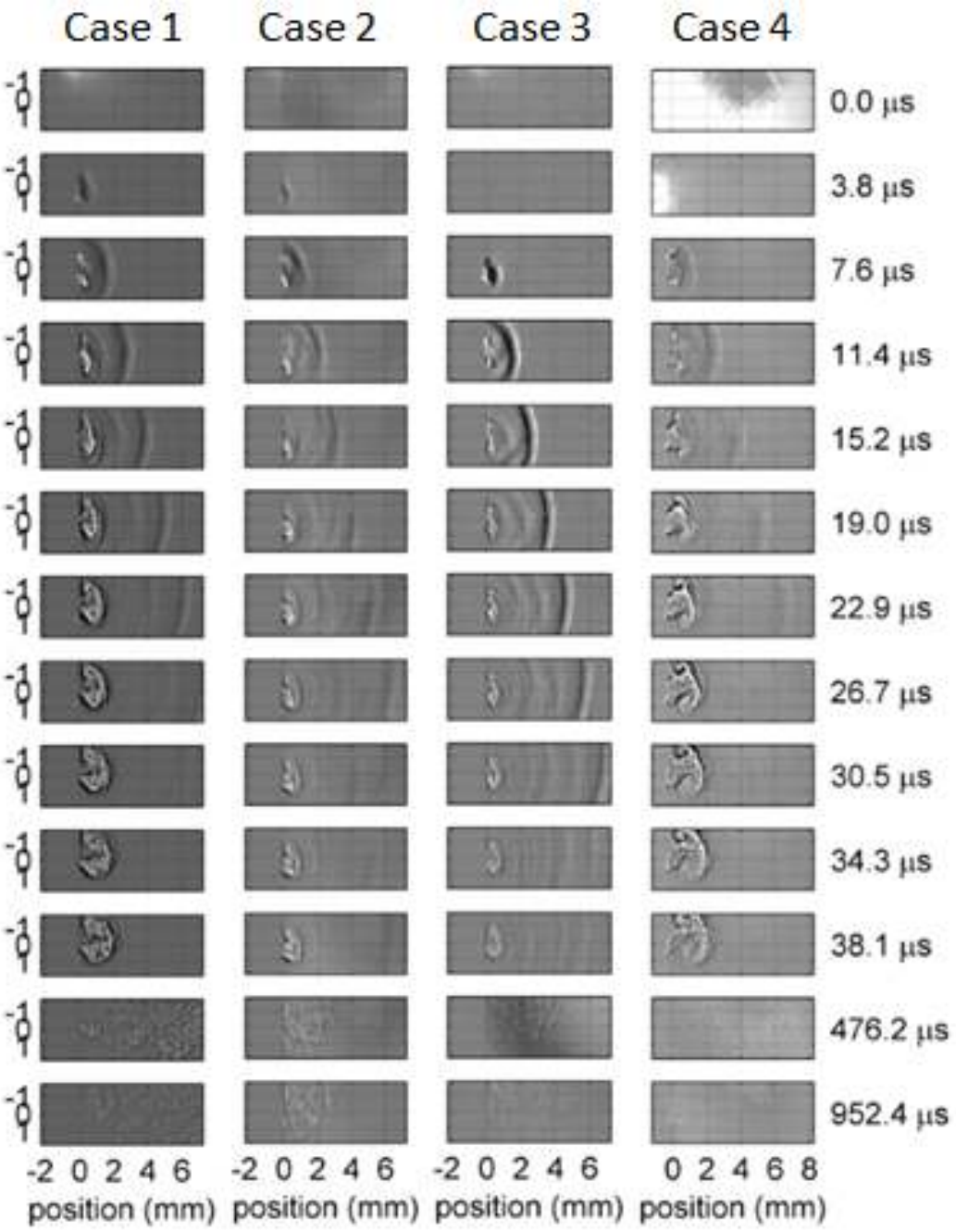

Figure 103. Comparison of actuator jet behavior for four experimental cases.

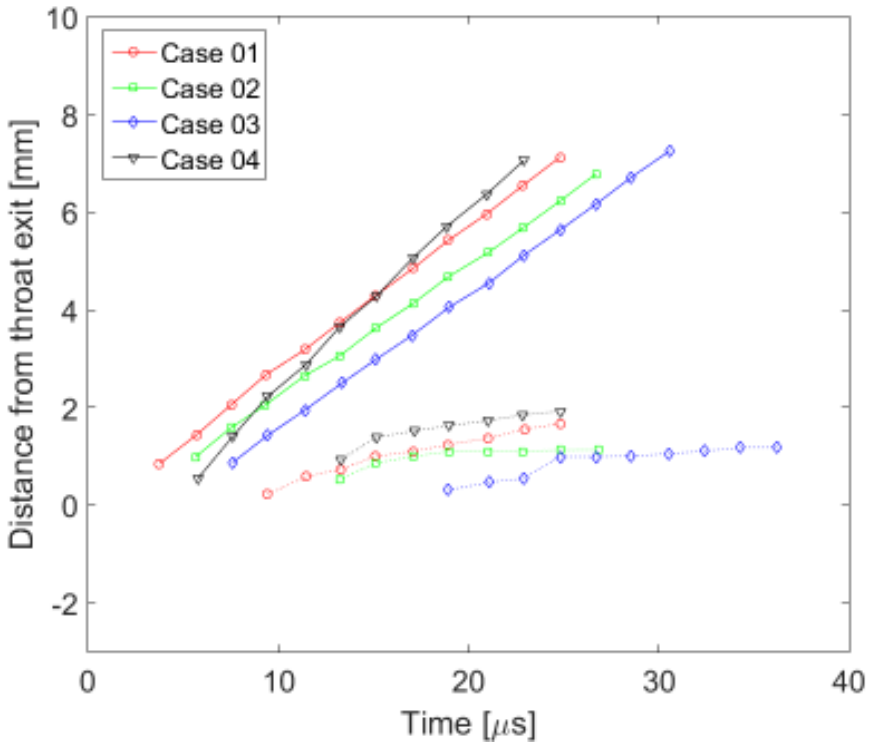

Figure 104. Displacements of characteristic jet features from the throat exit for Cases 1-4. Data is summarized in Table 20.

Table 20. Summary of actuator characteristic velocity data shown in Figure 104. See Table 19 for case descriptions.

	SHOCK		JET		e_{in}
Case	U_{max} [m/s]	U_{avg} [m/s]	U_{max} [m/s]	U_{avg} [m/s]	[MJ/kg]
1	320	300	180	95	0.91
2	330	275	190	45	0.91
3	300	280	230	50	0.91
4	460	380	230	85	0.55

The overall behavior of the jets is comparable to that predicted by the model.

Case 1 is used as a basis of comparison. Multiple shocks are noticed in Case 1-3 with a

strong initial shock because shocks do not dampen within the cavity. Also characteristic of large *AR* actuators observed in both modeling and experimentation is the fact that the secondary mass flux is weak. Case 2 corresponds to high frequency discharge, and the shock structure is similar to that observed in Case 1 but weaker. The jet in Case 2 is also not as strong as it is in Case 1 because there is likely less mass in the cavity due to elevated temperatures and lower density caused by greater input power. In Case 3 less energy (33% of Case 1) was supplied to the actuator by reducing circuit capacitance. Due to the lower energy input, weaker jets were generated, yet shock structure remains similar to Case 1. In Case 4 the shock structure is less prominent and there are fewer reflected shocks because they are trapped within the cavity where they contribute to higher pressure and extended secondary mass flux. The jet in Case 4 remains coherent for ~20 μs due to nozzleing by the restricted throat. These qualitative observations are in good agreement with the computational model. Specifically, high *AR* produces a stronger primary mass flux and weaker secondary fluxes. Conversely, the smaller *AR* jet produces a weaker primary mass flux and a more sustained more directed secondary flux. Jets from cases 1 & 4 show that they are able to sustain themselves for longer than the case 2 & 3 jets which initially have high velocity, but quickly slow. This behavior is most noticeable in Figure 104. The reason jets from case 1 & 4 are not tracked after ~25 μs is because the jets had expanded beyond the field of view. The mushroom cap shape of the head of the jet and the vortex rings around the emerging plume are visible in Case 4 and are similar to those of lower *AR* predicted by the modeling and also often observed in laminar starting plumes [127] [128].

5.8 Measuring momentum and thrust

Six actuators were tested on a torsional thrust stand to assess momentum and thrust generation of the actuators. The actuators varied with respect to their geometry exploring cavity diameter, cavity width, throat length, throat width, and throat angle. These conditions have been summarized in Table 18 in the actuator fabrication section. The thrust stand uses optical techniques (tracking a reflected laser beam) to determine deflection angles, so this aspect of the setup is free from electrical noise. The beam is reflected off of a mirror mounted to the thrust stand and is projected on a screen approximately 5 meters away from the thrust stand. The 5 meter working distance effectively amplifies angular displacements in the torsion stand since laser beam displacement increases with working distance for a given angular displacement. Additional amplification was achieved by orienting the projection screen at an angle ~60° off normal with respect to the laser beam. The thrust stand is capable of accurately detecting angular displacements of 0.003° which corresponds to an impulse bit of less than 5 μN-s in this system.

5.8.1 Thrust stand background

Thrust stands are often used to experimentally measure forces generated by jets/rockets and are essential in the fields of propulsion and aerodynamics. The basic principle behind this testing method is momentum conservation as described by Newton's third law which states that for every action there is equal and opposite reaction. Therefore, the reaction force from a jet secured to a stationary structure will be

countered by a restoring force in the structure which is equal in magnitude but opposite in direction, and these forces can be acting in either translational or rotational frames of reference. Recently, much work has been devoted to investigating μN thrust forces from solid propellant (continuous) thrusters [129], pulsed plasma thrusters [130] [131] and plasma actuators [81] [132]. Experimental techniques have been developed that are capable of resolving sub-μN thrusts at both high [133] and low [134] Knudsen numbers. Transducers are widely used in data acquisition, but due to the significant effects EMI has on signal to noise ratio, transducers are far from ideal when paired with systems pulsing high currents. Optical techniques [134] [[135] are an attractive alternative to this limitation. The thrust/momentum measurements in this section are similar to these optical techniques.

5.8.2 Experimental setup

The six new actuators, shown in Figure 93 were fabricated using similar techniques as those discussed earlier. Major differences in geometry for corresponding actuators were cavity diameter (D), throat length (ℓ), cavity width (W), throat width (d) and throat angle (θ), in comparison to the vanilla case, (V). Aspect ratios for all six actuators were in the 0.1-0.2 range. Relevant dimensions of all actuators are provided in Table 18.

An assembled actuator during discharge is shown in Figure 91. The MACOR cavity slices shown in Figure 93 are sealed with mica strips and a fastening slice on both sides. The mica strips had ~1 mm holes on the cavity axis to control discharge position

and diameter. The fastening slices had three holes. The center hole was tapped such that brass screws could be used for electrodes and the other two holes were through holes used to secure the fastening slices to the cavity slice. Assembled actuators had mass of 2.5 g except for the W actuator which had a mass of 3.5 g. The electrical connections shown in Figure 91 depict the use of heavy gauge high voltage wire, but when the actuators were mounted to the thrust stand electrical connections were made using 50 μm diameter silver wire so as to not impede thrust stand rotation by introducing unwanted spring stiffness. Longer fastening screws were used to mount the actuator to the thrust stand.

A picture of the thrust stand and a schematic of its operation is shown in Figure 105. As is, the torsion balance can resolve impulse bit of <1 μN-s. The thrust stand was made of an acrylic bar with dimensions 0.16 x 0.025 x 0.006 m. A hole was drilled in the center of the acrylic strip and a C-Flex model D-10 precision bearing with spring constant k_s =0.0117 N-m/rad was inserted. The other end of the spring was secured to a garolite post. The actuator was mounted on one end of the acrylic bar using the actuator fastening screws, and a small mirror with negligible mass was mounted on the opposite side of the acrylic strip. A small diameter plastic rod was suspended from the actuator side of the torsion arm, and the bottom portion of the rod was submerged in mineral oil so that unwanted oscillations were damped. The immersion depth of the damping rod was adjusted to damp frequencies higher than the torsion arm. A laser was reflected off the mirror and then focused by a lens near a viewing screen some 5 m away. Because of the small displacements involved, the lens had minimal interference on laser position.

The viewing screen was oriented such that the reflected beam was incident at an angle ~60° off normal. The viewing screen distance from the thrust stand and its shallow angle both served to amplify laser spot displacement. A camera with a macro lens imaged the viewing screen and recorded video at 24 fps during testing. The thrust stand was calibrated by using a micrometer to rotate the system through a known angular deflection and the corresponding laser spot displacement was captured in still images with the digital camera. This is shown in Figure 106. A grid with 5 mm spacing was placed on the viewing screen and used for image scaling. A sample calibration curve is shown in Figure 107. The system was re-calibrated prior to testing each actuator.

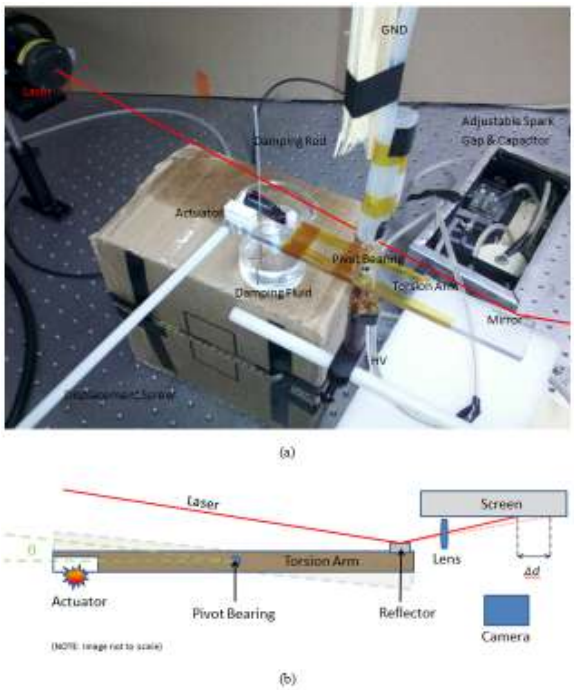

Figure 105. Annotated experimental setup. (a) laser to torsion arm (b) torsion arm to viewing screen.

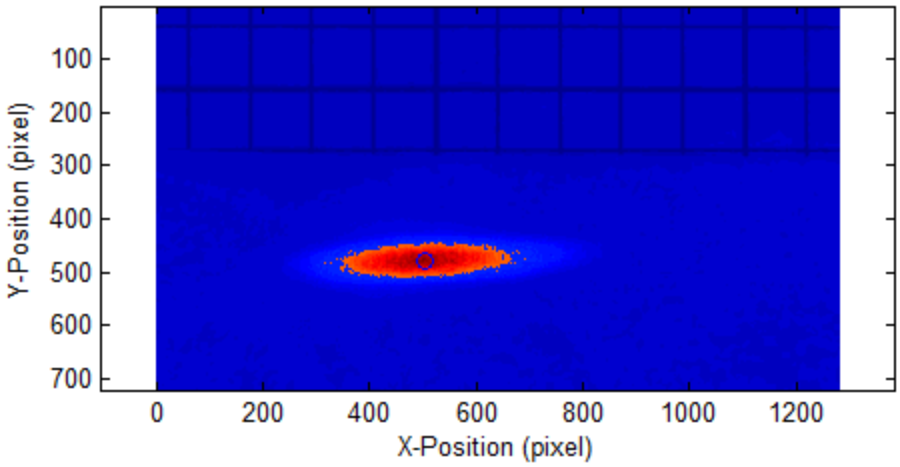

Figure 106. Data collection of momentum experiments. (top) image of laser spot on viewing screen.

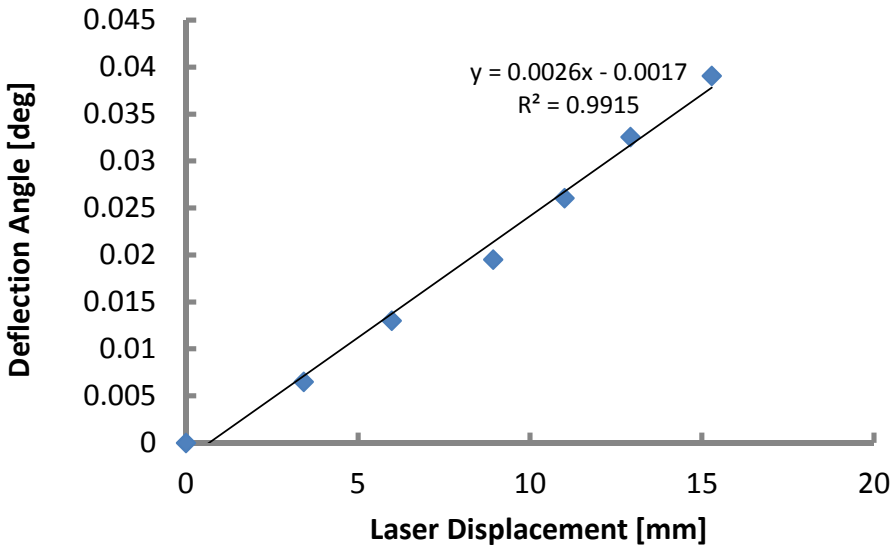

Figure 107. Sample calibration plot of torsion arm angular displacement as function of laser spot displacement. Calibration is taken from V actuator.

Actuators were powered by a circuit similar to that shown in Figure 108 but with addition of high voltage switch (spark gap type) so that 1) input energy was constant and 2) charge would not accumulate on the torsion arm and cause unintended deflection. A 15 kVDC current limited source trickle charged a 2 nF capacitor through a 3 MΩ ballast resistor so that single pulses could be more easily obtained. The actuator and switch were both connected in series and in parallel with the capacitor. The switch was necessary due to induced charges on the thrust stand causing unwanted rotation/drift. Without the corona wind switch, the laser spot was observed drifting to one side as the capacitor charged but prior to discharge within the actuator cavity. Electrical connections to the actuator were made using 50 μm diameter silver wire which was secured to the torsion arm with Kapton tape in a way such that the silver wire did not contribute to spring stiffness.

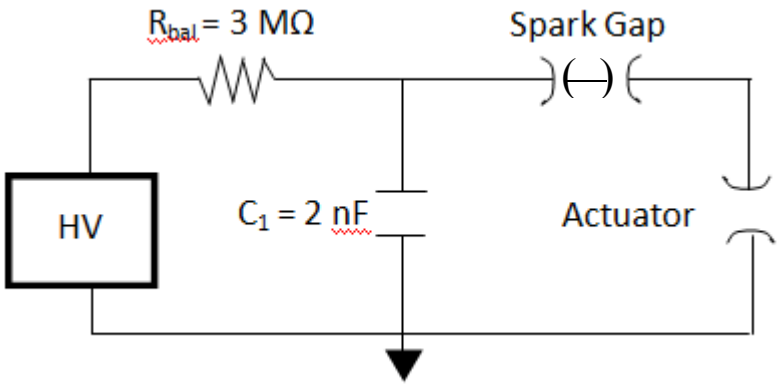

Figure 108. Pulsing circuit for momentum testing.

During testing, the pulsing circuit was charged very slowly with the supplied voltage set at 15 kV and gave an energy input of 225 mJ. This was over-voltaged for all but the W actuator due to differences in electrode spacing and helped maintain equal discharge energy input between actuators. Slow charging was necessary so that only one discharge would occur as rapid subsequent firings obfuscate the desired dynamics. Each of the six actuators (V, D, d, ℓ, W, θ) was tested and analyzed in this way.

5.8.3 Results and discussion

Post-processed video data from thrust stand measurements are shown in Figure 109 where angular displacement is determined from a particular calibration of laser spot lateral motion tracked by an algorithm. Image scaling (60 μm/pxl) and video frame rate (24 fps) were used to convert raw data to displacements and times. Figure 109 shows that prior to the actuator firing the torsion arm is mostly stable. Firings of the actuator are seen at $t = 2.5$ s and then again at $t = 3.9$ s when an unintended discharge occurs. When the actuator fires the torsion arm undergoes angular displacement and then continues to oscillate with natural frequency $9.4 < \omega_n < 12.6$ rad s^{-1}. All actuator showed a natural frequency within this range. Calibration curves were used to convert laser spot displacement to angular displacements and velocities. Dampening of the oscillations is observed and expected.

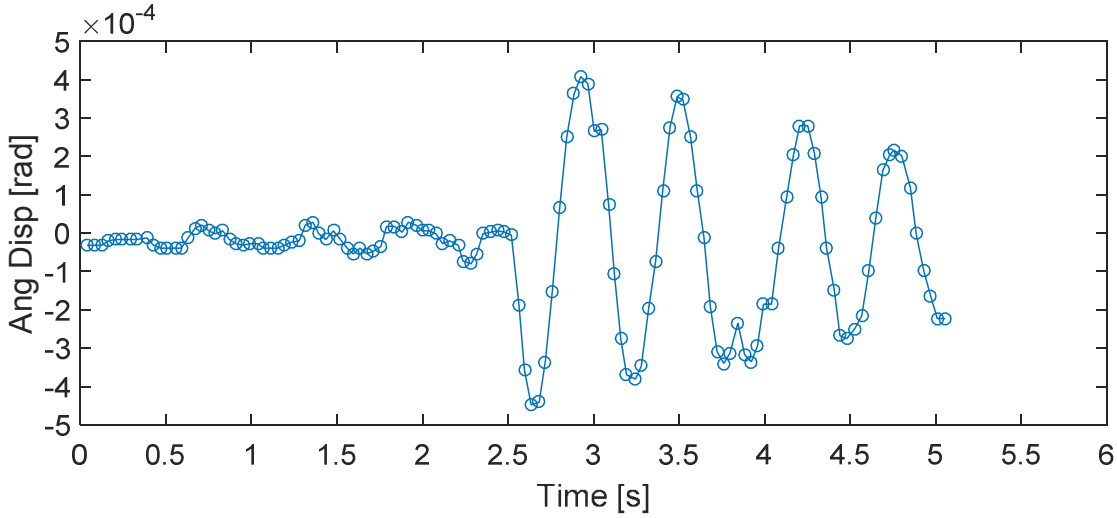

Figure 109. Post-processed data showing angular oscillations of V actuator. The pulse of interest occurs at $t = 2.6$ s, and a second unintended pulse is apparent around $t = 4$ s.

The following analysis has been previously described in the literature [130]. Impulse bit generated by the actuator is calculated using Equation 36 below

$$p = (mv) = \frac{\theta_r k_s}{\omega_n R} \tag{36}$$

where, p is momentum, m is mass, v is velocity, θ_r is the maximum angular deflection, k_s is the torsion spring constant, ω_n is the natural frequency, and R is half the length of the torsion arm. Calculated impulse bits ranged from 1.5-9.8 μN-s with the W actuator exhibiting the largest impulse bit and the θ actuator the least. The loaded torsion arm moment of inertia was approximated using Equation 37

$$I_L = \sum r_i^2 m_i \tag{37}$$

where, r_i is the radial position of the i^{th} element and m_i is the mass associated with that element. For the W actuator I_L = 91 mg m^2 and for the other actuators I_L = 86 mg m^2. Moment of inertia can then be checked by comparing observed natural frequency to that calculated using Equation 38.

$$\omega_n = \sqrt{\frac{k_s}{I_L}} \tag{38}$$

The calculated natural frequency was $\omega_n \approx 11.3$ rad s^{-1} which is in good agreement with observation and gives confidence to accuracy of the natural frequency.

A thermal-fluids analysis, which assumes a choked ($P_{cav} > 1.9P_{amb}$) isentropic jet issuing from an adiabatic cavity, as outlined by Grossman, Cybyk and VanWie [86] is used to estimate the mass flow rate, $\dot{m}_{chkd}$, and duration of ejection, Δt_{chkd}. Mass flow rates remained nearly constant across all actuators at 2 g s^{-1} lasting for several μs. From these quantities time averaged jet velocities, V_{avg}, and ejected mass fractions, X, can be estimated. The actual duration of ejection is somewhat longer since the jet eventually reaches unchoked conditions, but most of the mass ejection should occur while the actuator operates under choked flow conditions. Characterization of actuators' jet performance is summarized in Table 21 and actuator comparisons follow.

Table 21. Summarized actuator performance. The last two rows compare momentum and cavity air mass to that of V actuator. E_{in} = 225 mJ.

ACTUATOR	W	D	V	d	ℓ	θ
Δx [mm]	13.8	9.5	8.4	5.8	4.0	2.7
θ_r [rad]	7.8e-4	5.7e-4	3.5e-4	3.6e-4	1.7e-4	1.2e-4
Δt [s]	0.17	0.17	0.17	0.13	0.13	0.13
ω [rad/s]	4.7e-3	3.4e-3	2.2e-6	2.9e-3	1.4e-4	9.8e-3
(mv) [μN-s]	9.8	7.1	4.4	4.5	2.1	1.5
m_{act} [kg]	2.6e-8	6.0e-9	1.4e-8	1.5e-8	1.3e-8	1.4e-8
$\dot{m}_{chkd}$ [kg/s]	2e-3	2.4e-3	1.4e-3	2.8e-3	1.4e-3	1.4e-3
Δt_{chkd} [μs]	6e-6	1.6e-6	5.4e-6	2.7e-6	5.4e-6	5.4e-6
X [%]	0.47	0.61	0.57	0.51	0.60	0.55
V_{jet} [m/s]	360	1060	290	365	200	130
$(mv)/(mv)_V$	2.35	1.63	1.00	1.36	0.64	0.47
m/m_V	1.89	0.45	1.00	1.08	0.95	1.03

The impulse bit generated by the actuators ranges from 1.5 – 9.8 μN-s with actuators W and θ providing the most and least momentum, respectively. For the θ actuator momentum is the perpendicular component as mentioned previously. Impulse bit generation is compared between actuators. Uncertainties based upon the statistics of multiple measurements are generally less than 15%. With the exception of the D actuator, the jet velocities determined in Table 21 show good agreement (within factor of ~2) with jet velocities discussed in the literature [112] [101],predicted by computation model in section 5.4 (at similar *AR*), and those observed and presented in Table 20. Actuator D on the other hand, indicates relatively large velocities as compared to the other actuators when subjected to similar analysis.

- ***Comparing W to V:*** *W* has longer inter-electrode spacing and cavity length. *W* provides larger momentum and this is likely related to its larger cavities which

contain more air and hence more mass is able to be ejected upon actuation. Although the flow is choked, mass flow can increase and this is beneficial for momentum generation. Since the specific energy input in *W* is lower compared to other actuators the expected temperature is lower, but the pressure rise is still substantial enough to achieve a choked flow condition. The lower temperature and larger size of the actuator may help it operate at higher pulse frequencies by more rapid rejection of excess heat. An adiabatic, isentropic actuator would behave oppositely with increased specific power input. This indicates that heat loss, is a large inefficiency in high *E/V* actuators.

- ***Comparing D to V:*** *D* has a smaller cavity and higher aspect ratio (0.167 vs. 0.1), but calculations predict ejection of the largest mass fraction. The high velocity could be the result of an underestimate in the ejected mass fraction. Since the cavity is small, thermal energy may be more confined to the region as it has less surface area to participate in convective processes. This could help maintain higher pressures for longer which would ultimately reject more mass. However, continuous pulsing may indicate reduced performance because of this thermal entrapment, which would result in reduced mass filling the cavity because of warmer temperatures. The higher aspect ratio also likely improves performance.
- ***Comparing d to V:*** *d* has a wider actuator slot which facilitates mass ejection and reclamation thus increasing bandwidth of operation. Its aspect ratio (*AR* = 0.2) is slightly closer to optimum as determined from computational modeling

described previously. Based upon the percent change in performance relative to the percent change in mass both these effects appear to contribute to a slightly better performance than the nominal case.

- ***Comparing ℓ to V:*** ℓ has a 57% shorter throat length. The air mass in the cavity is the same as the V actuator, but the total air mass in the actuator is less so it is not immediately clear if specific energy input differences are significant. However, because the throat is shorter, thermal dissipation may be more rapid and reduce pressures and therefore ejected mass fractions. This may be the source of the performance decrease. In the computational modeling a smaller throat causes more spread in the ejected jet (due to less flow alignment along the throat) the threshold for this effect is unclear and typically only occurs at very short throats in modeling. This may also help explain the reduction in performance.
- ***Comparing θ to V:*** θ has a slot at a 45^{o} angle and also a 36% longer slot. Data from Table 21 give the perpendicular component of the momentum, so the true jet momentum is somewhat greater. Taking this into account, the jet actually has velocity of 190 m/s which is closer to the velocities of the other actuators. Some performance loss can be attributed to jet misalignment with the tangent vector. In computational modeling longer throats also decreased performance due to increased viscous losses along the throat (particularly for low aspect ratio throats like this one).

5.9 Wind tunnel testing

A wind tunnel was assembled for testing airfoil performance. The wind tunnel was not characterized and was used 'as is.' Motivation for wind tunnel testing was to ensure that unpowered actuators installed on an airfoil surface did not significantly affect lift and drag as compared to similar airfoils operating at or near the same *Re*. Flow visualization was used to qualitatively assess local boundary layer attachment. Additional tests were performed to characterize the impact of actuation on a mildly stalled airfoil.

5.9.1 Wind tunnel design

Wind tunnels are often used in aerodynamics to investigate forces acting on objects surrounded by a moving fluid and have been in use since the late 1800s. The goal of wind tunnel testing is to simulate flow patterns of full-scale test objects, and the primary forces of interest are lift and drag which result from the pressure distribution on the surface of test objects which can range in scope from aircraft to skyscrapers. The application under investigation dictate the flow velocity required of the wind tunnel. Some objects are designed for use a very high speeds where Ma > 1, but most applications, including those that are the topic of this research, are subsonic and Ma < 1. Because only low-speed testing is performed in this research, subsequent discussion will be limited to sub-sonic wind tunnel design.

Low speed wind tunnel design is thoroughly described in the literature [136] [137], but essential considerations are discussed here. By design, the flow in a wind

tunnel may follow either an open-circuit or return-circuit, but essential components are mostly similar. Air flow is generated either by pushing or pulling the air through the tunnel. In the pushing type wind tunnels, fans are located at the inlet, whereas the pulling type have fans located near the exit. For a pulling open-loop system, such as the one used in this research, air is pulled through a large cross-section inlet fitted with honeycomb mesh and a series of progressively finer screens. The honeycomb is used to straighten the flow while the screen are used to reduce spatial velocity variations by producing local total pressure drops proportional to local velocities. Honeycombs will effectively reduce swirl at the inlet if the length of the honeycomb is at least 6 cell diameters long and the incidence of incoming air does not exceed 10°. Screens reduce turbulent fluctuations, and multiple screens can be used to achieve greater reductions provided that the screens are separated by a distance of at least 500 wire diameters, which is the approximate spacing required for the decay of upstream turbulent wakes. Next, the flow is accelerated through a contracting section. The mean velocity in this section increases, but mean and fluctuating velocity variations are reduced to a smaller percentage. These sections are difficult to design since finite length contractors will have regions of adverse velocity gradient and the flow may detach from the walls and secondary flow patterns can develop in the boundary layer near the corners when rectangular contractors are used. Very often the boundary layer in a contractor will become turbulent, but a rapidly converging section will reduce the boundary layer thickness enough so that it becomes laminar. After the flow is nozzled it enters the test section where the object under investigation is mounted. This section usually contains

the bulk of the instrumentation, and therefore any penetration in the test section wall must be made so that it has minimal influence on the flow. In low-speed testing it is crucial to maintain dynamic similarity, and practically speaking this corresponds to matching Reynolds the number of the model to that of full-scale application. A diffuser is located downstream of the test section, although the shape of the diffuser is not critically important, there are arguments for maintaining divergence angles less than 5 degrees. In pulling type wind tunnels, a fan powered by a motor is located beyond the diffuser, and it ejects air to the environment through another diffuser in the case of open-circuit wind tunnels. The motor should be powerful enough to produce the desired velocities, and variable speeds can be achieved by using variable frequency drives, DC motors, or by adjusting the pitch of the fan blades. Fans are commonly equipped with a set of stators that will counter swirl induced by the rotors, and special consideration should be given to these primary air movers since flow through the fan will affect upstream flow, potentially including the test section, since fluid velocities are sub-sonic. For this reason it is important that the exit of the wind tunnel be free from obstruction. Additionally, rotating machinery should not impart excessive vibration to the wind tunnel structure itself. A good first check of wind tunnel performance is to compare actual and predicted test section velocities. A more detailed characterization of wind tunnel performance can be made using hotwire anemometry to determine the velocity components throughout the test section. While more complicated, this later approach gives a much more useful description of wind tunnel behavior.

5.9.2 Airfoil fabrication

Three airfoils were fabricated using basic manufacturing techniques consisting of foam core with fiberglass shells. The fabrication sequences are illustrated in Figure 110 & Figure 111. Foam stock is used (Figure 110-1) for the core of the airfoil. Airfoil cross sections for a NACA 0012 airfoil are plotted using CAD programs and transferred to two aluminum cross section templates (Figure 110-2). A hotwire cutter (Figure 110-3) is used to cut out the airfoil section from the foam (Figure 110-4). Epoxy resin, hardener and fiberglass (Figure 111-1) is used in two coats to form a durable surface finish on the airfoil (Figure 111-2). Prior to the fiber glass coating an aluminum mounting plate is placed in the foam and used to attach the wing to the AoA adjustment hinge. The wing is cut to a span of 0.58 m so that it does not touch the test section walls. The ends of the airfoil are about 6 mm from the test section walls. Having the airfoil ends near the test section walls reduces downwash effects that can influence the effective angle of attack resulting in misleading data. Three NACA 0012 airfoils were made with chords of 0.30 m and spans of 0.58 m, 0.59 m, and 0.10 m span. These airfoils are given labels A, B, and C respectively. Due to its narrow shape and imperfections with a test section modification, the 0.10 m span airfoil experienced significant end effects such as downwash and was only used to test out fabrication, actuator mounting and actuator wiring methods. A fourth 0012 airfoil was made with similar chord but with a span of 0.18 m.

Figure 110. Shaping the airfoil - sequence of fabrication images showing: 1) initial form, 2) airfoil forms, 3) hot wire cutting, and 4) cut foam airfoil.

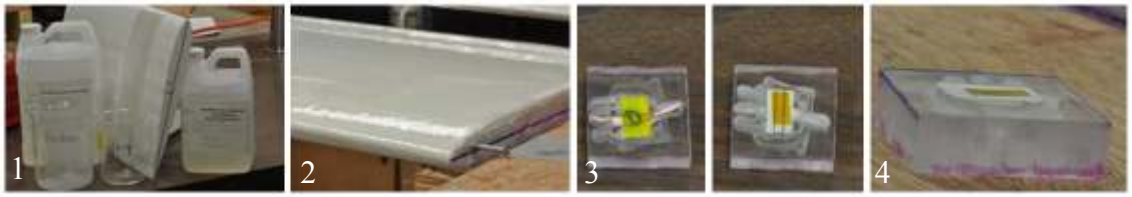

Figure 111. Airfoil fiber-glassing and actuator implanting - sequence of fabrication images showing: 1) fiberglass and epoxy application, 2) fiberglass coated airfoil, 3) bottom of actuator mounted in acrylic substrate, 4) top of actuator mounted in acrylic substrate.

The actuators (detailed in previous reports) were mounted into the airfoils using an acrylic substrate as shown in Figure 111 3-5. The acrylic substrate is a 4 cm x 4 cm x 1.3 cm rectangular prism with a milled out port for the actuator face and milled out recesses for the actuator screws and lead wires. The actuator is placed in the substrate with the wetted faces flush, and joint compound is used to encase the actuator (Figure 111-5). Once dry the joint compound is amenable to sanding and is sufficiently electrically insulating. Initially one actuator embedded in an acrylic substrate was mounted into airfoil C (s = 0.10), and then three actuator/substrate units were mounted into airfoil B as shown in Figure 112 and Figure 113. In airfoil B the

actuators were arbitrarily placed at location of 25%, 50%, and 75% of span. The embedded actuator is inserted into the wing by cutting into the fiberglass and foam stock and sealing the joints with drywall compound. A spanwise hole is bored in the foam stock at the actuator x/c for electrical connections. High voltage and ground connections are made at penetrations in the fiberglass near the sting mount. Electrical connections run along the bored hole and connect to the actuator at the airfoil edge. After installation, the airfoil, joint compound, and substrate surfaces are sanded flush.

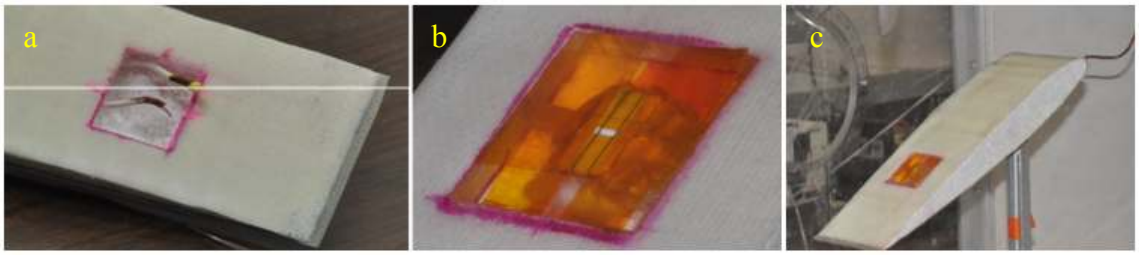

Figure 112. Embedding actuator and acrylic substrate into an airfoil with electrical connections. a) electrical leads through foam to actuator, b) electrically connected actuator in airfoil and c) mounted in wind tunnel.

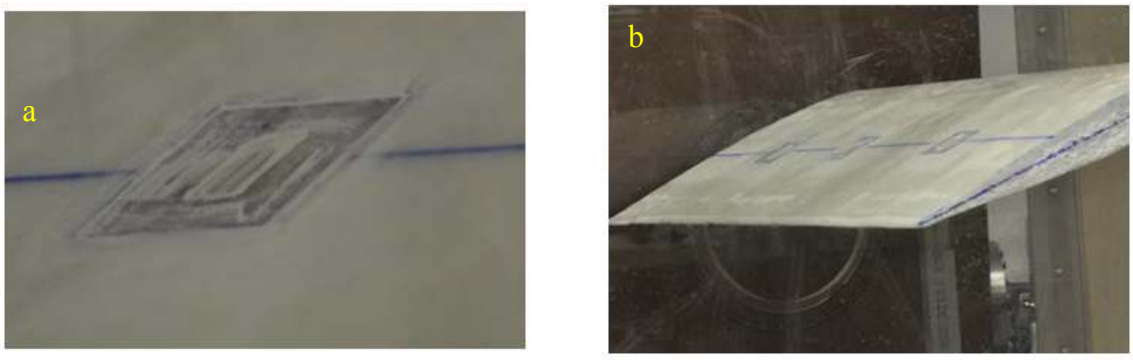

Figure 113. Airfoil with MACOR actuators. a) close-up - actuator and substrate inserted into airfoil and b) airfoil with three actuators positioned at 0.25s, 0.50s, and 0.75s mounted in wind tunnel test section. s is airfoil span and is either 0.18 m or 0.59 m.

Actuator D (as described in the actuator fabrication section) was mounted in the narrow airfoil C and electrically connected by 15kV rated, 3 mm diameter, lead wires (see Figure 112a). For airfoil C only Kapton tape, rather than joint compound, was used to hold the substrate in place as is shown in Figure 112b. This tape is not as flush as the joint compound and was only used for initial testing. The actuator was operated using a 20 kV, 1 mA power supply powered by a 12 V rechargeable battery and the power supply and electronics circuits was specifically housed in an electrically shielding metal box. The high voltage leads to the airfoil were similarly placed inside of electrically shielding metal conduit. These electrical precautions were taken to minimize EMI in the load cell when the actuator was firing.

Images demonstrating operation of airfoil C with the actuator off and on are shown in Figure 114. Although dimly lit, the light emission from the plasma discharge is

observable at the actuator throat exit near the center of the substrate. Images shown in Figure 114 are two successive frames from a 24 fps video (~42 ms between frames).

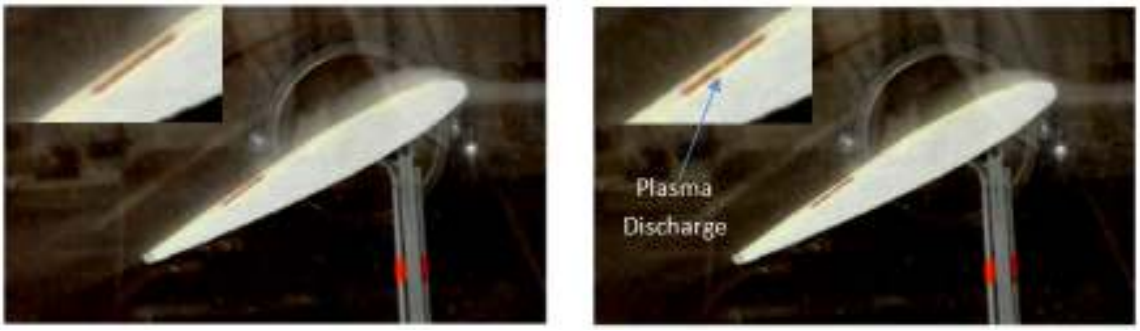

Figure 114. Actuated airfoil C in test section with flow visualization. a) actuator 'OFF' and b) actuator 'ON' for 4" inch span airfoil C with a single actuator embedded.

5.9.3 Experimental setup

Both qualitative and quantitative experiments were performed on full scale wind tunnel testing. Airfoils with and without actuators were placed in a wind tunnel and compared against tabulated data to check for any effect the actuator may have on performance. Lift and drag were measured using a load cell and controller box as the airfoil swept through a range of AoA. Tufts mounted to the surface of the airfoil indicated local flow patterns and were helpful in identifying stalled conditions. Using microscopic digital image scaling, drag and lift were measured to determine if the powered actuators had any effect on them.

5.9.3.1 Wind tunnel setup

A moderate scale open circuit wind tunnel was relocated to the plasma engineering and diagnostics laboratory for the purposes of this research. A diagram of the wind tunnel is shown in a plan view in Figure 115 and photos of the tunnel are shown in Figure 116. A blower wheel, blower housing and exhaust chimney were added to the existing wind tunnel sections. The blower wheel was belted to a 7.5 kW motor, and the motor was also contained in the blower housing. Ambient air enters through the horn and first passes through a ~ ¼" hole honeycomb flow straightener and then three taught screens with increasingly finer spacing to remove large scale eddies. The flow is accelerated through a converging section into a transparent acrylic test section which measures 0.61 x 0.61 x 1.22 m. Velocity in the test section was determined using a hand held vane anemometer and manometer. With the blower motor powered, test section velocities of 20 m s^{-1} are attainable. Lower velocities can be obtained by gradually separating the diverging section from the blower housing. Airfoils with chords of c = 0.30 m were used in these tests, giving Reynolds numbers of Re_c = 400,000.

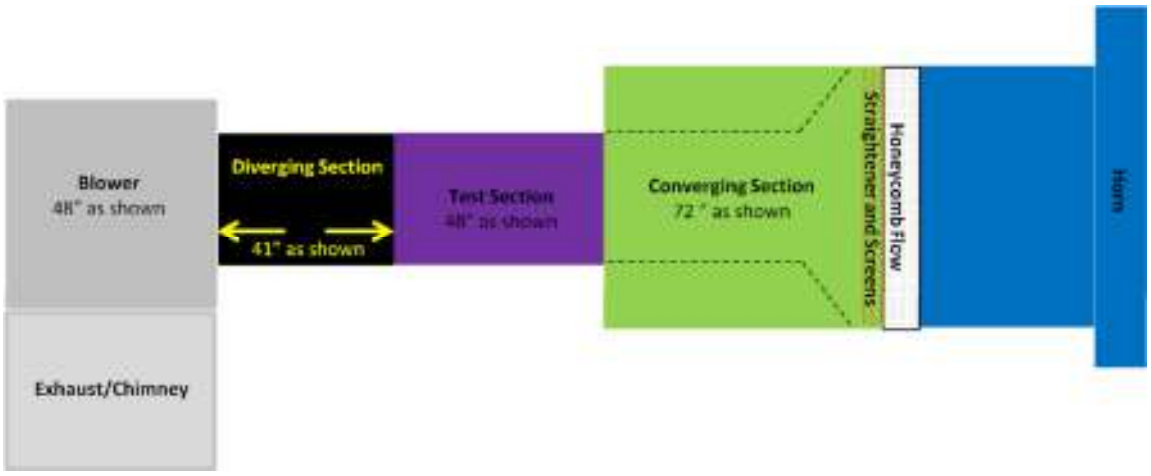

Figure 115. Plan view schematic of wind tunnel.

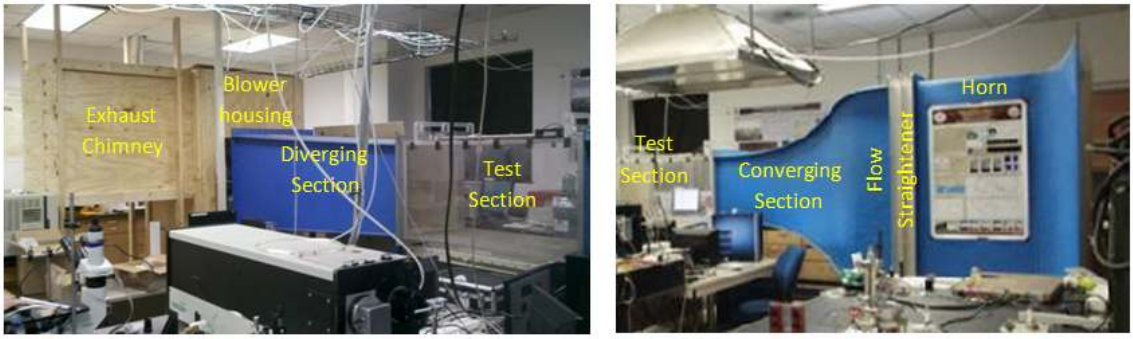

Figure 116. Photo of blower, test section and inlet of wind tunnel.

The wind tunnel came supplied with the load cell shown in Figure 117 and its control box. The load cell uses a linear variable differential transformer and its control box allows lift and drag measurements via calibrated voltage signals. The load cell could also be calibrated for lift and drag by hanging weights from a pulley system. The 0.5 mm diameter colored dots shown in Figure 117 were observed with a microscope and digital

camera so that slight deflections in color spots' centroids could be similarly calibrated to lift and drag forces on the airfoil. The high resolution camera (2848x4288) and microscope combination resulted in nominal image scaling of 700 nm/pxl. Centroid displacements were determined using a MATLAB script, and the displacements were calibrated by suspended masses directing their force in the appropriate direction for either lift or drag.

A sting with angle of attack (AoA) adjustment (-25° to +25°) held the airfoil in the tunnel. The adjustment hinge allows for manual AoA adjustment from outside of the test section during operation, and AoA is determined from images of the airfoil taken from a high resolution digital camera. Uncertainty on AoA measurement is ±0.5°.

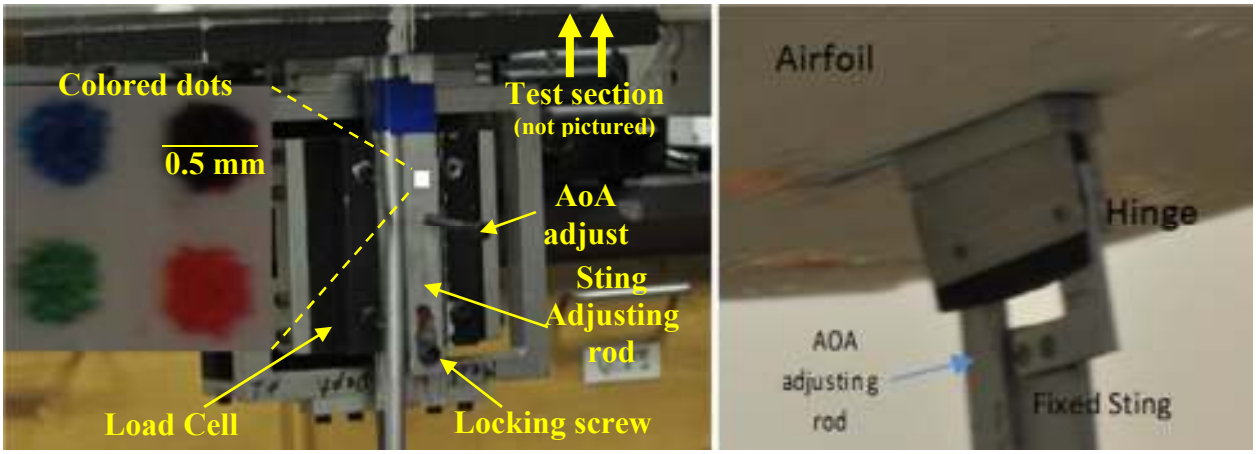

Figure 117. (a) Load cell for lift and drag measurements and (b) AoA adjustment hinge.

The existing wind tunnel test section was modified for higher velocity testing by inserting a second converging nozzle into the test section. A photograph of these inserts

inside the test section with a strip type actuator installed on a small span airfoil is shown in Figure 118. The shape of the nozzle was cut to approximately follows the curvature of the large intake nozzle on the tunnel inlet (see Figure 116).

Figure 118. Converging inserts used to increase free stream velocity and mitigate edge effects when using 0.18 m span airfoils in the test section. a) Front view b) Side view.

With the inserts the test section size was reduced to 0.20 m wide (spanwise), 0.61 m tall, and 0.61 m long. Reducing tunnel cross section area increases the test section velocity and *Re*. With inserts a maximum velocity of 27 m s^{-1} was achieved and gave Re_c = 540,000 in the test section which is a 35% increase from when the inserts are not installed.

Prior to any data collection lift and drag were calibrated with weights for 1) voltage when the control box was used or 2) colored spot centroid displacement if lift

and drag data were sought via image analysis, and then the airfoil was secured at a predefined AoA in the wind tunnel.

5.9.3.2 Pulsing circuit setup

The pulsing circuit is a DC pulsed RC circuit and is shown in Figure 119. Excluding the 10k:1 voltage divider branch, which is indicated with broken lines, this circuit was used during wind tunnel testing and is referred to as the experimentation circuit. The entire circuit shown in Figure 119, including the voltage divider with R_1 = 100 MΩ and R_2 = 10 kΩ, is referred to as the HV measurement circuit. The experimentation circuit consisted of a Spellman SL 300 series 100 kVDC power supply charging a 0.5 nF capacitor C_1 through a 100 kΩ ballast resistor, R_{bal}, and the full span strip actuator required 92 kV (as read from power supply display) for initial spark gap breakdown. It is likely that most discharges post initial breakdown require fewer than 92 kV. All electrical signals were acquired using a LeCroy WaveRunner 204 MXi oscilloscope, and effects of stray inductance and/or capacitance inherent in the circuit were neglected. A Pearson M#5046 current monitor was used to measure current through the actuator, but voltage across the actuator could not be measured because that voltage likely exceeded the 40 kV limit of the NorthStar PVM-4 voltage probe. In this circuit peak current was 720 A with FWHM = 140 ns.

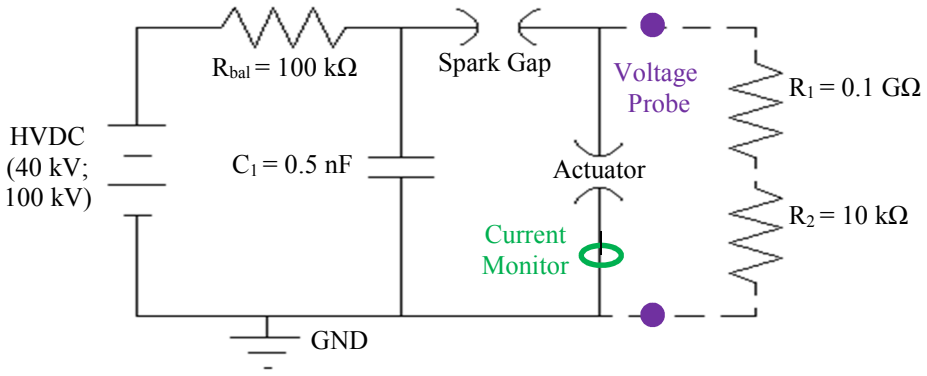

Figure 119. RC pulsing circuit used to power the strip actuator. A 10k:1 voltage divider (indicated by broken line) was used for high voltage measurement (100 kV) across R_2 and GND to estimate voltage across the full span actuator, but current leakage through the divider prevented the actuator from firing. Actuator voltage and current were measured using a quarter span actuator powered by a 40 kV power supply.

The measurement circuit was implemented with the 100 kV power supply to obtain voltage estimates across the full span actuator by measuring the voltage drop across R_2, but R_1 was insufficient to prevent current leakage through the divider, preventing discharge in the full span actuator. Thus, voltage measurements across the full span actuator were not possible. For comparison, current and voltage measurements were made using the experimentation circuit and a similar but smaller strip actuator consisting of 5 3.5 mm spark gaps in series. This shorter strip actuator was powered by a Spellman SL 300 series 40 kVDC power supply. Max voltage across the shorter actuator was 25 kV with a fall time was 85 ns, and max current through this actuator was 600 A with FWHM = 70 ns. All recorded voltage and current waveforms are provided in Figure 120, where timing of the signals has been shifted for clarity. The voltage divider side of the circuit was not connected during any of the experimental tests. It was only connected

for voltage measurement outside the test section. Because convection can alter breakdown behavior as previously shown in chapter 3, the electrical signals shown in Figure 120 may not be exactly the same as during wind tunnel operation, but they are probably not significantly different either due to the relatively low velocity.

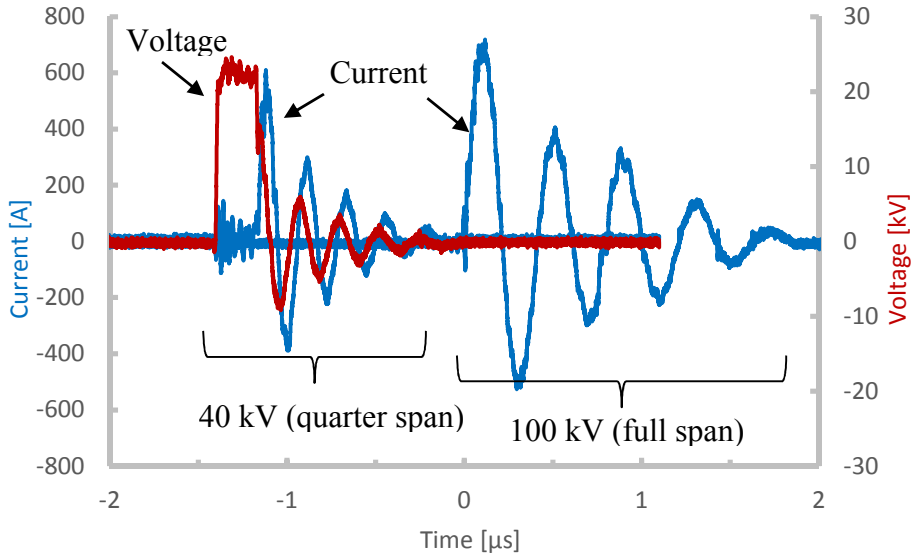

Figure 120. Pulse current and voltage waveforms for the actuator when powered by 40 kV and 100 kV power supplies. Voltage across the full span actuator could not be measured due to probe limitations and current leakage through the voltage divider. Timing of the measurements from each power supply have been time shifted for clarity.

The following investigations examine the actuator in several ways. The first experiments sought changes in lift and drag to determine if installing actuators on the airfoil surface had any effect on the airfoil's unaltered state. Multiple data sets were collected with two different airfoils to determine reproducibility and repeatability. In

these investigations MACOR actuators were encased in acrylic and then embedded within the airfoil. This was shown in Figure 111 - Figure 113. A range of AoA was swept out for airfoils with and without embedded actuators, and lift and drag were recorded from the load cell control box.

Another set of tests qualitatively examined airfoils at various Re and AoA to determine if the actuators could demonstrate boundary layer control. An airfoil with 0.30 m chord and 0.18 m span was placed in the test section at Re = 100,000 and at Re = 540,000 and cycled through a range of AoA. The objective of these experiments was to determine the range of AoA through which successful actuation was evident as indicated by flow visualization tufts. Neither lift nor drag data were sought in these experiments.

Another set of experiments sought to determine whether the mechanism of actuation was by direct momentum injection or by vortical entrainment of the freestream. These mechanism are described in the presentation of these results. To test the mechanism of actuation, a full span (s = 0.58) airfoil with a mica strip actuator mounted at x/c = 0.50 is operated with and without its cover at Re = 400,000. The airfoil is oriented at 11° and a qualitative comparison of tuft behavior was made. Lift and drag data were acquired for this test by measuring a calibrated displacement of color spot centroids.

The last set of experiments sought to directly measure changes in stalled airfoil lift and drag between actuated and unactuated conditions at Re = 400,000 and AoA = 11° which was just past the stall angle. In this test centroid locations were first measured in a still wind tunnel (no flow), then they were measured with 20 m s^{-1} flow and no

actuation, and then they were measured a last time with the actuator powered. These conditions are called 'OFF/OFF', 'ON/OFF', and 'ON/ON,' respectively. Forty images with 1/250 s exposure time were collected for each trial within a span of ~80 s for each trial. Aerodynamic forces were assessed by observing displacement of the black spot's centroid and statistical analysis was performed on the processed data to check for significant changes in aerodynamic forces as a consequence of the actuator being powered. This direct measure of displacement is immune to EMI but is sensitive to tunnel vibration.

5.9.4 Results and discussion

Several airfoils were created and tested in the wind tunnel. As a preliminary step, coefficients of lift and drag were determined and compared to published values for similar shaped airfoils at similar *Re*. Then flow visualization was performed to qualitatively observe flow separation in actuated and unactuated airfoils at *Re* up to 540,000. Finally, quantitative analysis of lift and drag was performed using an optical measurement system. At *Re* = 400,000, lift and drag are compared between full span actuated and unactuated airfoils at AoA = 11°, which is just above the stall angle of $AoA_{stalll} \sim 10°$.

5.9.4.1 Airfoil aerodynamic performance characterization

Different airfoils were tested in the wind tunnel while the lift and drag were measured at various angles of attack. Tufts were not mounted on the surface of these

airfoils and no qualitative data were collected. These are Airfoil A, Airfoil B (prior to installation of the actuators) and Airfoil B (after the actuators had been installed). Airfoils A and B were intended to have the same geometry and be otherwise as similar as possible, but comparison of lift and drag data between the two airfoils suggests otherwise. It is also possible that slight differences sting mount positions result in the observed differences measured.

Calibrated lift and drag forces were combined with air properties, airfoil geometry and free stream velocity to calculate the lift and drag coefficients for the tested airfoils. These C_L and C_D are plotted for airfoil B (with and without actuators) in Figure 121 and Figure 122. Angles of attack vary in these measurements from -10° to +20°. Lift increases nearly linearly with increasing AoA up till the point of stall at which point the lift decreases and the drag more rapidly increases. With these airfoils, stall occurs around $AoA_{stall} = 12°$. Also shown in Figure 121 and Figure 122 are C_L and C_D data available from the literature [77]. The Sandia reference data is for a NACA 0012 airfoil at Re=360,000. Airfoil B was tested at Reynolds numbers of 348,000, and 332,000 for the actuated and unaltered airfoils, respectively.

From these data two distinct trends are evident. First the airfoils behave similar to as expected based upon the literature. Lift coefficients shown in Figure 121 are within about 20% of the reference data prior to stall, but after stall there is more discrepancy. Drag coefficients determined from the wind tunnel testing are significantly higher than reference data, and this may be due to the drag on the sting mount which has neither been accounted for nor mitigated against with cowling. In addition, the lack of cowling

is likely the reason for the asymmetry about AoA = 0° in the drag coefficient shown in Figure 122. Because of the asymmetry in drag, only AoA >0° are analyzed. The second main finding is that the airfoils with actuator and without actuator have very similar characteristics. This indicates that the embedded actuators do not significantly alter the airfoil shape and consequently, its flow field.

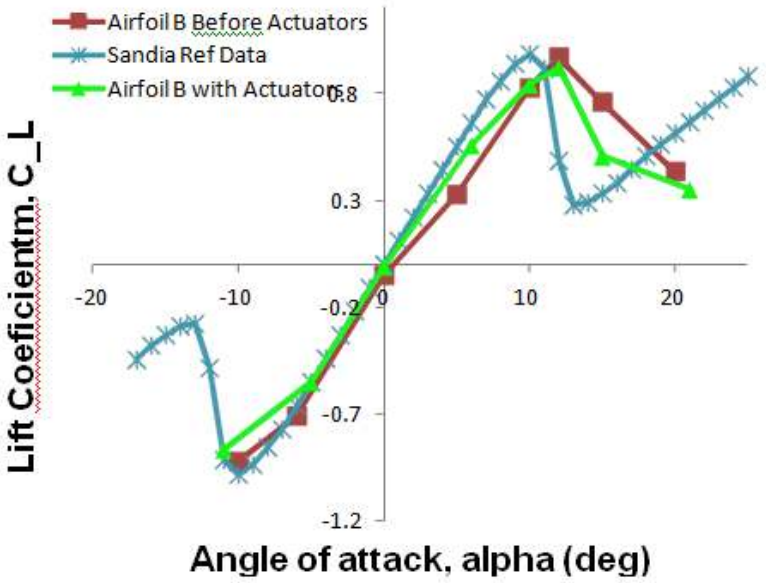

Figure 121. Measured lift coefficient for airfoil B before and after actuator insertion with comparison to reference data.

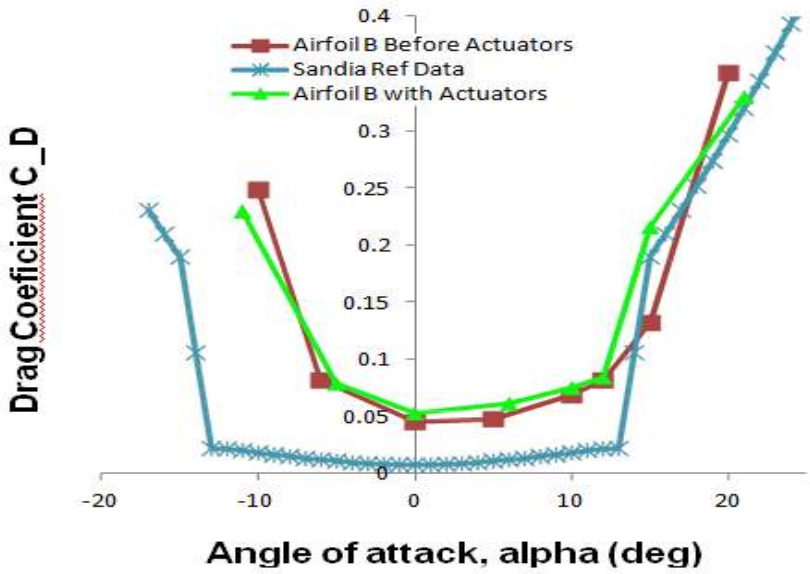

Figure 122. Measured drag coefficient for airfoil B before and after actuator insertion with comparison to reference data.

Consistency of measurement and airfoil sensitivity to surface modifications are illustrated in Figure 123. Figure 123a and Figure 123b show multiple measurements of the lift and drag coefficients for airfoil B. Shown are one case with actuators and 3 cases prior to actuator installation. Case B1 was the first measurement, and the airfoil was sanded after testing. Cases B2 and B3 were then taken as repeated measurements. At 15° test B1 lift and drag coefficients differ from the other tests by 30-40%, but other than this data point, there is good agreement in measurements and the process appears repeatable.

Lift and drag were also measured on Airfoil A and these data are shown in Figure 123c and Figure 123d. At pre-stall AoAs Airfoil A performs similar to Airfoil B

and the reference data. Airfoil A, however, appears to experience a much less dramatic stall as observed by the leveling off in C_L with AoA > 12°. With respect to the drag coefficient, Airfoils A and B behave similarly.

Some error is known to exist in fabrication and measurement techniques. Airfoil A was built first and some practice and experience with hot wire cutting likely affects the final product. Repeated testing of Airfoil A, shown in Figure 123c indicate the repeatability of our measurements with errors less than 5% (of the maximum lift) for the same geometry in unstalled conditions. A comparison of lift and drag measurements for all airfoils, both actuated and unactuated, against the reference data is shown in Figure 124. Slight oscillations in the lift and drag and are noticeable in the measured time averaged standard deviations of the output voltages from the load cell and are typically less than 1% for unstalled conditions and as high as 10% during stall. This drift may be due to drift in the airfoil AoA when the wind tunnel is powered for extended periods. There is also an uncertainty of ±0.5° in the angle of attack measurement.

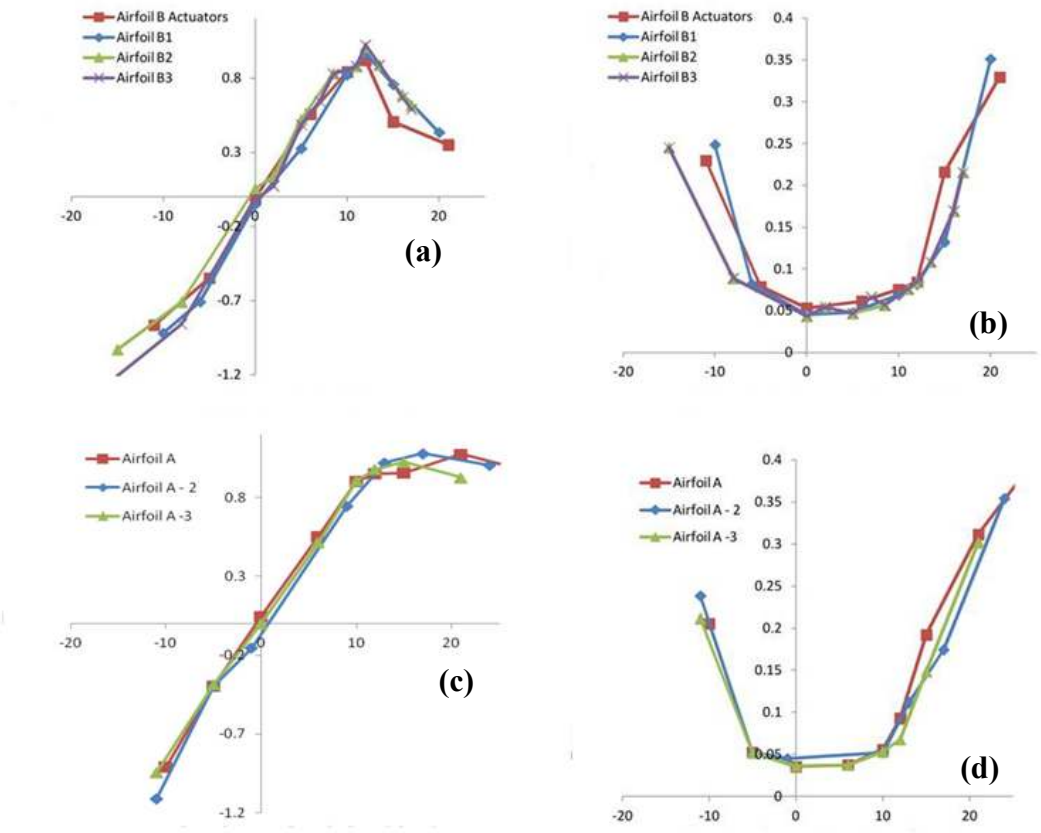

Figure 123. Multiple independent measurements of lift and drag coefficients for two different airfoils. (a) Airfoil B C_L, (b) Airfoil B C_D, (c) Airfoil A C_L, and (d) Airfoil A C_D. Re = 350,000.

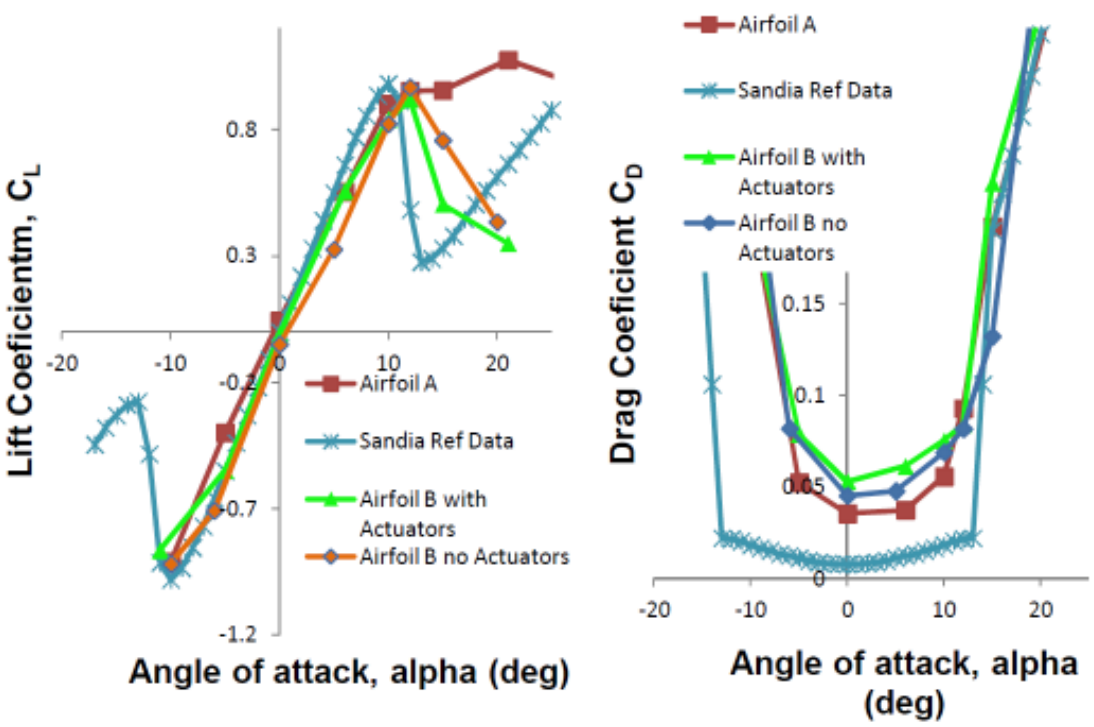

Figure 124. Comparison of all full span airfoils to one another and Sandia reference data. Re = 350,000.

5.9.4.2 Qualitative flow visualization

In order to visualize the flow over the 0.20 m span airfoil nine strings were arranged in a 3×3 array on the top surface of the actuated airfoil. Three rows of three 25-30 mm long strings were placed at *x/c:* 0.2, 0.4 and 0.8. The strings were used as visual indicators for when the flow was locally attached or separated. Strings laying flat in the direction of the flow indicate locally attached flow, and strings moving about erratically and/or pointing upstream (indication of a strong separation vortex) mean the flow is locally separated. An airfoil having c = 0.30 m and s = 0.18 m and with actuator at x/c =

0.50 was placed inside the wind tunnel at *Re* = 100,000, velocity of 5 m/s and 2) *Re* = 540,000, velocity of 27 m/s.

The effect of actuation at *Re*=100,000 and AoA=21° is shown by the close up image in Figure 125. In the top image the strings are seen to behave erratically and even point in a direction upstream. This indicates that the flow has become locally separated. In the picture on the bottom the strings are laying still, clearly in focus and point downstream. This indicates that the flow is locally attached. Light emitted by the plasma is easily visible in Figure 127. These pictures are frames taken from a video of the airfoil. For this flow condition, the airfoil, with actuators unpowered, experienced stall at AoA = 21°. It is believed that downwash exacerbated by flexion in the acrylic insert walls when tunnel was powered is the cause of such high stall AoA. Flow in the wind tunnel caused the pockets of air between the contoured inserts and the test section walls to become a low pressure region, which increased the size of the gap between the airfoil and the contoured insert wall. Such high stall angels are not observed with full span (*s* = 0.58 m) airfoils are tested and the inserts are not present.

When the actuator was powered it was observed that the strings transitioned from lying flat to moving about erratically. This was most easily observed on the leading edge and mid-chord strings. The AoA was adjusted in small increments to determine the range over which actuation caused the strings to indicate reattached flow. Actuation appeared to be effective in the range of $21° \leq AoA \leq 21.8°$. This range is shown by the series of images in Figure 127. If reattachment is truly successful, this corresponds to a 0.8° or 3.8% increase in AoA where the flow is attached.

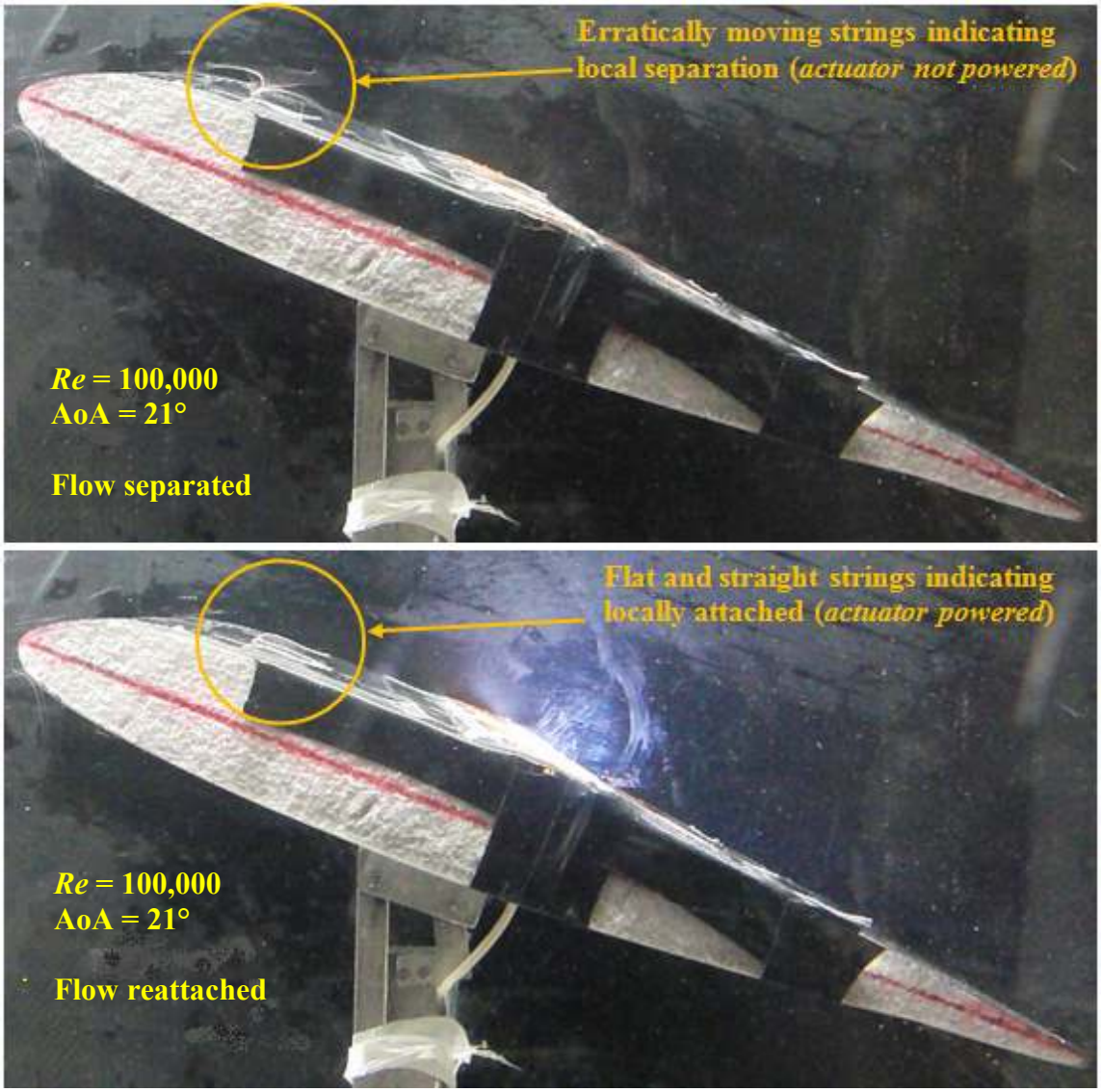

Figure 125. Successful actuation. String flow visualization of separated and attached boundary layer over NACA 0012 at AoA=21° and Re=100,000.

For the next set of visualization the wind tunnel free stream velocity was increased to 27 m/s (*Re* = 540,000) by using the contoured inserts and ensuring a good seal between the diffusing section and the blower housing. Two close up images from

this flow condition are shown in Figure 126 – one each for actuator off and actuator on conditions. At *Re* = 540,000, the actuated airfoil again experienced stall at AoA = 21°.

When the actuator was powered at this angle of attack the flow transitioned from indicating a separated flow to indicating attached flow. As was done for the low *Re* condition, AoA was adjusted in small increments to determine the range of AoA over which actuation appeared successful. This range of AoA is shown in Figure 127. The successful range of actuation at *Re* = 540,000 was 20.9° ≤ AoA≤ 22.7°. This corresponds to a 1.8^{o}, or an 8.6% increase in angle of attack where the flow is attached. Successful actuation was observed at AoA within the *Re* specific actuation limits for both trials. Assuming linear proportional lift vs. AoA relationships, an 8.6% gain in AoA is equivalent to a 8.6% increase in lift, but such assumptions of linear C_L vs. α are probably too generous considering that near stall the lift profiles tend to flatten.

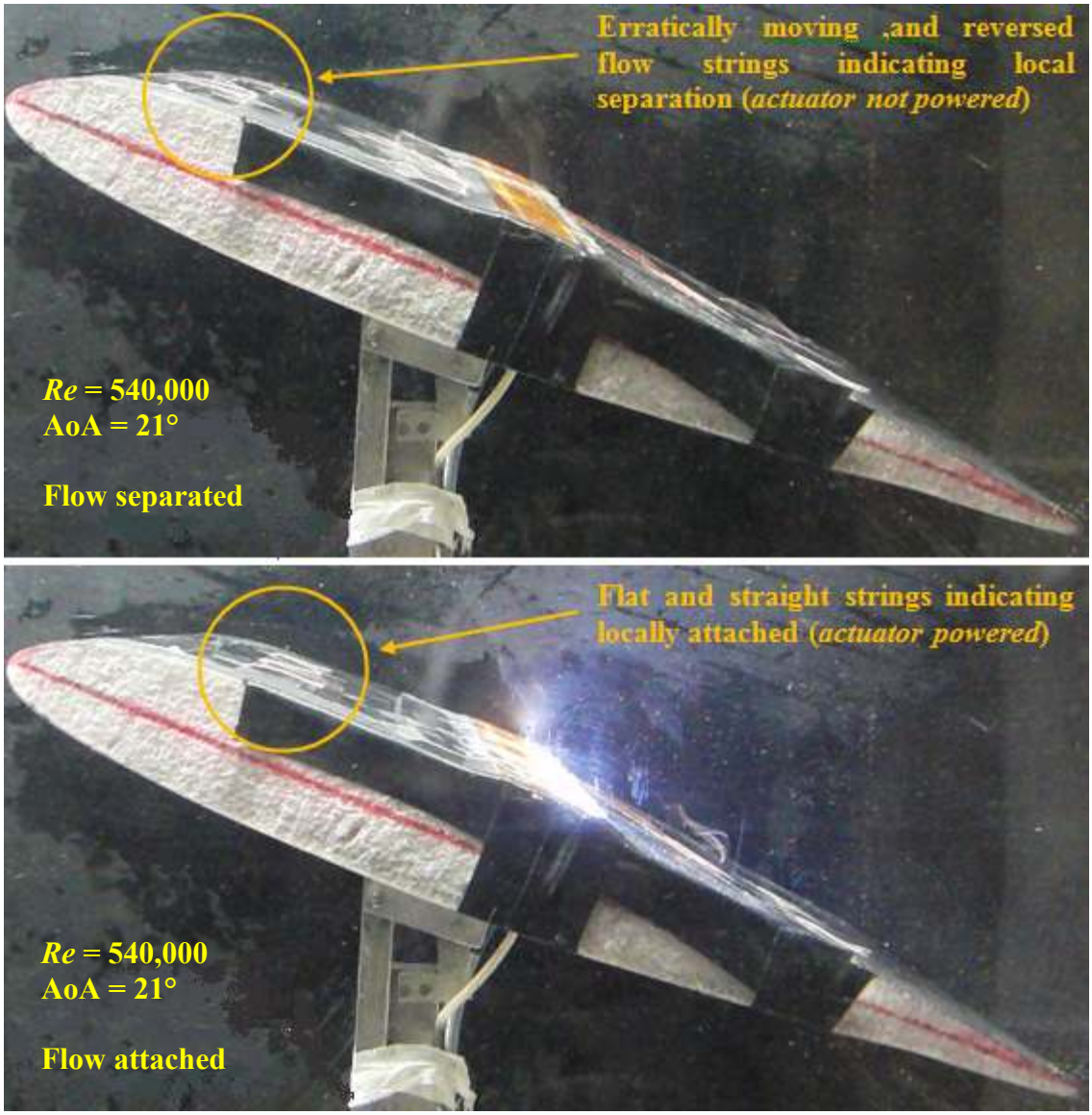

Figure 126. String visualization on actuated airfoil at Re = 540,000 showing (top) locally separated flow with actuators off and (bottom) locally attached flow when the actuators are on.

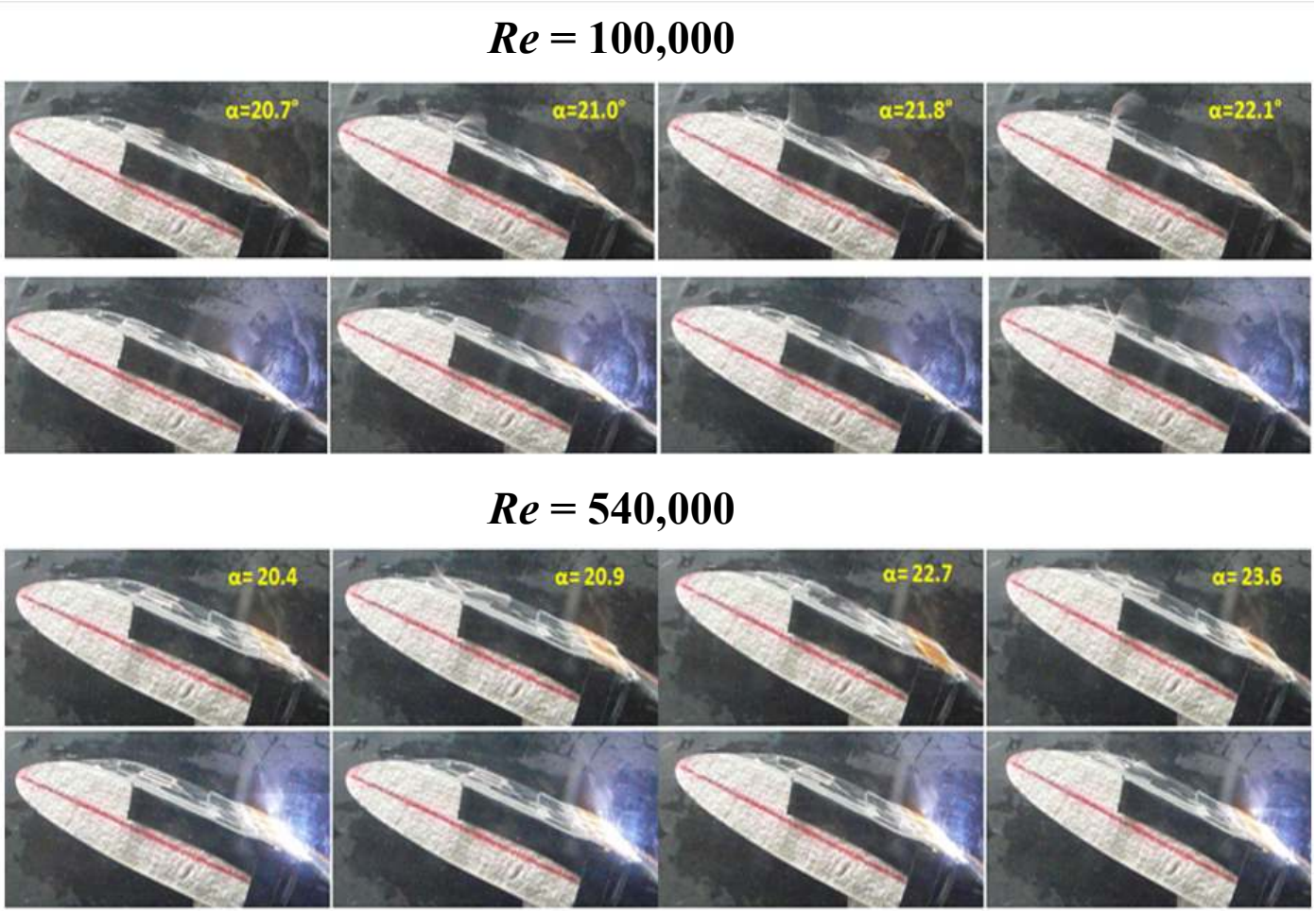

Figure 127. Range of α showing successful actuation for Re = 100,000 and Re = 540,000. Left column shows attached flow where actuation isn't necessary. Middle columns show successful actuation. Right column shows irrecoverable separation.

There is some issue with the observed high stall angle. This airfoil appears to stall at AoA ≈ 21°, which is significantly larger than those discussed in the literature [77] where under similar conditions stall occurs at AoA ~11°. At least three effects may lead to the high stall angle observed in the airfoil operation, and these can all be explained by "noisy" tunnel operating conditions. Free stream turbulence may be one cause. Free stream turbulence will typically induce earlier boundary layer transition on the airfoil, and this leads not only to faster boundary layer growth but also to postponed separation points. Also this transition can induce separation bubbles on the airfoil rather than complete separation. Large stall angles could also be due to the imperfect modifications of the test section (the use of inserts) that were necessary a) to increase *Re* from 400,000 to 540,000 and b) to allow for an easier to actuate (less voltage required) shorter span (0.58 m to 0.18 m). This modification possibly caused the airfoil's free stream turbulence to increase. Another cause may be because the actuators act as turbulence trips. The airfoil surface had a step discontinuity at the actuator due to its 2mm thickness. Kapton tape 60 μm thick was used to smooth this discontinuity out as best as possible. The same tape was used to affix the flow visualization tufts and actuator components. Lastly, tunnel wall effects may also cause a delay in stall. Boundary layers develop on the tunnel wall and can interact with flow over the airfoil. These add a complex 3D behavior to flow and stall characteristics. The chord to tunnel width (or span) ratio in this testing was 1.67, indicating a potential for undesirable wall effects. In subsequent lift and drag experiments this ratio was significantly less (0.52), and lift characteristics of the airfoil compared better with reference data. While these wind

tunnel effects are apparently significant they are nonetheless present in both the actuated and unactuated cases. Thus they do not detract from the ability of the actuator to effect change in the flow, which appears to increase with *Re*.

Another set of experiments examined strip actuator effectiveness on a full span NACA 0012 airfoil with $s = 0.58$ m at $Re = 400{,}000$. This purpose of this experiment was to discover whether or not a tangential jet generated by the plasma discharge was responsible for reattaching separated flow. Actuator effectiveness was again assessed by observing the behavior of tufts secured to the airfoil oriented at AoA=11°, just above stall threshold, while power to the actuator was cycled. For this wider airfoil, the stall angle was considerably less than that observed for the narrow airfoil in the $Re = 540{,}000$ experiment. This indicates that the large stall angles were likely due to the presence of the inserts and complex 3-D flow patterns and not turbulence caused by the actuators themselves. Turbulator effects may still be present, but they should at least be consistent and are certainly less significant than the dominating near wall effects.

The actuator was operated in two configurations: 1) with the mica cover in place, per the design shown in Figure 95, and 2) with the mica cover removed. In the first case jets are produced tangential to the airfoil surface and if actuation occurs, it would indicate that the mechanism responsible for actuation is momentum injection directly from the jet to the boundary layer. On the other hand, in the case without the mica cover, the jet is allowed to freely expand in a hemisphere, and if actuation is observed then vortical entrainment may be responsible for actuation. In this mechanism of actuation, shear layers between the jet and the freestream would create vortices due to the velocity

differences, and these vortices may pull the free stream towards the airfoil surface to help combat any adverse pressure gradient that may exist locally.

The results were similar for both covered and uncovered actuator configurations. The tufts indicated local separation and then attachment when the actuator was powered off and powered on, respectively. Images of this behavior are provided in Figure 128 showing an actuator without the mica cover. Non-uniformity can be seen in the flow patterns across the airfoil. Namely, separation does not occur evenly over the span of the airfoil because of imperfections in the setup including, but not limited to airfoil shape and unknown flow conditions in the test section. This is a problem inherent in the wind tunnel setup and could be caused by the primary air mover. In Figure 128(left) the flow is seen to remain attached at the far end of the airfoil while showing signs of local separation on the near side. In Figure 128(right), however, the flow is attached where it previously was not, and this is due to successful actuation.

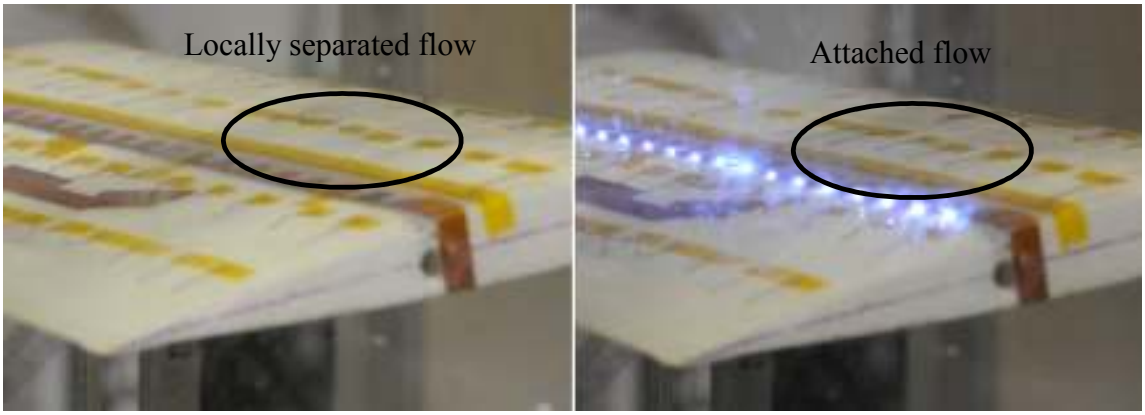

Figure 128. Strip actuator on a NACA 0012 airfoil at AoA = 11° & *Re* = 400,000. The flow visualization strings show local separation (left) and attachment (right) indicating that successful actuation is occurring.

The fact that actuation is observed under both covered and uncovered conditions shows that a directed jet is not necessary to reattach flow that has not severely separated. This implies that the boundary layer may be energized by two fundamentally different mechanisms. In the case where the mica cover was in place, jets of air were created by the plasma and directed tangentially along the airfoil. Thus, momentum is directly input to the boundary layer. In the case where the mica cover was removed, the boundary layer is energized by entrainment of the freestream. Upon ignition, the plasma creates a hemispherical point source of flow. The portion of the 'jet' with velocity normal to the airfoil surface interacts with and entrains some of the freestream. A portion of the freestream is pulled by vortices towards the airfoil surface where it then energizes the boundary layer causing reattachment if separation is not too severe. This is a significant finding because it radically expands the design space for flow actuators for aircraft. No longer must actuators be confined to hollow cavities that must be embedded within the

airfoil surface. Surface lying strip actuators are much simpler and can be placed along an airfoil without requiring significant surface modifications.

5.9.4.3 Quantitative optical lift and drag measurement

Measuring lift and drag in this experiment was a challenge due to rapidly changing electrical currents that ultimately produced EMI significant enough to permanently damage the load cell control box. The load cell could be calibrated using suspended masses to determine a functional relationship between output voltage and aerodynamic forces, but since the control box could not be used while the actuator was powered, and alternative optically isolated calibration/measurement system was explored.

The optical approach was used to measure lift and drag by calibrating suspended masses to microscopic deflections in the load cell. A marker with four colored dots arranged in a square pattern was affixed to the sting outside of the test section as was shown in Figure 117. The dots were colored red, blue, green and black and had 0.5 mm diameter. A microscope focused a digital camera's field of view on the colored dots, providing image resolution of 700 nm/pxl. Centroids of each colored dot could be located and tracked using a MATLAB script, but only results from the black spot are used since that color was recognized most reliably. The image in Figure 129 shows that color deposition was not even within the dots. Some regions were splotchy while some regions, namely the black one, contained more than one color. Careful RGB selection improved color identification and provided consistent centroid locations.

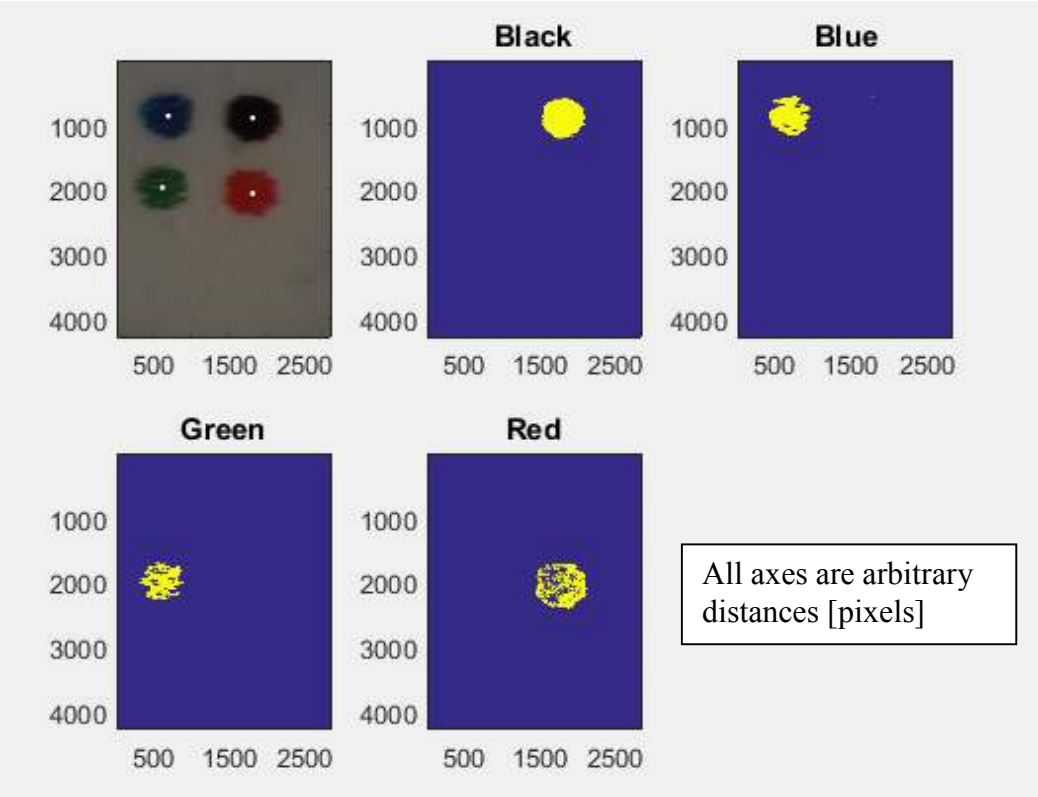

Figure 129. Colored dots showing centroid location (top left) used in optical lift and drag measurements. Figures with blue background are post processed images.

To simulate lift and drag forces on the airfoil, masses ranging from 0 – 1700 g were connected to the sting via a pulley using high test monofilament fishing line, and the camera was activated remotely as to avoid disturbing the field of view. In this way known applied forces could be related to centroid displacement. Drag and lift calibrations are shown in Figure 130 and Figure 131, respectively.

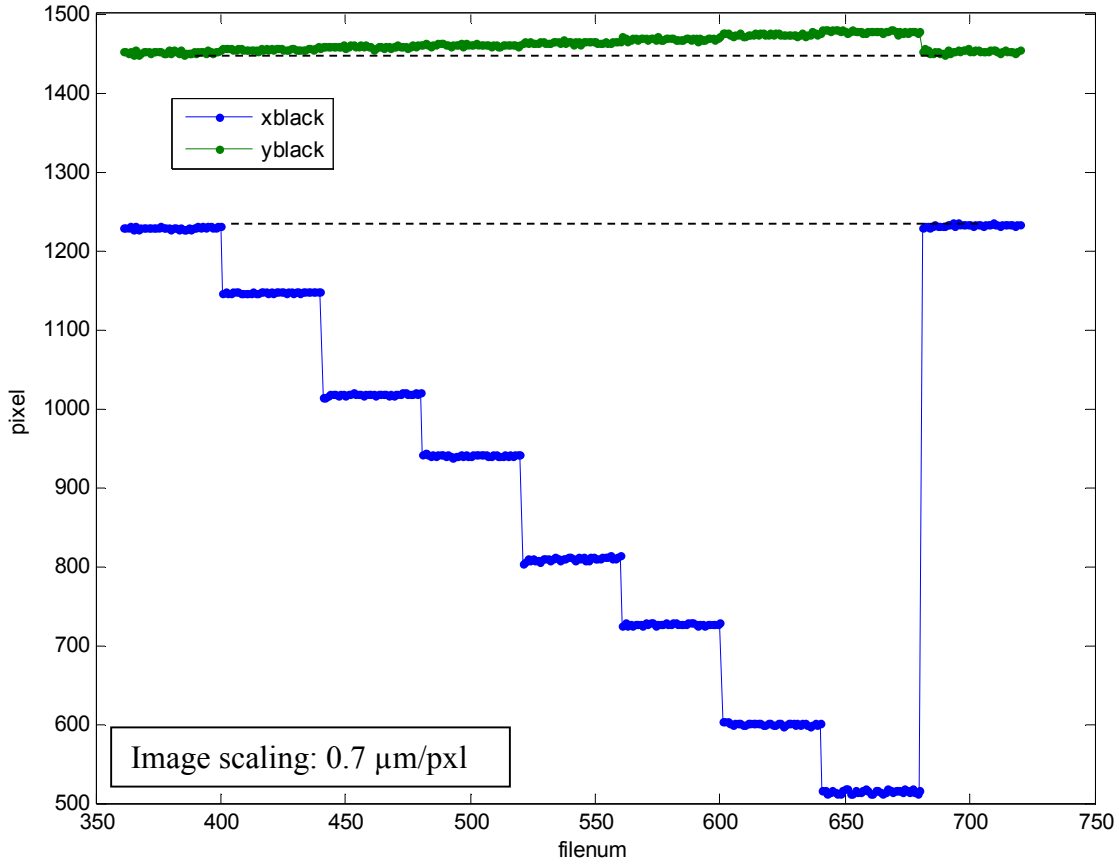

Figure 130. Optical drag calibration, raw data. Hysteresis is negligible.

Many images were collected for each applied mass for statistical averaging. The calibration sequence started with 0 g suspended and increased in alternating 0.2 and 0.3 kg increments to an ultimate mass of 1.7 kg. As a final step, a set of images was collected with 0 kg suspended to check for hysteresis in the measurement.

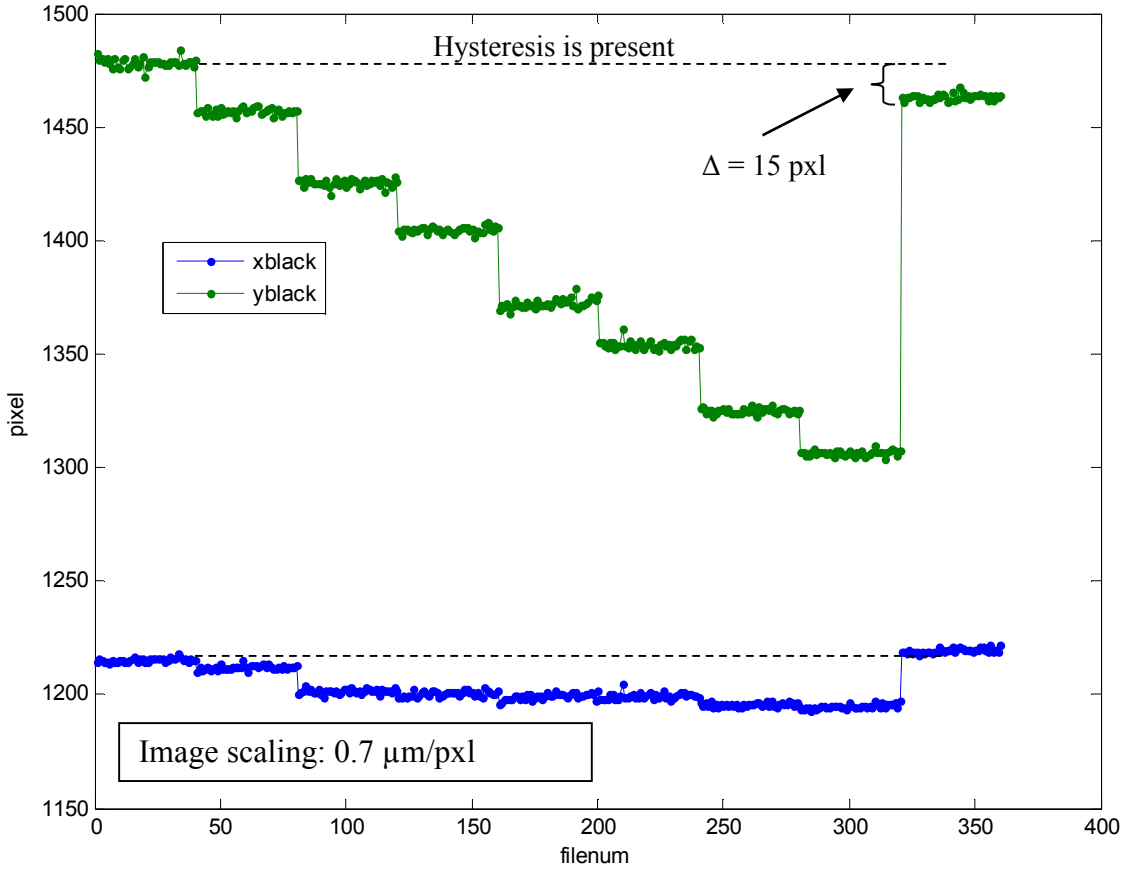

Figure 131. Optical lift calibration, raw data. Hysteresis is evident in the primary directional component and is accentuated by the dashed line.

Calibration of lift and drag reveals two issues regarding data fidelity. First, it is evident from both of the calibration plots that lift and drag forces are coupled. That is to say that each force has both *x* and *y* components. As mass is added to increase the applied drag and lift forces, their mutual influence increases. If forces remain relatively low, then their influence may not be problematic. In this application, lift forces are expected to be several times greater than drag forces. Close examination of the *x* and *y*-components of centroid displacement shows that the primary (uncoupled) directional

components (x for drag, and y for lift) show different sensitivities in the raw calibration data. Under full load, the centroid displacement in the primary directional component spans 710 pixels (0.519 mm) for drag and 170 pixels (0.125 mm) for lift. Interestingly, the centroid displacement spans for the coupled directional components under full calibration load are both ~25 pixels (0.011 mm). This will be discussed in more detail after the presentation of experimental results. The second issue regarding data fidelity is the presence of hysteresis in the primary directional component of lift. With respect to the initial unloaded position, a change of 15 pixels (0.011 mm) in the primary directional component was recorded when the load was removed. Post processed data from both calibrations is provided in Table 22 and calibration curves for force v. centroid primary directional component displacement (i.e., drag, Δx; lift, Δy) are plotted in Figure 132. Data points used to check for hysteresis are not included in the calibration curves. The calibration curves in Figure 132 exhibit a linear relationship, and lift is approximately 4 times as sensitive as drag to centroid displacement.

Table 22. Post processed calibration data for optical lift and drag measurements. Displacements of primary and coupled directional components are given.

Mass [kg]	Force [N]	DRAG		LIFT	
		Δx [mm]	Δy [mm]	Δx [mm]	Δy [mm]
0	0	0.000	0.000	0.000	0.000
0.2	1.96	0.060	-0.003	0.003	0.015
0.5	4.9	0.153	-0.004	0.010	0.039
0.7	6.86	0.209	-0.007	0.011	0.053
1	9.8	0.305	-0.009	0.012	0.077
1.2	11.76	0.364	-0.012	0.012	0.090
1.5	14.7	0.457	-0.017	0.015	0.112
1.7	16.66	0.519	-0.018	0.016	0.125
0	0	-0.003	-0.001	-0.003	0.011

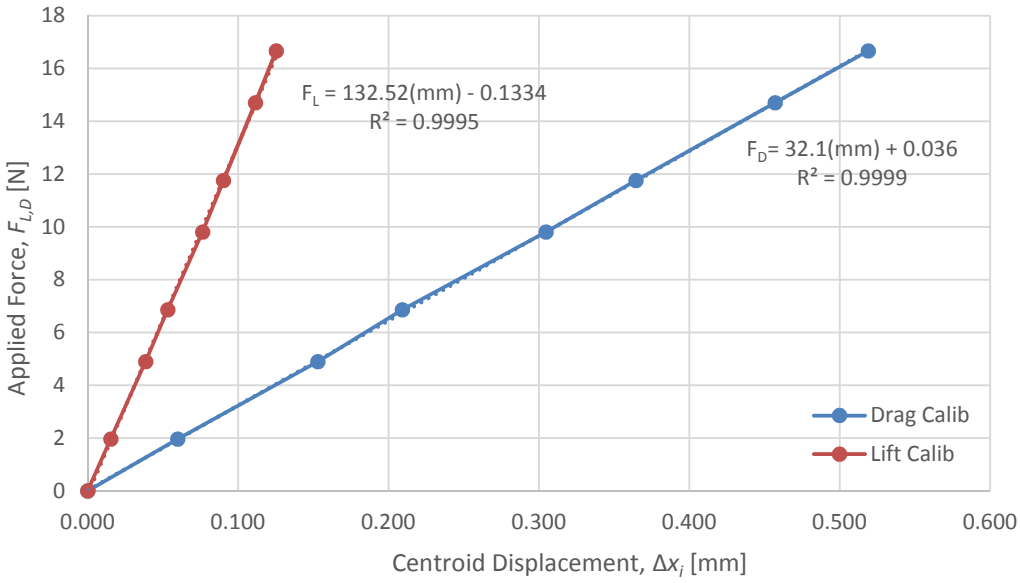

Figure 132. Drag and lift force plotted as a function of black spot centroid displacement in the primary directional component (i.e., drag, Δx; lift, Δy). Data collected to check for hysteresis is not included in the calibration.

A NACA 0012 airfoil with a strip type actuator with a mica cover was placed in the wind tunnel at AoA = 11° and *Re* = 400,000. Baseline data were collected with the wind tunnel powered off and the actuator powered off. This is the 'OFF/OFF' condition. A second set was collected with the wind tunnel powered and no actuation. This is the 'ON/OFF' condition. During this condition separation was evident and indicated by erratically moving strings affixed to the suction side of the airfoil. A final set of data was collected with both the wind tunnel and actuator powered. This was the 'ON/ON' condition. In this condition the strings on the suction side indicated that the flow was reattached. Images were collected and post-processed for each condition. These data are shown in Figure 133. The *x*-axis in this figure ('Image File') can also be thought of as approximately even increments of time since images were recorded sequentially and at regular intervals. This temporal consideration is important to subsequent analysis. Also note that lift forces measured far exceed those applied during calibration, so extrapolation, although undesirable, is necessary. Between unactuated and actuated trials, the average lift force measured was 26.3 and 27 N, respectively. Similarly, drag forces were 5.6 and 4.9 N.

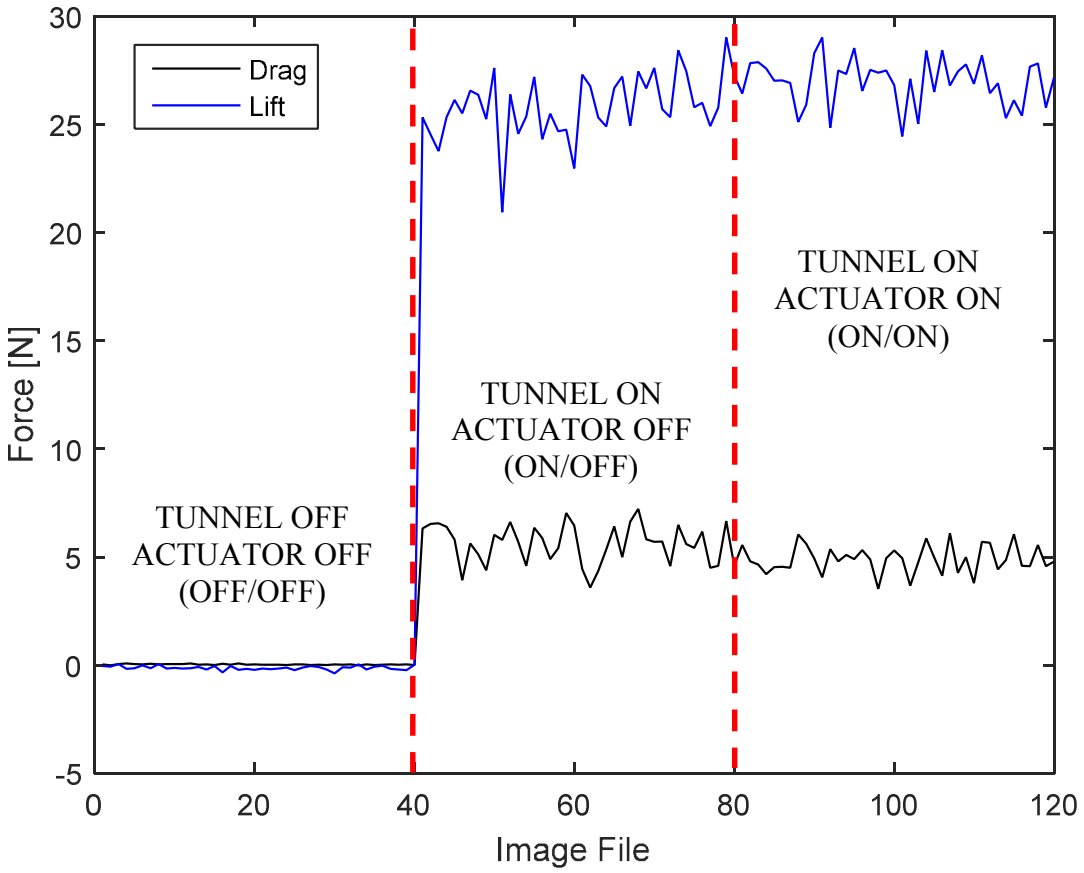

Figure 133. Lift and drag forces on NACA 0012 with strip type actuator installed. AoA = 11°; Re = 400,000.

The data in Figure 133 shows subtle trends that become more obvious when data from the 'ON/OFF' and 'ON/ON' conditions are overlaid. The data from Figure 133 has been reformatted to make these trends more clear and re-potted in Figure 134. The pseudo-time variable, 'Image File', has been temporally shifted to accommodate 0 at the origin and does not impact the analysis whatsoever. Statistical analysis is required to determine whether or not perceived trends are statistically significant.

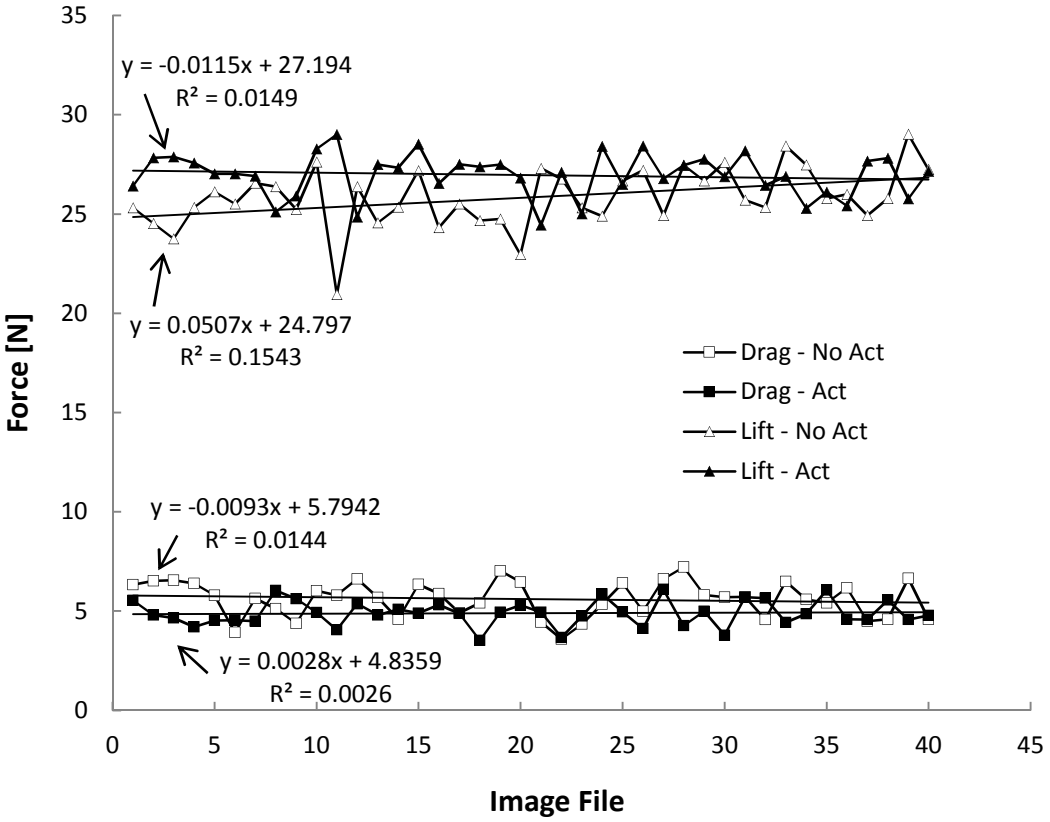

Figure 134. Overlaid lift and drag data from Figure 133. The wind tunnel is powered in all data shown and the actuator was powered as indicated. Least-squares linear fits are provided for clarity.

If sampling is truly independent, then time of acquisition should have no effect on the data. However, it appears that lift in the 'ON/OFF' condition gradually increases with time ('Image File'), and this is reflected in the relatively large slope given by the least-squares linear model. A single-variable linear regression analysis was performed on this data with null hypothesis, H_0: 'Image File' is not a predictor for the response variable

'Lift Force' (i.e., slope is zero). First, a residual plot was generated to check for normally distributed errors from the linear prediction, and this is shown in Figure 135.

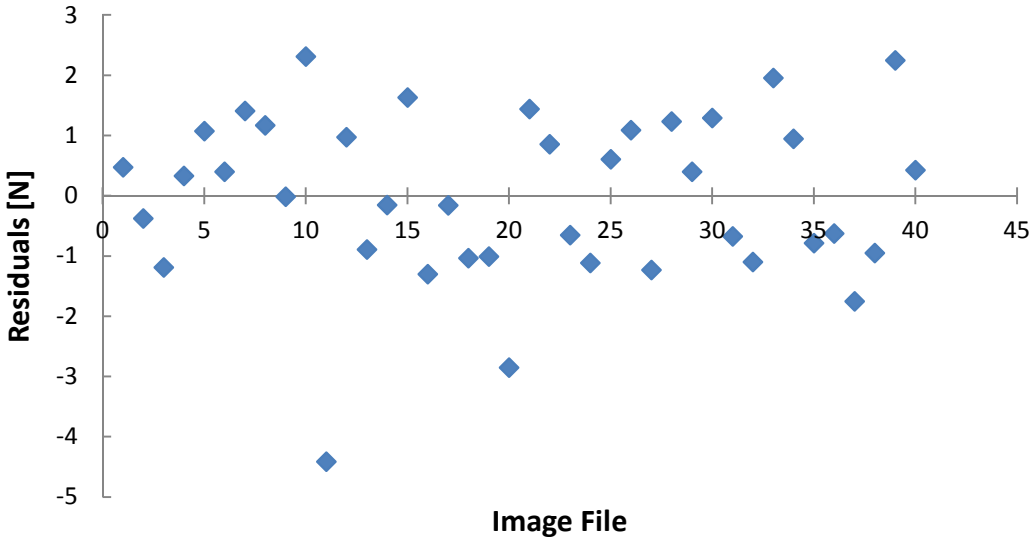

Figure 135. Residual plot for regression analysis of lift force in 'ON/OFF' condition.

The residual plot shows an even distribution of errors across image files, so the assumption of error normality is validated, warranting analysis of variance and t-test. The output of this test is provided in Table 23. The fact that the R^2 value is 0.15 has no impact on the validity of this output and only indicates that the signal to noise ratio is low. The test statistics ($F = 6.93$; $t = 2.63$; $p\text{-value} = 0.012$) show that the slope for lift in the 'ActOff' trial is a statistically significant estimation parameter at the $\alpha = 0.05$ level. Therefore, the apparent lifting force appears to be related to elapsed time. Since the

velocity in the wind tunnel is constant, a reasonable explanation for this behavior is that the sting to which the airfoil is mounted rotates gradually after the wind tunnel is powered. This would also explain the hysteresis observed in the calibration shown in Figure 131. Similar regression analysis was performed for the other least-squares slopes given in Figure 134. Residual plots from these trends show even error distribution about the modeled fit, and p-values of regression analysis were in the range $0.43 < p\text{-}value < 0.73$, indicating that time ('Image File') does not appear to influence measured aerodynamic forces. The other subtle trend is that the error in drag signal appears to decrease once actuation is initiated. This will be analyzed more rigorously in a following paragraph.

Table 23. Statistical linear regression analysis for lift force in the tunnel on/actuator off (ON/OFF_L) condition. Measured lift is time dependent with p-value = 0.012.

Model Summary (ONOFF_L)

R	*R Square*	*Adjusted R Square*	*Std. Error of the Estimate*
.39	.15	.13	1.41

ANOVA (ONOFF_L)

	Sum of Squares	*df*	*Mean Square*	*F*	*Sig.*
Regression	13.72	1	13.72	6.93	.012
Residual	75.20	38	1.98		
Total	88.92	39			

Coefficients (ONOFF_L)

	Unstandardized Coefficients		*Standardized Coefficients*		
	B	*Std. Error*	*Beta*	*t*	*Sig.*
(Constant)	24.80	.45	.00	54.70	.000
Image	.05	.02	.39	2.63	.012

The next set of statistical analysis examines whether or not the actuator is significantly affecting airfoil performance by increasing lift and/or decreasing drag. Group statistics and independent 2-sample t-test results are provided in Table 24 and Table 25, respectively. Analysis is also performed using a subset of the samples taken for the lift 'ON/OFF' condition. This was done in an attempt to capture and compare lift data after any potential airfoil drifting issues.

Table 24. Group statistics for lift and drag test conditions. Group names indicate tunnel power/actuator power. Asterisk denotes subset (last 25%) of population.

Group Statistics	Lift			Drag	
	ON/OFF	*ON/OFF**	*ON/ON*	*ON/OFF*	*ON/ON*
N	40	10	40	40	40
Mean	25.84	26.57	26.96	5.60	4.89
Std. Dev	1.51	1.39	1.10	0.91	0.64
S.E. Mean	0.24	0.44	0.17	0.14	0.10

Table 25. T-test results for lift and drag. Group names indicate tunnel power/actuator power. All groups are compared to the ON/ON group. Asterisk denotes subset (last 25%) of population.

Independent Sample Test (vs. ON/ON)	Lift		Drag
	ON/OFF	*ON/OFF**	*ON/OFF*
LEVENE'S TEST			
F	2.48	1.89	6.33
p-value	0.119	0.176	0.014
T-TEST			
t	3.80	0.96	4.04
df	78.00	48.00	70.25
p-value (2 tail)	0.000	0.342	0.000
Mean Diff	1.12	0.39	0.71
S.E. Diff	0.30	0.41	0.18
95% CI Lower	-1.71	-1.22	0.36
95% CI Upper	-0.54	0.43	1.06

Lift forces are examined first. A two sample t-test assuming equal variance is performed using data for the ON/OFF and ON/ON conditions. Equal variance should be assumed because the Levene Test for equality of variance is not significant at the $\alpha = 0.05$ level (*p-value* = 0.119) and the null hypothesis of equal variance cannot be rejected. All subsequent 2-sample independent t-test analysis assumes equal variance. The t-test checks the following null hypothesis - H_0: the mean lifting forces of the two conditions are equal. Results of this analysis show that the mean difference is statistically significant at the $\alpha = 0.05$ level, which can be interpreted as the actuator having a positive influence on lifting force. However, as was shown in the regression analysis, there is unaccounted for centroid displacement in the direction of the lift primary component. As such, a subset of the ON/OFF population was used as an additional

check. The ON/OFF* group is comprised of the last 25% (10 images) of recorded images in the ON/OFF condition. In this way the effect of unaccounted for centroid displacement can be minimized if most of the unaccounted for displacement is assumed to occur at the beginning of ON/OFF data collection. Comparing ON/OFF* v ON/ON with equal variance shows that the difference in means is not statistically significant at the $\alpha = 0.05$ level, and therefore, the actuator does not appear to significantly affect lift. Even if the last 50% of the ON/OFF data is used in the same analysis, effects are still not significant at the $\alpha = 0.05$ level with *p-value* = 0.166. Average lift forces for the NACA 0012 with strip type actuator at AoA = 11° and *Re* = 400,000 are approximately 26 N and unaffected by actuator usage.

A similar statistical comparison was performed for drag. Since the regression analysis indicated that drag could not be predicted by 'Image File' (pseudo-time) the entire sample could be used. Levene's test indicates unequal variance between the ON/OFF and ON/ON groups, so the following t-test is performed with the expectation of unequal variance between the conditions. The independent 2-sample t-test indicates that the mean drag in the ON/OFF condition is different than the ON/ON condition at the $\alpha = 0.05$ level ($t = 4.04$, *p-value* = 0.000). Therefore, the actuator appears to reduce drag. Drag in the unactuated case is 5.6 N and in the actuated case drag is 4.9 N, giving a drag reduction of 12%. Furthermore, the actuator appears to provide a more consistent flow field over the airfoil as indicated by the results from Levene's Test showing unequal variance.

It is necessary to compare these optical lift and drag measurements to those collected from the load cell control box which were given in Figure 123 and Figure 124. From the load cell voltage signal acquired data, lift and drag coefficient estimates are conservatively $C_{L,load} = 0.9$ and $C_{D,load} = 0.06$, respectively; from the optical measurements $C_{L,opt} = 0.7$, $C_{D,opt,unact} = 0.15$, and $C_{D,opt,act} = 0.13$. While the measurement from optical testing indicate that lift has decreased and drag has increased, both of which are undesirable effects, the comparison is not exactly fair because the airfoils where forces were measured via the control box had actuators embedded flush with the surface whereas in the optical tests the strip type actuator was not flush mounted and can act as a turbulator and affect the flow field and thus the aerodynamics. However, comparison between the two measurements is qualitatively consistent in the sense that it is somewhat consistent with prior research investigating the influence of NACA 0012 airfoil surface roughness and its impact on lift and drag [138]. While there is some discrepancy in the control box and optical aerodynamic force measurements, the differences are not radically different (< 22%) and vary in as would be expected with the presence of a turbulator. Therefore, the use of these optical diagnostics is sufficient to measure lift and drag in the presence of strong EMI that interferes with typical equipment used to measure aerodynamic forces, such as a load cell and control box.

The final consideration of the optical lift and drag measurement technique is the observed coupling of centroid displacement components which complicates the interpretation of results. According to the raw data calibration plots in Figure 130 and Figure 131 as applied drag increases lift appears to decrease, and as applied lift increases

the drag appears to increase, but these trends are not observed in the experimental data. Evidence of this claim lies in the ON/OFF condition. During this condition lift steadily increases over time, but there is no observed simultaneous shift in drag as would be expected if coupling were present. Furthermore, the drag is observed to decrease in the ON/ON condition, but there is no apparent change in lift when comparing the ON/OFF* and ON/ON conditions. Based on trends of the non-primary directional components as shown in Table 22, a 0.7 N reduction in drag should also give a displacement of approximately 0.0015 mm in the *y*-direction, and this corresponds to a 0.2 N increase in lift which is beyond the resolution limit of this experimental setup as the standard deviation of the lift primary directional component is >1 N. Therefore, the coupling effects seen during calibration are not clearly observed during measurement.

In summary, the actuated airfoil showed no statistically significant change in lift, but a 12% decrease in drag when the actuator was powered in slightly stalled conditions (AoA = 11°) at *Re* = 400,000. The optical approach to directly measure aerodynamic forces seems to be a reasonable technique for overcoming instrumentation limitations imposed by EMI from large pulsed currents, but excess noise in the wind tunnel resulted in signal-to-noise ratios that could be improved.

5.10 Conclusions

In these experiments a spark type plasma actuator for flow control over an airfoil was investigated. The actuator was first modeled in COMSOL to determine the effect of relevant dimensional scaling parameters, namely the aspect ratio, on produced jet

velocities. These numerical simulations suggested that the highest velocity jets were obtained when the aspect ratio was near 0.3. Mass flux across the throat exit plane was also examined numerically and was found to shift from longer duration low mass flux to short duration high mass flux as the aspect ratio approached unity. This information was helpful in the design of real actuators that were characterized with respect to their jet velocities and impulse bit generation.

High speed schlieren imaging and a torsional thrust stand were used to experimentally measure velocity and impulse bit generation, respectively. Max and average jet velocities were approximately 200 m s^{-1} and 100 m s^{-1}, respectively. Aspect ratios of 1 and 0.5 were compared as were the effect of increased pulsing frequency and discharge energy. Aspect ratio did not appear to strongly affect jet velocity as the average velocity for these two cases were both about 100 m s-1, but increased pulsing frequency and decreased discharge energy both resulted in average velocities of about 50 m s^{-1}. Measured velocities were approximately half that predicted by the simulations. Qualitative comparison of the jet structure for the two aspect ratios was in good agreement with the model. Lower aspect ratio actuators produced coherent jets representative of starting plumes discussed in the literature, and actuators with aspect ratio factor near unity produced jets that lacked well defined vortical features. Timing of experimentally observed jet behavior was also consistent with that shown in the model in that jet duration and refill times were similar.

A second set of six actuators was fabricated for thrust stand testing. These actuators differed in geometry and explored the effects of cavity length, cavity diameter,

throat length, throat width and throat angle. Each of the six actuators were individually tested on a calibrated thrust stand and impulse bit generation was determined by measuring angular deflections in the thrust stand. The actuator with the longer cavity (increased electrode spacing) imparted the greatest momentum which was measured as 9.8 μN-s and the actuator with the steep throat angle produced the minimum impulse bit of those actuators tested which was measured at 1.5 μN-s. A thermal fluids analysis was performed on the actuators to determine the jet velocity from the measured momentum by estimating the total amount of mass ejected in the jet from choked jet mass flow rates and duration of choked flow conditions. These velocities were within 50% of the max velocities measured using high speed schlieren imaging. These result help determine important parameters for designing actuators capable of producing higher impulse bit. The six actuators tested on the thrust stand were also imaged by infrared camera to assess their thermal performance. Actuator heating is a potential issue because it can result in decreased mass in the cavity as a result of thermal gas expansion. Reduced mass in the actuator cavity will likely result in a decrease in momentum generation. At constant power, the geometric variations did not appear to cause much variation in surface temperature, but large temperature increases were observed as power to a given actuator was increased, and this was expected. Steady state temperatures were achieved within 10 minutes for all thermal investigations, and at an input power of 94 W a maximum actuator outside surface temperature of 535 K was measured.

Several airfoils were fabricated, fitted with actuators (embedded and surface mounted strip type), and tested in a wind tunnel at $400{,}000 < Re < 540{,}000$. The first set

of experiments showed that actuators could be embedded within the airfoil without affecting the aerodynamics of the airfoil. A load cell and control box were used to make several repeated measurements of lift and drag at identical conditions, and these trials showed that airfoil fabrication techniques were somewhat inconsistent as indicated by qualitatively different lift versus AoA and drag versus AoA curves. Repeated measurements of the same airfoil showed measurement repeatability, but these same measurements also showed slight deviations from lift and drag characteristics given in the literature.

A small span airfoil was qualitatively tested in the wind tunnel at Re = 100,000 and 540,000. In these experiments the actuators effectiveness was assessed by the changing behavior of flow visualizing tufts affixed to the suction side surface of the airfoil. The airfoil was swept through a range of AoA and tuft behavior was observed. Imperfections associated with the installation of inserts in the test section resulted in complicated 3D flow patterns that delayed stall to AoA = 21°. When the actuators were powered stall was further delayed by an additional 0.8° and 1.8° for the Re = 100,000 and 540,000 tests, respectively.

To determine possible mechanisms of actuation, a full span (s = 0.58 m) airfoil equipped with a strip type actuator was tested at mildly stalled conditions when Re = 400,000. Actuation is thought to occur by some combination of the following two mechanisms: 1) direct momentum injection and/or 2) vortical entrainment of the free stream. Two trials were examined. In one case the mica strip actuator has its cover in place so that jets were directed tangential to the airfoil surface corresponding to the

direct momentum injection hypothesis, and in the other case the actuator did not have its cover so jets were effectively omnidirectional hemispherical point sources. This later case corresponds to the vortical entrainment hypothesis. Actuation was successful in both cases, and because no quantitative lift or drag data were collected, it is not possible to tell if either of these mechanisms is dominant. A better understanding of the mechanism by which actuation occurs would assist in designing more effective actuators, and this is an attractive area for future research.

The last experiment quantitatively and qualitatively investigated changes in lift and drag in an actuated and unactuated stalled (AoA = 11°) airfoil at Re = 400,000. In this experiment lift and drag forces were directly measured by observing microscopic deflections in a load cell while the actuator was power cycled. An optically-isolated method of directly measuring aerodynamic forces was required because of the severe EMI generated by the large sudden discharge currents that permanently damaged the load cell and its control box. The actuator was pulsed at ~50 Hz and had a pulse duration of 250 ns. Actuator effectiveness was also examined qualitatively by observing the motion of tufts secured to the airfoil suction surface, and the tufts indicated that actuation was possible between $10° < AoA < 11.5°$. Experimental results showed a 12% drag reduction when the covered strip actuator was powered, but no statistically significant changes were observed for lift forces.

The fact that a change in drag was measured without a corresponding change in lift is worthy of discussion. At similar *Re*, lift versus AoA curves for the NACA 0012 show linear increases in lift when $AoA < 10°$ and then a sharp drop in lift when $11° <$

AoA < 13°. Similar drag versus AoA curves show a sharp increase in drag when AoA > 13°. These lift and drag trends were presented in Figure 77 and Figure 78, respectively. In these experiments, lift and drag were measured at AoA = 11° which is near a range where drag changes more rapidly than lift. Lifting line theory predicts that if boundary layer separation is delayed to higher AoA then lift would continue to increase linearly with AoA, and drag would simultaneously decrease. However, this behavior is not observed and may be due to some combination of the following reasons. For one, some mechanical slack may be present in the airfoil-sting-load cell connections which allows for unwanted and unaccounted for deflection in the AoA. Such deflections would certainly impact lift and drag measurements depending on how much and in what direction the airfoil drifted during experimentation. The fact that the lift data increase with time in the tunnel on/actuator off condition supports the hypothesis that some airfoil drift did occur; however, if drift did occur, it would also be expected that similar trends manifest themselves in the drag data, which they do not. Another explanation for observing changes in drag without changes in lift could be due to the AoA at which the airfoil was tested. At 11° the slope of the lift line is somewhat flat but changes in drag occur abruptly. It is possible that changes in drag occur without corresponding changes in lift because near this AoA drag is more sensitive than lift to separation. In addition, the technique used to measure lift and drag relied on a calibration wherein the ratio of lift sensitivity to drag sensitivity was ~4:1, so similar perturbations are comparatively amplified in the lift direction. Ideally, sensitivities for the two measurements would be

similar. In either case these lift and drag measurements should be checked for repeatability.

This kind of full span actuator testing made it possible to calculate global performance characteristics of the strip actuator. The aforementioned drag reduction was accomplished using an active coverage, defined as ratio of total actuator spark gap length to airfoil span, of 13% with a pulsing duty cycle of 6 μs/s and a normalized power input of ~50 W per kW of flow power. These results are unique for spark actuator studies because this strip type sparking actuator has been integrated on a full span airfoil and tested in a wind tunnel where drag forces were directly measured.

6. CONCLUSIONS

6.1 Restatement of dissertation objectives

The objective of this dissertation is to enable and investigate new technologies which use pulsed plasmas to drive unique applications that require good control of energy delivery, and in general, this research is motivated by the need for a switching mechanism that can operate at kHz frequencies while switching 10s kV. To this end, a plasma switch capable of this extreme functionality was designed, fabricated and characterized. The switch itself was designed for the high pressures required to achieve 10 kV pulsing. In order to decrease gas cooling time scales and avoid thermal instabilities, convection was used in the switch. The connecting circuit was carefully designed to minimize stray inductance and capacitance for ns duration pulses. The use of small applied capacitance and minimized stray capacitance was also helpful in avoiding the thermal instability that encourages transition to stable modes. This work is the first to show such high voltage and high frequency operation by a plasma switch, and a manuscript is in preparation for journal submission.

The 100 μm DPF discussed in this work is the smallest reported on to date. The motivation for going to such small characteristic size is that 1) neutron production efficiency may scale as a^{-3}, and 2) smaller systems are more amenable to portability. However, smaller size DPFs typically require less energy input and thus produce fewer energetic particles than their larger counterparts. As such, small DPFs must be operated in an array and at high frequency to achieve a practically useful neutron flux. In addition,

DPFs of this size function best at pressures below atmospheric. This presents the challenge of driving a single DPF at kHz frequency. Such high frequency operation in low pressure environments will tend to transition to stable modes, and because the DPF is inherently a pulsed system, high frequency operation will essentially choke it. The high voltage high frequency switch, however, will allow for pulsed operation in relatively low pressure (< 1 atm) environments.

The spark type actuators for boundary layer reattachement discussed in this work have been numerically modeled, experimentally characterized and wind tunnel tested. The motivation for using spark type actuators is that they are mechanically simple devices that can produce synthetic jets having velocity in excess of 100 m s^{-1} and are amenable to control schemes. Dielectric barrier discharge actuators (an alternative plasma actuator) have been tested extensively, and their successes are documented in the literature. While DBD actuators are capable of affecting lift and drag, they cannot produce forces strong enough to overcome those encountered in high speed flow regimes. Spark actuators, on the other hand, are capable of operation at Ma > 2, and are an area of current research within the Plasma Experimental and Diagnostics Lab at Texas A&M. The issues with spark plasma actuation in high speed flow is that 1) this flow occurs at pressure below 1 atm and 2) pulsing frequencies must be comparable to a residence time characteristic of external flow conditions and surface geometry. Furthermore, successful spark plasma actuation will require strong synthetic jets which implies the need for high voltage operation. Specialized plasma switches are capable of attaining kHz/kV operation.

In summary, the objective of enabling new technologies via specialized plasma switching has been met with the development of a switching cell capable of kHz/kV operation. Two unique applications for this switch have been experimentally investigated in operating regimes that tend to resist plasma transition to stable modes so as to facilitate testing and understanding of their behaviors and capabilities. The following sections summarize experimental results, both qualitative and quantitative in greater detail.

6.2 Summary of completed tasks

Many individual tasks were required to complete the three different experiments discussed. The Gant chart in Table 26 itemizes major tasks completed for each project and the dates during which the work was performed. The labels given to these tasks are misleading in their brevity. For example, testing of each generation of DPF and switch required many sub-tasks such as design, fabrication, and troubleshooting. Such a process was often iterative. Manuscript(s) for each of these projects have either been published in the literature or are in various stages of preparation for submission.

Table 26. Gant chart of experimental tasks completed. For each academic year 1, 2 and S indicate Fall, Spring and Summer semesters, respectively.

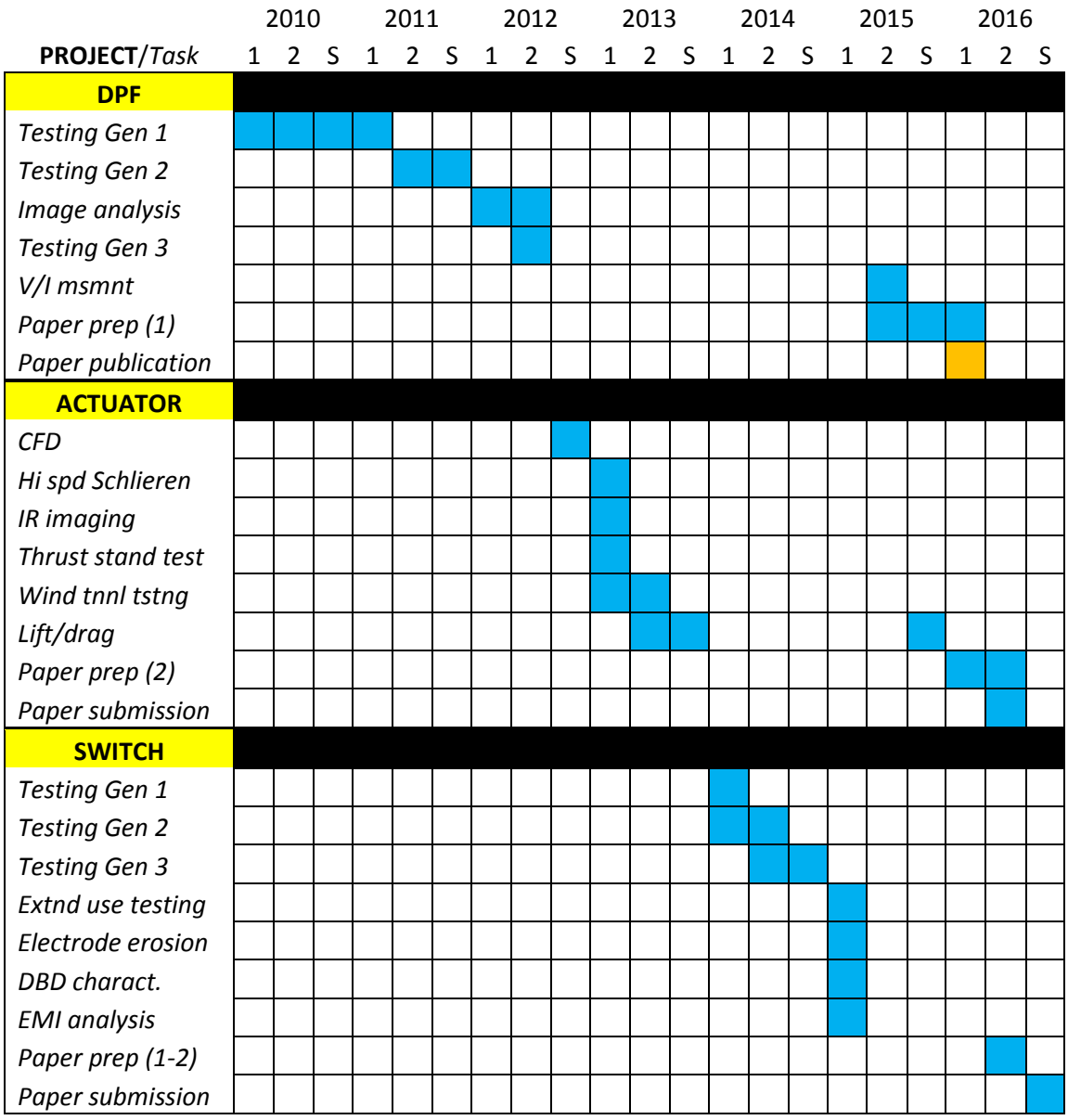

6.3 Summary of findings

6.3.1 High voltage kHz plasma switch

The plasma switch studies primarily investigated DC pulsing characteristics of three generations of switching cells. AC power sources were investigated using both switch generations, but available AC power supplies were underpowered and therefore insufficient to for the purposes of this study.

The first generation switch helped identify how plasma pulsing was affected by gas species, gas pressure, electrode material and use of convection in a direction normal to the discharge. Pulse waveform was also investigated as function of load side circuit elements. Responses to each of these effects were examined over relatively short duration samples that lasted on the order of 1 ms. Gases used in these experiments included helium, argon and molecular nitrogen. Helium was determined to be the preferred discharge gas because nitrogen discharges resulted in oscilloscope malfunction due to high current pulsing and argon discharges transitioned to stable modes at low currents. Generally, helium discharges in higher pressure delayed stable discharges to greater pulsed voltages at faster discharge frequencies. Both brass and graphite electrodes were used in high pressure helium discharges, and the use of graphite electrodes resulted in improved pulsing characteristics. Providing convection across the spark gap increased discharge voltage and consequently decreased discharge frequency as a result of the pulsing circuit requiring additional time to achieve higher voltages on the storage capacitor. Using 17 atm helium with cross convection in a spark gap having

graphite electrodes, a 10 kOhm resistor in parallel with a DBD received 11.2±0.3 kV pulses at 22.8±0.6 kHz with FWHM of 1000 ns.

The second generation switch allowed for comparisons between convection across the spark gap (Gen1) and axially along the spark gap (Gen2). Tungsten electrodes were used in these experiments due to the ablation of the graphite electrodes observed in the Gen1 experiments. Electrode ablation rates were quantified and will be elaborated upon later. The combination of tungsten electrodes and axial convection allowed for increased current from the power supply without having the switch discharge transition to a stable mode, and improved performance at short time scales was observed. The direction of convection (from anode to cathode or vice versa) had pronounced impact on pulse shaping and discharge frequency. Helium was used as the discharge gas, and with supplied current of 40 mA and a 10 kOhm resistor in parallel with a DBD load, convection from anode to cathode allowed pulsing of 23.0±1.4 kV at 12.2±1.4 kHz with FWHM of 20 ns and voltage rise rates of 700 V/ns. When convection was either 1) not applied, 2) directed from anode and cathode simultaneously, or 3) from cathode to anode, pulsed voltages were on average 12 kV with average pulsing frequency of 22 kHz. The pulsing characteristics between trial with anode sourced flow and the other three conditions are believed to be the result of unintended breakdown inside the pressure chamber. Loads were varied more extensively using the Gen2 set up. Load resistances of 1 kOhm and 500 Ohm were tested and pulse duration decreased with load resistance, but since there is less impedance in the load, charge is transferred more

easily, and this results in lower voltage at the load. Using a 500 Ohm load resistor, 7 kV pulses with FWHM = 200 ns were obtained.

The Gen3 tungsten electrode switch was designed to sustain operation at high pressure and also to provide axial convection through the spark gap. The Gen3 switch design also reduced conductor lengths to minimize stray inductance which extends pulse FWHM. This design allows high voltage high frequency operation within a circuit that has minimal impact on waveform time scales. Long duration trials of this switch showed a tradeoff between consistent pulsing and short pulse duration. Pulses with 7.2±0.3 ns FWHM were possible using a spark gap in parallel with DBD load. In this arrangement, pulsed voltages were 10.9±4.1 kV and pulsing frequencies were 25.1±8.7 kHz. With a 10 kOhm in parallel with DBD load, breakdown voltages and frequencies were more consistent, 9.9±0.9 kV and 19.6±1.6 kHz, respectively, but the FWHM of the pulses increased to 914±38 ns.

Electrode ablation and EMI mitigation were also studied during the switching tests. Anode and cathode electrode lengths were measured before and after extended use and changes in lengths were recorded. Changes in lengths were scaled by absolute number of pulses experienced by the electrodes. Graphite electrodes eroded at a rate of 211 $\mu m/10^6$ pulses. At a pulsing frequency of 20 kHz, this translates to an electrode erosion rate of 1 mm in about 4 minutes which is enough to significantly affect switch discharge characteristics after several minutes. The tungsten electrodes eroded at a maximum rate of 6 $\mu m/10^6$ pulses. Adhering to the previous usage assumptions, tungsten electrodes would require over 2 hours to erode by a similar amount. An antenna was

connected to an oscilloscope to record EMI radiated from the high voltage high frequency plasma switched circuit. Results from this test are somewhat intuitive. Detection of generated EMI is most accurate when excess cable lengths are eliminated from the measurement side of the test and when the measurement device is properly grounded. These steps alone reduced EMI detected at the scope by a factor of four and improves the accuracy of the measurement. Then EMI was compared with high voltage components unshielded and shielded. The shielding used in these experiments was a large stainless steel trough and the shielding was able to attenuate as much as 50% of the radiated EMI. This experiment shows that EMI, while a problem in the lab, is not necessarily an application issue since shielding can be incorporated into the final design.

Plasma switching is limited by the self-healing rate of the gas in the switch. The gas must undergo rapid ionization and then return to a mostly neutral state before subsequent discharge, and charged species removal is mostly dominated by diffusion, especially when ionization fractions are low. Ionization processes are sufficiently fast as evidenced by the < 10 ns voltage rise times and voltage rise times are mainly limited by inductance in the circuit. High pressure operation encourages faster diffusion as discharge diameters constrict at high pressure and cause larger gradients in charged species density.

Thermal instability can have a negative impact on switch behavior, especially at high frequency operation. Ideally, repetitive breakdown would maintain a cold cathode so that electron generation is dominated by secondary electron emission at the cathode and not thermionic emission, which would result in runaway electron generation and

consequently reduced breakdown voltages. Gas channels are also influenced by thermal instability. Repeated discharge heats the air and ultimately enhances *E/n*, which increases the number density of free electrons. The additional free electrons allow the plasma to carry more current and thus cause further gas heating. This chain reaction reduces breakdown voltage and pushes the plasma closer to a stable non-pulsing mode. Both of these effects, electrode and gas heating, become stronger as pulsing frequency increases, and they are believed to be the cause of the transition from the 10 kV/20 kHz mode to the 5 kV/40 kHz mode. Forced convection was used in these experiments to maintain cool temperatures at the electrodes and in the discharge gas, and prudent circuit design helped reduce stray capacitances which encourage thermal instability.

6.3.2 Microscale dense plasma focus

The dynamics of two microscale DPFs were investigated using ns time resolved ICCD imaging correlated with time to peak current. Both DPFs were located in a 50-200 torr He environment and were pulsed using a plasma switch in air. Anode radii of the DPFs were 550 μm and 100 μm, and at the time of writing were the smallest in the world. The operating pressure of these DPFs is relatively large compared to other similar devices that operate in 1-10 torr environments, and this is because good breakdown and rundown symmetry, both of which are required for successful pinching, occurs when *pd* scaling is maintained. Because the anode radii are μm scale, increased pressure is required to keep *pd* in the vicinity of minimum Paschen predicted breakdown voltage. Image analysis from the microscale DPFs showed symmetric breakdown and rundown

phases which are characteristic of pinching. This is encouraging for the exploration of smaller devices and will aid in device design. As was introduced in this work but not addressed, the efficiency of energetic neutron production from DPFs may scale as a^{-3}, thus further motivating exploration of smaller anode sizes. More efficient neutron production will facilitate the design of portable systems which would ultimately be power supply limited, but in order to achieve a practically usable neutron flux, thousands of microscale DPFs must be operated simultaneously at greater than kHz pulsing frequencies. Such a device would be portable and capable of producing energetic neutrons on demand. With these systems, neutron imaging, which is important for medical and military personnel, no longer relies on the use of radioactive materials that require special handling due to continuous emission, and remote locations may be actively interrogated as in the case for IED detection.

6.3.3 Plasma actuator for flow control

A unique slotted plasma actuator was simulated using COMSOL multi-physics software and the actuator jet characteristics were described as a function of actuator geometry. Actuators in the simulation generated the highest jet velocities when actuator aspect ratio was approximately 0.3. Qualitative jet behavior showed that at low aspect ratio, jets were longer lasting and had more coherent and directed structure. Jets from high aspect ratio actuator had reduced velocity and ejected their mass in more of a bulk fashion that lacked clearly visible coherent structure. Knowledge gained from the

simulations was used to design sets of slotted actuators that were experimentally characterized with respect to their jet behavior and impulse generation.

Schlieren imaging techniques were used on one set of actuators to image the jet. High speed videos of schlieren imaged jets were recorded and used to characterize jet velocity and jet structure. Aspect ratios of 1.0 and 0.5 were tested, and a maximum jet velocity of 95 m s^{-1} was observed. Jet velocity was proportional to energy input and inversely proportional to pulsing frequency. This indicates that actuators should be provided sufficient energy and pulsed only as fast as required by external flow conditions to maintain the highest velocities. This is a result of gas heating in the actuator cavity and pulsing at frequencies faster than characteristic actuator recovery times. The qualitative jet behavior seen in simulations was observed in experiments although predicted jet velocity was different. Interestingly little difference in jet velocity was observed between actuators having different aspect ratios.

Actuator single pulse impulse bit generation was investigated using a torsional thrust stand. For these experiments a second set of actuators having various geometries were mounted on the thrust stand and rotational deflections of the thrust stand were calibrated to impulse bit generation. Maximum impulse bit generation of 9.3 μN-s was observed for the largest actuator which had the largest spark gap distance. As a consequence, this actuator also had the largest cavity volume and therefore increased available discharge mass. All other actuators tested has similar cavity volumes, and among these the actuator with similar cavity and discharge diameters performed best with an impulse bit generation of 6.8 μN-s. This is likely due to more efficient transfer

of electric energy in the pulse to thermal energy in the working fluid. It can be concluded that actuators with long narrow diameter spark channels are best suited for impulse bit generation. All other actuators had impulse bits ranging from 1.5-4 μN-s.

At strip type actuator was tested on a NACA 0011 in a wind tunnel at *Re*=400,000 to measure changes in drag and lift. The airfoil had span of 58 cm and chord of 30 cm. The actuator consisted of a linear array of 21 spark gap actuators, each having a distance of 3.5 mm, and was mounted on the suction side surface of the airfoil so that jets were tangent to the airfoil surface and in the direction of the freestream. Actuators were powered by pulsing 92 kV at 20-40 Hz in an air plasma switch. The airfoil was set to AoA = 11° and tufts placed on the airfoil surface indicated local flow separation while the wind tunnel was powered. Drag and lift were directly measured using an optically isolated approach whereby microscopic deflections in a load cell were calibrated to lift and drag forces. Unactuated drag and lift were measured while the wind tunnel was powered and then drag and lift were measured again with the acutators on. Statistical analysis on the changes in aerodynamic forces showed a 12% reduction in drag, but no significant change in lift. Reductions in drag are expected as these forces are more closely related to boundary layer separation. Changes in lift may be present but undetectable due to noise inherent in the wind tunnel and this is worthy of future investigation. Full span wind tunnel testing of spark actuators is a new area of research and allows calculation of global actuator performance characteristics. The observed changes in drag utilized an active coverage of 13% with a pulsing duty cycle of 6 μs/s.

Actuator power was normalized by flow power and determined to be ~30 W per kW of flow power.

6.4 Conclusions

6.4.1 High voltage kHz plasma switch

These experiments demonstrate the shortcomings and robustness of plasma switches. The primary shortcomings of the plasma switch are its inconsistent operation and heavy reliance on convection, and the two are likely interconnected as previously discussed. On the other hand, these switches are capable of handling large current without sustaining damage and can hold arbitrarily large standoff voltages. The switches do not rely on complicated pulse shaping circuit topologies and excluding the intended load, they are therefore not limited by extraneous circuit elements. Because of their relative simplicity, they are inexpensive to fabricate and immune to EMI, which could be used to disrupt more complicated pulsing circuits. Experiments have shown that these switches can supply ns duration high voltage pulses at kHz frequencies which could be suitable for a wide array of applications. Among these applications are the dense plasma focus for high energy particle generation and the plasma actuator for flow control.

6.4.2 Microscale dense plasma focus

The microscale DPF is a very interesting application and is worthy of continued research. Although presently unoptimized, image analysis of the DPF indicates behavior characteristic of the pinching process. Therefore there is no convincing evidence

suggesting that the device will not function as an energetic particle source due to its small size. Furthermore, there is currently no indication of a minimum size limitation. Rather, it appears that smaller devices are more inclined towards symmetrical process that are imperative for effective pinching. The main limitation on array density is likely more closely related to interfering breakdown and post-pinch processes between neighboring DPFs rather than strict electrode geometrical considerations. The tendency towards symmetry at small electrode size is especially promising if the intention is to simultaneously operate many of these devices as part of an array, and such dense operation will be required if practically usable fluxes of energetic neutrons or x-rays are sought. The availability of these energetic particles in an 'on demand' basis provides an additional layer of safety to their use as compared to traditional energetic particle sources like the Cf-252 radioisotope that spontaneously fissions and constantly emits. Furthermore, Cf-252 is ~$15,000/emitter and usable only on time scales on the order of its half-life, which is <3 yrs, whereas deuterium gas is ~$20/L and is only consumed during application. Financial considerations thus make arrayed microscale DPFs more attractive by shifting one component of operating expense from an elapsed time basis to usage time basis, and this can have tremendous impact on cost savings depending on usage frequency.

Because arrayed microscale DPFs are ideally small densely packed systems, they may be portable with the main limitation being a suitable power supply. Portability allows these devices to be remotely operated in isolated regions, terrestrial or otherwise. Examples of use in remote locations include 1) medical imaging for those in

undeveloped areas, 2) active interrogation for IEDs in hostile areas, and 3) ignition source for sub-critical mass fission based power supply for space missions. One downfall of remote operation is the possibility of component failure. Since these are densely packed systems some degree of redundancy is inherent in their design. Should a single DPF in the array fail, performance of the system as a whole will only vary by N^{-1}, where N is the number of arrayed elements. Further development of this application is required but technical issues associated with delivering sufficient pulsed power to the DPF array in unfavorable environmental conditions are largely addressed with gas phase switching.

6.4.3 Plasma actuator for flow control

The plasma actuator for flow control is capable of reattaching separated flows and this has been experimentally verified through measured drag reduction and flow visualization. Sparking plasma actuators have several practical advantages other than drag reduction. They are inexpensive to fabricate, highly configurable, amenable to retrofitting & control schemes, and safe under failure. With respect to commercial use, this presents a financially and socially valuable opportunity to safely reduce operating costs by decreasing fuel consumption. Determining a generalized fuel cost savings that can be applied to all aircraft is difficult, but comparing drag reduction to thrust savings for specific flight conditions can provide case specific fuel cost savings. The savings are not only financial, but environmental as well. Reducing fuel consumption helps reduce emission of CO_2, a known greenhouse gas. Simple payback periods are minimized due

to their low material cost and ease of installation. These factors working in concert can have significant impact on their economic attractiveness, especially considering the large scale of commercial flight operation.

Potential usefulness also exists from a military perspective where high performance is the goal. The data presented in this work showed drag reduction but no corresponding change in lift, but this may be due to limitations in testing. Theoretically, these actuators can suppress boundary layer separation and extended flight regimes to increased angles of attack beyond those which traditionally result in stall. Greater lift will improve craft maneuverability and allow for slower stall speeds, and both of these benefits provide pilots with additional safety. Aggressive maneuvering may be required for evasive tactics, and reduced stall speed facilitates landing on spatially confined areas such as aircraft carriers. Increased lift also allows increased payload and/or operational range, and these are important considerations for all variety of flight missions whether their intent is combat or aid.

Much of the prior work on spark type actuators is involved in characterization of single actuator performance with respect to generated jet velocity and impulse bit, but there remains a lack of full span wind tunnel testing and this is where future actuator research should be directed. Typical flight conditions for those applications previously discussed occur at $Re>10^6$ and at altitudes where the pressure is <225 torr and temperature is near -50° C. Actuator pulsing frequency is an important operational parameter, and more energetic pulses are demanded at higher frequency as external flow

conditions become more extreme. Gas phase switching enables this technologies use in these low pressure environments where discharges want to shift to stable modes.

6.5 Future work

This dissertation investigates and enable new technologies that rely on pulsed plasma switches to drive specific applications. In this work plasma switches are investigated as are two unique applications, the microscale DPF and the spark plasma actuator for flow control, that are driven by the switch. Both of these applications have potential use in environments where the required high pulsing frequency is limited by the plasma dynamics controlled by the environment. Although isolated and studied as an individual discharge, a large array of DPFs could be implemented as a high energy neutron source for a subcritical mass of fissile material that could be used as a power-dense fuel for long duration operations such as space exploration. In order to achieve the required neutron flux for fission, thousands of these actuators must be operated at kHz frequencies. The plasma actuators have demonstrated their effectiveness at controlling boundary layer separation and drag reduction on airfoils at $Re < 106$ and $Ma < 1$, but other current research [139] has investigated the application of similar actuators operating in low pressure environments and $Ma = 2.2$. At such high speeds, actuator discharge frequencies should be on a time scale of the order of the external flow transit time, which is quite rapid. Both of these potential applications will require high pulsing frequency in a low pressure environment, and obtaining such high discharge frequency is only possible by controlling plasma dynamics at the switch. Therefore, it is important to

identify and understand conditions necessary to shift the plasma dynamics at the switch to a regime that is amenable to pulsing conditions required by the ultimate application.

6.5.1 High voltage kHz plasma switch

The following list of tasks itemizes known issues or areas of interest. Solutions to these items are then elaborated upon.

1) Testing with larger power supply
2) Closed loop gas flow and cooling for switch
3) Modified geometries and flow patterns to enhance cooling and mode stability
4) Long term stability testing

- **Task 1:** *Testing with larger power supply*

  The attainment of high voltages and frequencies requires the use of high power drivers for the switching system. Using lower power systems (currently available, ~ 1.5 kW) frequencies as high as 1.0 MHz have been demonstrated with the switching technology, as have voltages as high as 50 kV. These have been demonstrated independently. In combination the best operation has been around 20 mJ at 20 kV and 20 kHz. This requires a power through the switch of at least 400 W and average current of 40 mA for operation. The DC system used in this work was current limited at 40 mA. A fraction of the power going through the switch is dissipated in the switch depending on the impedance of the load. Additional power and voltage are needed by the driver due to the ballast

resistance in the circuit. This ballast resistance is needed for two reasons 1) to filter and attenuate the reflected power from the switch and load that can damage the solid state switches and diode in the DC power supply and 2) to isolate the switch and circuit from the output capacitance of the power supply, which alters the energy per pulse. Investigations typically used R_{bal}=500 kΩ which dissipated about 800 W and 20 kV. The ballasting is inefficient and consumes almost 67% of the pulsing circuit input power. This ballasting was a low cost solution allowing the use of existing laboratory power supplies for this research.

The same methods for powering the ns-pulser will not scale to 50 kV and 50 kHz. Using the current circuit the DC power supply would require 275 kV, 0.5 A, and 138 kW performance characteristics. The ballast resistance would consume an undesirable 91% of the power. The preferred solution is to purchase a less regulated and conditioned DC power supply as the driver for the switch. The power supply would be specifically designed for this application and compatibility with the switch. The DC driver would have a variable output capacitance requiring no isolation of the output capacitance from our switch, and also would be unregulated with regards to current (only having voltage control) and thus would be significantly more robust to reflected power. As the system has a positive impedance, pulsing frequency and current would still be voltage controlled, and no ballast resistance would be required, making system efficiencies significantly higher. Minimum system requirements would be about 60 kV, ~0.5 A (unregulated), and 15 kW to pulse 125 mJ at 50 kV and 100 kHz.

To account for uncertainties in efficiency and adaptability for other pulse energies a system capable of 75 kV, ~1 A (unregulated) and 35 kW would be used. This solution is more efficient and very robust. A second advantage of such a power supply is that the DC rectifier can be removed giving a high voltage AC signal usable in testing of the AC configurations explored. The advantage of the AC operation is further improved efficiency and bipolar pulsing. The disadvantage is a narrow range of frequencies (~75 kHz - 400 kHz, dictated by the transformer design). In DC operation the frequency range would be 0 Hz to about 150 kHz (for 0.125 J/pulse).

- **Task 2:** *Closed loop gas flow and cooling for switch*

Helium was selected as the operating gas in the experiments due to its high thermal conductivity, inertness, and relatively low rate of electronic to translational energy transfer. Trace addition of other gases (such as N_2) was also shown as beneficial as they can reduce switch size, reduce required pressure while maintaining voltage, and also quench more rapidly. Use of mixed gases could provide 'best of both worlds' operation, but helium will likely remain a major component due to its attractive thermal properties. The high flow rates of helium used in the convective cooling of the spark gap switch and electrodes is not sustainable for extended operation unless recirculation is incorporated. The helium can be recirculated relatively simply using a compressor and heat exchanger in a closed loop. The compressor would need to make up the

approximately 50-75 psi drop in pressure through the spark gap. The system would be charged with an appropriate amount of gas to have the desired pressure. The heat exchanger would potentially need to dissipate as much as 12.5 kW when load impedance is very low (< 1 Ω, and significantly less than the switch impedance), but would more likely handle 3-5 kW on a regular basis. As the gas leaving the switch is typically about 50-100 ^{o}C above the inlet temperature, the switch inlet gas temperature need only be constant and within 50° C of ambient.

- **Task 3:** *Modified geometries and flow patterns to enhance cooling and mode stability*

  Significant effects on the switching behavior were noted based upon gas flow and electrode configuration. For example, flow from the hot cathode into the gap of the switch favored a higher temperature, higher frequency, lower voltage pulsing mode. Flow exiting over the cathode favored a lower temperature, lower frequency, higher voltage pulsing mode. Conceivably, either mode could be optimized to be repeatable and satisfy the voltage and frequency requirements. Adjusting flow rate would control the switch to ensure repeatable mode operation in either cold or warm gas mode. Maintaining cold cathode was a goal in this research, and it was challenging in long duration runs. Actually operating in the higher temperature mode and increasing voltage by increase gap length and pressure may actually be easier to control. There are also some minor optimization in fabrication and geometries to get more symmetric flow patterns

to enhance cooling and mode stability. Additionally, electrode geometries other than collinear, such as concentric, can be explored.

- **Task 4:** *Long term stability testing*

  In long duration testing, repeatable operation and electrode wear and lifetime have been tested. Electrode wear does occur but is not a significant issue as the rates are relatively slow, on the order of 10,000 μm^3 / 10^6 pulses (6 $\mu m/10^6$ pulses on the wire electrodes). Nonetheless for very long duration runs electrode erosion could become an issue affecting a 10% change in gap length and 10% change in voltage after about 3 billion pulses, which would take about 8 hours at 100 kHz switching. Electrode wear could lead to an increase in voltage and decrease in frequency. Installing a voltage monitor and controlling for voltage by changing the pressure would be one way to address this. Pressure could be varied by a factor of 2, allowing for a 200% change in gap length and increasing lifetime by a factor of 20. Others ways to address this are to have replaceable or parallel electrode systems as these are low cost components. A third way to increase lifetime is to increase electrode surface area. Thus the volumetric erosion rate would have less of an effect on gap length. This could be done with larger wire electrodes or changing from a coaxial geometry to a concentric electrode geometry. Convective effects may be enhanced using a concentric geometry by restricting gas passage to the immediate electrode region.

6.5.2 Microscale dense plasma focus

The following list itemizes known issues or areas of interest. Solutions to these items are then elaborated upon.

1) Optimization of load side circuit to reduce stray inductance
2) Operation in deuterium environment and neutron measurement
3) Operation of a single DPF at high pulsing frequency
4) Operation of multiple DPFs simultaneously using a single plasma switch

- **Task 1:** *Improve load side circuit to minimize stray inductance that impedes rapid switching.*

  Stray inductance in the load side circuit resists rapidly pulsed current, and large peak currents are required for magnetic compression to be sufficient for fusion. Inductance in the circuit extends the duration of the discharge so that charge is transferred over longer time scales, thus reducing peak current. The present DPF system is known to be unoptimized in this respect. Estimated inductance of the tested circuit is on the order of 1000 nH which is large compared to similar devices which have inductance in the 5-20 nH range. The stray inductance in this system likely comes from the ~30 cm lengths of mm diameter conductor used to connect the DPF head in the pressure chamber to load side circuit, and this is mainly because of the large size of the pressure vessel used. A smaller pressure vessel will not require such long cable runs to high voltage and ground side connections.

- **Task 2:** *Operate the microscale DPFs in deuterium/tritium environment and measure neutrons.*

  These experiments used image analysis to assess behavior characteristic of the pinching process that causes fusion. Although the DPF shows evidence of pinching, fusion is not likely occurring because 1) He^4 will not readily fuse with itself and 2) DPF pulsing has not been optimized (see Task 1 above). Once pulse durations have been minimized, DPF operation in deuterium/tritium environments should be investigated. Both deuterium and tritium will fuse with themselves and they will also fuse with each other. The ultimate proof of fusion is the production of energetic neutrons which can be measured using either gas detectors or scintillators. Other high energy components, such as x-rays, can be measured with appropriate film.

- **Task 3:** *Explore upper limits of pulsing frequency*

  These experiments examined a single microscale DPF assembly at low pulsing frequency. In practice one such unit cannot provide a practically useful neutron flux, so higher frequency operation is required. Determining the upper limit on pulsing frequency will provide necessary information for sizing an array of these devices. The anticipated limitation to pulsing frequency is recovery of the gas in the vicinity of the DPF anode, and this has been observed to require at least several μs. One benefit here of moving to smaller anode geometries is the dependence on increased operating pressure. Higher pressure operation will

promote diffusion of species away from the anode region and decrease recovery time.

- **Task 4:** *Drive multiple DPFs simultaneously using a single plasma switch*

  This is essentially and extension of Task 3 above. If one only one DPF assembly were used, it would require pulsing frequencies on the order of MHz to provide a practically useful neutron flux. Since these devices require high voltage pulses, MHz frequency operation is even a challenge for the switch. Therefore, many DPFs must be fired simultaneously. A good first investigation would examine whether or not it is possible to fire two DPFs simultaneously from the same pulsing circuit. Breakdown in DC pulsed systems typically occurs along a single channel since charge follows the path of least resistance. However, the DPF geometry is different from typical planar breakdown, and changes in the plasma resistance during the compression process may self-correct and more readily allow simultaneous breakdown across two or DPF assemblies.

6.5.3 Plasma actuator for flow control

The following list itemizes known issues or areas of interest. Solutions to these items are then elaborated upon.

1) Full span actuator testing in higher quality wind tunnel
2) High fidelity flow visualization using PIV and/or CFD to determine mechanism of boundary layer reattachment

3) Investigate actuated drag reduction as a function of AoA
4) Optimization of global performance characteristics

- **Task 1:** *Full span actuator testing in higher quality wind tunnel*

  Actuated airfoil testing was limited by the primary air mover to Re ~400,000. Furthermore, the wind tunnel was not characterized, so it is difficult to determine if the flow contains turbulence which could affect lift and drag measurements by providing undesirable flow conditions at the airfoil surfaces. During operation the mounted airfoil would knock against the test section walls, and this may indicate that some large scale low frequency eddies are present in the free stream. Ideally the airfoil would be mounted directly to the walls of the test section so that forces on the sting (primarily drag) are removed from measurements.

- **Task 2:** *Elucidate mechanism of boundary layer reattachment*

  Boundary layer reattachment was originally thought to be due to momentum injection. In this mechanism momentum from the actuator jet is directly used to combat the adverse pressure gradient development responsible for separated flows. However, when the strip actuator was uncovered which allowed free hemispherical gas expansion, boundary layer reattachment could still be controlled. Thus air from the freestream may be entrained by the expansion and pulled by vortical structures toward the airfoil surface. This high

velocity, which did not originate from the jet is then used to overcome adverse pressure gradients. Temporally and spatially resolved CFD simulations will help identify whether direct momentum injection or vortical entrainment is the dominant contributor to boundary layer reattachment. Experimentally, high fidelity PIV systems could be used to observe prevailing flow patterns and determine reattachment mechanisms.

- **Task 3:** *Investigate drag reduction as a function of AoA*

  Drag reduction was only measured at one AoA when the airfoil was just above the stall AoA. It would be beneficial to determine the actuators effect on lift and drag through a range of AoA to learn how the actuator interacts with these aerodynamic forces in different flight conditions including normal flight (no separation) as well as hard stalls where the actuators do not appear to be able to reattach the flow.

- **Task 4:** *Optimization of global performance characteristics*

  Global performance characteristics were used to describe actuator operation. These characteristics included time required to initiate reattachment, delay to detachment, pulsing duty cycle, active coverage and flow normalized power requirements. Although these global characteristics were introduced and described, no attempt was made to optimize them. A very direct impact on operating efficiency can be made by investigating each of these characteristics

and adjusting actuator operation. It may be possible to minimize pulsing frequency and active coverage, and reductions in both of these parameters result in reduced power consumption.

WORKS CITED

[1] R. Nuccitelli, U. Pliquett, X. Chen, W. Ford, J. Swanson, S. Beebe, J. Kolb and K. Schoenback, "Nanosecond pulsed electric fields cause melanomas to self-destruct," *Biochemical and Biophysical Research Communications,* vol. 343, no. 2, pp. 351-360, 2006.

[2] Z. Li, S. Sakari, C. Yamada, D. Wang, S. Chung, X. Lin, T. Namihira, S. Katsuki and H. Akiyama, "The effects of pulsed streamerlike discharge on cyanobacteria cells," *IEEE Transactions on Plasma Science,* vol. 34, no. 5, pp. 1719-1724, 2006.

[3] M. Simek and M. Clupek, "Efficiency of ozone production by pulsed positive corona discharge in synthetic air," *Journal of Physics D: Applied Physics,* vol. 35, no. 11, 2002.

[4] T. Oda, T. Takahahshi and K. Yamaji, "Nonthermal plasma processing for dilute VOCs decomposition," *IEEE Transactions on Industry Application,* vol. 38, no. 3, pp. 873-878, 2002.

[5] J. Rossi and M. Ueda, "A 100kV/200A blumlein pulser for high-energy plasma implantation," *IEEE Transactions on Plasma Science,* vol. 34, no. 5, pp. 1766-1770, 2006.

[6] Z. Shen, M. Johnsson, Z. Zhao and M. Nygren, "Spark plasma sintering of alumina," *Journal of the American Ceramic Society,* vol. 85, no. 8, pp. 1921-1927, 2002.

[7] J. Eden, C. Wagner, J. Gao, N. Ostrom and S. Park, "Microdischarge array-assisted ignition of a high-pressure discharge: Application to arc lamps," *Applied Physics Letters,* vol. 79, no. 26, pp. 4304-6, 2001.

[8] National Research Council, Plasma Science: Advancing Knowledge in the National Interest, Washington D.C.: The National Academies Press, 2010.

[9] Q. Hong and A. van de Walle, "Prediction of the material with the highest known melting point from ab initio molecular dynamics calculations," *Physical Review B,* vol. 92, no. 2, 2105.

[10] Y. Raizer, Gas Discharge Physics, Berlin: Springer-Verlag, 1991.

[11] J. Meek, "A theory of spark discharge," *Physical Review,* vol. 57, no. 8, p. 722, 1940.

[12] L. Loeb and J. Meek, "The mechanism of spark discharge in air at atmospheric pressure," *Journal of Applied Physics,* vol. 11, no. 6, pp. 438-447, 1940.

[13] D. Staack, B. Farouk, A. Gutsol and A. Fridman, "Stabilization of the ionization overheating thermal instability in atmospheric pressure microplasmas," *Journal of Applied Physics,* vol. 106, no. 1, 2009.

[14] A. El-Hag, S. Jayaram and M. Griffiths, "Inactivation of naturally grown microorganisms in orange juice using pulsed electric fields," *IEEE Transactions on Plasma Science,* vol. 34, no. 4, pp. 1412-1415, 2006.

[15] E. Shcolnikov, A. Chebotarev, S. Maslennikov, N. Netchaev and D. Petrov, "Atmospheric pulsed diffuse discharge in highly non-uniform fields to be used for sterilization and decontamination," in *IEEE Pulsed Power Conference*, Monteray, 2005.

[16] M. Sack, C. Schultheiss and H. Bluhm, "Triggered Marx generators for the industrial-scale electroporation of sugar beets," *IEEE Transactions on Industry Applications,* vol. 41, no. 3, pp. 707-714, 2005.

[17] W. Wang, Z. Zhao, F. Liu and S. Wang, "Study of NO/NOx removal from flue gas contained fly ash and water vapor by pulsed corona," *Journal of Electrostatics,* vol. 63, no. 2, pp. 155-164, 2005.

[18] J. W. Mackersie, I. Timoshkin and S. MacGregor, "Generation of high-power ultrasound by spark discharges in water," *IEEE Transactions on Plasma Science,* vol. 33, no. 5, pp. 1715-1724, 2005.

[19] M. Gaudreau, T. Hawkey, J. Petry and M. Kempkes, "Solid-state power systems for pulsed electric field (PEF) processing," in *IEEE Pulsed Power Conference*, Monterey, 2005.

[20] E. Schamiloglu, R. Barker, M. Gundersen and A. Neuber, "Modern pulsed power: Charlie Martin and beyond," *Proceedings of the IEEE,* vol. 92, no. 7, pp. 1014-1020, 2004.

[21] S. Roche, "Solid state pulsed power systems," *Physique & Industrie,* vol. 17, 2003.

[22] L. Redondo and J. Silva, "Flyback versus forward switching power supply topologies for unipolar pulsed-power applications," *IEEE Transactions on Plasma Science,* vol. 37, no. 1, pp. 171-178, 2009.

[23] S. Bae, A. Kwasinski, M. Flynn and R. Hebner, "High-power pulse generator with flexible output pattern," *Power Electronics,* vol. 25, no. 7, pp. 1675-1684, 2010.

[24] W. Saito, Y. Takada, M. Kuraguchi, K. Tsuda, I. Omura, T. Ogura and H. Ohashi, "High breakdown voltage AlGaN-GaN power-HEMT design and high current density," *IEEE Transactions of Electron Devices,* vol. 50, no. 12, pp. 2528-2531, 2003.

[25] M. Gundersen, J. Dickens and W. Nunnally, "Compact, portable pulsed power: physics and applications," in *IEEE Pulsed Power Conference*, Dallas, 2003.

[26] M. Gaudreau, J. Casey, T. Hawkey, M. Mulvaney and M. Kempkes, "Solid-state pulsed power systems," in *IEEE Power Modulator Symposium*, Rancho Mirage, 1998.

[27] J.-J. Laurin, S. Zaky and K. Balmain, "On the prediction of digital circuit susceptibility to radiated EMI," *IEEE Transactions of Electromagnetic Compatibility,* vol. 37, no. 4, pp. 528-535, 1995.

[28] H. Rahaman, J. Nam, S. Nam and K. Frank, "Investigation of spark-gap discharge in a regime of very high repetition rate," *IEEE Transactions on Plasma Science,* vol. 38, no. 10, pp. 2752-2757, 2010.

[29] T.-Y. Hsu, G. Kirkman-Amemiya and M. Gundersen, "Multiple-gap back-lighted thyratrons for high power applications," *IEEE Transactions of Electron Devices,* vol. 38, no. 4, pp. 717-719, 1991.

[30] P. Xiao and D. Staack, "Microbubble generation by microplasma in water," *Journal of Physics D: Applied Physics,* vol. 47, no. 35, 2014.

[31] D. Roupassov, A. Nikipelov, M. Nudnova and A. Starikovskii, "Flow separation by plasma actuator with nanosecond pulsed-periodic discharge," *AIAA Journal,* vol. 47, no. 1, pp. 168-85, 2009.

[32] M. Krishnan, "The dense plasma focus: a versatile dense pinch for diverse applications," *IEEE Transactions on Plasma Science,* vol. 40, no. 12, pp. 3189-3221, 2012.

[33] J. Mather, "15. Dense Plasma Focus," *Methods in Experimental Physics,* vol. 9, pp. 187-249, 1971.

[34] L. Soto, "New trends and future perspectives on plasma focus research," *Plasma Physics and Controlled Fusion,* vol. 47, pp. A361-A381, 2005.

[35] V. Gribkov, "Current and perspective applications of dense plasma focus devices," in *17th IAEA Technical Meeting on Research Using Small Focus Devices*, Lisbone, 2007.

[36] S. Mulyodrono, A. Smith, U. Suryadif'W and M. Zakaullahf, "A simple facility for the teaching of plasma dynamics and plasma nuclear fusion," *American Journal of Physics,* vol. 1, no. 1, 1988.

[37] M. Chernyshova, I. Ivanova-Stanik, L. Karpinski, M. Scholz, B. Ulejczyk and I. Demchenki, "Deposition of nanolayers by means of dense plasma focus," *Czechoslovak Journal of Physics,* vol. 56, pp. B237-42, 2006.

[38] T. Hussain, R. Ahmad, I. Khan, J. Siddiqui, N. Khalid and A. Bhatti, "Deposition of titanium nitride on Si(100) wafers using plasma focus," *Nuclear Instruments & Methods in Physics Research Section B - Beam Interactions with Materials and Atoms,* vol. 267, pp. 768-772, 2009.

[39] E. Ghareshabani, R. Rawat, R. Verma, S. Karamat and S. Sobhanian, "Low energy repetitive miniature plasma focus device as a high deposition rate facility for synthesis of DLC thin films," *Applied Surface Science,* vol. 256, pp. 4977-4983, 2010.

[40] T. Zhang, J. Lin, A. Patran, D. Wong, S. Hassan and S. Mahmood, "Optimization of a plasma focus device as an electron beam source for thin film deposition," *Plasma Sources Science & Technology,* vol. 16, pp. 250-256, 2007.

[41] Z. Wang, H. Yousefi, Y. Nishino, H. Ito and K. Masugata, "Perparation of silicon carbide film by a plasma focus device," *Physics Letters A,* vol. 372, pp. 7179-7182, 2008.

[42] R. Rawat, P. Lee, T. White, L. Ying and S. Lee, "Room temperature deposition of titanium carbide thin films using dense plasma focus device," *Surface & Coatings Technology,* vol. 138, pp. 159-165, 2001.

[43] I. Khan, M. Hassan, R. Ahmad, G. Murtaza, M. Zakaullah and R. Rawat, "Synthesis of zirconium oxynitride (ZrON) nanocomposite films on zirconium substrate by dense plasma focus device," *International Journal of Modern Physics B,* vol. 22, pp. 3941-3955, 2008.

[44] C. Kant, M. Srivastava and R. Rawat, "Thin carbon film deposition using energetic ions of a dense plasma focus," *Physics Letters A,* vol. 226, pp. 212-216, 1997.

[45] F. McDaniel, B. Freeman and C. Fowler, "Applications of a neutron producing dense plasma focus," in *Neutrons in Research and Industry*, Crete, Greece, 1997.

[46] L. Soto, P. Silva, J. Moreno, M. Zambra, W. Kies and R. Mayer, "Demonstration of neutron production in a table-top pinch plasma focus device operating at only tens of Joules," *Journal of Physics D: Applied Physics,* vol. 41, pp. 1-7, 2008.

[47] A. Bernard, P. Cloth, H. Conrads, A. Coudeville, G. Gourlan and A. Jolas, "Dense plasma focus - high intensity neutron source," *Nuclear Instruments & Methods,* vol. 145, pp. 191-218, 1977.

[48] R. Verma, R. Rawat, P. Lee, S. Lee, S. Springham and T. Tan, "Effect of cathode structure on neutron yield performance of a miniature plasma focus device," *Physics Letters A,* vol. 373, pp. 2568-2571, 2009.

[49] P. Silva, J. Moreno, L. Soto, L. Birstein, R. Mayer and W. Kies, "Neutron emission from a fast plasma focus of 400 Joules," *Applied Physics Letters,* vol. 83, pp. 3269-3271, 2003.

[50] M. Yokoyama, Y. Kitagawa and Y. Yamada, "Neutron emission studies in a dense plasma focus," *Dense Z-pinches,* vol. 195, pp. 530-534, 1989.

[51] H. Asai and I. Ueno, "Neutron source based on the repetitive dense plasma focus model," *Fusion Engineering and Design,* vol. 7, pp. 335-343, 1989.

[52] H. Bhuyan, S. Mohanty, N.K.Neog, S. Bujarbana and R. Rout, "Comparative study of soft x-ray emission characteristics in a low energy dense plasma focus," *Journal of Applied Physics,* vol. 95, pp. 2975-2981, 2004.

[53] C. Pavez and L. Soto, "Deomonstration of x-ray emission from an ultraminiature pinch plasma focus discharge operating at 0.1 J nanofocus," *IEEE Transactions on Plasma Science,* vol. 38, pp. 1132-1135, 2010.

[54] M. Zambra, P. Silva, C. Pavez, D. Pasten, J. Morena and L. Soto, "Experimental results on hard x-ray energy emitted by a low energy plasma focus device: a radiographic image analysis," *Plasma Physics and Controlled Fusion,* vol. 51, no. 12, pp. 1-10, 2009.

[55] M. Barbaglia, H. Bruzzone, H. Acuna, L. Soto and A. Clausse, "Experimental study of the hard x-ray emissions in a plasma focus of hundred Joules," *Plasma Physics and Controlled Fusion,* vol. 51, no. 4, pp. 1-9, 2009.

[56] R. Verma, R. Rawat, P. Lee, M. Krishnan, S. Springham and T. Tan, "Miniature plasma focus device as a compact hard x-ray source for fast radiography applications," *IEEE Transactions on Plasma Science,* vol. 38, pp. 652-657, 2010.

[57] S. Hussain and M. Zakaullah, "Study of plasma focus as a hard x-ray source for non-destructive testing," *Modern Physics Letters B,* vol. 21, pp. 1643-1650, 2007.

[58] H. Conrads, "Dense plasam focus as a neutron source for fusion research," *Nuclear Science and Engineering,* vol. 106, pp. 299-307, 1990.

[59] L. Soto, C. Pavez, A. Tarifeno, M. Cardenas and J. Moreno, "Fusion studies using plasma focus devices from hundred of kilojoules to less than one Joule. Scaling, stability, and fusion mechanisms," in *Proceedings of the 22nd IAEA Fusion Energy Conference*, Geneva, 2008.

[60] S. Saw and S. Lee, "Scaling the plasma focus for fusion energy considerations," *International Journal of Energy Research,* vol. 35, pp. 81-88, 2011.

[61] L. Soto, C. Pavez, A. Tarifeno, J. Moreno and M. Cardenas, "Scaling, stability and fusion mechanisims. Studies using plasma focus devices from tens of kilojoules to tenths of Joules," in *Dense Z-Pinches: 7th International Conference*, Alexandria, 2009.

[62] V. Gribkov, A. Dubrovsky, L. Karpinski, R. Miklaszewski, M. Paduch and M. Scholz, "The dense plasma focus opportunities in detection of hidden objects by using nanosecond impulse neutron inspection system (NINIS)," *Plasma and Fusion Science,* vol. 875, pp. 415-418, 2006.

[63] A. Gribkov, S. Latyshev, R. Miklaszewski, M. Chernyshova, K. Drozdowicz and U. Wiacek, "A dense plasma focus based neutron source for a single shot detection of illicit materials and explosives by a nanosecond neutron pulse," *Physica Scripta,* vol. 81, pp. 1-12, 2010.

[64] M. Paduch, R. Miklaszewski, V. Pimenov, L. Ivanov, E. Dyomina, S. Maslyaev and M. Orlova, "PF-6: an effective plasma focus as a source of ionizing radiation and plasma streams for applications in material technology, biology and medicine," *Nukleonika,* vol. 51, no. 1, pp. 55-62, 2006.

[65] L. Soto, C. Pavez, A. Tarifeno, J. Moreno and F. Veloso, "Studies on scalability and scaling laws for the plasma focus: similarities and differences in devices from 1 MJ to 0.1 J," *Plasma Sources Science & Technology,* vol. 19, pp. 1-9, 2010.

[66] S. Lee and A. Serban, "Dimensions and lifetime of the plasma focus pinch," *IEEE Transactions on Plasma Science,* vol. 24, pp. 1101-1105, 1996.

[67] S. Saw and S. Lee, "Scaling laws for the plasma focus machines from numerical experiments," *Energy and Power Engineering,* vol. 2, no. 1, pp. 65-72, 2010.

[68] S. Lee, "Plasma focus radiative model: Review of the Lee model code," *Journal of Fusion Energy,* vol. 33, no. 4, pp. 319-335, 2014.

[69] A. Abdou, M. Ismail, A. Mohamed, S. Lee, S. Saw and R. Verma, "Preliminary results of Kansas State University dense plasma focus," *IEEE Transactions on Plasma Science,* vol. 40, no. 10, pp. 2741-2744, 2012.

[70] L. Soto, C. Pavez, J. Moreno, J. Pedreros and L. Altamirano, "Non-radioactive source for field application based in a plasma focus of 2 J: pinch evidence," *Journal of Physics: Conference Series,* vol. 511, no. 1, pp. 1-3, 2014.

[71] L. Soto, C. Pavez, J. Moreno, M. Barbaglia and A. Clausse, "Nanofocus: and ultra-miniature dense pinch plasma focus device with submillimetric anode operating at 0.1 J," *Plasma Sources Science & Technology,* vol. 18, pp. 1-5, 2009.

[72] J. Moreno, P. Silva and L. Soto, "Optical observations of the plasma motion in a fast plasma focus operating at 50 J," *Plasma Sources Science & Technology,* vol. 12, pp. 39-45, 2003.

[73] C. Silva, L. Soto, W. Kies and J. Moreno, "Pinch evidence in a fast and small plasma focus of only tens of joules," *Plasma Sources Science & Technology,* vol. 2004, pp. 329-332, 2004.

[74] S. Hassan, E. Clark, C. Petridis, G. Androulakis, J. Chatzakis, P. Lee, N. Papadogiannis and M. Tatarakis, "Filamentary structure of current sheath in miniature plasma focus," *IEEE Transactions on Plasma Science,* vol. 39, no. 11, pp. 2432-2433, 2011.

[75] S. Hassan, T. Zhang, A. Patran, R. Rawat, S. Springham, T. Tan, D. Wong, W. Wang, S. Lee, V. Gribkov, S. Mohanty and R. Lee, "Pinching evidence in a

miniature plasma focus with fast pseudospark switch," *Plasma Sources Science & Technology,* vol. 15, pp. 614-619, 2006.

[76] V. Gribkov, B. Bienkowska, M. Borowiecki, A. Dubrovsky, I. Ivanova-Stanik, L. Karpinski, R. Miklaszewski, M. Paduch, M. Scholz and K. Tomaszewski, "Plasma dynamics in PF-1000 device under full-scale energy storage: I. Pinch dynamics," *Journal of Physics D: Applied Physics,* vol. 40, no. 7, 2007.

[77] R. E. Shedldahl and P. C. Klimas, "Aerodynamic characteristics of seven symmetrical airfoil sections through 180-degree angle of attack for use in aerodynamic analysis of vertical axis wind turbines," Sandia National Labs, Albuquerque, 1981.

[78] H. Janocha, Actuators: Basics and Applications, Berlin: Springer, 2004.

[79] L. Cattafesta and M. Sheplak, "Actuators for active flow control," *Annu Rev Fluid Mech,* vol. 43, pp. 247-72, 2011.

[80] P. Bletzinger, B. N. Ganguly, D. V. Wie and A. Garscadden, "Plasmas in high speed aerodynamics," *Journal of Physics D: Applied Physics,* vol. 38, no. 4, pp. R33 - R57, 2005.

[81] M. Samimy, I. Adamovich, B. Webb, J. Kastner, J. Hileman, S. Keshav and P. Palm, "Development and characterization of plasma actuators for high speed jet control," *Experiments in Fluids,* vol. 37, pp. 577-588, 2004.

[82] M. Samimy, J.-H. Kim, J. Kastner, I. Adamovich and Y. Utkin, "Active control of high-speed and high Reynolds jets using plasma actuators," *Journal of Fluid Mechanics,* vol. 578, pp. 305-330, 2007.

[83] F. Thomas, A. Kozlov and T. Corke, "Plasma actuators for bluff body flow control," in *AIAA Flow Control Conference*, San Francisco, 2006.

[84] J. Huang, T. Corke and F. Thomas, "Plasma actuators for separation control of low pressure turbine blades," *AIAA Journal,* vol. 44, no. 1, pp. 51-57, 2006.

[85] J. D. Anderson, Fundamentals of Aerodynamics, New York: McGraw-Hill, 1991.

[86] K. R. Grossman, B. Z. Cybyk and D. M. VanWie, "Sparkjet actuators for flow control," in *AIAA - 41st Aerospace Sciences Meeting and Exhibit*, Reno, NV, 2003.

[87] E. Moreau, "Airflow control by non-thermal plasma actuators," *Journal of Physics D: Applied Physics,* vol. 40, no. 3, pp. 605-636, 2007.

[88] T. Corke and M. Post, "Overview of plasma flow control: concepts, optimization and applications," in *AIAA - 43rd Aerospace Sciences Meeting and Exhibit*, Reno, NV, 2005.

[89] T. Corke, C. L. Enloe and S. Wilkinson, "Dielectric barrier discharge plasma actuators for flow control," *Annual Review of Fluid Mechanics,* vol. 42, pp. 505-529, 2010.

[90] J. J. Wang, K. Choi, L. Feng, T. N. Jukes and R. D. Whalley, "Recent developments in DBD plasma flow control," *Progress in Aerospace Sciences,* vol. 62, pp. 52-78, 2013.

[91] C. L. Enloe, T. E. McLaughlin, R. D. VanDyken and J. C. Fischer, "Plasma structure in the aerodynamic plasma actuator," in *AIAA - 42nd Aerospace Sciences Meeting and Exhibit*, Reno, NV, 2004.

[92] C. He and T. Corke, "Plasma flaps and slats: an application of weakly ionized plasma actuators," *Journal of Aircraft,* vol. 46, no. 3, pp. 864-873, 2009.

[93] M. Post and T. Corke, "Separation control on a high angle of attack airfoil using plasma actuators," *AIAA Journal,* vol. 42, no. 11, pp. 2177-2184, 2004.

[94] M. Post and T. Corke, "Separation control using plasma acutators - stationary and oscillating airfoils," in *42nd AIAA Aerospace Sciences Meeting and Exhibit*, Reno, NV, 2004.

[95] M. Post and T. Corke, "Separation control using plasma actuators: dynamic stall vortex control on oscillating airfoil," *AIAA Journal,* vol. 44, no. 12, pp. 3125-3135, 2006.

[96] J. Jolibois, M. Forte and E. Moreau, "Separation control along a NACA 0015 airfoil using a dielectric barrier discharge actuator," in *IUTAM Symposium on Flow Control and MEMS*, Netherlands, 2008.

[97] M. Bolitho and J. J, "Use of aggregate plasma synthetic jet actuators for flow control," in *45th AIAA Aerospace Sciences Meeting and Exhibit*, Reno, NV, 2007.

[98] A. Santhanakrishnan and J. Jacob, "Flow control using plasma actuators and linear/annular plasma synthetic jet actuators," in *3rd AIAA Flow Control Conference*, San Francisco, CA, 2006.

[99] B. Z. Cybyk, K. R. Grossman and J. T. Wilkerson, "Single pulse performance of the sparkjet flow control actuator," in *AIAA - 43rd Aerospace Sciences Meeting and Exhibit*, Reno, NV, 2005.

[100] B. Z. Cybyk, J. T. Wilkerson, K. R. Grossman and D. M. Van Wei, "Computational Assessment of the sparkjet flow control actuator," in *33rd AIAA Fluid Dynamics Conference and Exhibit*, Orlando, FL, 2003.

[101] B. Z. Cybyk, J. T. Wilkerson and K. R. Grossman, "Performance characteristics of the sparkjet flow control actuator," in *2nd AIAA Flow Control Conference*, Portland, OR, 2004.

[102] V. Narayanaswamy, L. Raja and N. Clemens, "Characterization of a high frequency pulsed plasma jet actuator for supersonic flow control," *AIAA Journal,* vol. 48, no. 2, pp. 297-305, 2010.

[103] V. Narayanaswamy, J. Shin, N. Clemens and L. Raja, "Investigation of plasma generated jets for supersonic flow control," in *46th AIAA Aerospace Sciences Meeting and Exhibit*, Reno, NV, 2008.

[104] V. Narayanaswamy, N. Clemens and L. Raja, "Investigation of a pulsed-plasma jet for shock boundary layer control," in *48th AIAA Aerospace Sciences Meeting*

Including the New Horizons Forum and Aerospace Exposition, Orlando, FL, 2010.

[105] V. Narayanaswamy, L. Raja and N. Clemens, "Control of a shock/boundary layer interaction by using a pulsed plasma jet actuator," *AIAA Journal,* vol. 50, no. 1, pp. 246-249, 2012.

[106] J. Shin, N. V, L. Raja and N. Clemens, "Characterization of a direct-current glow discharge plasma actuator in low pressure supersonic flow," *AIAA Journal,* vol. 45, no. 7, pp. 1596-1605, 2007.

[107] U. Kogelschatz, B. Eliasson and E. W, "Dielectric barrier discharges - principles and applications," *Journal of Physics IV France,* vol. 7, pp. C4-47 - C4-66, 1997.

[108] K. Anderson and D. Knight, "Characterization of a single pulse of a plasma jet," in *50th AIAA Aerospace Sciences Meeting including the New Horizons Forum and Aerospace Exposition*, Nashville, TN, 2012.

[109] S. Haack, T. Taylor, J. Emhoff and B. Cybyk, "Development of an analytical sparkjet model," in *5th Flow Control Conference*, Chicago, IL, 2010.

[110] T. Reedy, N. Kale, J. Dutton and G. Elliott, "Experimental characterization of a pulsed plasma jet," *AIAA Journal,* vol. 51, no. 8, pp. 2027-2031, 2013.

[111] B. Z. Cybyk, D. H. Simon and H. B. Land III, "Experimental characterization of a supersonic flow control actuator," in *44th AIAA Aerospace Sciences Meeting and Exhibit*, Reno, NV, 2006.

[112] J. Di, Y. L, J. Min, S. Huimin, C. Wei, S. Quan and L. Fanyu, "Experimental characterization of the plasma synthetic jet actuator," *Plasma Science and Technology,* vol. 15, no. 10, 2013.

[113] S. Haack, T. Taylor, B. Cybyk, C. Foster and F. Alvi, "Experimental estimation of sparkjet efficiency," in *AIAA - 42nd Plasmadynamics and Lasers Conference*, Honolulu, HI, 2011.

[114] M. Golbabaei-Asl and D. Knight, "Novel technique to determine sparkjet efficiency," *AIAA Journal,* vol. 53, no. 2, pp. 501-504, 2015.

[115] A. Belinger, P. Hardy, N. Gherardi, N. Naude, J. Cambronne and D. Caruana, "Influence of the spark discharge size on a plasma synthetic jet actuator," *IEEE Transactions on Plasma Science,* vol. 39, no. 11, pp. 2334-2335, 2011.

[116] T. Emerick, M. Ali, C. Foster, F. Alvi and S. Popkin, "SparkJet characterizations in quiescent and supersonic flowfields," *Experiments in Fluids,* vol. 55, no. 12, pp. 1-21, 2014.

[117] H. Zong, Y. Wu, M. Jia, H. Song, H. Liang, Y. Li and Z. Zhang, "Influence of geometrical parameters on performance of plasma synthetic jet actuators," *Journal of Physics D: Applied Physics,* vol. 49, no. 2, 2015.

[118] W. Pollard, S. Mathew, A. Balasubramanian and D. Staack, "Computational and experimental characterization of synthetic jets from a slotted spark type plasma actuator for flow control," *To be submitted,* 2016.

[119] D. Caruana, F. Rogier, G. Dufour and C. Gleyzes, "The plasma synthetic jet actuator, physics, modeling and flow control application on separation," *Aerospace Lab,* no. 6, pp. 1-13, 2013.

[120] R. Hooke, "Of a new property in the air," *Micrographia Observation,* vol. 58, 1665.

[121] J. Meyer-Arendt, Selected papers on schlieren optics, Forest Grove: SPIE Optical Engineering Press, 1992.

[122] S. Mitra, M. Chaskar and S. Phadke, "Design and fabrication of simple schlierenscope," *American Journal of Physics,* vol. 49, no. 2, pp. 158-161, 1981.

[123] A. Kantrowitz, "A sharp-focusing schlieren system," *Journal of the Aeronautical Sciences,* vol. 17, no. 5, 2012.

[124] A. Vogel, I. Aptiz, S. Freidank and R. Dijkink, "Sensitive high resolution white light schlieren technique with a large dynamic range for the investigation of ablation dynamics," *Optics Letters,* vol. 31, no. 12, pp. 1812-1814, 2006.

[125] P. Cords Jr, "A high resolution, high sensitivity color schlieren method," *Optical Engineering,* vol. 6, no. 3, 1968.

[126] E. Goldhahn and J. Seume, "The background oriented schlieren technique: sensitivity, resolution and application to a three dimensional density field," *Experiments in Fluids,* vol. 43, no. 2-3, pp. 241-249, 2007.

[127] M. Rogers and S. Morris, "Natural versus forced convection in laminar starting plumes," *Physics of Fluids,* vol. 21, no. 8, 2009.

[128] D. Shlien, "Some laminar thermal and plume experiments," *Physics of Fluids,* vol. 19, no. 8, pp. 1089-1098, 1976.

[129] S. Orieux, C. Rossi and D. Esteve, "Thrust stand for ground test of solid propellean microthrusters," *Review of Scientific Instruments,* vol. 73, no. 7, pp. 2694-2698, 2002.

[130] T. Haag, "Thrust stand for pulsed plasma thrusters," *Review of Scientific Instruments,* vol. 68, no. 5, pp. 2060-2067, 1997.

[131] M. Wilson, S. Bushman and R. Burton, "A compact thrust stand for pulsed plasma thrusters," in *IEPC Paper*, 1997.

[132] R. Durscher and S. Roy, "Evaluation of thrust measurement techniques for dielectric barrier discharge actuators," *Experiments in Fluids,* vol. 53, no. 4, pp. 1165-1176, 2012.

[133] A. Jamison, A. Ketsdever and E. Muntz, "Gas dynamic calibration of a nano-Newton thrust stand," *Review of Scientific Instruments,* vol. 73, no. 10, pp. 3629-3637, 2002.

[134] C. Phipps, J. Luke, W. Helgeson and R. Johnson, "A low-noise thrust stand for microthrusters with 25 nN resolution," in *AIP Conference Proceedings*, 2006.

[135] E. Cubbin, J. Ziemer, E. Choueiri and R. Jahn, "Pulsed thrust measurements using laser interferometry," *Review of Scientific Instruments,* vol. 68, no. 6, pp. 2339-2346, 1997.

[136] P. Bradshaw and R. Pankhurst, "The design of low-speed wind tunnels," *Progress in Aerspace Sciences,* vol. 5, pp. 1-69, 1964.

[137] G. Johl, M. Passmore and P. Render, "Design methodology and performance of an indraft wind tunnel," *The Aeronautical Journal,* vol. 108, no. 1087, pp. 465-473, 2004.

[138] W. Chakroun, I. Al-Mesri and S. Al-Fahad, "Effect of surface roughness on aerodynamic characteristics of a symmetric airfoil," *Wind Engineering,* vol. 28, no. 5, pp. 547-564, 2004.

[139] N. Gawloski, Interviewee, *Discussion of actuators for reducing skin friction drag at high Ma.* [Interview]. 14 October 2015.

[140] A. Bernard, H. Bruzzone, P. Choi, H. Chuaqui, V. Gribkov, J. Herrera, K. Hirano and V. Zoita, "Scientific status of plasma focus research," *Journal of Moscow Physical Society,* vol. 8, pp. 93-170, 1998.

[141] J. Robertson, "Diamond-like amorphous carbon," *Materials Science and Engineering,* vol. 37, no. 4, pp. 129-281, 2002.

[142] J. Gaudet, R. Barker, J. Buchenauer, C. Christodoulou, J. Dickens, M. Gundersen and R. Joshi, "Research issues in developing compact pulsed power for high peak power applications on mobile platforms," *Proceedings of the IEEE,* vol. 92, no. 7, pp. 1144-1165, 2004.

[143] C. Reddy, A. Patel, P. Naresh, A. Sharma and K. Mittal, "Experimental investigations of argon spark gap recovery times by developing a high voltage double pulse generator," *Review of Scientific Instruments,* vol. 85, no. 6, 2014.